

ABSTRACT

Stiff clays and weak rocks are quasi-frictional materials in which the total shearing resistance is the by-product of the mutual contribution of interlocking or bonding between particles and frictional resistance. The shearing response of such geomaterials at low confining stresses usually indicates a reduction in strength in the post-peak regime. Back analysis of the failures for the engineered systems constructed in these geomaterials showed that the operational strength could not be expressed in terms of either the peak or residual strength.

This thesis focuses on establishing a framework to identify the operational strength of quasi-frictional materials as well as the distribution of strength parameters at low confining pressure with plastic strain. In the first part of the thesis, two pre-peak strength thresholds are identified as promising candidates to quantify the operational strength of geomaterials instead of their peak and residual strengths. In the second part a comprehensive experimental investigation on a McMurray locked sand Formation is presented to reveal the upper and lower strength thresholds, based on local strain measurements. In the third part of the thesis, a simplified approach is suggested to partition shear strength parameters with plastic strain. Its significance in revealing the similarity in the shearing responses of bonded geomaterials irrespective of their origins, and in capture the transition between soils and rocks is presented. In the fourth part of the thesis, a numerical simulation was carried out to reveal the merits of

strain-dependent parameters in capturing progressive failure of slopes in stiff clays.

Based on the current investigation, it was shown that the onset of volumetric strain reversal may be considered as the upper strength threshold for interlocked/bonded geomaterials to avoid localization and excessive deformation. On the other hand, to avoid initiation of interlocking/bond degradation between particles, the onset of lateral strain nonlinearity may be assigned as the lower strength threshold. The high uniaxial compressive strength of locked sand is due to the interlocked fabric in the absence of virtual bonding, as revealed from SEM images and examination of colored thin sections. The failure of locked sand under uniaxial compressive stress condition is achieved by the creation of dilation bands in the direction of the major principal stress, forming columns/walls that buckle to form a persistent shear band. The interlocking and frictional resistance components are not mobilized simultaneously in locked sand. For stiff clays, the cohesion and friction are not mobilized simultaneously as implied in Mohr-Coulomb criterion. The similarity in the shearing response of various bonded geomaterials (existence of a plateau in pre-peak regime) and the transition between frictional and bonded materials can be sufficiently captured by using the strain-dependent strength parameters. The concept of strain-dependent parameters is also a powerful approach to capture the progressive failure of slopes in stiff clays and to interpret the deviation of the operational strength from the laboratory peak strength at the instant of failure.

TABLE OF CONTENTS

	Page
CHAPTER 1: INTRODUCTION.....	1
1.1 General.....	1
1.2 Classification of geomaterials and shear response	2
1.3 Source of peak strength in stiff clays	3
1.4 Laboratory stress-strain curves and failure modes of geomaterials	5
1.5 Mobilized field strength in field problems.....	7
1.6 Simultaneous mobilization of strength parameters.....	9
1.6.1 Laboratory and field stress-strain perspective for quasi-frictional materials	11
1.7 Laboratory local and global strain measurements	13
1.7.1 Testing conditions and strain measurements.....	15
1.8 Locked sands	18
1.9 Objective of the thesis	21
1.10 Methodology.....	23
1.11 Organization of the thesis.....	25
 CHAPTER 2: ONSETS OF DILATION AND LOCALIZATION THRESHOLDS IN SOILS AND ROCKS	 36
2.1 Introduction.....	36
2.2 Definition of shear-induced dilation and localization	38
2.3 Shear-induced dilation and localization thresholds.....	39
2.3.1 Coarse-grained soils and weak rocks	40
2.3.1.1 Dense sand.....	40
2.3.1.2 Locked sand.....	41
2.3.1.3 Sandstone.....	43

2.3.2	Fine grained soils and weak rocks	46
	2.3.2.1 Overconsolidated silty clay.....	46
	2.3.2.2 Bonded clay	47
2.3.3	Hard crystalline rock (granite)	48
2.4	Significance of onset of dilation threshold	50
2.5	Onset of shear-induced dilation and long-term strength.....	51
	2.5.1 Sand.....	52
	2.5.2 Granite	52
	2.5.3 Soft crystalline rock (rock salt)	54
2.6	Extension-induced dilation in bonded geomaterials	56
2.7	Summary and Conclusions.....	60

CHAPTER 3: HIGH-HILL RIVER FORMATION GENERAL CHARACTERISTICS AND UNIAXIAL TEST SET-UP 81

3.1	Introduction.....	81
3.2	General characteristics of locked sands.....	83
	3.2.1 Locked sands among geotechnical materials	83
	3.2.2 Diagnostic aids for locked sands identification.....	84
3.3	Investigated area and sampling.....	86
	3.3.1 Oil-free slopes and sampling area	86
	3.3.2 Geological settings of McMurray Formation.....	87
	3.3.2.1 Stratigraphy and depositional history of McMurray Formation	88
3.4	Physical properties	90
3.5	Micro-fabric analyses and mineralogical composition	91
	3.5.1 Source of interlocking due to diagenesis.....	92
	3.5.3 Thin sections under petrographic microscope.....	96
	3.5.4 Fabric orientation using Digital Image Analysis (DIA)	99
3.6	Experimental procedures and measuring technique	101
	3.6.1 LVDTs and data acquisition	101
	3.6.1.1 LVDT calibration.....	102
	3.6.1.2 Stability characteristics and proof testing	103

3.6.2	Sample preparation and mechanical configuration	105
3.6.2.1	Sample preparation and dimensions.....	105
3.6.2.2	Mechanical configuration set-up.....	106
3.7	Significance of local strain measurements	110
3.7.1	Local vs. external stress-axial strain curves.....	110
3.7.2	Local and external axial strain rates.....	111
3.8	Summary and conclusions	113

CHAPTER 4: MOBILIZED STRENGTH OF HIGH-HILL RIVER LOCKED SAND FORMATION AND FAILURE MODES 143

4.1	Introduction.....	143
4.2	Effect of testing conditions on laboratory results	146
4.3	Damage thresholds for brittle rocks	148
4.3.1	Crack closure stress.....	148
4.3.2	Damage initiation stress.....	149
4.3.3	Damage coalescence threshold	149
4.4	Experimental results.....	150
4.4.1	Axial stress vs. axial-strain curve	150
4.4.2	Axial stress vs. lateral strain curve	151
4.4.3	Volumetric strains and inception of localization.....	152
4.4.4	Damage and failure evolution	154
4.4.4.1	Detection of damage thresholds for locked sand ...	154
4.4.4.2	Evolution of failure in locked sand.....	156
4.4.5	Mobilized strength components in locked sands	158
4.4.5.1	Interlocking and frictional strength contributions with plastic strain	160
4.4.5.2	Pre-peak interlocking brittleness and friction hardening.....	163
4.4.5.3	Mobilized strength parameters at damage thresholds	165
4.5	Development of columnar structures and dilation bands	167
4.5.1	Theoretical prediction of dilation band occurrence.....	169
4.6	Multistage uniaxial creep test	172

4.6.1	Testing procedure	173
4.6.2	Stress- strain and volumetric strain curves	174
4.6.3	Creep strains and strain rates	176
	4.6.3.1 Axial creep strains and strain rate.....	176
	4.6.3.2 Lateral creep strains and strain rate	177
	4.6.3.3 Volumetric creep strain	178
4.6.4	Implications of creep test	179
4.7	Direct shear box (DSB) results at low normal stress	180
4.7.1	Direct shear results	181
	4.7.1.1 Shear stress vs. horizontal deformation.....	181
	4.7.1.2 Vertical deformation vs. horizontal deformation	182
	4.7.1.2 Failure envelope at low normal stress	182
	4.7.1.3 Corrected shear stress vs. horizontal deformation	183
	4.7.1.4 Mobilized strength under DSB	184
4.8	Summary and conclusions	185

**CHAPTER 5: MOBILIZED STRAIN-DEPENDENT STRENGTH
PARAMETERS FOR TWO NATURAL STIFF CLAYS 203**

5.1	Introduction.....	203
5.2	Historical development of strength parameters in clays	204
5.3	Partitioning of strain-dependent strength parameters in Mohr- Coulomb space	206
5.4	Partitioning of strain-dependent strength parameters for two natural stiff clays.....	209
	5.4.1 Pietrafitta clay	209
	5.4.2 Nanticoke clay.....	211
5.5	Bonding and frictional resistance in q-p space	212
	5.5.1 Incremental form of the strength equation in q-p space	215
5.6	Parametric study of the bearing of confining stresses on stress strain curves	216
	5.6.1 Contribution of frictional and bonding resistance at different confining stresses	216
	5.6.2 Failure, bonding, and plateau envelopes	218

5.6.3	Resemblance of stress-strain curves' shapes and failure envelopes of bonded geomaterials with different origin	219
5.7	Remarks on mobilized strength of bonded geomaterials.....	220
5.8	Summary and Conclusions.....	222

CHAPTER 6: SIGNIFICANCE OF STRAIN-DEPENDENT STRENGTH PARAMETERS IN THE ASSESSMENT OF SLOPE STABILITY PROBLEMS..... 241

6.1	Introduction.....	241
6.2	Limit equilibrium and deformation analysis.....	243
6.3	Slope geometry and material properties.....	245
6.4	Peak strength parameters simulations	246
6.4.1	Finite difference simulations.....	246
6.4.2	Limit equilibrium simulation	248
6.5	Strain-dependent strength parameters simulation	249
6.5.1	Deviation of operational strength from peak strength.....	250
6.6	Comparison between slip surfaces' positions.....	254
6.7	Summary and conclusions	254

CHAPTER 7: SUMMARY, CONCLUSIONS, AND RECOMMENDATIONS 273

7.1	General.....	273
7.2	Objectives of the thesis	273
7.3	Summary and conclusions	275
7.3.1	Pre-peak strength thresholds for geomaterials	276
7.3.2	High-Hill River characteristics and significance of local strain measurements	278
7.3.3	High-Hill river geomechanical characteristics: damage thresholds, mobilized strength parameters, failure kinematics, and long-term strength	281
7.3.4	Simultaneous mobilization of strength parameters for bonded geomaterials.....	285
7.3.5	The significance of strain dependent strength parameters in slope stability problems	287

7.4	General framework for simulation of boundary value problems in strain weakening materials	289
7.5	Recommendations for future investigation	290
REFERENCES		292
Appendix A : Published conference papers		319

LIST OF TABLES

	Page
Table 3.1 Summary of physical and mechanical characteristics of locked sands.....	116
Table 3.2 Summary of Depositional environment as well as lithology of McMurray Formation members.....	117
Table 3.3 Summary of main physical properties of High Hill river formation.....	117
Table 3.4 Calibration factors for transducers.....	118
Table 4.1 Elastic deformation parameters and damage thresholds.....	189
Table 4.2 Summary of testing steps and results.....	189
Table 6.1 Summary of M-C parameters.	257
Table 6.2 SRFs and average unbalanced forces.....	257
Table 6.3 Factor of safety based on LEM.....	257

CHAPTER 1: INTRODUCTION

1.1 General

In the field of geotechnical engineering, there is a wide spectrum of geomaterials ranging from soils to hard rocks. Geotechnical engineers have the responsibility of assuring the short- and long-term performance of civil engineering systems, e.g., underground excavations, foundations, earth-retaining structures, and slopes constructed on these geomaterials. As most civil engineering activities occur at relatively shallow depths, the geomechanical response of geomaterials at low stress levels is significant. Traditionally, the design of engineering systems has been based on the laboratory peak strength envelope with a suitable factor of safety to limit deformation to the pre-peak regime. However, back analyses of failures in stiff clays and weak and hard rocks has revealed an operational strength lying between the peak and residual strengths. Hence, a design based on the peak strength may be unconservative even with the application of a conventional factor of safety. On the other hand, accounting for residual strength may lead to a conservative and expensive design. Therefore, the main question is what operational strength, based on laboratory results, can be accounted for at low confining stresses to prevent short- and long-term failures? (see Figure 1.1). Answering this question will require an understanding of the mechanical behaviour at low confining stress to assign such a strength threshold.

This chapter provides a brief description of the problem, followed by an explanation of the thesis' objectives, methodology, and organization.

1.2 Classification of geomaterials and shear response

Figure 1.2 presents a simplified classification of geomaterials as well as their inherent shearing response and failure envelopes. For simplification, weak and hard rocks (i.e., bonded stiff clays, clayshales, locked sands, and sandstones) are considered as competent materials formed through the introduction of bonding or interlocking during diagenesis of soils. "Diagenesis" is defined as the process through which sediments are transformed into rocks. It is the sum of the physical, inorganic, chemical, or biochemical changes in a sedimentary deposit after initial accumulation, including mechanical compaction, addition of new material, removal of materials and transformation by change in the mineral phase, and the replacement of the mineral phase by another one (Friedman and Sanders 1978). Granular and cohesive soils are thought to be particulate in nature, and, hence, their strength is governed by the frictional resistance between particles with no virtual bonding. Cohesion in cohesive soils is understood to be the result of electrostatic, electromagnetic attraction, primary valence, and adhesion in contrast to true bonding in rocks partly due to the precipitation of cementation in pores (Mitchell 1993). The frictional component in all geomaterials is a function of the basic friction angle dictated by the mineral characteristics and dilation to allow for grains' arrangement at low stress levels (Taylor 1948; Thurairajah 1961; Rowe 1962; Bolton 1986). For rocks, strength is

derived from both friction (basic friction and dilation) and is dominated by diagenetic effects (interlocking and/or bonding).

The stress-strain curves for dense sands, overconsolidated (OC) clays, and rocks at low confining pressure show a reduction in load-carrying capacity after attaining the peak strength (the post-peak strain weakening), and the post-peak strain weakening is accompanied by positive volumetric strain (dilation). The extra component of the strength at peak is dominated by the dilation and bonding/interlocking for soils and rocks, respectively. On the other hand, loose sands and normally consolidated (NC) clays show a constant resistance that is dictated by the basic frictional resistance of particles with contractive volumetric strain and no dilation component (see Figure 1.2). For intermediate materials (quasi-frictional materials, i.e., stiff clays and weak rock), the extra component cannot be attributed completely either to bonding/interlocking or dilation as in soils or rocks.

1.3 Source of peak strength in stiff clays

The significance of cohesion and its contribution to peak strength for stiff clays as quasi-frictional materials constituting the boundary between soil and rocks remains controversial. However, no confusion should result when the cohesive component in clays is due to electrostatic, electromagnetic attraction, primary valance, and adhesion, in contrast to true bonding due to the precipitation of cementation in pores (Mitchell 1993). This issue has been clarified by comparing

the mechanical response of natural stiff or bonded clays with that of reconstituted clays (clays with the same mineralogical composition at water contents close to the liquid limit). Leroueil and Vaughn (1990), Burland et al. (1996), Cotecchia and Chandler (1997), Amorosi and Rampello (1998), and Cotecchia and Chandler (2004), attributed the behavioral deviation between reconstituted clays (particulate frictional material) and natural clays at peak due to the existence of bonds acquired during diagenetic processes.

Schofield (1998, 2006) argued that the extra resistance in stiff/overconsolidated reconstituted clays is an interlocking component (due to the dilatancy rate) and cannot be attributed to the cohesive effect at peak strength. Hence, a design should be based on critical state friction angle (the state at which no change in volumetric strains and shear stresses and can be approximated by the basic friction angle). This argument is in agreement with Rowe et al.'s (1963) analysis of two reconstituted clays, by using Rowe' (1962) correction for dilation. In contrast, Rampello et al. (1994) compared the failure envelopes of a natural bonded clay (Vallerccia clay) under the reconstituted and natural state. Accounting for the dilation rate (by using Rowe's stress dilatancy relation) and the void ratio at failure resulted in zero cohesion for reconstituted clay; however, a cohesive component was evident for the natural clay. Hence, it is recognized that bonding represents a main source of strength in natural stiff clays at peak strength regardless of its value. Figure 1.3 presents a schematic illustration for the corrected envelopes, accounting for dilation for both reconstituted and natural

clays. As this figure reveals, bonding is an intrinsic source of strength for natural clays, in contrast to unbonded clays (reconstituted clays), in which only basic frictional resistance can be accounted for.

1.4 Laboratory stress-strain curves and failure modes of geomaterials

The stress-strain response and the failure modes of tested cylindrical geomaterials under compression are dependent on the investigated range of stresses. Novello and Johnston (1995) showed that soils and weak and hard rocks show identical mechanical behaviour, and that their behaviour is solely a function of the confining pressure.

Figure 1.4 shows a schematic diagram of typical failure modes for geomaterials as a function of the confining stresses and the magnitude of bonding/interlocking. The increase in confining pressure or reduction of bonding between particles results in a transition from rock to soil. The first mode (A) corresponds to pure localized extension in the direction of the major principal stress, a failure mode common in rocks. Mode (C) corresponds to the localized shear mode of failure encountered at medium confining pressures. Mode (B) is an intermediate stage where geomaterials fail under mixed modes of localized extension and shear failure when tested at low to medium confining pressures. Mode (D) corresponds to distributed multiple shear cataclasis resulting in bulging of the tested geomaterials and occurs at high confining pressures, at which diagenetic effects are alleviated due to breakage of bonding or interlocking. For soils, Mode (C) is

recognized for both dense sands and OC clays. However, Mode (D) is the failure mode associated with loose sands and normally consolidated clays. The reduction of diagenetic effects with the increase of confining pressure results in a transition from purely bonded/interlocked geomaterials (Mode (A)) to purely frictional material (Mode (D)).

Figure 1.5 presents the stress-strain curves associated with such deformation modes. These curves can be divided into three stages that are dependent on the range of confining pressures as well as the diagenetic effects. These stages are purely elastic responses followed by strain hardening and/or weakening. For modes of deformation A through C, a significant reduction in strength occurs due to the brittleness of interlocking or bonding as well as the localization of the deformation into a distinct band. However, the reduction in strength and its rate tend to be less abrupt with an increase in confining pressure, partly due to reduction in interlocking/bonding effect. In case (D), no reduction in strength occurs and geomaterials experience infinite plastic strain and ductile behaviour with an indistinct localized mode of deformation. The general effect of the confining pressure is to increase the plastic (permanent) strain experienced by geomaterial within the failure surface. For case A, the loss of strength is sudden, and the strength along the failure surface is due to bonding/interlocking with almost negligible mobilized frictional resistance. For cases B and C, the strength on the failure surface is governed by both the friction and bonding/interlocking resistance. However, the contribution of the bonding/interlocking resistance is

more significant in case B than in case C. In case D, the resistance is governed by friction as most of the contribution due to bonding/interlocking is lost due to the application of high confining pressures.

The failure modes as well as the source of strength are understood in case A (strength is governed by bonding/interlocking), in case C (strength is governed by basic frictional resistance and dilation), and in case D (strength is governed by basic frictional resistance). However, the source of strength in case B and the mutual contribution of friction (its basic and dilation contributions) and bonding/interlocking resistance are not fully understood as the failure mode is the combined contribution of extension and shear, which is encountered mainly in quasi-frictional materials (e.g., stiff clays and weak rocks).

1.5 Mobilized field strength in field problems

The geotechnical literature provides extensive case histories of excessive movement and failures in stiff clays and rocks, and attributes these failures to the post-peak strain weakening and progressive failure due to bond degradation (e.g., Skempton, 1964, 1970; Conlon 1966; Bjerrum 1967; Pelli et al. 1991; Martin and Chandler 1994; Cooper et al. 1998; Olalla and Cueallar 2001). The back-analysis of failures usually indicates an operational strength somewhere between the peak and residual strengths. In this case, a design based on the peak strength can be unconservative. On the other hand, a design based on the residual strength can be utterly conservative and cost-ineffective.

Figure 1.6 shows the relationship between the mobilized strength normalized to the peak strength and plasticity index, based on the back analysis of several case histories involving stiff clays and weak rocks for clarification purpose (Mesri and Abdel-Ghaffar 1993). The brittleness index of such geomaterials, compiled by the author according to the available data, is imposed on this figure. The brittleness of stiff clays and weak rocks was calculated by using the brittleness index (IB) introduced by Bishop (1967) to describe the reduction of the load-carrying capacity from the peak (τ_p) to the residual strength (τ_r) as follows:

$$[1.1] \quad IB = \frac{\tau_p - \tau_r}{\tau_p} .$$

Figure 1.6 reveals that the increase in the brittleness index (the increase in the post-peak strength reduction) results in a reduction in the mobilized strength ratio from 100% to 50%. Up to a brittleness index of 35%, the mobilized strength is equivalent to the peak strength. For brittleness indices greater than 35 %, a significant reduction in the mobilized strength ratio occurs. For most of the collected points, the mobilized strength is almost 50-75% of the peak resistance. For hard rocks, Martin (1997) found that the mobilized strength in underground excavations could be as low as 30% of the laboratory peak strength. This level of strength corresponded to the level at which bond degradation was initiated in the pre-peak regime. Martin and Chandler (1994) argued that the strain hardening to attain peak resistance is a temporary effect that cannot be accounted for or even

mobilized in the field (see case B in Figure 1.4). Conlon (1966) argued that at the instant of failure in slope stability problems in stiff natural clays, the strength is governed by the bonding resistance and that the full frictional resistance cannot be accounted for. This argument is in agreement with that of Martin and Chandler (1994) for hard rocks.

Leroueil and Vaughn (1990) revealed the similarity in strength and volume change characteristics for natural soils and weak rocks due to bonding despite the difference in the bonds' formation condition. These researchers stated that the bond degradation is a progressive process resulting in the release of locked-in elastic energy that is best described as a function of the strain or strain energy. In the author's opinion, many bonded geomaterials including natural stiff clays, weak rocks, and hard rocks share the same characteristics, as nature does not differentiate among many types of bonded geomaterials. Bonded geomaterials possess a component of strength (the bonds between particles) that is initially responsible for extra resistance, and in spite of the bond strength, are susceptible to degradation during the shearing process.

1.6 Simultaneous mobilization of strength parameters

In practice, engineers traditionally use the peak strength parameters, for intact geomaterials with no weakness surfaces, with a suitable factor of safety based on experience in an attempt to ensure stability and to avoid excessive deformation by limiting the strength to the pre-peak regime. This goal is

customarily achieved for geomaterials by using the empirical Mohr-Coulomb hypothesis with the cohesion intercept and friction components of the strength. This approach adopts the assumption that friction and cohesion mobilize simultaneously throughout the deformation process, and that they are constant and independent of strain. However, many researchers have cast doubt on the validity of this approach, and have postulated the conceptual mechanism of the non-simultaneous mobilization of the frictional and bonding strength for natural clays, weak rocks, and hard rocks (e.g., Schmertmann and Osterberg 1960; Lambe 1960; Conlon 1966; Mencl 1965; Trollope 1967; Lajtai 1974; Martin and Chandler 1994).

If the assumption of simultaneous mobilization of the strength parameters is valid, then the parameters used despite applying the factor of safety, will be in error, for they will not correspond to the mobilized strength parameters at the working strain level, particularly where the bonding resistance degrades well before the peak strength (De Mello 1988), see Figure 1.7. These observations lead to the following questions:

1. What is the distribution of the strength parameters with the strain?;
2. What is the contribution of the frictional and bonding/interlocking resistance to the peak resistance at different confining pressures?, and, more importantly;
3. What defines the onset of failure in terms of stress and strain?

To prevent excessive movements and to ensure the short- and long-term stability of geotechnical structures, the shearing behavior of geomaterials in the pre-peak regime must be assessed to establish the threshold at which failure commences in favor of the peak and residual strengths, which are the signatures and consequences of failure. Observations of stress-strain curves showed that geomaterials exhibit significant change in their behaviour in the pre-peak regime, as will be shown in Chapter 2. Once this threshold is determined, it can be assigned as a safety boundary beyond which failure is imminent. Consequently, more attention should be paid to the pre-peak regime, in which failure is initiated, instead of focusing on the peak and post-peak regimes.

1.6.1 Laboratory and field stress-strain perspective for quasi-frictional materials

Figure 1.8 shows a typical stress strain curve for a quasi-frictional material at low confining pressure that is similar to case B in Figure 1.5. The peak resistance can be attributed to both frictional resistance and bonding/interlocking resistance, a combination of case A and C. The diagenetic resistance (interlocked or bonding resistance) tends to degrade in the pre-peak regime (point 1) followed by the mobilization of the basic frictional resistance and dilation at the peak (point 2). Hence, the peak strength is the by-product of dilation, basic friction, and the residual diagenetic effect. However, the residual strength is governed by the basic frictional resistance and residual bonding/interlocking, if it persists.

Figure 1.9 shows a schematic diagram for two materials, (E) and (I), derived from the same particulate source (O). The two configurations, E and I, differ in the way the particles are constrained even though macroscopically they are assumed to have equivalent strength. For configuration E, the particles are constrained externally (confining stresses, σ_3) and for configuration I, the particles are internally constrained (interlocking/bonding, σ_i). Although both materials are equally constrained, each displays different behaviour upon shearing. Configuration E shows higher strength when tested under higher confining pressure ($\sigma_3^1 > \sigma_3^2$), due to mainly its frictional nature (Figure 1.10). However, configuration I, although sheared at a confining pressure of σ_3^1 , can display a reduction in strength that is corresponding to a reduction in the applied confining stress (from σ_3^1 to σ_3^2) for configuration E. This result can be attributed to the reduction in local confinement between particles due to the bonding/interlocking degradation. As a result, the frictional resistance will not be fully mobilized, unlike dense frictional material with no diagenetic effect (E). This difference implies that the frictional resistance is not fully mobilized and that the strength is governed by the residual bonding/interlocking component and the partially mobilized frictional resistance (basic frictional resistance). Several investigators have found that the dilation tend to be suppressed prior to the bond degradation by comparing the mechanical behaviour of natural and reconstituted geomaterials (e.g., Coop and Atkinson 1993; Cotecchia and Chandler 1997; Cuccovillo and Coops 1999; Lo and Wardani, 2002,2003; Cresswell and Barton, 2003). These researchers

suggested that the dissipated energy prior to bond degradation should be accounted for along with the energy dissipated in friction. Fedda (2004) came to similar mechanistic conclusions for strength mobilization in bonded geomaterials.

In order to allow for the full mobilization of frictional resistance (basic friction and dilation), the loss of internal confinement should be compensated for by an extra confinement or even by allowing materials to attain higher strain levels after failure initiation, as shown in Figure 1.10. In a laboratory, this reduction in confinement can be compensated for by automatically adjusting the confinement, but it cannot be adjusted in the field, where the confining stresses cannot be controlled. In addition, most failures are sudden, but they will not be so if geomaterials actually deform the same way as they do in laboratory to reach full frictional resistance (Crawford 1963). Hence, a deviation should be expected between the laboratory results and the field mobilized strength.

1.7 Laboratory local and global strain measurements

In the previous sections, most of the discussion was related to stress and variation in geomaterials' strength. In this section, the discussion focuses on the measurement of strain in the laboratory and the significance of local strain measurements. Roscoe (1970) pointed out that "stress is a philosophical concept ... deformation is a physical reality". In engineering practice, problems are

customarily expressed in terms of stresses because geomaterials experience little strain before failure and because stresses can be indirectly calculated or measured (Watterson 1999). However, if the aim is to integrate stresses and strains into a unified framework, accurate measurement of strain is indispensable. For soils, Roscoe (1970) stressed the value of understanding failure's precursory strains, because eventual failure surfaces and their orientation are determined well prior to the peak strength. Desrues and Chambon (2002) also highlighted the importance of appropriately simulating the pre-peak response of soils up to the onset of localization instead of matching the peak strength, which is merely a sign of established failure.

Currently, it is recognized that local axial and lateral strain measurements in soils, weak and hard rocks are mandatory to reveal behavioral response in both the pre-peak and post-peak regime. (e.g., Shibuya et al. 1994; Martin and Chandler 1994; Scholey et al. 1995; Sheng et al. 1997; Fujii et al. 1998; Hayano et al. 1999; Bésuelle et al. 2000; Yimsiri et al. 2005; Sulem and Ouffroukh 2006). It is generally agreed that external axial strain measurements overestimate axial strains at any strain level due to bedding effects (irregularities at specimen extremes). As well, local strain measurements can reveal additional information regarding the onset of localization (the loss of strain uniformity) and the onset of bond degradation. Martin and Chandler (1994) investigated the behaviour of Lac Du Bonnet granite (strong bonded geomaterial) by using a triaxial apparatus while monitoring the local axial and lateral strains. These researchers revealed

additional strength thresholds in pre-peak regime through variation in local axial and lateral strains. These strength thresholds were true material properties independent of the scale and loading rate. Furthermore, Martin and Chandler (1994) argued that the peak strength was related to the testing boundary conditions, i.e., the length to diameter ratio, sample size and loading rate.

1.7.1 Testing conditions and strain measurements

Testing of cylindrical samples for both soils and rocks under compression is one of the common tests in geotechnical laboratories. It is implicitly assumed that the stress and strains are homogenous within the tested specimens, or that specimens deform as a right cylinder. Hence, arbitrary measurement of the deformation within specimens is acceptable. In geotechnical laboratories, axial strains are traditionally measured externally between the top and bottom platens. Lateral strains are customarily inferred from volume change measurements assuming uniformity of strains. However, this assumption is invalid when the end effects interfere with the experimental results, leading to data misinterpretation. The existence of rough platens results in the development of local confinement due to the mobilized shear stresses at the sample ends. As a consequence, samples become more restrained laterally at the ends compared to elsewhere. Hence, global measurements of the strain can be in error and reflect a system response rather than a behavioral response. An important factor also affecting the measured axial strains is the bedding errors due to irregular surfaces at the specimen/platen interface

(Figure 1.11). The bedding errors result in an increase in the measured global axial strains due to the breakage of asperities at the specimen/platen interface for soils and rocks (e.g., Hawkes and Mellor 1970; Brady and Brown 1985; Scholey et al. 1995; Hayano et al. 1999; Korinets and Alehossein 2002).

Figure 1.11 shows a schematic diagram of a typical 2:1 cylindrical soil specimen in a triaxial test with conventional upper and lower platens. The same effects recognized for a soil specimen are recognized for a rock specimen due to end effects and bedding errors. Along the specimen axis, the distributions of axial, lateral, and volumetric strains accounting for bedding errors and end restraints are shown. Accordingly, the specimen can be divided into three zones along its axis (Rowe and Barden 1964). The top and bottom zones are called “dead zones”. The middle zone (the “active zone”) represents the most homogeneous zone, which is not influenced by platen effects where deformation is not impeded. Within the dead zones, the deformation is highly restrained due to the end effects imposed by platens, causing shear stresses and frictional resistance at sample’s extremes. The distribution of shear stresses on the platens was studied by Lee (1978). Lee (1978) showed that for soils, the shear stresses tend to diminish within the middle of the specimen. Such shear stresses result in non-uniform deformation within the specimen, and, thereby, inherent strain non-homogeneity. An additional result of end effects is the development of a predominant shear band in soils at failure (Rowe and Barden 1964; Bishop

and Green 1965; Kirkpatrick and Belshaw 1968; Lade 1982). In the absence of shear stresses (perfect end conditions), the specimen should deform homogeneously, as in the middle zone, and multiple shear bands due to the uniformity of the strain should be rendered (Raju et al. 1972; Lade 1982).

Frost and Yang (2003) investigated the effect of end restraints and microstructure evolution in sand specimens, tested under the triaxial compression condition, at a confining pressure of 50 kPa. The specimen with lubricated ends showed the most uniform axial strains, lateral strains, and void ratios during the course of shearing along the specimen's vertical axis. The inclusion of the lubricated ends resulted in a slight reduction in the peak strength and the initial secant modulus, in contrast to the results with non-lubricated ends with the same slenderness ratio due to a reduction in the shear stresses at sample/platen interface. A direct effect of end restraints is the reduction in the expansive lateral strains and void ratio (dilation) at sample extremes, in contrast to the effects at the middle third (see Figure 1.10). Frost and Lang (2000) provided a quantitative measure of the local void ratio distribution for fine uniform quartz sand during triaxial compression test by using optical image analysis of images for resin impregnated specimens. The test results showed that the local void ratio was the largest near the center of the tested specimens (see Figure 1.10). The local void ratio first increased at the center of specimens during shearing and migrated towards the ends as the axial strain increased due to the end effects for lubricated

specimen regardless of the slenderness ratio. Frost and Lang (2000) stressed on the importance of the localized measurements in preference to global measurements to ensure true material response.

As the end effects are due to the mismatch between the stiffness of the platen and samples, it is more significant in soils than in rocks. However, the bedding errors due to the irregularity of samples ends are generally unavoidable in both soils and rocks. Although these effects are completely understood, local strain measurements are still for research purposes, especially for soils.

1.8 Locked sands

In the intermediate zone within the spectrum of geomaterials, a class of geomaterials displayed both soil and rock characteristics because of mild diagenesis. These geomaterials can be classified into bond-dominant geomaterials (bonding is responsible for the material's coherent mass) and fabric-dominant geomaterials (interlocking is the binding agent between particles). Bond-dominant geomaterials have been frequently studied in the literature (e.g., Vaughn and Leroueil (1990) have presented a comprehensive data compilation and analysis for stiff clays and weak rocks), where as the exploration of fabric-dominant geomaterials' behavior has been comparatively neglected in geotechnical studies (Barton 1993). An example of fabric-dominant geomaterials is locked sands where mild diagenesis is reflected in the material's

unusual particles' contact characteristics resulting in an interlocked fabric with no virtual bonding (Dusseault and Morgenstern 1979).

Locked sands are classified as *arenaceous* (predominately quartz sand particles) weak sedimentary rocks that constitute the boundary between soils and rocks. In dense sands, the strength is primarily a function of density, which yields a weak interlocking between particles with relative densities less than 100%. In sandstone, the strength is primarily a function of the amount of interstitial cement between sand particles. Despite the lack of cementation in locked sands pores, locked sands possess strength properties much higher than those of dense sands and much lower than those of sandstones. In addition, in contrast to dense sands, locked sands exhibit relative densities greater than 100% (Dusseault and Morgenstern 1979). The deviation from dense sand strength properties stems from mild diagenetic processes that reduce sand mass porosity with negligible or no cementation (Barton, 1993).

In north-eastern Alberta and particularly within 115 km of Fort McMurray, Dusseault (1977) recorded the existence of oil-sand and oil-free sand natural steep slopes. Dusseault (1977) found no interrelationship between slopes' heights and inclination, and the oil content. Dusseault and Morgenstern (1978) showed experimentally that the strength of oil sands was merely a reflection of their interlocked fabric, and, hence, was independent of the oil content. Protulipac (1991) recommended oil-free locked sands as a reasonable substitute

for oil sands to avoid sample disturbance due to gas expulsion where strength and deformation characteristics are a concern. Entire experimental investigations of locked sands from the McMurray area and other localities have typically focused on ultimate strength and volume change characteristics by using external strain measurements (Dusseault and Morgenstern 1979; Barton et al. 1986; Richards and Barton 1999; Wong 1999; Dittes and Labuz 2002; Creswell and Barton 2003).

Recently, Creswell and Powrie (2004) investigated the shearing response of locked sand using local strain measurements. However, no attention was paid to the significance of the local lateral strains' variation during shearing. Creswell and Powrie (2004) argued that due to the large difference between the peak and critical state strengths of locked sands, a geotechnical design based solely on the critical state friction angle would be unduly conservative even with a factor of safety of 1. Alternatively, these researchers recommended a design based on a limiting stress envelope corresponding to the onset of dilation (the point at which the reversal of the volumetric strain occurs) with a no-tension cut-off and a factor of safety on the peak stress ratios to avoid progressive failure. However, Creswell and Powrie (2004) also recommended further investigation into this design approach.

1.9 Objective of the thesis

Despite the wealth of information on the strength of geomaterials, no generalized framework exists for identifying the operational strength, particularly in the intermediate zone between soils and rocks (quasi-frictional materials). The main challenge in determining the operational strength for such materials lies partly in capturing the relative contribution of the interlocking/bonding and frictional resistance at working stress and strain levels, or in the pre-peak regime.

The main objectives of this thesis are summarized as follows:

1. To examine high-quality laboratory results for various geomaterials to understand failure precursors in the pre-peak regime, and to capture the onset of failure strength thresholds for soils and rocks.
2. To conduct a comprehensive experimental study on a McMurray fabric-dominant weak rock (locked sand) to reveal the following:
 - a. The source of the exceptional uniaxial strength of such a sand formation in the absence of bonding between particles and to confirm this formation's fitting into locked sands category;
 - b. The significance of local strain, compared to our routine external strain measurements for McMurray sand formations, in terms of failure mechanism, deformation modulus, and post-peak response;
 - c. The pre-peak damage thresholds for locked sand to capture the damage evolution based on the variation of local axial and lateral strains;

- d. The contribution of the frictional and the interlocking strength components with the plastic shear strain;
 - e. The relationship between the onset of localization and the onset of dilation as a candidate for the strength threshold;
 - f. The mechanism and kinematics of failure of locked sand;
 - g. The relationship between the onset of dilation and the long-term strength (onset of creep) of locked sand as a possible candidate for long-term strength; and
 - h. The upper and lower strength thresholds for locked sand.
3. To develop a simplified approach for partitioning the shear strength parameters (cohesion and friction angle) with plastic strain for stiff clays, and to show the significance of non-simultaneous mobilization of strength parameters in revealing:
- a. The resemblance in bonded geomaterials' shearing responses at low confining pressure irrespective of these geomaterials' origin; and
 - b. The transition between soils (frictional materials) and rocks (bonded materials) based on the mutual contribution of frictional and bonding resistance to overall resistance.
4. To highlight the significance of the concept of non-simultaneous mobilization of strength parameters in capturing the progressive failure of slopes and to interpret the deviation of the operational strength of stiff clays from the peak strength with such conceptual framework.

1.10 Methodology

The objective was achieved through the compilation and reanalysis of high-quality experimental results using local strain measurements and modern techniques to reveal the relationship between the onset of the shear-induced dilation and the onset of localization. The compiled data included examples for dense sands, overconsolidated clays, sandstones, locked sands, and granite. To extend the value of the shear-induced dilation threshold, examples were given for different geomaterials to show the relationship between the onset of shear-induced dilation and long-term strength. For bonded geomaterials (where strength is governed by the bonding resistance), another threshold (extension-induced dilation) was shown to be the lower strength threshold where bonding resistance is in effect.

The second objective was accomplished by testing specimens cut from block samples of oil-free McMurray sand formation from the High-Hill River banks. Preliminary tests served to reveal the sand's fitting into locked sand category. These tests consisted of microstructure observations of SEM images, blue-dyed thin section, and mineralogical compositions using the energy dispersion spectrum. Uniaxial compressive strength tests were conducted to reveal this formation's intrinsic strength by using local axial and lateral strain measurements. These tests highlighted the significance of local strain measurements of McMurray sand formations. The experimental results revealed the pre-peak strength thresholds, the failure kinematics based on the variation of the local

axial and lateral strains, the relationship between the onset of dilation and localization, and the contribution of frictional and interlocking strengths at different strain levels. To further investigate the long-term strength of such a formation and the relationship between the long-term strength and the onset of dilation, multistage creep test was conducted. Finally, the minimum mobilized strength under pure shear was investigated in a direct shear box (DSB) to show the relationship between the maximum mobilized strength in a DSB test and the pre-peak strength thresholds estimated from the uniaxial compression test.

In order to meet the third objective, stress strain curves, based on triaxial compressive strength results, for two natural bonded stiff clays were investigated as an example to show the mutual contribution of cohesion/bonding and frictional resistance at different plastic strain levels. The analysis highlighted the effect of the mobilization and degradation of strength parameters on stress-strain curves and post-peak brittleness at different confining pressures. Parametric study within such a framework revealed the concept of non-simultaneous mobilization of strength's significance by providing evidence from experimental results for other bonded geomaterials with different origins.

The fourth objective was achieved by carrying out a numerical simulation using the peak strength parameters and strain-dependent parameters using the finite difference code FLAC. The analyses also included a comparison between the position of slip surface obtained by using the strain-dependent strength

parameters and those associated with peak strength parameters, estimated from limit equilibrium analysis. The analyses highlighted the significance of the concept of non-simultaneous mobilization of strength parameters in capturing the progressive failure of slopes in stiff clays and in interpreting the deviation of the operational strength from the peak strength.

1.11 Organization of the thesis

Chapter 1 explains the problem's background and the thesis' objectives, methodology, and organization.

In Chapter 2, two pre-peak strength thresholds (the onset of shear-induced dilation and the extension-induced dilation thresholds) are discussed. The relationship between the onset of shear-induced dilation and localization is established by using compiled high-quality test results for dense sands, sandstones, locked sand, stiff clay, granite, and rock salt. The data are based on local strain measurements, acoustic emissions, and shear velocity tests. The significance of the onset of shear-induced dilation for all classes of geomaterials will be revealed by showing the relationship between the onset of dilation, the onset of localization, and the long-term strength. As well, the extension-induced dilation will be shown to be an important lower strength threshold where bonding is a major source of strength.

Chapter 3 presents the details of the experimental set-up and preliminary tests conducted on samples from the High-Hill River sand formation, procured from north-eastern Alberta, as well as a summary of locked sands' characteristics. The tests include index tests, microstructure observations using SEM, analysis of thin sections under a petrographic microscope, and qualitative mineralogical composition using the energy dispersive X-ray spectrum to reveal the fit of this formation into the locked sand category. The remainder of the chapter provides details on the testing procedures, including the calibration of miniature LVDTs for local and axial strain measurements, proof testing, stability tests, and temperature effects. The details of the modification for an existing mechanical configuration are also presented. Finally, the significance of local strain measurements is presented by contrasting local and external axial strain results.

Chapter 4 presents the results of the uniaxial compressive strength results from testing locked sand using local strain measurements. The first series of analyses reveals the relationship between the onset of dilation and localization, the damage thresholds and failure evolution and kinematics, the contribution of interlocking resistance and frictional resistance at different strain levels, and the mobilized strength parameters at different strain levels. The second series of analyses shows an attempt to rule out the heterogeneity associated with boundary conditions (end effects, strain rate, and specimen slenderness ratio) allowing for propagation of pre-peak columnar structures in the axial direction. The third series of analyses shows the relationship between the onset of dilation

and the long-term strength by conducting a multistage uniaxial creep test. Finally, the least mobilized strength and its relationship to the damage initiation threshold will be shown by using direct shear box test results.

Chapter 5 describes the methodology used to partition the cohesion/bonding and frictional resistance with the plastic strain level in Mohr-Coulomb and q-p spaces to show the mutual contribution of frictional and bonding resistances at different strain levels. Their contribution was illustrated by using two triaxial compressive strength results for bonded stiff clays. Once the parameters have been partitioned, a parametric study was conducted to reveal their contribution at different strain levels and confining pressures. The non-simultaneous mobilization of the strength parameters was used to capture the peak strength envelope's nonlinearity and the transition between soils and rocks based on their mutual contribution at different confining pressures. The parametric study also revealed the source of the initial "plateau" in the pre-peak regime at low confining pressures. This plateau is a characteristic behavior of various bonded geomaterials, as will be shown by using examples from the literature for weak rocks, sensitive clays, and artificially bonded soils.

Chapter 6 describes a numerical simulation to reveal the significance of strain-dependent parameters in the assessment of slope stability. To achieve that purpose, a homogeneous slope, with a height of 20 m and a side slope of 45°, was used for illustration. The peak strength parameters and the strain dependent

strength parameters estimated for a stiff clay (Nanticoke clay) in chapter 5 was used in the analyses. The analyses comprised a comparison between the slip surfaces and factors of safety, associated with peak strength parameters, obtained from the limit equilibrium analysis and the finite difference analysis by using the strength reduction technique. The rest of the chapter was devoted to show numerically the merits of the non-simultaneous mobilization of strength parameters in capturing the progressive failure and to interpret the deviation of the operational strength from the peak strength.

Chapter 7 summarizes the conclusions reached in the research and their significance, and provides recommendations for further investigations.

CHAPTER 2: ONSETS OF DILATION AND LOCALIZATION THRESHOLDS IN SOILS AND ROCKS

2.1 Introduction

The design of geotechnical structures necessitates a comprehensive understanding of the stress-strain curves of geomaterials to ensure the safety, stability and reliability of our structures under working stresses. By far, uniaxial and triaxial compression stress paths are the most common testing conditions used in soil and rock mechanics laboratories to determine strength and deformation characteristics. Under low confinement, or in the conditions in which most civil engineering applications are situated, most geomaterials exhibit strain weakening (strength reduction from peak to residual strength) accompanied by localized deformation in a single band or multiple bands, and also by volumetric strain reversal (dilation). As illustrated in the introductory chapter, experience gained through failures showed that a design based on the peak strength might result in an un-conservative design. On the contrary, a design based on residual strength can be over-conservative and cost-ineffective. In order to solve this dilemma, studies of microstructure changes during shearing are necessary to visualize the onset of damage and initial yielding. In pre-peak regime, geomaterials undergo changes in their microstructure, which reflect other strength thresholds rather than the peak and residual strengths as will be shown in this chapter. It should be noted that all the used terms in this chapter are in terms of effective stresses.

Although many studies of various geomaterials have been published, it remains unclear at what stress level localization is initiated and eventually results in strain weakening in the post-peak regime, and how it is related to the onset of shear-induced dilation (the onset of volumetric strain reversal). To clarify such points, a meticulous examination of high-quality experimental data, based on localized measurements, was carried out to draw attention to two pre-peak strength thresholds rather than peak and residual strengths, which are merely markers for failure. As Roscoe (1970) stated, understanding failure's precursory strains and structures is essential, because failure surfaces and their orientation are determined well prior to the peak strength.

The compiled strength and deformation data include examples for soils, weak rocks, and hard rocks to reveal the relationship between the onset of localization and the onset of volumetric strain reversal (the onset of shear-induced dilation). The bulk of this chapter discusses the relationship between the onset of shear-induced dilation and the long-term strength by using the reported creep test results for some geomaterials. In addition to exhibiting shear-induced dilation, brittle hard rocks also exhibit extension-induced dilation during compression testing due to the initiation of bond degradation, which is suggested to be the lower bound strength for all bonded geomaterials.

2.2 Definition of shear-induced dilation and localization

The phenomenon of shear-induced dilation was used by Reynolds (1885) to describe the increase in volume when dense granular materials are sheared. Reynolds (1885) attributed this distinctive feature to geometrical constraints imposed by particle packing (fabric) for dense granular materials. He believed that the unique condition for dilation was that boundary grains held interior grains so as to prevent the commencement of rearrangement. Today, it is recognized that shear-induced dilation (volumetric strain reversal) is not restricted to dense granular geomaterials but also occurs in most geomaterials at low confining pressures. Consequently, shear-induced dilation can be considered as a direct result of overcoming the different constraints (fabric and/or bonding constraints) that act as internal constraints, and reflects a transition in the behaviour of geomaterials.

The formation of a shear band (an inclined deformation band), which is a direct result of the localization of deformation and divergence from homogenous deformation is associated with shear-induced dilation. Once localization is initiated, irreversible plastic deformation takes place, and particles move with respect to each other along thin surfaces that appear as thin lines in the sample's body. Localization takes place when deformation bifurcates from a homogeneous mode to a localized mode on one or many surfaces that coalesce to form what is called a "dominant shear band". After formation of the shear band, most

deformation occurs through the rigid body motion of one part of the sample relative to the others (Saada et al. 1999).

Volume change (compression and dilation) in compression laboratory tests, and, in particular, triaxial tests is measured by using three techniques (Alva-Hurtado and Selig 1981; Leong et al. 2004). The first technique is by monitoring the change in the volume of fluids within specimen pores, which represents a global volume change. In the second technique, the volume of fluid entering or leaving the confining pressure cell to compensate for the volume change of the soil specimen is measured. In the first two techniques, lateral strains are calculated based on the assumption of right cylinder. The third technique depends on measuring, independently, axial (ε_1) and lateral strains (ε_3) from contact or non-contact elements. The volumetric strain of a cylindrical specimen (ε_v), which is tested under triaxial test conditions, is typically calculated by using the following equation:

$$\mathbf{[2.1]} \quad \varepsilon_v = \varepsilon_1 + 2\varepsilon_3.$$

2.3 Shear-induced dilation and localization thresholds

Advances in laboratory testing techniques enabled several researchers to investigate the deformation mechanism in compression tests for soils, weak rocks, and hard rocks. These researchers used local and global measurements,

acoustic emissions, and computerized tomography to monitor the deformation process. The results from their work are presented, reviewed, and discussed.

2.3.1 Coarse-grained soils and weak rocks

2.3.1.1 Dense sand

Finno and Rechenmacher (2003) investigated the deformation of medium-to-dense concrete sand in a drained plane-strain compression test. Samples were prepared by using the vibratory method to achieve an initial void ratio of 0.543. Figure 2.1a shows the deviator-stress versus the axial-strain curve at a confining pressure of 98 kPa.

The onset of localization was identified via local lateral strain measurements by using 4 horizontally mounted LVDTs as shown in the insert in Figure 2.1c. The divergence of local lateral strains with shearing progression at point A shows the onset of localization (Figure 2.1c), which is coincident with the onset of dilation (volumetric strain reversal) in Figure 2.1b. This result is also supported by Figure 2.1d. At peak strength (point B), the strain localization results in a partially formed shear band, and subsequent shearing results in the formation of a continuous band at large strains (point C) reflected in the constant value of one of the lateral strains reflecting the rigid body motion of un-failed element. The shear band appears to be developed at point C (the critical state), where the volumetric strain and deviator stress remains constant.

Figure 2.1d shows the evolution of the dilation angle with axial strain. At point A, the dilatancy angle is equal to zero where localization commences. At point B, the dilation angle reaches its maximum value followed by a reduction in the post-peak regime. Finno and Rechenmacher (2003) stated that the peak strength is a direct result of the localization and loss of homogeneity in sheared specimens of dense sand. In these researchers' paper, point D marked the onset of localization according to their interpretation, which resulted from the subjectivity in selecting of divergence point. However, even if this interpretation is correct, the onset of dilation can be considered as a very good indicator of the onset of localization.

The results suggests that for dense sands tested under plane strain conditions, the onset of localization can be determined from the global volumetric strains and that the volumetric strain reversal is representative of the onset of shear-induced dilation, which also corresponds to the onset of shear localization. In addition, strength reduction in the post-peak regime is a direct consequence of the localization process that commences in the pre-peak regime.

2.3.1.2 Locked sand

Locked sands' behaviour was first investigated by Dusseault and Morgenstern (1978), who concluded that the sands' fabric, and not the bonding due to the cementation, was responsible for the high strength and

dilation angles at low confinement. Cresswell and Powrie (2004) carried out triaxial compression tests on locked sand to investigate its stress-strain characteristics. The sand used in their tests had a tangential index (the ratio of tangential contacts to long straight contacts) of 26%, a relative density index of 136%, and a void ratio of 0.47. Axial deformation was monitored by using 4 axial LVDTs, and the radial deformation was monitored with a radial strain caliper. Figure 2.2a shows the stress-ratio (q/p) versus the axial strain curve at a confining pressure of 100 kPa and Figure 2.2b depicts the volumetric strain as well as the local axial strains measured by using internal LVDTs. According to Cresswell and Powrie (2004), the divergence of the local axial LVDTs in Figure 2.2b (point A) indicates the onset of localization where the strain field becomes discontinuous. This point also coincides with the point of the shear-induced dilation (the onset of the volumetric strain reversal), as shown in Figure 2.2b. The progression of deformation from point A (the onset of localization) to B (the partial formation of shear band) to C results in the complete formation of a shear band, as was indicated previously for dense sands. Cresswell and Powrie (2004) indicated that onset of shear induced dilation represents the stress level at which sand starts to unlock and loses its integrity. They also recommended that this threshold should be the limiting strength envelope for locked sands. The ratio of the onset of dilation to peak strength is plotted in Figure 2.3, which reveals the ratio independency of the confining pressure and that the onset of dilation occurs at almost 85% of the peak strength.

2.3.1.3 Sandstone

Besuelle et al. (2000) carried out triaxial compression tests on Vosges sandstone. This sandstone is a poorly cemented sedimentary soft rock, and most of its characteristics are derived from particle contact details. It is a pink quartz sandstone (quartz = 93%) with a small percentage of feldspar and white mica, and a porosity of 22%. Axial and lateral strains were measured by using three axial and four lateral transducers based on the concept of a flexible strip with attached strain gauges. The localization was detected by comparing the three axial strain measurements. If the difference between the mean axial strain (the average of three measurements) and each of the three axial measurements remains constant, the strain field can be assumed to be homogeneous with no localization. Figure 2.4a shows the stress-strain curve at a confining pressure of 20MPa. The figure reveals a strength reduction in the post-peak regime due to localization. Figure 2.4c shows the relationship between the differences of the axial strain and mean axial strain. Besuelle et al. (2000) suggested that the first divergence (represented at point A) of the three measurements was due to bedding errors in the experiment. Once seating had occurred, the differences among the three axial strains remained nearly constant up to point C where the difference of the three transducers increased dramatically. Besuelle et al. (2000) selected this point (point C) as the onset of localization based on the axial strains' differences. By using the axial strains' differences as well as lateral strains' differences, the onset of localization can be shown to commence at point B. The volumetric strain was

also determined by using the axial and lateral strain measurements as shown in Figure 2.4b. Note that the onset of shear-induced dilation (the volumetric strain reversal) was again close to and almost coincident with the onset of localization (point B in Figure 2b). Besuelle et al. (2000) also showed that the onset of localization generally occurs at a progressively lower normalized deviator stress as the confining pressure is increased. Normalization of the onset of dilation with respect to the peak also reveals its independency of the confining pressure (see Figure 2.5). Lockner et al. (1992) also revealed the coincidence of the shear-induced dilation and the onset of localization for Berea sandstone with a porosity of 18% and tested in triaxial test at a confining pressure of 50 MPa, by using acoustic emissions.

Recently, Sulem and Ouffroukh (2005) investigated the behaviour of Fontainebleau sandstone under drained and undrained triaxial compressive stress paths at various confining pressures. The samples had a porosity of 21% and were composed of 98% quartz. Axial and lateral deformations were monitored by using two local vertical LVDTs and four diametrically opposite lateral LVDTs, respectively. The onset of shear banding was detected through the difference between the individual axial strains and/or the radial strain difference between the two opposite points. Theoretically, as long as the deformation was homogenous, the difference between the readings would be negligible unless localization commenced. Figure 2.6 shows the results of a drained compression test under a confinement pressure of 28 MPa. Figure

2.6b shows the volumetric strain axial strain relationship. The initial stages of the testing are dominated by compressive volumetric strains up to point A. Beyond point A, volumetric reversal commences, signifying the onset of shear-induced dilation. This point corresponds to the increase in nonlinearity (see Figure 2.6a). Figure 2.6c shows the relationship between the axial strains' differences, lateral strains' differences and average axial strains. In terms of the axial strains' differences, the difference between axial strain readings is negligible as long as the strains are homogeneous. Once localization commences, significant differences in the strains occur. For the lateral strain difference, the difference increases slightly and is followed by a reversal in the value. The point at which reversal occurred was taken as the onset of localization and coincided with the recorded localization strain level as manifested by the vertical strains. This point (B) lies very close to the onset of dilation threshold and occurs in the pre-peak regime. However, this result is caused by the subjectivity in selecting the points at which strain difference occurs. In undrained conditions, the transition from contractant to dilatant behaviour occurs much earlier than in drained tests and increases with confining pressures due to the effect of pore-pressure generation. The relationship between the onset of localization and onset of shear-induced dilation normalized to the peak strength at different confining pressures under drained conditions is illustrated in Figure 2.7, which reveals that both thresholds are almost coincident and occur at 82 % of the peak strength.

2.3.2 *Fine grained soils and weak rocks*

2.3.2.1 *Overconsolidated silty clay*

Su et al. (2004) studied the deformation mechanism of undisturbed silty clay samples under undrained triaxial compression test conditions by means of computerized tomography. Scanning was recorded at different strain levels and for different slices during shearing. The CT images were quantified by using the CT number, which is a representative number for the sample's density and has a linear relationship with it. The change in density can be observed from the changes in the brightness between two cross-sectional images at the same location. The white areas in the images are considered to represent damage and localization. Figure 2.8a shows the deviator-stress versus the axial-strain relationship at a confining pressure of 300 kPa. The sample has a void ratio of 1.043, plasticity index of 14.31, and water content of 37.72 %. The letters on the curve represent the strain levels at which CT images were taken. Figure 2.8b gives the relationship between the CT number and the axial strain obtained from the middle slice as it represents the most homogeneous location in a specimen (a location away from boundary effects). Based on the variation in the CT numbers, the stress-strain curve is divided into four portions: (a) a portion where micro-defects close up (O-A); (b) a portion where new microcracks open and develop (bond-degradation stress level, A-B); (c) a portion where local deformation and damage starts (point B); and (d) a portion where softening and a reduction in load-carrying capacity occur. According to Su et al.'s (2004) experiments, localization starts

to occur at point B where local defects and damage commence. The X-ray portion shown at this axial strain level reveals separate locations of damage sites (indicated by the light grey points) that coalesce after this stress level to form the major shear band. At peak (point C), the shear band is partially developed, and the clay loses its homogeneity. Beyond point C, a significant reduction in the CT number occurs because of the reduction in the density due to localization. Hence, the peak strength (point C) is a direct result of localization, and one can argue that point B represents the onset of shear-induced dilation and localization in these tests. Normalization of the onset of dilation (as predicted from their results) to the peak at different confining pressures is also illustrated in Figure 2.9, which shows that the ratio is independent of the confining pressure and that the onset of dilation occurs at 84 % of the peak strength.

2.3.2.2 *Bonded clay*

Vallericca Clay is a bonded overconsolidated clay and can be considered as a weak sedimentary rock. It has a plasticity index of 31.6%, water content of 28.6% and a carbonate content of 30%. In order to investigate the formation of shear bands in this weak rock, Viggiani et al. (1994) carried out a plane-strain compression test using the same technique as that used by Finno and Rechenmacher (2003). Viggiani et al. (1994) also showed that the onset of localization took place pre-peak and was coincident with the onset of shear-induced dilation for this kind of geomaterial.

2.3.3 Hard crystalline rock (granite)

Lockner et al. (1992) studied the deformation mechanism of western granite by using acoustic emissions. These researchers conducted triaxial compression tests on granite samples with a porosity of 0.01 at a confining pressure of 50 MPa. The cell was provided with six piezoelectric transducers to monitor deformation mechanism by using acoustic source-locating techniques. Figure 2.10a shows the deviator-stress versus the axial-strain curve for a granite sample as well as the acoustic emission events recorded during deformation. The letters (A to G) on the deviator stress versus axial strain curve represent the strain levels at which acoustic emissions were recorded. Figure 2.10b gives the volumetric strains-axial strain relationship. According to Lockner et al.'s (1992) acoustic emission observations, localization starts at point A where several distributed damage sites start to coalesce. This point is also coincident with the volumetric strain reversal based on the researchers' volume change measurements. At peak strength (point B), the shear band is partially formed, and the progression of deformation beyond this point results in the complete formation of a shear band, as shown by the transition from point B to G, accompanied by a reduction in strength as a direct result of localization. Eberhardt et al. (1998), using acoustic emissions, also reported the coincidence of the onset of localization and the onset shear-induced dilation for granite.

Martin and Chandler (1994) carried out a series of damage-control tests on Lac du Bonnet Granite by using strain gauges to monitor local axial and lateral strains. The granite was medium- to coarse-grained and composed of 30% feldspar, 30% plagioclase, 30% quartz, and 10% biotite minerals. Martin and Chandler's (1994) experimental results revealed a threshold after which unstable cracks propagated. This threshold was found to be coincident with the onset of the volumetric strain reversal, which marked the onset of localization due to the coalescence of microcracks. This threshold was shown to be independent of the strain rates and the sample size and was suggested to be the long-term strength instead of the peak strength. Martin and Chandler (1994) showed the independence of this stress on the confining pressure when normalized to the peak strength (see Figure 2.11) and that the onset of dilation occurred at almost 75% of the peak strength.

Takemura and Oda (2005) carried out triaxial compression tests at different confining pressures on Indiana granite from Japan. Indiana granite is composed of 37% quartz, 33% plagioclase, 24% orthoclase, and 6% biotite and clay minerals. After loading and unloading from different stress levels relative to the peak, Takemura and Oda (2005) recorded a major reduction in transversal wave velocities at 75% of the peak strength (onset of dilation).

2.4 Significance of onset of dilation threshold

The laboratory tests reviewed clearly reveal that the failure process in a wide spectrum of geomaterials is dominated by the formation of shear bands and volumetric strain reversal. The initiation of these bands is indicated in the volumetric strain curve as it changes from compression to dilation. The onset of shear-induced dilation, i.e., volumetric strain reversal, appears to be an excellent indicator of the initiation of localization. The peak strength, however, appears to be related to the strain hardening associated with the progressive development of the shear band throughout the sample once localization onsets, and, hence, to be only a signature of the failure process in laboratory tests. Therefore, the onset of dilation is considered of significant importance compared to the peak strength. The onset of dilation signifies the occurrence of non-homogeneous deformation, which should be prevented, and, hence, it should be regarded as an upper bound of strength to avoid the onset of shear-induced failure.

The stress magnitudes associated with the onset of shear-induced dilation (q_{dil}) in the laboratory tests presented have been normalized to the peak strength (q_p) and expressed as follows:

$$[2.2] \quad NDR = \frac{q_{dil}}{q_p}.$$

Figure 2.12 shows that for the geomaterials examined, this ratio ranges from 0.75 to 0.86, regardless of whether the geomaterial is soil or rock. Once localization is initiated, failure appears to be imminent regardless of the geomaterial's bonding or fabric characteristics. This ratio has also been found to be unique for each of the investigated geomaterials and independent of the confining pressures, as shown in the previous figures. In terms of the absolute values of the normalized dilation ratio and the geomaterials' type (soil or rock), no relation exists between the void ratio and the normalized dilation ratio.

2.5 Onset of shear-induced dilation and long-term strength

The relationship between the onset of shear-induced dilation and the long-term strength of three different geomaterials is illustrated below. If the onset of shear-induced dilation can be verified to be a good indicator of the long-term strength, its significance as a limiting strength threshold is assured. The presented data are taken from recent creep tests for sand, granite, and rock salt. Most of the extensive published laboratory data for creep and long-term strength of various geomaterials do not relate the onset of dilation to the long-term strength for the tested geomaterials. However, Rusch (1959, 1960) suggested the volumetric strain reversal as the long-term strength for concrete and Beiniawiski (1967a) recommended this also for hard rocks.

2.5.1 Sand

Kuwano and Jardine (2002) investigated the creep potential of granular materials under triaxial test conditions by using local axial and lateral strain measurements. Figure 2.13 shows the undrained creep axial strain versus time for Ham River sand at various deviator stress levels. Ham River sand is a uniform sub-angular-shaped quartz sand with a mean particle size of 0.27 mm. A specimen was tested under a mean stress of 200 kPa and had a void ratio of 0.76 and a relative density of 30% (loose state). As the figure shows, the creep potential increased with the increase in the creep stress level. However, the creep potential became more significant after a deviator stress level of 200 kPa, which marked the phase transformation point (the reversal in pore pressure value from a positive value to a negative value) that is equivalent to the shear-induced dilation points in the drained tests. As a result, the onset of shear-induced dilation can be regarded as a safe boundary for excessive deformation in this geomaterial.

2.5.2 Granite

Lau and Chandler (2004) carried out damage controlled tests to determine the damage thresholds as well as the long-term strength of Lac Du Bonnet granite. The axial and lateral strains were measured by using strain gauges glued onto the specimen's surface along with three vertical LVDTs for measuring the axial strains, and a radial extensometer for the circumferential

strains. Lau and Chandler (2004) showed that the state of stresses close to the peak can be sustained for a short period prior to failure due to the temporary strain hardening after the onset of dilation. Hence, the peak strength cannot be relied on for long-term stability, as previously suggested by Schmidtke and Lajtai (1985). To investigate this concept, creep tests were conducted at different confining pressures before and after attaining the onset of dilation stress level. In creep tests, the targeted stress levels (deviator stress) remained constant while the deformation was monitored for at least 24 hrs. The conducted series of experiments revealed that samples tested below this threshold cracked in a stable manner with no signs of creep failure or rupture. Only samples tested above this threshold tended to fail and showed excessive deformation. It was also observed that a significant change in lateral deformation took place before failure, when the axial strains remained almost constant or negligibly varied. Only when failure was initiated did the axial strain accelerate with the lateral strains, and, hence the failure process was dominated by creation, extension, and coalescence of vertical cracks. Creep stress levels (σ_{cp}) were assigned as a percentage of the onset of dilation stress level (σ_{cd}). The ratio between them was represented by the stress ratio parameter (β) and was expressed as follows:

$$\mathbf{[2.3]} \quad \beta = \frac{\sigma_{cp}}{\sigma_{cd}} .$$

Figure 2.14 shows the relationship between the stress ratio (β) and the time to failure in hours at different confining pressures. Increasing confining pressures at the same stress ratio resulted in an increase in the time required to attain creep failure. Within the investigated range of confining pressures, the increase in time to failure was proportional to the increase in stress ratio. In other words, as long as the stresses remained closer to the onset of dilation stress level, the time to failure was delayed. Consequently, the onset of the dilation stress level appeared to be a plausible approximation of the creep stress level at any confining pressure. These observations were also confirmed by the experimental investigation conducted by Lin et al. (2004) by using acoustic emissions on granite samples.

2.5.3 *Soft crystalline rock (rock salt)*

Rock salts are usually used as the geological host rock for caverns and considered for the disposal of radioactive waste due to these materials' low permeability and ductility (Schulze et al. 2001). The most critical requirement for such application is the prevention of material from cracking to avoid the increase in permeability and hence ensuring the tightness of such rocks. To avoid such effects, Cristescu and Hunsche (1998) recommended that the dilation boundary (the onset of dilation threshold) be considered as the long-term strength. This boundary basically marked the culmination of cracking, damage, increase in acoustic emissions, increase in permeability, and promotion of creep failure. Schulze et al. (2001) conducted triaxial

compression tests on a rock salt formation in Germany to investigate the concept of the dilation boundary. These researchers used ultrasonic wave velocity to detect the onset of dilation, and, hence, damage accumulation. Figure 2.15 shows the relationship between the normalized ultrasonic wave velocities, deviator stress and axial strain for a sample tested under a mean effective stress of 5 MPa. Schulze et al. (2001) identified the onset of dilation boundary by using the reversal of the shear wave velocity. As soon as microcracks commenced, the shear wave velocity exhibited a reduction in its value, reflecting the increase in axial cracks propagating in the vertical direction and the onset of localization. No failure was recorded beyond this boundary of up to 20% strain. This was basically a case of uniform localization as opposed to what occurred in the previously discussed geomaterials where localized dilation was the mechanism of failure.

Hunsche and Hampel (1999) reported Hunsche's (1990) results of true triaxial compression results, to identify the dilation boundary and its relationship to the long-term strength. The normalization of the onset of dilation with respect to the peak strength is plotted in Figure 2.16, which shows that the ratio is independent of the confining pressure, but much lower than the recorded values for all previous geomaterials. Figure 2.17 presents an example of one of the creep tests conducted at a mean stress of 10 MPa. The creep stages and the change in the volumetric strains at each stage of testing are plotted in the figure. According to Hunsche and Hampel's (1999) results, a slow

decrease or a constant volume was observed as long as the stresses were below the onset of dilation (the dilation boundary). In the dilatant regime (where this is an increase in volumetric strain), creep rupture was attained after a certain time or deformation along with a remarkable increase in acoustic emission rate and a decrease in seismic wave velocity. According to their observations, humidity induced creep also occurred above the onset of dilation boundary. These observations suggested that the onset of dilation can be considered as a safe boundary for such geomaterials to prevent long-term instability.

Based on the presented examples, it can be inferred that the onset of dilation can be considered as an excellent candidate for long-term strength. In order to avoid excessive long-term deformation, stresses should be kept below this threshold.

2.6 Extension-induced dilation in bonded geomaterials

In the testing of hard rocks, surface-mounted strain gauges are normally used to monitor the stress-strain response and frequently combined with acoustic emissions (Brace 1964; Brace et al. 1966; Bieniawski 1967*b* ; Wawersik and Fairhurst 1970; Lajtai and Lajtai 1974; Martin and Chandler 1994; Eberhardt et al. 1998; Chang and Lee 2004; Diederichs et al. 2004). Brace et al. (1966) and Lajtai et al. (1990), among others, found based on their observations during the middle stages of compression test conducted on Lac De Bonnet granite, that only

lateral dilation of the cylindrical sample was recorded, with no axial shortening. This suggested that damage initiation and propagation in Lac du Bonnet granite was caused by extension-induced cracking in the vertical direction. The extension-induced dilation can be simply defined as the uniaxial dilation that occurs in the direction of the minor principal stress direction creating microcracks align in the major principal stress direction. These microcracks tend to coalesce, leading to shear failure and the formation of macro-fractures (Lockner et al. 1990).

Martin and Chandler (1994) used damage-controlled triaxial tests on Lac du Bonnet granite to identify the damage stress thresholds, and, more importantly the crack initiation and damage thresholds (see Figure 2.18). The crack initiation stress was caused by extension-induced dilation (30-40% of peak resistance) marked by the initial nonlinearity in lateral stiffness and volumetric strains. In zone (III), microcracks propagated in the vertical direction and formed columnar structures separated by discrete microfractures. At 70-80% of the peak resistance (zone (IV)), the onset of shear-induced dilation, these columns started to buckle, and microcracks coalesced to form major macrofractures (Sammis and Ashby 1986), resulting in the reversal of volumetric strains and localization. Martin and Chandler (1994) argued that strain hardening observed from the onset of shear-induced dilation to the peak strength resulted from the testing methodology and was not a material property. Martin (1997) has shown that the operational strength around the Mine by test tunnel, constructed at the

Underground Research Laboratory, was coincident with the deviator-stress required to cause extension-induced dilation (crack initiation stress) in laboratory tests.

Lajtai et al. (1990) indicated that up to the onset of dilation, the formation of vertical cracks propagating in the axial direction dominated the failure mechanism. Figure 2.19 illustrates the results of a cyclic uniaxial compression test on Lac Du Bonnet granite sample. Below the onset of shear-induced dilation threshold, the axial strains were predominantly elastic, and the permanent axial strains remained unchanged; however, a significant change in permanent lateral strains took place. The observation of such vertical cracks and their propagation in the major principal direction prior to the onset of dilation in triaxial testing conditions was also recorded for Oshima granite from Japan with similar mineralogical composition to that of Lac Du Bonnet granite (Schubnel et al. 2003). By using ultrasonic wave velocities, Schubnel et al. (2003) showed that the transversal wave velocities decreased at the onset of shear-induced dilation, along with an increase in acoustic emissions, signifying localization, while the vertical velocity remained constant. In other words, formation of vertical cracks parallel to the axial stress dominated the deformation mechanism.

Vallejo (1987) carried out direct shear tests on brittle kaolinite clay with preexisting cracks. He observed that the failure in the samples started in the form of secondary cracks developed from the tips of the original cracks. These

secondary cracks were developed in the region of the tensile stresses in the samples due to shear stresses. Secondary cracks tended to extend in a direction perpendicular to maximum tensile stresses regardless of the direction of original cracks. Vallejo (1989) also studied the effect of fissures on the strength of brittle kaolinite. He showed that under compressive stresses, local tensile stresses developed at the crack tips. The extension of cracks in the direction of the major principal stress dominated the fracture process of the specimens. The original fissures were acting as stress concentrators from which cracks propagated in the tensile stress regimes so that bridges between the artificial fissures dictated the final strength.

In bonded geomaterials (regardless of the degree of bonding), another characteristic strength threshold exists after which bonds start to degrade, i.e., the extension-induced dilation threshold. The degradation of these bonds under compression is due to the geomaterials' heterogeneity where local tensile stresses develop. The cracks open laterally and extend in the direction of the major principal stress under the compression stress path in a stable fashion, forming vertical columns separated by discrete vertical microcracks. At a certain stress level, (the onset of shear-induced dilation, i.e., the volumetric reversal stress level) these separated columns start to interact to form a shear band, and strain becomes localized in a band composed of these microcracks (Figure 2.20). Directly capturing the extension-induced dilation threshold would be difficult, if not impossible, to achieve from global volume change measurements.

Determining the extension-induced dilation requires local lateral strain measurements so that the nonlinearity of lateral strains can be accurately captured.

2.7 Summary and Conclusions

In this chapter, high-quality laboratory data for various geomaterials were compiled and reviewed to reveal the salient pre-peak strength thresholds observed in these data sets. The first part revealed the relationship between the onsets of shear-induced dilation (the volumetric strain reversal stress level) and localization (loss of strain uniformity) for various geomaterials. In the second part, three examples were given to clarify the investigation of the relationship between the onset of shear-induced dilation and the long-term strength (it is defined here as the excessive creep induced deformation that ultimately can lead to rupture). In the third part of the chapter, another threshold was introduced for bonded geomaterials (extension-induced dilation, i.e., the initiation of bond degradation). Based on these investigations, the following conclusions can be drawn.

1. Geomaterials display a marked change in their behaviour prior to reaching the laboratory peak strength, and, hence, pre-peak characteristics may be very important to understand failure and its evolution.
2. The onset of shear-induced dilation (volumetric strain reversal) is an excellent indicator of the onset of localization for a wide spectrum of

geomaterials regardless of their origin and can be directly estimated from global measurements.

3. The peak and residual strengths measured in our laboratory are a direct result of localization and can be considered as signs of failure. The peak strength is due to temporary strain hardening resulting from the localization and propagation of failure.
4. The ratio of the stress level required for initiating shear-induced dilation normalized to the peak strength, for the investigated materials except for the rock salt, ranges from 0.76 to 0.86. This ratio is independent of fabric and/or bonding as well as the confining pressures for the investigated geomaterials.
5. For the investigated geomaterials, the onset of shear-induced dilation may also be an excellent indicator of the creep limit. Beyond this threshold, creep potential becomes significant, and, hence, the onset of shear-induced dilation can be considered suitable for avoiding excessive deformation.
6. The onset of shear-induced dilation may be considered as upper strength boundary threshold for many geomaterials.
7. The onset of extension-induced dilation marks the initiation of bond degradation for bonded geomaterials regardless of the bonding strength. The extension-induced dilation can be estimated only by interpreting the variation in local lateral strains and simply marks the commencement of bond degradation in the pre-peak regime.

8. The pre-peak strength thresholds (the onset of shear-induced dilation and the onset of extension-induced dilation) revealed in this chapter seem promising for determining the upper and lower bounds for geomaterials instead of using the peak and residual strengths.

CHAPTER 3: HIGH-HILL RIVER FORMATION GENERAL CHARACTERISTICS AND UNIAXIAL TEST SET-UP

3.1 Introduction

Nature provides a wide spectrum of geomaterials ranging from soils to hard rocks. In the middle range, a class of geomaterials exists that exhibits the characteristics of both soils and rocks. This zone's geomaterials can be classified into bond-dominant geomaterials (bonding is the binding agent between particles) and fabric-dominant geomaterials (interlocking is the binding agent between particles) or *argillaceous* (clay-based) and *arenaceous* (sand-based) intermediate geomaterials. Only recently, the mechanical behaviour of these bond-dominant geomaterials has received considerable attention (e.g., Leroueil and Vaughn 1990; Burland et al. 1996; Cotecchia and Chandler 1997; Amorosi and Rampello 1998; Cotecchia and Chandler 2004). In contrast to bond-dominant geomaterials, fabric-dominant geomaterials have been relatively neglected in geotechnical studies. Our understanding of the mechanical behaviour of this class of geomaterials behaviour has been limited due to the difficulty of sampling, the difficulty in samples preparation due to friability, and the scarcity of such geomaterials, where strength is derived from the grain surface characteristics (fabric) rather than bonding (Barton 1993).

The oil reserves in Alberta's oil sands are a huge source of reliable energy and income for Canada (20.4 billion \$CDN in 2004, according to Statistics Canada). Canada's oil reserves are estimated to be 179 billion recoverable oil barrels (175

billion are located in oil sand) and rank second only to the reserves of Saudi Arabia (259 Billion barrels), see Figure 3.1. The extraction of the synthetic oil from the oil-sand formations has resulted in many studies particularly of the Athabasca oil sands as the richest oil reservoir (approximately $210 \times 10^9 \text{ m}^3$ of bitumen). Figure 3.2 shows the major oil locations in Alberta. Nearly $142 \times 10^9 \text{ m}^3$ of the recoverable reserves is located in the lower cretaceous McMurray sand Formation and the Wabasca member of the Clearwater Formation. These reserves have an aerial extent of 46800 km^2 and an average thickness of 34m (Wightman et al. 1989; ERCB 1990). In these types of Formations, particles are interlocked with each other and have heavy bitumen and gas in their pores.

Dusseault and Morgenstern (1978) revealed that factors like gas-bitumen-water minerals, bitumen's viscosity, mineral cementation, and negative pore pressures make no contribution to locked sand strength. Protulipac (1991) showed that oil-free locked sands could be employed to investigate the behaviour of oil sands to avoid the sample disturbance caused by the expansion associated with gas evolution during the sampling of oil sands (McKay 1989), and, hence, disruption of the interlocked fabric (Agar 1984). Experimental investigations of oil sands have revealed that a small increase in the porosity may result in a significant reduction in strength (Agar et al. 1987). Oil-free sand was recovered from cliffs 70 m high along the High-Hill river approximately 60 km east of the McMurray area. This sand is regarded as a perfect candidate for studying the behaviour of fabric-dominant geomaterials and oil sands. In Alberta, a better understanding of

the oil-free locked sand's mechanical behaviour results in a better understanding of oil sands as a geomaterial with interlocked fabric. This understanding may result in enhancing the recovery processes.

This chapter provides a synopsis of the general characteristics of the locked sands according to the previous research on such formations. Microstructure observations and mineralogical composition analyses are then used to verify that the investigated sand formation fits into the locked sands category. Next, the experimental set-up for uniaxial compression test is described in detail, including the LVDTs' calibration, stability and proof testing, and the testing mechanical configuration and modifications. Finally, the significance of local strain measurements in investigating the behaviour of locked sand behaviour is shown by contrasting local axial and external strains' results.

3.2 General characteristics of locked sands

3.2.1 Locked sands among geotechnical materials

Locked sands are unique formations that constitute the sands/sandstones borderline and retain properties that are not entirely analogous to those of either soil properties or rocks. Figure 3.3 schematically illustrates a classification of geomaterials in terms of diagenetic effects and uniaxial strength. This figure shows that locked and cohesive sands are on the borderline between soils and hard rocks and belong to the arenaceous family.

The overlap between the boundaries is intentional, for demarcating them is very difficult. Sand and sandstone behaviors have been explored in soil mechanics and rock mechanics, respectively, in terms of compressibility and strength. In dense sand, the strength is a function of the degree of densification and yields a weak interlocking between particles with relative densities of less than 100%. In sandstone, strength is primarily a function of the amount of interstitial cement. Locked sand, despite the lack of authigenic cementation in its pores, possesses strength properties that are much higher than those of dense sand and much less than those of sandstone. Moreover, locked sands can exist at relative densities greater than 100%, in contrast to those of dense sands (Dusseault and Morgenstern 1979). The peculiar strength properties and the deviation from dense sands' characteristics stems from mild diagenetic processes that reduce the original sand mass's porosity after sedimentation to a compact mass with negligible or no cementation (Barton, 1993).

3.2.2 *Diagnostic aids for locked sands identification*

Dusseault and Morgenstern (1979) coined the expression "locked sands" to distinguish the characteristics of geologically old sands from recently deposited sands, compacted sands, and sandstones. Table 3.1 lists these deposits' characteristics as they have been identified in previous investigations. These characteristics are summarized as follows:

1. Quartzose sands: these formations are older than Quarternary in age, poorly cemented, and can be reduced to their grains component through rubbing (they are friable). They belong to the orthoquartzite family, which is characterized by the existence of at least 95% quartz-rich detrital grains cemented with authigenic quartz (Pottijohn et al. 1972). These formations show a tendency to disintegrate when immersed in water (Barton et al. 1986). However, this tendency is dependent on the amount of fine-grains in the matrix. Frequent cross beddings with traces of fine grains (such as kaolinite, illite, and iron oxide) have been reported in various investigations (Dusseault 1977; Barton et al. 1986; Richards and Barton 1999).

2. Microfabric characteristics: grain-to-grain contacts are large with interpenetrative fabric and rugose texture (see Figure 3.4 for classification of the contacts). The unusual contacts' characteristics are usually attributed to pressure solution at the particle contacts and/or post-depositional quartz overgrowth. Interlocking is measured through the tangential index (TI, the percentile of tangential contact to the total contact). Richards and Barton (1999) showed that no relation exists between the TI and the porosity of such sands.

3. Packing: porosities are lower than those of dense sands and cannot be reproduced in a laboratory, and relative densities can be in excess of 100%.

Therefore, locked sand exhibits low compressibility and can be used to support foundations where small deformation is expected.

4. Shear strength characteristics: locked sand is characterized by brittle behavior, small strain at failure, high friction angles of 57° - 70° , extreme dilation, a higher residual friction angle of 30° - 35° compared to that of the usual Quartzose sands due to rough surface textures, and a reduction in strength and dilation rates due to wetting. The high TI (less interlocking) results in a negligible cohesion intercept (Richards and Barton 1999). Fabric cohesion (the cohesion intercept due to interlocking) is observed only in fine- to medium-grained sands due to interlocking. In contrast, fabric cohesion is negligible in coarse-grained locked sands. Furthermore, the cement content, if it exists, and the fabric cohesion for such materials have no obvious relationship.

3.3 Investigated area and sampling

3.3.1 Oil-free slopes and sampling area

Dusseault (1977) carried out an extensive laboratory and field investigation of the lithology and stratigraphy of immature (created during glaciations) oil-sand outcrops in the Athabasca Region. All oil-sand and oil-free sand slopes were found to be within 115 km of Fort McMurray, and its formation was attributed to the erosive force created via the down-cutting action of young vigorous streams (the shaded area in Figure 3.5). As glacial influence

operated a short time ago, these slopes are considered to be young in age, and they follow river streams in this regime.

Within this regime, several exposed oil-free sand cliffs up to 70 m high, along High Hill River and Cottonwood Creek exist in the McMurray area. Block samples were procured from the outcrops along the High-Hill River banks. The block samples retrieved from the cliff exposure were located 60 km east of McMurray and one kilometer northeast of the junction of the High Hill and Clearwater Rivers (see Figure 3.5). The oil-free block sample was completely dry in situ, presumably due to a shale cap at the top of the oil sand formation. The blocks had dimensions of 22 cm by 22 cm by 15 cm and were cut from the exposed faces by using an electrical wire saw. These blocks were placed in wooden boxes encased with expanding foam for transportation and storage.

3.3.2 Geological settings of McMurray Formation

Figure 3.6 shows a geological survey map, depicting the bedrock in Alberta, produced by The Alberta Energy and Utilities Board and Alberta Geological Survey agencies (EUB and AGS 2005). According to the geological survey and the identified geological elements, the investigated formation belongs to the McMurray formation of the Mannville group (the group included the base of the McMurray formation to the Grand Rapids Formation), which was deposited in the lower Cretaceous period and includes the McMurray

Formation, the Wabiskaw member, the Clearwater Formation, and the Grand Rapids Formation. As most of the bitumen in the Athabasca oil sands is within the McMurray formation (ERCB 1990), several researchers have endeavored to identify the stratigraphy, geological settings and depositional history by using sedimentological, palaeontological, and ichnological data sets (e.g., Carrigy 1959; Flach and Mossop 1985; Ranger and Pemberton 1992; Wightman and Pemberton 1997; Hein et al. 2000).

3.3.2.1 Stratigraphy and depositional history of McMurray Formation

The word “McMurray” was first proposed by F.H. McLean in 1917 in order to describe strata containing tar sands. Carrigy (1959) provided the first informal tripartite stratigraphic subdivision of the McMurray Formation’s members as the lower, middle, and upper McMurray Formation, for a schematic depiction see Figure 3.7a. The lower McMurray Formation unconformably overlies a succession of Devonian evaporates and carbonates (Carrigy 1973a; Wightman and Pemberton 1997). In the Devonian period, dissolution of evaporites caused the overlying carbonates of the Waterways Formation to collapse and subside, creating the basin where the sediments were accumulated. Large paleovalleys formed by the salt dissolution collapsed, and less resistant carbonates developed on the unconformity surface, creating a localized central trunk drainage system (Ranger and Pemberton 1992; Wightman and Pemberton 1997) and hosted the McMurray Formation, which was originally exposed to extreme weathering before deposition. The

McMurray Formation was deposited in the early Cretaceous period marked by continental subsidence as well as sea transgression. Sedimentation continued until the late Cretaceous period, and approximately 760-1220 m of sediments were deposited over the McMurray Formation after its deposition termination due to a relative fall in the sea level. Subsequently, erosion began in late Cretaceous period for over 70 Ma until the onset of continental glaciations in North America where large quantities of McMurray sands were removed by glacial scour.

The McMurray Formation accumulated in incised valleys formed by fluvial processes and subsequently transgressed by marginal-marine environments during an early Cretaceous sea-level rise. Thus, the McMurray Formation displays a continuum of sedimentary environments, from fluvial in the lower parts, to estuarine in the middle, to marine shoreface near the top. The Lower McMurray Formation is generally medium- to coarse-grained and massive-appearing to crudely cross-bedded, and contains no ichnofossils. The formation's beds are most commonly interpreted as having a fluvial nature. The Middle McMurray deposits are dominated by inclined heterolithic stratification, which is interpreted to represent deposition on tidally influenced point bars and which forms the primary reservoir unit in the Athabasca Oil sands. Notably, the Middle McMurray Formation contains a brackish-water trace fossil assemblage and, accordingly, is interpreted as representing a fossil estuary (Pemberton et al. 1982). The Upper McMurray deposits are

variable, but generally contain a comparatively open marine signal. These deposits are normally interpreted as shallow and low-energy shore-face deposits, and small deltaic complexes (Gingras and Rokosh 2004).

3.3.2.2 Lithology of McMurray members

Dusseault (1977) summarized the related lithological features of McMurray oil sand formation. According to his description, this formation is heterogeneous with respect to its grain size but homogeneous in terms of its mineralogy. The formation is characterized by well sorted un-cemented sand consisting of over 94% quartz (belonging to the orthoquartzite family) and clay minerals which are mostly illite and kaolinite. Figure 3.7b shows the grain-size distributions of all the McMurray members, marked as Group band I (Lower member), band II (Middle member), and band III (Upper member). The same figure shows the grain-size distribution of our samples, which will be discussed subsequently. Table 3.2 summarizes the depositional environment as well as the lithology of McMurray Formation sand members.

3.4 Physical properties

The sampled blocks appear as white to light gray in color, characterized by thin cross-black beddings and a rough texture. Under an optical microscope, the majority of the detrital grains are clear, white, or translucent. A light finger tip's pressure, along with continuous rubbing, results in a degradation of the interlocked structure, reflecting either extremely weak or no cementation.

Table 3.3 presents a summary of the pertinent physical properties of such a formation based on grain-size analysis and maximum and minimum void ratio test results in accordance with ASTM Standards. According to the ASTM Classification of Soils for Engineering Purposes (Unified Soil Classification System) (D 2847), this deposit is classified as poorly graded fine to medium sand (SP). A calculated relative density of 125% reflects the existence of exceptional grain packing, which cannot be reproduced in the laboratory and confirms that this deposit fits into the locked sands category, described in Table 3.1. Based on the locked sands' classification introduced by Barnes and Dusseault (1982), describing the degree of diagenesis and its reflection of the contact nature based on the difference between the minimum and the actual porosities, this sand belongs to the second category (which has a porosity reduction of 2.7 %). This category is characterized by small fabric cohesion (an interlocked fabric) and mild diagenesis reflected in tangential, long, and occasional interpenetrative contacts. This deposit is composed mainly of well-sorted sand particles with a small portion of fine particles and a high relative density due to mild diagenesis.

3.5 Micro-fabric analyses and mineralogical composition

The visual inspection of the blocks showed their extreme friability, interlocking of particles, and existence of crystals with different colors. In order to investigate such observations scan electron microscope (SEM) observations, examination of colored thin sections by using an optical microscope, as well as energy

dispersion X-ray analysis were carried out on these samples. Before interpreting the results, the source of diagenesis in sedimentary rocks is discussed.

3.5.1 Source of interlocking due to diagenesis

Diagenesis processes of predominantly sand-size particles have been extensively studied in Sedimentology and Petrology for decades to reveal the source of pore reduction of detrital grains. "Diagenesis" is defined as the process through which sediments are transformed into rocks. It is the sum of physical, inorganic, chemical, or biochemical changes in a sedimentary deposit after initial accumulation including mechanical compaction, addition of new material, removal of materials and transformation by change in the mineral phase, and replacement of the mineral phase by another one (Friedman and Sanders 1978). The mechanical compaction stage of sediments is achieved by rotation to a stable position under overburden. During this stage, fractures can be easily formed as a result of the huge pressure on the particles, forming floating and tangential contacts (Taylor 1950). The second stage is composed of the alteration of sedimentary deposits through chemical and/or physical processes. In this stage, other kinds of contact such as concavo-convex (interpenetrative), long and short contacts, and sutured contacts are formed (Taylor 1950; Siever 1959). The transformation of sand to sandstone (lithification) is achieved through pressure solution and quartz overgrowth. Pressure solution occurs at particle contacts in aqueous solution where dissolution at contacts takes place due to

unequal stress distribution at them. This process results in a wavy interlocked fabric with liberation of silica in solution. The increase in the thickness of the fine-grains at particle contacts results in an increase in pressure solution due to the increase in diffusivity (Heald and Larese 1974). Quartz overgrowth (Authigenic silica or Syntaxial rim) is a direct result of silica introduced into the solution either by pressure solution or silica-rich streams, the infiltration of silica, or the diagenesis of shales and the transformation of smectite to illite with an increase in soluble silica (Sibley and Blatt 1976). The overgrowth occurs on detrital grains, giving a euhedral shape (well-formed crystal with a sharp, easily recognized faces) as a secondary growth in selective directions based on the density of the fine-grained coatings. Fine-grained coating can result in uneven growths of detrital grains (Heald and Larese 1974). This growth is responsible for the grain's unusual shapes of grains and can produce high interlocking by pushing adjacent grains or even by overlapping two growths of two adjacent grains (Pittman 1972). Unfortunately, differentiating between the two mechanisms by using simple optical analysis is very difficult, due to the same crystallographic and optical orientation of the overgrowth and the underlying nucleating detrital grains, unless a dust ring is detectable on particle surfaces (Pittman 1972). However, this mechanism can be identified by using the Cathode luminescence petrology introduced by Sippel (1968), which is beyond the scope of this investigation. Authigenic clays exist in such formations in the form of pore lining, pore filling,, or even fracture filling (Wilson and Pittman 1977). Heald and Larese (1974) found that

argillaceous coating can prevent quartz overgrowth from forming strong bonds, with uneven growths or throat nature with neighboring grains, and, hence, can result in high friability through failure of the coating.

3.5.2 SEM and Energy Dispersive X-ray Analyses

An examination of the locked sand samples was carried out by utilizing a JEOL 6301F (Field Emission Scanning Electron Microscope) to provide high-resolution digital images at magnifications ranging from 20x to 250,000x, as well as an energy-dispersive X-ray analysis of the identified elements. The undisturbed specimens were trimmed, and broken off in the middle to give a clean, fresh face for observations. The base of each specimen was attached to a metallic scanning electron microscope stub by using low-resistance contact glue. After the special silver glue had been cured for 24 hours, the top fracture surface was blown gently with air to disperse any possible debris. Dried SEM specimens were coated with a conducting gold film to prevent surface charging by the electron beam. Throughout the SEM process, the specimens were kept under room temperature and subjected to 4×10^{-7} torr of vacuum. Figure 3.8 shows selected SEM images for illustration.

The particles shown in Figure 3.8 are characterized by high angularity and irregular shapes. Fine materials acting as coating and pore filling are also evident. Most of the particle contacts are tangential, long, and short straight with a few concavo-convex and sutured contacts. Fractures within detrital

grains are also clear in most images, which can be attributed to the initial stage of diagenesis (mechanical compaction). Figure 3.8 also reveals crystal overgrowth resulting in intimacy between neighboring particles and frequently pushing of neighboring grains. The pitting cavities shown in Figure 3.8 indicate the severe chemical dissolution experienced during diagenesis. Magnification of the fine-grained particles, acting as bridges and coating between grains, did not reveal any particular orientation and reflected the flocculation of the flakes. The fine grains could be a direct result of either the dissolution of the feldspar grains (silicates of aluminum) in the matrix, which also produces amorphous silicates, or the of diagenesis of the overlying shale as common sources of the fine- grained particles in sandstones (Pettijohn et al. 1972).

The X-rays of the targeted particles noted during the SEM examination could not clearly identify the particles' mineralogy due to the coating of the detrital grains with fine-grained materials, which was expected as a reflection of the sedimentary rocks' nature. Therefore, it was decided to conduct the analysis by using a mapping technique. The analysis was accomplished by collecting grains with different colors attached to a metallic scanning electron microscope stub (Figure 3.9). The particles were numbered and labeled as clear, white, red, purple, and black. The clear and white particles numbered (1-5) were basically silicates with an insignificant portion of aluminates (mainly quartz particles) (see Figures 4.10a and 4.10b). Several investigators

(e.g., Pettijohn et al. 1972; Friedman et al. 1978) have indicated that quartz minerals dominate the mineralogical composition of orthoquartzite family. Particle No. 6 was a white kaolinite particle, as evidenced by the nearly equal ratio between the silicates and the aluminates and the existence of potassium (Figure 3.10c), which is a typical clay mineral in sandstones of the lower Cretaceous age in Alberta (Carrigy and Mellon 1964). Particle No. 7 was a red feldspar particle, which was presumably the source of the kaolinite, and indicated that the source of the parent rock as either igneous or metamorphic rock (Figure 3.10d). Particle No. 8 was purple in color and identified as belonging to the amphibole family (Figure 3.10e). Particle No. 10 was a black chert identified by the existence of multiple quartz crystals in the same particle (Figure 3.10f) and particle No. 11 was a black titanium particle which is typically found in sedimentary rocks, as shown in Figure 3.10g (Pettijohn et al. 1972). The results of the X-ray analysis suggested that the black bands were fine rock fragments and chert particles, reflecting the depositional layering common to sedimentary environments. In order to confirm these observations, thin sections were also prepared to provide additional insights into this deposit's depositional history.

3.5.3 *Thin sections under petrographic microscope*

Thin sections were prepared to provide details of the grain shapes, the post-depositional processes, and the layering of the black bands. Sections were prepared with dimensions of 75x55mm after impregnation with a blue-dyed

epoxy resin under a high vacuum. These sections were oriented both parallel and perpendicular to the layering. Examination of the thin sections was carried out by using a petrographic microscope, under different magnifications, connected to a Nikon digital camera. In the well-sorted bands, the particles ranged from angular to very angular with frequent sub-angular particles (Figure 3.11). Approximately 90% of the particles were quartz particles with 5% polycrystalline quartz originating from a metamorphic rock, 4% were very fine -grained rock fragments (mostly chert), and less than 1% were clay minerals, bridging quartz particles as shown in Figure 3.12. The observed contact nature was generally short and long contacts with a few tangential and interpenetrative contacts.

In the less-sorted bands, most particles were angular in shape. Variable fine rock fragments were present in the band under examination. Their presence implies the variability in the parent rocks from which the sediments were transported. This less-sorted band was composed of approximately 60% monocrystalline quartz, 5% polycrystalline quartz, 10% siliceous siltstone, 20% chert, and 5% feldspar and clay minerals.

Figure 3.13 shows a partially clean fractured quartz grain. The deposit appears to have been subjected to overburden loads that were substantial enough to cause this fracturing and, hence, to influence the deposit's structure. The clean cracks within the quartz grains implies either that the clay

minerals were deposited following the compaction stage or that they were too weak to prevent loss of porosity due to compaction by early cementation. In the poorly sorted layers, evidence that compaction embedded the quartz particles between the fine-grained rock fragments was found, reflecting the influence of the burial depth after deposition (Figure 3.14). The overgrowth was distinguished by dust lines as one of the diagnostic aids for identifying the overgrowth (Pittman 1972) (see Figure 3.15). A fresh skeletal grain derived by dissolution is also apparent in Figure 3.16, suggesting that the process of dissolution occurred after the compaction stage and is still in progress; otherwise, the compaction process would have destroyed this skeleton.

Based on these results, the characteristics of this formation are consistent with locked sand characteristics as summarized by Barton et al. (1986) and introduced by Dusseault and Morgenstern (1979). The formation is basically a lower cretaceous middle McMurray Formation that is best described as over-consolidated un-cemented and well sorted friable sand with interlocked fabric, stems from deposition of authigenic silica, and has insignificant portions of clay minerals, acting as bridges and coating, that are responsible for the friable nature of its weak interlocked fabric. The fine particles presumably originated due to either the diagenesis of the overlying shale formation or the feldspar inherited from parent rocks. The clean cracks within quartz grains imply that clay minerals were deposited following the compaction stage or its

weak nature, preventing the loss of porosity due to compaction by early cementation.

3.5.4 Fabric orientation using Digital Image Analysis (DIA)

Baghini (1998) investigated the anisotropy of the same block samples used in the current investigation. The SEM images were analyzed quantitatively and qualitatively by using public-domain digital image analysis software (NIH 1997). The density slices technique, using a range of gray level thresholds, was used for segmentation instead of standard digital image techniques to overcome non-uniform lighting and noise in images. Both vertical and horizontal sections cut from the original block were investigated to identify the particle shapes as well as the preferred orientations of the long particle axis and their intensity. The vector mean direction (θ_m) and vector magnitude (V.M (%), as recommended by Curray (1956), were used to analyze two-dimensional orientation data to establish the preferred orientations and their intensity (the measure of disperse), respectively. The axial ratio adopted by Oda (1972a and 1972b) was employed for particle-shape identification. The three parameters can be expressed as follows:

$$[3.1] \quad \theta_m = \frac{1}{2} \tan^{-1} \left[\frac{\sum \sin 2\theta_k}{\sum \cos 2\theta_k} \right],$$

$$[3.2] \quad V.M(\%) = \frac{100}{\sum a_k} \sqrt{(\sum a_k \sin 2\theta_k)^2 + (\sum a_k \cos 2\theta_k)^2},$$

$$[3.3] \quad \text{Axial ratio} = \frac{1}{\sum a_k} \sum_{k=1}^{a_k} \left(\frac{L_2}{L_1} \right)_k,$$

where θ_k is the direction of the observed quantity (the orientation of the particle long axis with respect to a horizontal reference) on an image from -90 to $+90$; L_2 and L_1 are the length of short and long axis, respectively; and a_k is the number of observations. The complete random orientation of particles gives a vector magnitude value of 0. On the other hand, a 100% value means a complete preferred orientation. Selected results for vertical as well as horizontal sections are reproduced in polar coordinates in Figure 3.17. For vertical sections, the particles show a unimodal distribution while horizontal sections show a polymodal distribution. The vertical sections show a mean vector of (1-10) and a magnitude of 18-25%. The horizontal sections show a mean vector of (15-39) and a magnitude of 7.5-15.5%. Axial ratios range from 0.68-0.71. The axial ratios indicate the high angularity of this formation as revealed from particle analysis. Baghini (1998) compared these values with those of other sand formations and concluded that diagenesis has no effect on particle shape and orientation.

The vertical sections show an almost horizontal preferred orientation. The low intensity of the vector magnitude indicates the absence of perfect horizontal orientation for the particles. In terms of porosity, the vertical sections do not exhibit any preferred flow path. For the horizontal sections, there is no

preferred orientation for all sections, and particle-orientation randomness is higher than those of vertical sections. As Baghini (1998) showed, the mechanical response of vertical and horizontal samples is different due to their inherent anisotropy. Vertical cores tend to give higher strength and higher dilation than horizontal cores, basically because the preferred orientation of contacts' normal parallel to the major principal stresses' direction (particularly in the triaxial compression state) (Oda and Konishi 1974).

3.6 Experimental procedures and measuring technique

The uniaxial compression test was favored for two reasons: (a) it directly reflects the effect of the interlocking on the strength as an intrinsic strength component independent of the confining pressures; and (b) by testing this formation in its natural dry state, one avoids the problems associated with pore fluid, which could possibly alter this formation's delicate micro-structure.

3.6.1 *LVDTs and data acquisition*

The axial and lateral strains were measured by using AC-operated miniature 100 MHR series LVDTs manufactured by Schaevitz. These transducers possess a nominal linear range of ± 2.54 mm and a linearity of 0.15% over the full range at 10 kHz and, hence, have the ability to capture small deformations. An additional advantage is the light weight of the transducer (6 g.) and relatively small dimensions: a length of 25.4 mm and a diameter of 9.4 mm. The primary coil is excited with an input voltage of 3 V RMS, which

requires a special signal conditioner connected to a DT800 datataker, produced by dataTaker Ply Ltd., acting as a data acquisition and data logger system. The DT800 has the ability to scan data from each sensor channel at 40Hz, and has an analog-to-digital converter with a resolution of 18 bits and a noise rejection of 50dB. Communication is done through a connection with a personal computer to store and upload the data in real time. The DT800 has a range of $\pm 10V$ and a resolution of 1mV for the input voltage and $1\mu V$ for the displayed output voltage (1mV input can be displayed up to 0.001mV output voltage). Another signal conditioner (a LVM 110 produced by Schaevitz sensors with a range of $\pm 5V$) was provided to augment the system with an additional three LVDTs from the same manufacturer. Figure 3.18 presents a schematic diagram of these components.

3.6.1.1 *LVDT calibration*

The LVDTs were calibrated by using a small micrometer, as shown in Figure 3.19. The transducers were calibrated at their middle range to achieve the best accuracy and to avoid the nonlinearity at the transducers' extremes. All transducers showed linearity for their full working range; an example is shown in Figure 3.20. Figure 3.21 shows the relationship between the residuals, defined as the difference between the actual and ideal output reading, normalized to the full range in percentage (accuracy) and the output voltage. The accuracy of the transducers is less than 0.1%, which translates into a percentage error in strain of less than 0.0078% for a 63.5 mm specimen and

a deformation magnitude of less than 0.005 mm based on the transducers' full scale. Although this kind of transducer (LVDT) has infinite resolution, the transducer's resolution is limited by the data acquisition system. For the selected data acquisition system, the transducer's resolution can be as low as 0.02 μm (0.072 mV for $\pm 10\text{V}$ LVDTs), which translates into 0.00003% strain for a 63.5 mm specimen.

3.6.1.2 Stability characteristics and proof testing

One of the central issues related to transducers is their stability for long-term performance, or the variation of the output readings with time. The stability is understood as an integrated effect of the noise in the system (e.g., the cables' type and length, the A/D converter's resolution, the extent of the amplification and the filtration in the signal conditioner) as well as the sensitivity of the transducers to the temperature. The stability was quantified for all LVDTs at room temperature in a stationary position, as shown in Figure 3.22. The temperature was monitored by using YSI 44007 thermistors, excited through the Datataker (15 mW), with a working range of -80°C to 120°C and a resolution of 0.1°C . The thermistor was calibrated by immersing it in a container filled with ice and water while continuously stirring the thermistor in the container to identify the thermistor's zero drift, which was recorded to be in the range of 0.06°C (see Figure 3.23).

Table 3.4 summarizes the calibration factors and the nomenclatures for the whole set of LVDTs. Figure 3.24 shows the variation of the deformation as a function of time for one of the calibrated transducers. The variation of the output voltage for the whole set of transducers corresponds to a deformation of $0.15 \mu\text{m}$ - $0.8 \mu\text{m}$ (0.00023 - 0.00125% strain for a 63.5 mm specimen). The temperature's variation recorded in the laboratory was in the range of $0.8 \text{ }^\circ\text{C}$ for almost 24 hrs (Figure 3.25). Figure 3.26 shows a linear relationship between the variations in the deformation as a function of the temperature variation for one of the calibrated LVDTs. Table 3.4 shows that the temperature corrections factor ranges from $-0.14 \mu\text{m}/^\circ\text{C}$ (compression) to $1.15 \mu\text{m}/^\circ\text{C}$ (extension). However, as the table also shows, this range of variation was insignificant when translated into strain.

The reliability of the LVDTs in capturing deformation characteristics was assessed by comparing the calculated modulus with the known Young's modulus of a PVC cylindrical sample. The PVC sample has a Young's modulus of approximately 2.76 GPa and a compressive strength of 48 MPa . Figure 3.27 shows a typical result from the measurement system in the form of deviator stress versus axial strain. The calculated Young's modulus for the PVC sample was 2.8 GPa , with a relative standard error of 1.4% which confirms the transducers' reliability in measuring deformation.

3.6.2 Sample preparation and mechanical configuration

3.6.2.1 Sample preparation and dimensions

Block samples were cut in the laboratory by using a core barrel to reduce them to the required size of cylindrical samples. Extremes were flattened by using a blade to give the best smooth surface for testing purpose. The cutting of such samples required extreme patience due to the friable nature and brittleness of this kind of sand. Frequently, irregular end surfaces were unavoidable, and, hence, it was decided to abrade them by scarping meticulously on a horizontal metal plate while they were encased within a hollow aluminum cylinder. The preparation of samples for testing was done on a Perspex plate to reduce friction, and, hence, to prevent the loss of sample during the preparation stage. The extreme brittleness of the samples made is impossible to make efficient use of the blocks. The preparation of one sample took between 5-6 hrs. Cresswell (2001) recommended, for the preparation of Reigate Silver sand, spraying a hairspray on samples, forming a small shell around them. This shell could be removed through flushing when the samples were mounted in a triaxial cell. One of the concerns with this approach is how penetrative the hairspray is in the sample. Another concern is the effect of flushing, which can result in the loss of particles due to their friability. Wetting can also result in a reduction in the strength of this kind of sand (Richards and Barton 1999, Cresswell and Barton 2003).

Most of the tested samples in this investigation had a slenderness ratio ranging from 1:1 (63.5 mm diameter x 63.5 mm height) to 2:1. The size of tested specimens was intentionally selected to be large (compared to the regular sizes of previously tested locked sands; 36 mmx76mm) for two reasons: (a) the bigger the sample, the more representative the results; and (b) preparation disturbance effects have more adverse effects on small-sized samples than on larger ones. A total number of 12 samples were extracted from the blocks. The presented results in this chapter and the subsequent one are representative of the obtained results obtained from the experimental work.

3.6.2.2 Mechanical configuration set-up

The loading system consisted of a load frame and a loading cell with capacities of 17 MPa and 7 MPa, respectively (for a 63.5 mm sample diameter). These capacities were considered satisfactory for this kind of sand, which was expected to exhibit a low uniaxial compressive strength. Figure 3.28 presents an illustration of the various components of the original measuring system's configuration. The adopted configuration (provided by SBEL (Structural Behaviour Engineering Laboratories Ltd.) included two loading platens with a circumferential groove into which the deformation rings were fixed by means of spring-loaded screws/pins, three LVDTs (two vertical LVDTs and a horizontal spring-loaded one), two aluminum deformation rings provided with LVDTs' mounting holes, and horizontal spring-loaded pins to fix

the rings to the platens' grooves, two non-magnetic threaded connecting rods containing a screw nut in the upper extreme (attached to the upper ring) to lock the vertical LVDT into the core position with respect to the core body attached to the lower ring holes, a light aluminum chain connected at each extreme with two blocks attached to each other by using a guide bar (linear bearing), and an O-ring connecting two steel posts. The horizontal spring-loaded LVDT was attached to one block and fixed into position by using a vertical spring loaded pin and facing a screw attached to the other block for adjusting the initial reading.

The original mechanical configuration was later modified to facilitate the set-up procedure as well as to obtain replicate measurements for comparison. In particular, with the original system it was not possible to ensure either the verticality of vertical LVDTs or the parallelism of upper and lower deformation rings. The inability to ensure the verticality of LVDTs or the parallelism of the deformation rings can result in a stick-slip problem, and, hence, the development of friction between the cores and the LVDT's core bodies.

For these reasons, the existing system was modified. The system was augmented with 3 additional LVDTs (two for lateral deformation and one for vertical deformation) besides the two existing vertical LVDTs and the chain's spring-loaded LVDT. The upper and lower deformation rings were re-fabricated to carry the three vertical LVDTs as well as two vertical aluminum

alignment posts. For each of the horizontal LVDTs (H-LVDTs), the core body was fixed into position by using an extended mobile arm connected to a vertical post fixed on the loading frame. The LVDT core was attached to a short threaded rod that extended horizontally to a small puncture created on the sample's surface at one end. The other end carrying the LVDT core was adjusted to be at the center of the LVDT core body to record the relative movement between the core and the fixed core body. Figure 3.29 presents an illustration of the mounting procedure and the final configuration. The mounting procedure was carried out in the following steps:

1. Step I included placing the lower platen with the lower deformation ring attached to it as well as the vertical LVDTs' core bodies fixed into position by using the spring-loaded pins. Afterwards, the chain was attached to the sample's circumference at the sample's mid-height and the blocks (carrying the horizontal spring-loaded LVDT) were connected by using an O-ring. Next, the sample was placed on the lower platen. Direct interference between the platen and the sample's end was alleviated by using a thick layer of silicone grease sandwiched between two latex membranes (Figure 3.29a).
2. Step II consisted of placing the upper platen with the upper deformation ring on the specimen and locking the system to the frame by applying a minimal sitting load. The system locking was necessary to prevent sample movement during the adjustment of the LVDTs' verticality. Once the

system had been locked, the two vertical alignment bars were connected to the upper and lower deformation rings and fixed into position by using the spring-loaded pins (machined in the rings' sides) (Figure 3.29b).

3. Step III consisted of placing the connecting rods with the cores attached to the lower end, tightening the upper end to the upper deformation ring, and removing the adjustment bars. This stage ensured the verticality of the connecting rods to prevent the potential friction between the cores and the cores' bodies (Figure 3.29c).
4. Step IV included the mounting of the two horizontal LVDTs to complete the set-up. The horizontal LVDTs' bodies were fixed into position by using two fixed arms extended from the vertical posts on the loading frame. Once fixed, a short rod with the core attached was inserted into the core body by meticulously rotating the free end into the sample. Once a puncture had been created in the sample, the LVDTs' core bodies were again adjusted to prevent friction (Figure 3.29d).

Samples were then sheared at a constant strain rate of 0.05% and data were logged every 10 seconds to capture both the pre- and post-peak response. The system was also augmented with an unguided free armature external LVDT to compare the local and external axial strain measurements.

3.7 Significance of local strain measurements

In this section, the significance of local strain measurements is described by comparing the local and external axial strains as well as the strain rates. The tested specimen had a slenderness ratio of 1:1 and sheared at a constant strain rate of 0.05%. The axial strain was averaged based on the reading of the three vertical LVDTs for comparison with the externally measured axial strain.

3.7.1 Local vs. external stress-axial strain curves

Figure 3.30 shows the deviator stress ($q = \sigma_1 - \sigma_3$; $\sigma_3 = 0$)-axial strain (ε_1) relationship based on local and external axial strain measurements. In general, the specimen attained a peak strength of 2.0 MPa at axial strains of 0.32% and 0.57% according to the local and external measurements, respectively. Both strain systems showed an extremely brittle post-peak response. According to ISRM (1978b), the specimen tested is classified as a very low strength rock (weak rock), which lies close to the soil boundaries (the soil boundary is characterized by a uniaxial compressive strength < 0.25 MPa) and constitutes the boundary between soils and hard rocks. The source of the high uniaxial strength is presumably due to the relatively extensive area of contacts as well as the increase in the coordination number, or the number of contacts per particle. That is, particles interact as surfaces rather than point contacts (as in dense sands), and, hence, the rotational resistance is enhanced. As a consequence, in the absence of bonding, individual contacts

can sustain considerable contact forces, moments, and stress obliquity due to interlocking (Creswell and Powrie 2004).

The external measurements had a tendency to overestimate the axial strain at any stage during the shear evolution and particularly in the pre-peak regime, as has been found with other geomaterials (e.g., Ibrahim and Di Benedetto 2005; Yimsiri et al. 2005). Only at very large axial strains did the internal and external measurements converge together. In the pre-peak regime, both stress-strain curves were initially concave followed by a linear region. The size of the initial concave portion of the stress-strain curve was significantly overestimated by the external strain measurement as compared to the local one. Within this zone, the nonlinear behaviour suggested the closure of the existing fractures and the soft inclusions identified in the microstructural studies. In the linear portion of the stress-strain curves where the elastic zone is traditionally identified, the axial stiffness based on the local strain measurement was approximately 0.87 GPa and almost 2 times the externally measured axial stiffness. In the post-peak regime, both measuring systems indicated strain weakening; however, the local one exhibited a slightly less abrupt reduction in strength.

3.7.2 Local and external axial strain rates

Figure 3.31 shows the variation of the instantaneous local and external strain rates ($d\varepsilon/dt$) with the axial strain as well as the local axial stress - axial strain

curve. Despite assigning a controlled constant rate of strain (0.05%) at the start of the test, the external and local strain rates deviated from that assigned value. The external values were higher than the assigned value at the initial stages due to the beddings effect and coincided with the assigned values upon closure of the fractures throughout shearing evolution. On the other hand, the local strain rate value was recorded to have smaller values, up to 40% of the average value, before the closure of the fractures. Upon attaining an intimacy between the grains and full contact, a linear increase in the axial strain rate occurred as a reflection of the initiation of the unlocking mechanism, followed by a sudden increase around peak strength (around a 64% increase in the axial strain rate). This sudden increase probably signified the unlocking of most sample elements and the initiation of localization in the post-peak regime. In this regime, the strain rate oscillated above the specified value, reflecting, on average, an increase in the strain rate and non-uniformity of the strain rate as an indication of progressive rupture of the interlocked fabric. Consequently, local strain rates are indicative of the failure process at all stages of shearing as compared to the constant values estimated from the external measurements. Extreme caution is necessary when assigning strain rates for the sake of comparing geomechanical responses or when the creep rates are of special interest. Hayano et al. (2001) made a similar recommendation in their study of soft rock, in which the creep axial strains measured locally were noticeably less than the externally measured ones.

In the present study, the interlocking between particles was found to be the main source of such high strength in the absence of virtual bonding between sand particles. For proper characterization of such geomaterials, experimental results' interpretations founded on external measurements are in error, particularly when coupling strength and deformation is targeted. Moreover, local axial strain measurements provide more insight than external measurements into failure mechanisms.

3.8 Summary and conclusions

This chapter provided a synopsis of the common characteristics of locked sands to create a framework to identify such deposits. Based on this framework, experimental work was presented to identify the fit of the High-Hill oil-free sand formation into the locked sands category. The experimental work was comprised of micro-structural observations, mineralogical composition analyses, and fabric analysis. A uniaxial compressive strength test was also carried out to reveal the strength of this formation's unbonded coherent mass and to explore the significance of the local strain measurements. The experimental set-up as well as the calibrations, proof testing, and stability tests were presented and discussed in detail.

Based on the investigation, the High Hill river sand formation is a lower Cretaceous McMurray Formation. The dense nature of the samples, their mineralogical composition, and micro-structural observations are in keeping with

characteristics of locked sands. The formation is best described as overconsolidated, well-sorted, unbonded, friable, locked sand with characteristics similar to those of oil-sands' middle members. This deposit was subjected to mild post-depositional diagenesis rendering transformation of its detrital sand-sized particles into a weak rock with interlocked fabric through deposition of authigenic silica. SEM images and petrographic analysis of thin sections disclosed that grains' contacts were dominated by tangential, long-to straight, occasional interpenetrative and sutured contacts created via overgrowth and dissolution. The minor percentage of kaolinite in the form of coating or bridges is responsible for the friable nature of this deposit. The fine particles presumably originated from either the diagenesis of the overlying shale formation or the feldspar inherited from parent rocks. The deposit appears to have been subjected to overburden loads that were substantial enough to cause this fracturing, and, hence, to influence the deposit's structure. The clean cracks within quartz grains imply that clay minerals were deposited following the compaction stage or its weak nature to prevent loss of porosity due to compaction by early cementation. The existence of a fresh skeletal grain by dissolution suggests the process of dissolution occurred after the compaction stage (otherwise, the compaction process would have destroyed this skeleton) and that the dissolution is still in process.

A local measurement system for both axial and lateral strain was used and modified for this friable material in conjunction with a routine external axial

measurement system for proper characterization. The formation exhibits a uniaxial compressive strength of 2 MPa and hence may be classified as a weak rock. The interlocking between particles is the main source of such high uniaxial strength and axial stiffness in the absence of bonding between sand particles. The axial stiffness based on local strain measurement is approximately 0.87 GPa and almost 2 times the externally measured axial stiffness. In the post-peak regime, both measuring systems indicate strain weakening; however, the local one exhibits a slightly less abrupt reduction in strength. In terms of the failure mechanism and strain rate effects, the variation in local axial strain rate provides more insight than externally measured axial strain rate into failure evolution stages. This discrepancy is most critical when the strain rate effects are a concern or when the creep behaviour is targeted. Hence, for proper characterization of such geomaterials and their oil-sand counterparts, experimental results' interpretations founded on commonplace external strain measurements are less reliable, particularly when the coupling strength and deformation is targeted. Local strain measurements are necessary for proper behavioral characterization and failure mechanism interpretation of locked sands.

Table 3.1 Summary of physical and mechanical characteristics of locked sands.

Authors	Formation	Porosity (%)	RD (%)	Density (kN/m ³) and/or D ₅₀ (mm)	Peak/secant friction angle, normal stress and strain at failure (direct shear test- dry else stated)	Strength parameters, confining pressure and strain at failure(Triaxial tests)	Uniaxial compressive strength and youngs modulus	Contact Nature/ or TI(%).
Dusseault and Morgenstern (1979) Dusseault and Morgenstern (1978)	Athabasca oil sand (Lower Cretaceous)	31.3	>100-135	18.5-23.3 D ₅₀ =0.2mm	44°-46° (100-800kPa) 1.5-2.5% φ _{sec} = 39.9°-66.4°* (98-785kPa)	φ _{sec} = 50°		Mostly concavo/convex contacts with tangential contacts
Barton et al. (1986)	Barton sand (Eocene)	35.6	119	17	40.6°-47° (50-900kPa) 1.9-5.5%	C= 0 kPa φ = 40° (100-700kPa) 2.9-7.9%	q _u 5-134 kPa	Tangential contacts- slight concavo/convex contacts (TI=54%)
Barton et al. (1986)	Bagshot sand(Eocene)	36.4	110	16.8	44.2°-50.3° (50-900kPa) 2.5-7%	C= 0-77.4 kPa φ= 41.5°-50° (100-700kPa) 0.56-2.8%	q _u 20 kPa	Tangential and straight contacts- slight concavo/convex contacts (TI=41%)
Dusseault and Morgenstern (1979)	Swan River sandstone (Lower Cretaceous)	34.5	125		63°-70° (100-800kPa) 1.0-2.5%	-----	-----	Mostly concavo/convex contacts
Dusseault and Morgenstern (1979) Dittes and Labuz (2002)	St. Peter friable sandstone (Ordovician)	27 27	135	19 kN/m ³	63°-69° (100-800kPa) 0.5-1.75% φ = 57°-63° ψ=45°(19kPa)-21° (152 kPa) φ _{sat} =46°	φ= 57°-69° φ _{field} = 56°	q _u =0.6-2 MPa E=1 GPa ν=0.2-0.33	Mostly concavo/convex contacts
Dusseault (1980)	Itacolumites (flexible sandstone)				Much stronger than locked sands with no cementation due to intense diagenesis			High concavo/convex contacts due to quartz overgrowth
Richards and Barton (1999)	Folkstone bed sands Uniform (including Reigate silver sand) Thin bedded(iron oxide)	28-35 25.7-33.6		D50 = 0.2-0.3mm	C= 7.7-179.4 kPa φ _{sec} =34°-65.5° C= 20.5-65.4 kPa φ _{sec} =34°-65.5°^ (0.15-0.8mm for zero) (0.6-2mm for normal loads up to 674kPa)		q _u =101.9-725.2 kPa q _u =85.5-218 kPa	TI=29.7-65.4% TI= 27.3-66%
Cresswell and Powrie (2004) Cresswell and Barton (2003)	Reigate silver sand	32	136%	18.62 D50 = 0.25mm	φ = 70° (low stress and 40° and 10 MPa) (0.25mm at 1.5 kPa-2.5mm at 10Mpa)	(50-800kPa) 0.4%-0.8% M=2.25 (p=0-1000 kPa)	q _u =108-101.9 kPa	TI=26%

* function of bedding plane orientations

^ depends on the orientation of bedding. General trends that cohesion tends to decrease for parallel beddings and friction increases for normal beddings.

* TI (Tangential index defined as the proportion of tangential contacts amongst all grain/grain contacts)

Table 3.2 Summary of Depositional environment as well as lithology of McMurray Formation members.

McMurray Formation stratigraphy members	Depositional Environment	Lithology of Athabasca Oil sands “ McMurray formation sand members”*
Upper	Low energy shoal/ Shore-face (coastal plain sediments)	-Fine-grained quartzose sands to clayey silts (Group III). - doesn't belong to the orthoquartzite family due to existence of significant percentage of clay minerals and non-quartz clastics.
Middle	Marine influenced estuarine channel complex	-Fine to medium grained quartzose sands. - Well sorted sand and largely fall in Group II.
Lower	Braided to meandering fluvial sand channels (paleovalley- fills)	- medium grained sand and pebble conglomerates fall within Group I

Table 3.3 Summary of main physical properties of High Hill river formation.

Main Physical properties
<p><u>Grain size analysis (ASTM D 422):</u> -D₁₀= 0.075mm, D₃₀= 0.132mm, D₆₀=0.19mm - Coefficient of curvature = 1.22, Coefficient of uniformity= 2.53. - Percentage of fines < 10%. - Well graded fine to medium sand</p> <p><u>Average porosity and unit weight:</u> Average porosity=34% Average unit weight= 17.6 kN/m³</p> <p><u>Relative density (ASTM D 4254, D 2847):</u> Average maximum void ratio = 0.86, average minimum void ratio = 0.61, average in-situ void ratio= 0.54 Average relative density (RD%)= 125%</p>

Table 3.4 Calibration factors for transducers.

Transducer	Measurement	Calibration factor (mm/mV)	Temp. calibration factor ($\mu\text{m}/^\circ\text{C}$)	Change in strain/1 $^\circ\text{C}$ reduction for a 2.5" sample (%)
LVDT V1*	Vertical strain	0.000245	0.59	0.0009
LVDT V2*	Vertical strain	0.000191	0.3	0.0005
LVDT 3AV	Vertical strain	0.000828	-0.14	-0.0002
LVDT 3HCHAIN*	Circumferential strain	0.00020	0.24	0.0004
LVDT 1AH	Horizontal strain	0.000828	1.15	0.0018
LVDT 2AH	Horizontal strain	0.000938	1.04	0.0016

* Original set of transducers.

CHAPTER 4: MOBILIZED STRENGTH OF HIGH-HILL RIVER LOCKED SAND FORMATION AND FAILURE MODES

4.1 Introduction

As shown in Chapter 3, locked sands are classified as *arenaceous* (predominately quartz sand particles) weak sedimentary rocks that constitute the boundary between soils and rocks. The source of the high strength of locked sands compared to dense sands stems from the mild diagenesis that forms a coherent interlocked sand mass without the cementation commonly encountered in sandstones (Barton 1993). Previous investigations of the geomechanical response of locked sands typically focused on the ultimate strength and volume change characteristics by using external strain measurements (Dusseault and Morgenstern 1979; Barton et al. 1986; Richards and Barton 1999; Wong 1999; Dittes and Labuz 2002; Creswell and Barton 2003). It is now recognized that local axial and lateral strain measurements in soils and rocks are indispensable and can reveal important information in the pre-peak regime (e.g., Shibuya et al. 1994; Martin and Chandler 1994; Scholey et al. 1995; Fujii et al. 1998; Hayano et al. 1999; Bésuelle et al. 2000; Yimsiri et al. 2005; Sulem and Ouffroukh 2006). For locked sands, Abdelaziz et al. (2006) contrasted local and external axial strain results under uniaxial compression test conditions and showed that external measurements overestimated axial strains at various strain levels. Local strain results were shown to be more valuable for comprehending the failure mechanism, its evolution, and strain rates' effects. Recently, Creswell and Powrie (2004) carried out an experimental investigation of locked sand by using local

strain measurements. These researchers recommended the onset of dilation threshold as a strength threshold candidate to prevent the destruction of the interlocked fabric. However, no attention was paid to the variation in local lateral strain and its significance. For hard rocks, Martin and Chandler (1994) showed that the pre-peak damage thresholds of a hard rock (granite), determined from the local axial and lateral strains, were true material properties independent of the scale and loading rate. Furthermore, Martin and Chandler (1994) argued that the peak strength was related to the testing boundary conditions, i.e., the length-to-diameter ratio, the sample size, and the loading rate. These investigators also recommended the onset of dilation to be the long-term strength for granite instead of the peak strength. Roscoe (1970) stressed the value of understanding failure's precursory strains in soils, because the eventual failure surfaces and their orientation were determined well prior to the peak strength. Desrues and Chambon (2002) highlighted the importance of appropriately simulating the pre-peak response of soils up to the onset of localization instead of matching peak strength, which was merely a sign of the established failure.

Recent experimental and theoretical work on the failure kinematics of dense sands revealed that the shearing resistance was in principle governed by sliding, rolling, and mostly rotational resistance at grain contacts (e.g., Oda and Kazama 1998; Wan and Guo 2004; Alshibli and Alramahi 2006). Investigations of the shear strength of dense sands and locked sands indicate that sheared specimens tended to form columns/block of particle groups parallel or sub-

parallel to the major principal stress's direction in the pre-peak regime (Oda and Kazama 1998; Oda et al. 2004; Rechenmacher 2006; Cresswell and Barton 2003). These columns tend to dilate and buckle at peak stress to form a persistent inclined shear band creating large voids through the rotation of individual particles or blocks of particles. This dilatant mode of deformation through creation of voids in the direction of major principal stress is analogous to the concept of the dilation bands recognized in unconsolidated sands and weak sandstones (Bésuelle 2001; Du Bernard et al. 2002; Shultz and Siddharthan 2005) and the dilatant microcracks in brittle rocks (e.g., Schulson et al. 1999; Renshaw and Schulson 2001). For locked sands, the reported experimental results indicted a dominant shear band at failure (e.g., Dusseault and Morgenstern 1979; Cresswell and Powrie 2004). No experimental evidence has been reported for such column structures when cylindrical specimens are tested under compression.

The first part of this chapter deals with the evolution of failure by identifying damage thresholds at various stages of deformation, and the relationship between onsets of dilation and localization for a traditional 2:1 specimen with lubricated ends. Based on the experimental results, mobilized strength parameters are partitioned in terms of the interlocking, friction angle, and dilation angle contributions with the plastic shear strain. The second part examines the formation of the vertical columns, under a uniaxial compression test, where samples are tested by using a slenderness ratio of 1:1 and a low strain rate. In

the third part, multistage uniaxial creep test results will be presented and discussed in terms of the relationship between the onset of dilation and the long-term strength. Finally, the results of direct shear tests at low normal stress levels will be presented and discussed to show the minimum mobilized strength.

4.2 Effect of testing conditions on laboratory results

Testing conditions in terms of specimen geometry, end effects (end confinement effects), and strain rate are vital in the assessment of experimental results, i.e., the strength, strain, onset of localization, and failure modes. Bishop and Green (1965) investigated the effects of the slenderness ratio and end effects on the strength of dense sands under triaxial compression test conditions. To prevent end effects on strength, Bishop and Green (1965) advocated the use of slenderness ratios greater than 2 (lubricated or non-lubricated) or, alternatively, 1:1 specimens with thick lubricated ends between two membranes. However, Frost and Yang (2003) used optical image analysis to show for dense sands, that despite using a slenderness ratio greater than 2, the strains and void ratio were not homogenous within the tested specimens under triaxial conditions. Higher values of the void ratio and strain at the specimens' mid-height (the weakest elements) were noted as compared to the values at the specimens' extremes. Based on their findings, Frost and Yang (2003) recommended a slenderness ratio of 1:1 with thick lubrication at the specimen/platen interfaces to achieve homogeneity in the strains and void ratio within tested specimens during shearing. Desrues et al. (1996), using computer tomography for dense sands tested in triaxial tests, found that for tested specimens with a slenderness ratio of

1:1, the onset of localization was delayed compared to that of long specimens with a slenderness ratio of 1.9:1. Desrues et al. (1996) concluded that constraints favoring symmetry, such as a lubricated end-platen and a small slenderness ratio induced multiple localization modes instead of a persistent single band. Samieh and Wong (1997) compared the behavior of oil locked sand specimens with different slenderness ratios and end conditions in triaxial compression tests at low confining pressures. Samieh and Wong (1997) found that specimens with a slenderness ratio of greater than 1:1 failed with the formation of a single shear band. Shorter specimens with free ends resulted in a more stable and uniform deformation than that of longer specimens.

Another influential factor affecting the strain's homogeneity and the deformation's mode is the applied strain rate. Bhandari and Inoue (2005) recently explored the significance of low strain rates by using image analysis to capture strain rate effects on an artificial weak rock tested under biaxial conditions. Bhandari and Inoue (2005) found that low strain rates promoted uniform strain distribution among a sample's elements compared to high strain rates where localization became concentrated in narrow zones confined to the affected elements. In view of these studies, the formation of a single localized shear band (a preferred localization band) seems to preclude the propagation of reported pre-failure columnar structures in dense and locked sands due to early localization (loss of strain uniformity within specimen). Hence, in order to experimentally capture such reported column structures, specimens with a slenderness ratio of 1:1 and

thick lubricated ends tested under a low strain rate are preferable to achieve a uniform strain field, and, hence, render multiple localization zones at failure. However, these conditions are considered herein only to reveal such pre-peak structures, and are rarely encountered in the field as stresses and strains are never homogeneous due to either the inherent heterogeneity of geomaterials or the anti-symmetry of our civil engineering applications (complex boundary conditions).

4.3 Damage thresholds for brittle rocks

Damage thresholds are well recognized for low-porosity (<1%) brittle rocks and are measured by using electrical wired strain gauges mounted on the test specimen and, occasionally, with acoustic emissions measurements (e.g., Brace et al. 1966; Bieniawski 1967*b*; Lajtai and Lajtai 1974; Martin and Chandler 1994; Eberhardt et al. 1998; Chang and Lee 2004). Each threshold marks a distinct stage of damage recorded by the local stress-strain responses. Despite the difference in origin and fabric between locked sands (interlocked fabric) and hard rocks (bonded fabric), these thresholds can be exploited as damage indicators as manifested by the variation in the axial and lateral strain responses. Such thresholds are defined for hard rocks as follows:

4.3.1 Crack closure stress

The crack closure stress is the axial stress level at which original open cracks, oriented at large angles to the direction of the axial loading close.

Crack closure stress is manifested by the shift of the stress-axial strain curve from an incremental rate increase to a constant rate increase (the axial stiffness levels off). Once the majority of the existing cracks are closed, linear elastic deformation commences. However, this initial portion of the stress-axial strain response may not always be observed and may be obscured by bedding effects due to the irregular surfaces at specimen ends during preparation.

4.3.2 *Damage initiation stress*

The damage initiation stress represents the initiation of the extension-stress-induced tensile micro-cracks. Damage initiation stress marks the onset of the stable micro-crack growth aligned with the direction of the major principal stress. The identification of this stress level can be captured only by detailed examination of the stress-lateral strain response, since the damage in the axial direction has no effect on the axial strains (Lajtai et al.1990).

4.3.3 *Damage coalescence threshold*

The damage coalescence threshold marks the reversal of the volumetric strains from compression to dilation. Beyond this stress level, crack propagation and interaction occur and result in the progression of strain localization and formation of the macro-scale shear bands. Martin and Chandler (1994) showed that this threshold is independent of sample size

and loading rate and should be regarded as a material property instead of the peak strength, which is dependent on the loading rate and scale effects.

4.4 Experimental results

The tested specimen was prepared with a slenderness ratio of 2:1, as traditionally used in our laboratories, and a diameter of 63.5 mm. The axial and lateral strains were monitored by using two vertical LVDTs and an aluminum chain at the mid-height of the specimen. End effects were alleviated by using two latex membranes placed at the specimen/platen interface to reduce friction effects. The specimen was sheared at a strain rate of 0.1%/hr. In the reported results, the compressive strains are positive while the dilative (extensile) strains are negative.

4.4.1 Axial stress vs. axial-strain curve

Figure 4.1a shows the axial stress ($q = \sigma_1 - \sigma_3$; $\sigma_3 = 0$)- average axial strain ($\varepsilon_{1avg.}$) response for the tested specimen. The axial strain (the axial shortening with respect to the original height) is calculated based on the averaged vertical strain values of the two LVDTs. The specimen failed at an axial strain of 0.28% and attained peak strength at 1.8 MPa. According to the ISRM's (1978) classification of rocks, locked sand is classified as a very low-strength rock situated at the boundary between soils and weak rocks. The source of high uniaxial strength presumably stems from the relatively extensive area of grain contacts as well as the increase in the coordination number, i.e., the

number of contacts per particle. Thus, particles interact as surfaces rather than point contacts (as in dense sands), and, hence, the rotational resistance is enhanced. Therefore, in the absence of bonding, individual contacts can sustain considerable contact forces, moments, and stress obliquity due to this sand's interlocked fabric (Cresswell and Barton 2003).

In Figure 4.1a, the axial stress-axial strain curve is partitioned into three major stages. In the first stage (OA), the material undergoes an incremental increase in the axial stiffness up to point A. This point marks the closure of the inter-granular pores and the intra-granular cracks as well as the compression of soft inclusions in the specimens, as manifested by the microstructure studies. In stage AB, the axial stress-axial strain curve becomes linear with an average constant axial stiffness (E) of 0.85 GPa and an average Poisson's ratio (ν) of 0.2. At point B, the material undergoes a significant nonlinear change in axial stiffness up to the peak strength (C). Beyond point C, the strength drops abruptly. The inability to track the post-peak response results from the lack of servo-control in the post-peak region.

4.4.2 Axial stress vs. lateral strain curve

Figure 4.1b shows the relationship between the axial stress (q) and the lateral strain (ϵ_3) recorded by the chain LVDT located near the middle of the sample. The lateral strain exhibits lateral expansion all the way up to the peak strength. The axial stress-lateral strain curve can also be divided into three

stages based on changes in the nonlinearity. In stage OA, the axial-stress-lateral strain curve is characterized by negligible nonlinearity (almost constant). Beyond point A, an increase in nonlinearity occurs during stage AB. In the last stage (BC), a significant increase in the lateral strains and significant nonlinearity up to failure occur.

4.4.3 Volumetric strains and inception of localization

Figure 4.1c shows the volumetric strain (ε_v)-axial strain(ε_1) relationship. The volumetric strains integrate the variation of both the local axial and lateral strains ($\varepsilon_1+2\varepsilon_3$). The material exhibits an initial compression followed by a reversal in the volumetric strain (the onset of dilation). At the initial stage and up to point A, the volumetric strain is compressive and linear. Beyond this point, the volumetric strain remains compressive but non-linear up to point B. Point B marks the volumetric strain's reversal and the transition from compression to dilation up to the peak strength (C). Rowe (1969) showed that for extremely dense sands (with relative densities close to 100%), the maximum dilation factor ($1-d\varepsilon_v/d\varepsilon_1$) is equivalent to 2 and decreases with the reduction in the relative density. For the investigated sand, the maximum-recorded dilation factor is equivalent to 3.6 and is attributable to the particles' unusual contact characteristics, which are reflected in the exceptionally elevated relative density. According to the theory of internally constrained continua introduced by Goddard and Bashir (1990) and also according to Reynolds (1885), the dilatancy is a direct result of the internal and external

kinematic constraints. In granular materials, internal constraints are due to granular packing, so that the boundary grains prevent rearrangement during shearing. In bonded geomaterials, the bonds provide the source of internal kinematic constraint, which hinders rearrangement. In locked sands, the constraints are due primarily to the interlocked fabric. Therefore, higher energy is required to overcome such interlocking, and a higher dilation angle is expected as compared to that of dense sands with regular constraints (due to packing).

Localization of deformation in geological materials results in non-uniformity in strains. Consequently, constitutive models based on continuum approaches are less reliable once localization occurs. The non-uniformity of strains is considered by many researchers to be a good indicator of the onset of localization (e.g., Bésuelle et al. 2000; Sulem and Ouffroukh 2006; Abdelhamid et al. 2000; Labuz and Dai 2000). Fig. 4.1d depicts the relationship between axial strain differences ($\varepsilon_1 - \varepsilon_{avg}$), divergence of individual values from the mean value, and the average axial strain. During the early stage of loading, the readings are constant, signifying the relative uniformity of the axial strains. Immediately prior to the volumetric strain reversal, a significant divergence from the mean value occurs at point B', marking the onset of localization (the loss of strain uniformity). In this test, localization commences prior to the peak strength and in the hardening regime. This observation has been unequivocally reported in the literature as opposed to

the assumption of localization of deformation in the post-peak regime for most constitutive relations. For instance, localization in the hardening regime was reported by Desrues et al. (1985) for dense sand tested under biaxial condition, by Bésuelle et al. (2000) for Vosges sandstone under triaxial compression condition, by Sulem and Ouffroukh (2006) for Fontainebleau sandstone, and by Ord et al. (1991) for Gosford sandstone. Abdelaziz et al. (2005) demonstrated that the onset of dilation is an excellent indicator of localization for other geomaterials including dense sands, overconsolidated clays, locked sands, sandstones, and granites. This threshold is of paramount importance as strain measurements become less reliable once exceeded so that efforts to simulate geomaterials' behavior beyond this threshold within the framework of continuum approaches will be problematic.

4.4.4 Damage and failure evolution

4.4.4.1 Detection of damage thresholds for locked sand

Damage threshold will be established and discussed for the tested specimens by using the previously established framework. Figure 4.2a shows the relationship between the tangential axial stiffness ($E_{tan.}$), the incremental change in the axial stress with an incremental change in the axial strain, and the axial stress in a logarithmic plot. The tangential stiffness tends to increase nonlinearly up to point A, which marks the crack closure strength threshold (σ_{cc}) where the specimen's elements come into contact. After this point, the tangential stiffness in the axial direction is almost constant (0.85 MPa) up to

point B' where the initial reduction occurs in tangential stiffness, marking the initiation of damage coalescence. In addition, point B' is identical to the stress level where localization commences, as shown previously in Figure 4.1d.

Figure 4.2b shows the relationship between the tangential volumetric stiffness, the incremental change in axial stress with an incremental change in the volumetric strains, and the axial stress. The testing's initial stage up to point B' shows a constant slope reflecting the correspondence between the axial stress and the volumetric strain. At point B', volumetric stiffness accelerates nonlinearly and therefore can represent the initiation of damage coalescence (σ_{dl}) due to an increase in the density of unlocked sites throughout the specimen. At point B, volumetric stiffness discontinuity occurs, representing the change in the sample's behaviour from compression to dilation. This result implies the acceleration of damaged sites coalescence as well as the uncontrolled progression of the damage (the damage coalescence strength threshold (σ_{dc})).

Figure 4.2c shows the relationship between the tangential lateral stiffness (the incremental change of the axial stress with incremental change in the lateral strains) and the axial stress. Up to point A, a negligible variation in the lateral stiffness takes place. Beyond this point, the maximum lateral stiffness degrades nonlinearly and marks the damage initiation threshold (σ_{di}) due to the progression of fabric unlocking. At point B, the tangential lateral stiffness

starts to decrease linearly, signifying the complete interaction of the unlocked sites as well as the significant progression of lateral unlocking.

From the previous analysis, several thresholds were identified. The damage initiation of the interlocked fabric and the crack closure stress thresholds coincided and occurred at 28% of the peak strength. Sporadic unlocking at several sites within the specimen resulted in an increase in the number of damaged sites. At the damage localization stress threshold, these damaged sites started to coalesce to form a persistent band where localization commenced. This threshold was shown to take place immediately before the volumetric strain reversal at 55% of the peak strength. After initiation of the damage coalescence, the damage started to accumulate in an accelerated manner at damage coalescence stress threshold, which marked a reversal in the volumetric strains. This threshold occurred at 67% of the peak strength, as identified from the current analysis. Table 4.1 provides a summary of the damage thresholds and the elastic parameters.

4.4.4.2 Evolution of failure in locked sand

Figure 4.3 shows the deviator stress vs. the plastic axial, lateral, and volumetric strains. The plastic axial and lateral strains can be approximated as the difference between the total strain and the elastic strain by using Hooke's elasticity law ($E=0.85$ GPa, $\nu=0.2$). The plastic volumetric strain can be expressed as

$$[4.1] \quad \varepsilon_v^p = \varepsilon_1^p + 2\varepsilon_3^p,$$

where ε_1^p and ε_3^p are the plastic axial and lateral strains, respectively.

The pre-peak observations of shearing can be divided into three stages. Stage I is marked by the closure of cracks, pores, and fractures within the quartz particles created due to the huge burial depth as well as the compression of soft inclusions: clay coating and bridging. This process causes plastic compressive strains, with negligible sliding between the adjusted particles. The second stage marks the initiation of fabric unlocking through lateral expansion creating inter-granular voids (damaged sites) parallel or sub-parallel to the axial direction, similar to the inter-granular microcracking encountered in sandstones (Sangha et al. 1974; Santarelli and Brown 1989; Menendez et al. 1996). In stage II, the plastic axial strains are quite constant, indicating the progression of sporadic fabric unlocking and damage in the axial direction through lateral expansion. The same observation has been reported for hard rocks during the extension of the cracks in the maximum principal stress direction (e.g., Lajtai 1998). In stage III, vertically unlocked damaged sites coalesce to form columns through which the load is transferred to the sample in conjunction with an increase in the plastic axial strains (refer to Figure 4.3). Once coalescence occurs, the formation of macro-fractures (vertical and inclined bands) commences. It is

argued that the formation of inclined bands is dictated by these columns' ability to buckle, which is a function of the rotational resistance of the particles constituting each column. In locked sand, the interlocking between particles is considerable, and, hence, the dominant admissible mechanism is the separation of these columns horizontally with slight buckling and the formation of inclined bands with low vertical angles (the higher the degree of constraint, the lower the failure surface's vertical angle due to the inability to buckle). The failure is presumably a combined effect of significant geometric dilation between columns, columns buckling, and the falling of the failed portions between columns, and, hence, the loss of the columns' load-carrying capacity. The inclination of the formed bands with the axial stress direction ranged from zero vertical bands to 15° (slightly inclined bands that are dominant). The examination of the failed specimen did not reveal the full formation of these columns, so that the early localization inhibited its complete formation in the axial direction and promoted the formation of inclined bands and the buckling of the specimen. Figure 4.4 presents a schematic illustration of the proposed mechanism of failure.

4.4.5 Mobilized strength components in locked sands

One of the earliest attempts to partition strength parameters was done by Taylor (1948) for dense sands. Taylor, using direct shear test results of dense sands, attributed the dissipated energy at the peak to the energy dissipated by the basic friction between the particles and the energy needed to increase

in volume (dilation). Thuraiajah (1961) carried out a series of drained and undrained triaxial tests on sand and kaolinite. After integrating out the effect of dilatancy and change in soil grains' elastic deformation, Thuraiajah (1961) found that the dissipated work in plastic deformation was related to the critical state friction angle (a constant deviator stress with no change in volumetric strain) at all stages of the test path. Rowe (1962) used the principle of the minimum energy ratio (the existence of a preferential sliding direction at particle contacts so that the internal energy absorbed is minimum) to separate the basic frictional component and the dilatancy component for a wide range of dense sands. According to his approach, the peak strength of dense sands is the end-product of a basic friction angle and a dilation component that is absent for loose sands. Ladanyi and Archambault (1970) and Barton (1973) proposed a similar concept to express the strength of jointed rocks.

Muhunthan et al. (2004) determined, by using drained triaxial compression tests for Ottawa sand at different relative densities, the shear resistance against particle-to-particle frictional deformation (the true friction resistance) after applying corrections to the measured shear strength for plastic volumetric and stored elastic deformations. Muhunthan et al. (2004) indicated that the shear resistance from particle-to-particle frictional deformation is the sand's critical state strength, which is mobilized and stabilized at a low strain before the peak. Wong (1999) applied the stress dilatancy relation proposed by Rowe (1962) to reveal the source of the strength in oil-rich locked sands.

The normalization with respect to dilation did not reveal a constant stress ratio, which Rowe (1962) had found for dense sands. Wong (1999) indicated that the stress- dilatancy relationship did not account for the interlocking component and rolling in locked sands. In addition, the strength in the pre-peak regime was dominated by the interlocking strength component. This component mobilized at a low strain well before the peak and started to degrade prior to the peak strength.

According to preceding discussion, the strength parameters for dense and locked sands can be expressed as the sum of three components: (a) the basic frictional component (ϕ_f) governed by the surface texture and mineralogy and bounded by the interparticle friction angle (ϕ_m) and critical state angle (ϕ_{cv}); (b) the intrinsic interlocking component, which is responsible for its coherent mass due to the interpenetrative, tangential, sutured contacts, and which resembles the role of bonding in weak and hard rocks; and (c) the dilation component controlled by the degree of angularity and dictated by the freedom of grains to override each other after the occurrence of significant unlocking.

4.4.5.1 Interlocking and frictional strength contributions with plastic strain

The generalized form of the 2D stress dilatancy relationship for geomaterials can be expressed as the sum of three terms (Rowe 1962; Ueng and Chen 2000) as follows:

$$[4.2] \underbrace{\left[\frac{\sigma_1}{1 - \frac{d\varepsilon_v}{d\varepsilon_1}} \right]}_{\text{Basic resistance}} = \underbrace{\sigma_3 \tan^2 \left(\frac{\pi}{4} + \frac{\phi_f}{2} \right)}_{\text{Frictional resistance}} + \underbrace{\frac{dE_b (1 + \sin \phi_f)}{d\varepsilon_1 \left[1 - \frac{d\varepsilon_v}{d\varepsilon_1} \right]}}_{\text{Particle Breakage}} + \underbrace{2c_f \sqrt{\tan^2 \left(\frac{\pi}{4} + \frac{\phi_f}{2} \right)}}_{\text{bonding resistance}},$$

where σ_1 and σ_3 are the major and minor principal stresses, respectively; ϕ_f is the basic friction angle; $d\varepsilon_v/d\varepsilon_1$ is the dilatancy rate; $d\varepsilon_1$ is the axial strain increment; c_f is the intrinsic bonding resistance; and dE_b is the energy consumption due to particle breakage.

The basic resistance integrates out the effect of dilatancy by normalizing the major principal stress with the dilatancy factor $(1-d\varepsilon_v/d\varepsilon_1)$. This resistance reflects the energy dissipated through the frictional resistance between particles, the particles' breakage, and overcoming the bonding between particles. The first Right hand side term in Equation [4.2] is considered to be controlled by mineral type and surface texture (small asperities). The second term expresses the energy consumption due to particle breakage (Ueng and Chen 2000). However, Ueng and Chen (2000) found that particle breakage is insignificant for strong particles under low confinement stresses. Herein, this term will be ignored because the majority of the grains (quartz) of locked sands are strong in nature. The third term represents the bonding resistance, which is the resistance in excess of the basic frictional resistance, particle breakage, and dilation. The stress dilatancy relationship is applicable for

sands not only at peak but also in the pre-peak regime (Rowe 1962; Shibuya et al. 1994).

Equation [4.2] can be reduced to Equation [4.3] by using the current geometric and boundary conditions for the tested specimen ($\sigma_3=0$ and replacing the bonding component ($2c_f$) with an interlocking component (I)).

$$[4.3] \quad \frac{\sigma_1}{\left[1 - \frac{d\varepsilon_v}{d\varepsilon_1}\right]} = I \sqrt{\tan^2\left(\frac{\pi}{4} + \frac{\phi_f}{2}\right)}.$$

Equation [4.3] can be utilized to reveal the interlocking's contribution at any strain level. The basic friction angle is substituted by using the critical state friction angle for quartz sand (30°) (Rowe 1962; Rowe 1969; Bolton 1986). The total frictional resistance contribution (σ_1^f) can be then approximated as the difference between the axial stress and the interlocking resistance and expressed as follows:

$$[4.4] \quad \sigma_1^f = \sigma_1 - \frac{\sigma_1}{\left[1 - \frac{d\varepsilon_v}{d\varepsilon_1}\right] \sqrt{\tan^2\left(\frac{\pi}{4} + \frac{\phi_f}{2}\right)}}.$$

Assuming that the total frictional resistance (σ_1^f) is the by-product of the dilatancy and the basic frictional resistance with no interlocking for a frictional material, one can further partition the strength due to the dilatancy component

(σ_1^d) and basic friction resistance (σ_1^b) by applying Rowe's dilatancy correction to the total frictional resistance as follows:

$$[4.5] \sigma_1^b = \frac{\sigma_1^f}{\left[1 - \frac{d\varepsilon_v}{d\varepsilon_1}\right]},$$

$$[4.6] \sigma_1^d = \sigma_1^f - \sigma_1^b.$$

4.4.5.2 Pre-peak interlocking brittleness and friction hardening

Figure 4.5 shows the approximate distribution of the total resistance, the total frictional resistance, the individual contribution of the basic frictional resistance and dilation, and the interlocking resistances with the plastic shear strain (ε_s^p) , which is calculated by using the following equation:

$$[4.7] \varepsilon_s^p = \frac{2}{3}(\varepsilon_1^p - \varepsilon_3^p).$$

The analysis reveals that the interlocking contribution to overall strength tends to decrease exponentially with an increase in the plastic shear strain. The interlocking contribution tends to be consumed in the pre-peak regime and levels off before attaining the peak strength. The total frictional contribution to the overall strength mobilizes once the interlocking component starts to degrade and increases exponentially toward the peak strength. The basic frictional resistance contribution mobilizes when approximately 40% of the interlocking is overcome and stabilizes at low strain levels well before the

peak strength is attained. The dilation contribution increases exponentially and progressively due to the acceleration of damage (fabric unlocking). Hence, the frictional and interlocking resistances are not mobilized simultaneously. The interlocking strength should be destroyed so that the frictional resistance can be fully mobilized. Consequently, the peak strength in uniaxial compression stress conditions is the by-product of the residual interlocking component as well as the frictional component, which is dominated by dilation of the unlocked grains as well as the basic friction angle.

Bishop (1967) introduced a brittleness index to characterize the brittleness in the post-peak regime in terms of the peak and residual strength. Hajiabdolmajid (2001) introduced a strain-dependent brittleness index ($I_{B\varepsilon}$) to express the ability of brittle geomaterials to withstand deformation during the entire failure process (pre-peak to post peak) as well as their susceptibility to brittle fracture and progressive failure. The strain-dependent brittleness index is intended to capture the relative mobilization and degradation of the strength components and is expressed as follows:

$$[4.8] \quad I_{B\varepsilon} = \frac{\varepsilon_f^p - \varepsilon_c^p}{\varepsilon_c^p} \quad I_{B\varepsilon} \leq 0; \quad 0 \leq \varepsilon_f^p \leq \varepsilon_c^p$$

$$I_{B\varepsilon} > 0; \quad \varepsilon_f^p > \varepsilon_c^p ,$$

where ε_f^p is the plastic shear strain at which frictional resistance is fully mobilized, and ε_c^p is the plastic shear strain required for bonding resistance to attain the residual value. Based on the results shown in Figure 4.5, a brittleness index value of 1.5 is computed. This value is indicative of brittle failure as the loss of interlocking exceeds the mobilization of frictional resistance. Hence, the mobilized strength in boundary value problems constructed in or on these geomaterials will be much lower than the peak strength unless full mobilization of the frictional resistance is guaranteed. Non-simultaneous mobilization of strength component is regarded as a major concern in stress-induced excavation problems where the confining pressure is reduced, resulting in less mobilization of the frictional resistance, so that brittle failure is inevitable.

4.4.5.3 Mobilized strength parameters at damage thresholds

The distributions of the friction angle (ϕ), interlocking component, and dilation angle with plastic strain are important for design purposes. In the previous section, the interlocking component was obtained at different strain levels. The dilation angle (ψ) can be approximated by using the following equation (Vermeer and De Borst 1984):

$$[4.9] \quad \psi = \arcsin \left[\frac{\frac{2d\varepsilon_3^p}{d\varepsilon_1^p} + 1}{\frac{2d\varepsilon_3^p}{d\varepsilon_1^p} - 1} \right] = \arcsin \frac{d\varepsilon_v^p}{-2d\varepsilon_1^p + d\varepsilon_v^p} .$$

The friction angle (ϕ) can be calculated by using Rowe's stress-dilatancy relationship for frictionless geomaterials, as derived by Vermeer and De Borst (1984) and expressed as follows:

$$[4.10] \sin\phi = \frac{\sin\phi_f + \sin\psi}{1 + \sin\phi_f \sin\psi}.$$

Figure 4.6 shows the approximate distribution of the interlocking component, dilation angle, and mobilized friction angle with the plastic shear strain. The maximum interlocking strength component is recorded at the damage initiation stress where the unlocking of the interlocked fabric starts to develop sporadically throughout the specimen. Once unlocking takes place, friction starts to mobilize due to the interaction of the particles at damaged sites. At the damage coalescence strength level, 40% of the interlocking component is lost, and only the basic friction angle is mobilized. Beyond this damage threshold, a continuous reduction of the interlocking component occurs with the mobilization of the dilation angle due to the severe dilation of the interlocked fabric at this stress threshold. The dilation angle increases exponentially from zero at the damage coalescence strength to 36° at the peak where the particles or the blocks of particles become less constrained after unlocking. The maximum friction angle increases dramatically from zero at the damage initiation strength threshold, where sliding occurs between newly unlocked particles or in a block of particles, to 30° (the basic friction

angle) at the damage coalescence strength and reaching 57° at the peak strength. The friction angle at the peak strength agrees with the reported maximum friction angles for the arenaceous McMurray Formation (Dusseault and Morgenstern 1978; Dusseault and Morgenstern 1979) .

With regard to design approaches, Cresswell and Powrie (2004) argued that due to the large difference between locked sand's peak and critical state strengths, a geotechnical design based solely on the critical state friction angle would be unduly conservative even with a factor of safety of 1. Alternatively, Cresswell and Powrie (2004) recommended a design based on the limiting stress envelope corresponding to the onset of dilation and no-tension cut off, with a factor of safety on the peak stress ratios to avoid progressive failure. The results from this investigation support their recommendation, as the onset of dilation is also an excellent indicator of localization.

4.5 Development of columnar structures and dilation bands

A specimen, prepared with a 1:1 slenderness ratio, was sheared at a slow strain rate of 0.05%/hr to achieve a relatively homogeneous deformation throughout the specimen to allow for the propagation of the pre-peak's vertical structures to failure, and to delay the onset of localization. A thick layer of grease sandwiched between two latex membranes was placed at the specimen/ platen interfaces to alleviate the end effects.

Figure 4.7 shows the rendered failure surfaces based on the previously mentioned testing conditions. Failure of the sample occurred through the formation of vertical columns extending in the direction of the axial stress, as numbered in the figure. These axially oriented columns tended to form the load-carrying members. The presence of such columns suggests that the lateral extension and unlocking at discrete locations along the specimen's vertical axis were the main cause of failure. Examination of the column-to-column interface revealed the existence of the columns' curvature (see Figure 4.7). This curvature signifies the possibility of horizontal rotation of such columns after their formation so that the rotational resistance is governing the shearing behavior, as several investigators have suggested for dense sands (Oda and Kazama 1998; Oda et al. 2004; Wan and Guo 2004; Alshibli and Alramahi 2006). As well, Cresswell and Barton (2003) speculated that this process is a key component of locked sand's failure.

During the shearing of the 1:1 specimen, dilation was initiated well before reaching the peak strength and took place at the same stress level as that for 2:1 specimen (the damage coalescence threshold). The specimen deformed uniformly during the shearing evolution, and the localization commenced slightly after peak strength was attained. This result was predictable due to the distributed dilation, which corresponded to a delay in the onset of localization as compared to that in 2:1 specimens. Furthermore, the short specimen attained a peak strength of 2 MPa, which is 10% greater than the recorded value for the

long specimen, and failed with a less abrupt drop in strength due to the low strain rate and the strain's relative uniformity as compared to that of the long specimen.

4.5.1 Theoretical prediction of dilation band occurrence

The failure of geomaterials in laboratories or the field is customarily associated with the formation of localized deformation bands classified into two categories summarized by Borja and Aydin (2004). The first category includes mixed-mode deformation bands consisting of both shear strains (parallel to the band boundary) and volumetric strains (the volume increases or decreases perpendicular to the band boundary) along the band boundaries. Examples of mixed-mode bands are dilative and contractive shear bands. The second category consists of pure shear bands (shear along the band boundary), compaction bands (compressive volumetric strains), and dilation (extension) bands (dilative volumetric strains). The prediction of the onset of localized bands as well as their orientation with the maximum principal stress plane for dilative porous rocks has been studied by several investigators (e.g., Rudnicki and Rice 1975; Perrin and Leblond 1993; Issen and Rudnicki 2000; Bésuelle 2001).

The developed rigorous mathematical formulation for band formation was subjected to two conditions (Rudnicki and Rice 1975): (a) kinematic compatibility so that the velocity field was continuous at the inception of localization and (b) stress equilibrium so that the traction rates were

continuous across the boundary. By combining these conditions along with a constitutive relation that describes material behavior, and assuming an identical constitutive modulus for the material inside and outside the band at the onset of localization, the following equation is obtained:

$$\mathbf{[4.11]} \quad (n_i C_{ijkl} n_l) g_k = 0 ,$$

where the subscripts are index notations; n_i and n_l are the normal vector projections on the principal stress directions; C_{ijkl} is the modulus tensor; and g_k is a vector function of the distance across the band and related to the velocity gradient difference (inside and outside the band) within the band that vanishes at boundaries. One possible solution for the above equation was obtained for $g_k=0$ (a homogeneous strain field). An alternative solution can be achieved for $g_k \neq 0$ (the determinant of the coefficient is zero), resulting in the bifurcation criterion. By solving Equation [4.11], it was realized that the hardening modulus is a function of the band orientation. The critical hardening modulus (the slope of the axial stress- plastic axial strain curve) and the associated orientation were obtained by assuming that the plane of the deformation band is parallel to the intermediate principal stress direction. The solution was shown to be valid for the following range of $(\beta+\mu)$ expressed as follows (Issen and Rudnicki 2000; Bésuelle 2001):

$$[4.12] \underbrace{(1-2\nu)N - \sqrt{4-3N^2}}_{\text{compaction bands}} \leq \frac{2}{3}(1+\nu)(\beta + \mu) \leq \underbrace{(1-2\nu)N + \sqrt{4-3N^2}}_{\text{dilation bands}},$$

where N is the normalized stress ratio (s_{22}/τ); τ (equivalent stress) = $\sqrt{\frac{1}{2}s_{ij}s_{ij}}$ and s_{ij} (deviator stress) = $\sigma_{ij} - \frac{1}{3}\delta_{ij}\sigma_{kk}$ (δ_{ij} is the Kronecker delta, which =1 if $i=j$ and =0 if $i \neq j$), and equivalent to $(1/\sqrt{3})$ for the axisymmetrical compressive stress path; $\mu = \tan \phi$ (the slope of yield surface) ; and $\beta = -d\varepsilon_v^p/d\varepsilon_s^p$ (dilatancy factor).

If the lower inequality is violated, compaction bands are manifested with the band normal parallel to the major principal stress direction. On the other hand, if the upper inequality is violated, dilation bands are manifested with the band normal parallel to the minor principal stress direction. The dilation bands are described as the separation of the material's mass into walls being filled by parent material without shear offsets). Within the specified range, the mode of deformation can be described as a pure shear band, a dilative or contractive shear band. Figure 4.8 shows the deformation bands boundaries of occurrence and orientations in terms of μ and β for axisymmetrical compression conditions at the onset of localization based on the previous equation. The same figure indicates the data points estimated at the onset of localization, where divergence of local axial strains occurs, for both long and short specimens.

In the case of a high slenderness ratio, the data point lies at the upper boundary of the dilative shear bands with an orientation of 85° , which corresponds to the experimental observations. On the other hand, for a low slenderness ratio, dilation bands are observed. These results are in agreement with Chau's (1993) theoretical study of bifurcations in pressure-sensitive circular cylinders under axisymmetric compression. Chau (1993) found that the first possible mode of localization was always the buckling of long specimens as compared to short specimens where a diffused mode of localization occurred.

The previous results showed that the samples with a high slenderness ratio hindered the propagation of columnar structures due to buckling effects and the early localization of the deformation. Hence, dilation became restricted to a distinct shear band. For short specimens, multiple localized sites were observed, and, hence, dilation was not localized in a distinct band, allowing for propagation of vertical columns and multiple dilatant bands. Multiple dilation bands separated these columns, resulting in higher dilation as compared to that in long specimens.

4.6 Multistage uniaxial creep test

The design of geotechnical structures not only necessitates the stability under short-term conditions to avoid tensile/shear failures but also long-term stability under constant loading conditions to avoid excessive deformations. Creep

potential has been recorded for a wide range of geomaterials including sands (e.g., Lade and Chi-Tseng 1999; Kuwano and Jardine 2002; Bowman and Soga 2003), weak sedimentary rocks (Maranini and Brignoli 1999; Fuji et al. 1999) and hard rocks (Lin et al. 2004; Lau and Chandler 2004). In this section, the results of a multistage uniaxial creep test conducted on the locked sand are described and discussed. The chief objective of this test was to compare the creep potential before and after reaching the onset of dilation stress threshold to verify its significance as a safety threshold for long-term strength.

4.6.1 *Testing procedure*

A cylindrical specimen was prepared with a height of 65mm and a diameter of 60 mm. The axial and lateral deformations were monitored by using three local LVDTs and a circumferential chain, respectively. End effects were alleviated via a thick layer of silicone grease sandwiched between two latex membranes at the specimen/platen interfaces. Once the specimen and measuring devices set-ups were completed, the specimen was sheared at a constant strain rate of 0.05%/hr. Data were logged every 20 seconds during both shearing and creep stages. The test program was comprised of three stages of creep followed by unloading, once the peak strength was attained. Upon reaching the creep stress level, the deviator stress was halted for at least 24 hrs monitoring the variation in axial as well as lateral deformation were monitored. At the end of each creep stage, the specimen was re-sheared at the same strain rate to attain the next level of the creep stress

level. The creep stress levels were intentionally selected so that the first creep stage (at 750 kPa) was conducted below the onset of dilation threshold (1200-1250 kPa) as determined from the monotonic uniaxial compression tests. The second and third creep stress levels (1500 kPa and 2000 kPa) were carried out above the onset of dilation threshold.

4.6.2 Stress- strain and volumetric strain curves

Figure 4.9a shows the deviator stress vs. the average axial strain relationship during the shearing and creep stages. The conducted stages of creep as well as the onset of dilation threshold are marked on the figure. The tested specimen failed at a uniaxial strength of 2.45 MPa, which is approximately 1.23 of the uniaxial test compaction bands are manifested with the band normal parallel to the major principal stress direction without creep stages for similar testing conditions. This result was expected due to the ageing effect under a constant deviator stress that could result in an increase in the specimen's ability to carry more load, as other investigators have shown this phenomenon for granular materials (e.g., Murayama et al. 1984; Mitchell 1986; Mesri et al. 1990; Schmertmann 1991). Creep effects were not only evidenced through the increase in uniaxial strength value, but also were reflected as an increase in initial stiffness upon reloading for the next creep stage (see Figure 4.9a). During creep stages, a slight reduction in the deviator stress was recorded. The reduction in deviator stress was more pronounced in the second and the third stages of creep. On the other hand,

no reduction of deviator stress was noted in the first stage below the onset of dilation threshold. It is postulated that during the course of shearing, the zones of the material became stressed. With the progression of the creep, some of the stressed zones had a propensity to relax, and, thereby, distribute stresses to their unstressed neighboring elements. This redistribution could reduce the overall deviator stress. Upon reloading, the unstressed elements carried some of the imposed stresses, and, hence, an increase in initial stiffness was the result upon attaining the previous stress-strain path. However, the reduction in stresses could be otherwise due to the stiffness of the loading frame.

Figure 4.9b shows the deviator stress vs. lateral strain relationship. During the course of the experiment, the lateral strains exhibited extension. The same observation regarding the initial increase in the lateral stiffness was recorded upon reloading to the next stage of creep, as the figure reveals. Figure 4.9c depicts the volumetric strain- axial strain relationship. The volumetric strains remained contractive up to almost 1200 kPa, followed by dilation up to the peak strength. However, the maximum rate of dilation was not coincident with the peak resistance. The volumetric strains during the creep seemed to be a continuation of the original volumetric strain relation.

4.6.3 Creep strains and strain rates

In soil mechanics, the variations of creep strains are traditionally investigated in terms of axial strains. Three stages of creep are usually described: primary, transient, and tertiary creep. During the primary creep, strains are accelerating with time, and strain rates are progressively reduced to reach the transient creep (the constant rate of strain). The third zone is the tertiary creep, where the strain rate accelerates in an unstable manner resulting in failure.

For efficient and reliable quantification of creep strains, temperature effects should be considered to avoid error with temperature variations. The temperature effects seemed to have minor effects on the LVDTs' readings during creep stages. The variation in temperature was in the range of 1- 2 °C. This is manifested as a deviation in average vertical and lateral strains of 0.0008% based on the previously shown temperature calibration factors. Table 4.2 presents the test results at each creep stage in terms of axial, lateral, and volumetric creep strains. Following the same convention, positive and negative strains indicate compression and expansion (dilation), respectively.

4.6.3.1 Axial creep strains and strain rate

Figure 4.10 shows the variation in axial strains with time during creep stages. Axial strains were calculated as the average of the three vertical LVDTs'

readings. The axial strains at any stage of creep are characterized by a sudden increase in strain, followed by a reduction in the axial strain rate to a constant rate of strain, and finally reach a plateau. Figure 4.11 indicates the relationship between the axial strain rates and the elapsed time in a logarithmic scale. A monotonic reduction in axial strain rates occurs with elapsed time. For comparison, the axial strain rate at each stage is calculated based on the linear portion of the axial strain vs. the elapsed time relationships shown in Figure 4.10 and summarized in Table 4.2. The axial strain rate in the first creep stage is almost 58% lower than the creep rate in the second and third stages. On the other hand, the difference in axial strain rates in the second and third stages is insignificant and in the order of magnitude of 10^{-6} %/min.

4.6.3.2 *Lateral creep strains and strain rate*

Figure 4.12 shows the variation in lateral strains with time during creep stages. The lateral strain curves at any stage of creep are characterized by a sudden increase followed by a reduction in the lateral strain rate to a constant rate of strain and eventually reaching a plateau. Nonetheless, the increase in lateral strain values during creep stages is more noticeable as compared to axial strain values. Figure 4.13 indicates the relationship between the corresponding lateral strain rates and time in a logarithmic scale. Like the measured axial strain rates, the lateral creep strains rate is reduced at each stage of creep. The same methodology for determining the axial strain rates

and adapted for axial strains is repeated for lateral strain. Below the onset of dilation threshold, the lateral creep strain rate is insignificant and is comparable to the variation in axial strain rates ($2.6E-06$ %/min). Beyond the onset of dilation threshold, during the second and third stages of creep, an order of magnitude increase in the creep strain occurs by an order of magnitude. On the other hand, the difference in lateral strain rates in the second and third stages is insignificant and in the order of magnitude of 10^{-5} %/min. A comparison of the axial and the lateral strain responses suggests that the variation in lateral strain values and its corresponding rates are more significant than those of axial strain values and corresponding rates for locked sands.

4.6.3.3 *Volumetric creep strain*

Figure 4.14 shows the relationship between the elapsed time and the volumetric strains. The volumetric strains indicate dilation during all creep stages. The volumetric strains initially increase dramatically followed by a reduction in the volumetric strain rates and eventually attain a plateau. The volumetric strains are negligible only in the first stage of creep. In the second and third stage of creep, the volumetric strains are more significant than those in the first stage and are increased by an order of magnitude as shown in the figure.

4.6.4 *Implications of creep test*

The results clearly indicate that creep resulted in an increase in the uniaxial compressive strength due to ageing effects. In the first stage of creep, the geomaterials behaved in an elastic-plastic manner (with no reduction in the creep stress level). On the other hand, the second and third stages showed a reduction in the creep stress level (strain weakening). Although the reduction in strength was insignificant (corresponding to 10-12% of the original creep stress level), it signified a variation in response above the onset of dilation threshold.

The tested geomaterials exhibited all stages of creep in the axial and the lateral directions but no creep failure (tertiary creep) was observed. The variation in the axial and lateral strain rates was insignificant below the onset of dilation (the first creep stage). The axial and lateral strain rates were shown to be comparable in the first stage of creep. Beyond this stage, the lateral strain rates increased by an order of magnitude; however, the variation in the axial strain rates became double. In general, no major variation occurred in the axial or lateral strain rates, once the onset of dilation threshold was attained. Before and after the onset of dilation threshold was reached, the volumetric strains were dilative. However, they were negligible below this threshold and increased by an order of magnitude in the second and third stages.

In fact, the dilative nature of locked sand under constant loading conditions implies the dominance of lateral damage of its interlocked fabric and its propagation in the axial direction. In the first stage of creep, the volumetric strains are negligible and indicate the existence of minor or sparse fabric unlocking (damage) as compared to the propagating and newly formed unlocked elements in the second and the third stages as also manifested by the reduction in load-carrying capacity and the increase in volumetric strain rates. Beyond the onset of dilation, the dilative volumetric strains significantly increased. This implicitly implies the propagation of unstable damage, whereas below the onset of dilation, negligible volumetric strains were recorded. Based on the preceding discussion, the onset of dilation can be considered to be an indicator of the long-term strength of locked sands when tested under uniaxial compression test conditions. However, additional work should be carried out to generalize such conclusion under higher confining pressure.

4.7 Direct shear box (DSB) results at low normal stress

The short- and long-term experimental results from uniaxial compression tests showed that the onset of dilation can be regarded as an excellent indicator of both short- and long-term strengths. In this section, the direct shear test results for locked sand specimens tested under low normal stresses will be presented and discussed. The DSB test was carried out to reveal the strength that can be mobilized at low stress levels. To achieve this objective, four specimens in a dry

state were prepared to be tested under normal stress ranges of 10, 100, 300, and 500 kPa, respectively.

The direct shear tests were conducted in an automated direct shear apparatus. Figure 4.15 presents an illustration of the various components of the apparatus is shown in. In this type of equipment, cylindrical samples can be used and fitted within the two halves of a box with an internal cylindrical hole of a diameter of 63.2 mm and a height of 43.12 mm. The lower part of the box can be displaced with respect to the upper one in either direction. The shear load, axial displacement, and horizontal displacements were recorded at each 10s intervals and logged into a computer connected to the apparatus. Intact samples were sheared at a strain rate of 0.0025 mm/min.

4.7.1 Direct shear results

4.7.1.1 Shear stress vs. horizontal deformation

Figure 4.16 shows the nominal shear stress (τ_{xy}) vs. the horizontal deformation (δ_x) relationships at normal stress ranges of 10-500 kPa. The samples failed at an average horizontal deformation of 0.8 mm. After the maximum shear stress was reached, a sudden reduction in strength occurred, reflecting the material's extreme brittleness. However, this brittleness decreased with the increase in the normal stresses. Up to a normal stress of 300 kPa, the maximum mobilized strength was only slightly dependent of the normal stress and was presumably governed by the interlocking strength

component. For normal stresses greater than 300 kPa, the material exhibited a significant increase in the maximum shear stresses, and, hence, marked the destruction of the interlocking and the initiation of the full mobilization of the fictional resistance.

4.7.1.2 Vertical deformation vs. horizontal deformation

Figure 4.17 shows the vertical deformation (δ_y) - horizontal deformation (δ_x) relationships at a normal stress range of 10-500 kPa, revealing that samples showed dilation throughout the shearing process. An initial increase in the dilation rate occurred in pre-peak regime, followed by a reduction in the dilation rate in the post-peak regime. The dilation rates continued to increase, and, hence, the samples did not attain the critical state in the post-peak regime. This result was due to the rotation of the loading cap as well the persistence of a residual interlocking between the particles. At 10 kPa, the sample exhibited extreme dilation before attaining the peak, followed by a reduction in the dilation rate at the peak, whereas, for the range of normal stresses of 100-500 kPa, the maximum rate of dilation was coincident with the peak strength.

4.7.1.2 Failure envelope at low normal stress

Figure 4.18 presents a plot of the peak strength for all ranges of normal stresses. The failure envelope is bilinear and can be divided into two portions. The first portion is a linear envelope with an intercept of 287 kPa and a friction

angle of 7° up to a normal stress of 300 kPa. The second portion can be approximated by a friction angle of 46° at higher normal stresses.

4.7.1.3 *Corrected shear stress vs. horizontal deformation*

The shear strength of granular materials is usually attributed to the combined effect of friction and dilation. In locked sands, the interlocking between grains results in a third component. In order to quantify the interlocking strength component, the integration of the dilatancy component is necessary. Once this component is integrated out, one can quantify the contribution of the interlocking component and the frictional resistance. The corrected shear stresses to estimate the interlocking contribution can be calculated by using the following equation by integrating out the contribution of the dilation and the basic friction (Taylor 1948):

$$[4.13] \tau_c = \tau - \sigma_n \tan \psi - \sigma_n \tan \phi,$$

where τ is the total shear stress; τ_c is the corrected shear stress; σ_n is the normal stress; and $\psi = \text{atan}(-\delta y / \delta x)$ is the dilation angle.

Figure 4.19 shows the original shear stress-horizontal deformation curve and the corrected one for an intact sheared sample at a normal stress at 10 kPa. Provided the shearing resistance is dominated by the dilation and basic friction angle as in dense sands (e.g., Rowe 1962; Taylor 1948), the corrected

shear stresses should be nil. However, as shown in Figure 4.19, the corrected shear stresses are identical to the original ones. Hence, the maximum shear stresses for locked sand cannot be expressed only as a function of the dilation and basic friction angle as they can be expressed in dense sands. This finding indicates that the interlocking component dominates the shearing resistance of intact locked sand samples at low normal stresses.

4.7.1.4 Mobilized strength under DSB

In a direct shear test, the principal stresses continuously rotate with the progression of shearing. At low normal stress levels, the minor principal stress can be in tension, and failure can be due to tension (Lajtai 1969). This tension results in a progressive reduction in the interlocking component during the course of shearing.

In the uniaxial compression tests, it was found that the damage initiation stress level was around 510 kPa. It was argued that fabric unlocking commenced at this stress level and was manifested through initiation of the lateral strain nonlinearity. In direct shear tests, the initial portion of the failure envelope was approximated by a friction angle (ϕ) of 7° and an intercept of 287 kPa. The deviator stress ($\sigma_1 - \sigma_3$) can be expressed as

$$[4.14] \quad \sigma_1 - \sigma_3 = \frac{2\tau_{xy}}{\cos(\phi)} .$$

Substituting the values in Equation [4.14] renders a deviator stress level of 556 kPa, which is almost equivalent to the damage initiation stress level (510 kPa) estimated from the uniaxial compression test. Hence, the minimum mobilized strength in direct shear box tests can be taken as the damage initiation stress level, as estimated from uniaxial compression test results. This stress level is dominated by the interlocking component with a negligible mobilization of friction, as previously shown in uniaxial stress conditions.

4.8 Summary and conclusions

In this chapter, an experimental investigation was carried out on locked sand from the McMurray area. Local axial and lateral deformations, for the tested specimens under uniaxial compression test conditions, were monitored by using miniature LVDTs. The focus was on identifying the damage thresholds and the partitioning strength parameters with plastic strain. Finally, the reported columnar structures for locked sands were captured by altering the tested specimen's configuration and testing conditions. The existence of such columns due to the formation of dilation bands was substantiated by the theoretical consideration of the localization theory for porous rocks. A multistage creep test was also carried out to reveal the relationship between the onset of dilation and long-term strength of locked sand. Finally, the experimental results in a DSB test were presented and discussed to reveal the minimum mobilized strength under pure shearing conditions.

The results revealed that the exceptionally high uniaxial strength and axial stiffness were the by-products of the particles' angularity and the interlocking between particle contacts, which enhanced the ability to resist moments at the contacts. Stress-strain curves were partitioned in the pre-peak regime based on the local axial and lateral strains' response to describe the evolution of failure: the closure of cracks and pores, the initiation of unlocking, the onset of localization, and the coalescence and unstable propagation of damaged sites. The onset of unlocking (the damage initiation threshold) occurred at 28 % of the peak strength and, according to our observations, was coincident with the crack closure strength threshold. The onset of localization and dilation occurred at 55% and 67% of the peak, respectively. The partitioning of the strength components with the plastic strain showed that the interlocking and frictional strength components were not simultaneously mobilized. The interlocking component degraded with the plastic strain, resulting in the progressive mobilization of frictional resistance. The interlocking component was consumed in the pre-peak regime and leveled off before attaining peak strength. The basic frictional resistance mobilized and stabilized at low strain levels in the pre-peak regime once approximately 40% of the interlocking was overcome. At the peak strength, the resistance resulted from the frictional contribution (the basic friction and dilation) with less contribution from the interlocked component (17% of the peak strength) due to its consumption during the unlocking process. At the onset of dilation, 60% of the mobilized resistance was attributable to the interlocking

strength component. The remaining resistance reflected the basic frictional resistance's contribution.

A brittleness index value of 1.5 was calculated according to our experimental results. This value indicated brittle failure as the rate loss of the interlocking component superseded the mobilized rate of the frictional resistance. Hence, the mobilized strength in boundary value problems constructed in or on this geomaterial would be much lower than the peak strength unless the frictional resistance is fully mobilized. Non-simultaneous mobilization of the strength component is considered as a major concern in stress-induced excavation problems, where the confining pressure is reduced so that little frictional resistance can be mobilized, and, hence, brittle failure is inevitable.

Columnar structures were captured by creating a relatively homogeneous strain field to hinder the onset of localization and to allow for complete formation of these columns. The pattern of failure is best described as the formation of vertical slabs/walls in the direction of the axial direction as a result of uniform unloading through the lateral expansion and formation of dilation bands. The experimental results, compared to those in theoretical studies of failure modes for porous brittle rocks, revealed that the dilation bands were the dominant mode of deformation (a predominantly open-mode of deformation propagating in the direction of the major principal stress), and, hence, were responsible for such columnar failure patterns.

Under constant loading conditions, the material exhibited a creep potential that became more significant beyond the onset of dilation. Creep lateral strains and their rates were more significant than axial strains. Creep lateral strain rates were one order of magnitude greater than axial strain rates beyond the onset of dilation. Creep volumetric strains were dilative at all stages of the creep test. This result supports the premise that significant lateral unlocking occurs and its propagation in the axial direction during creep stages. Hence, the onset of dilation was recommended to be an indicator of the long-term strength of such a formation, based on the conducted creep tests.

The results of a DSB testing indicated that the mobilized strength under low normal strength was independent of the normal stress levels. The mobilized strength was dominated by the interlocking strength component and was equivalent to the damage initiation strength threshold estimated from the uniaxial compression test results.

Based on our experimental results, in boundary value problems constructed in or on locked sands, the damage coalescence and initiation thresholds are recommended to be the upper and lower strength boundaries. However, more work is needed to confirm such conclusion under higher confining pressures.

Table 4.1 Elastic deformation parameters and damage thresholds.

Elastic parameters	Tangential axial stiffness ($E= 0.85$ GPa)
	Poisson's ratio ($\nu=0.2$)
Damage thresholds	Crack closure threshold ($\sigma_{cc}= 510$ kPa)
	Damage initiation threshold ($\sigma_{di} = 510$ kPa)
	Damage localization threshold ($\sigma_{dl} = 1000$ kPa)
	Damage coalescence threshold ($\sigma_{dc} = 1200$ kPa)

Table 4.2 Summary of testing steps and results.

Stage	q (kPa)	Axial strain rate (%/min)	Lateral strain rate (%/min)	Creep volumetric strain (%)
1	750	2.46 E-6	2.6E-06	-0.003
2	1500	4.7 E-6	1.50E-05	-0.028
3	2000	4.0E-6	1.27-05	-0.08

CHAPTER 5: MOBILIZED STRAIN-DEPENDENT STRENGTH PARAMETERS FOR TWO NATURAL STIFF CLAYS

5.1 Introduction

In the previous chapter, the experimental analysis of a quasi-frictional material with interlocked fabric (locked sand) test results under uniaxial compression conditions revealed the non-simultaneous mobilization of strength parameters (friction and interlocking) and the degradation of the interlocked fabric with strain. In this chapter, this finding is used to interpret the mechanical behaviour of various bonded geomaterials at different confining pressures and to capture the transition between soils (frictional materials) and hard rocks (bonded materials) based on the mutual contribution of the strength parameters to the overall shearing resistance.

To achieve this objective, stress strain curves for two natural stiff clays (bonded quasi-frictional materials) were analyzed to reveal the contribution of the strength parameters at different strain levels by using a simplified partitioning approach. Shear strength parameters are partitioned in terms of the cohesion/bonding and the friction angle in Mohr Coulomb (M-C) space for the two clays, and in terms of normalized friction and bonding parameters in q-p space for Nanticoke clay as it produces the extreme case of bonding brittleness distinguished in most bonded geomaterials. A parametric study is carried out to reveal the similarity in the behaviour of different bonded geomaterials and to capture the transition between soils and rocks according to the mutual contribution of the bonding and frictional

resistances components to the overall resistance. In the rest of the chapter, the terms “bond” and “cohesion” are interchangeably employed to express resistance in excess of the frictional resistance, i.e., the combined effect of dilation and basic frictional resistance. In addition, all results are generally expressed in terms of effective stresses so that there is no differentiation between primed and unprimed parameters unless otherwise stated.

5.2 Historical development of strength parameters in clays

Deformations rather than a soil's limiting strength govern the design of many structures. The limiting soil strength is often taken into consideration by using allowable strengths, which correspond to small but arbitrary selected strains in the stress strain curve obtained from laboratory tests. On this basis, two classes of strength parameters can be distinguished (Bishop 1971). The first arises from the Mohr-Coulomb failure hypothesis (M-C), which is widely applied in soil mechanics and assumes the simultaneous mobilization of strength parameters. The second class emerges from the basic shear strength properties of soils and which is not readily applicable or observable in laboratory tests but helps to enhance our understanding and provide a physical basis for soil behavior.

Hvorslev (1960) carried out the first investigation into the physical meaning of strength parameters. He showed that the shear strength of remolded saturated clays could be partitioned into two components regardless of their history (their consolidation state): (a) effective cohesion, which is a function of void ratio and (b) effective friction, which is a function of effective stresses. Gibson (1953)

pointed out that the effect of volume change should be accounted for when estimating the effective strength parameters. Nonetheless, no significant variations in parameters were observed after correction for remolded clays. Lambe (1960) proposed a mechanistic picture for the mobilization of strength parameters, arguing that the strength is comprised of three components which were not mobilized simultaneously: the cohesion, the basic friction, and the dilatancy component. According to his argument, cohesion is mobilized at low strain and does not contribute to the peak resistance. Schmertmann and Osterberg (1960) carried out the first experimental program to partition shear strength parameters. Schmertmann (1963) did not agree with Hvorslev (1960) that the variation in void ratio represents the variation in structure (fabric and bonding) in natural soils. In contrast, Schmertmann (1963) proposed that the shear strength parameters should be expressed as a function of the strain rather than the void ratio. He found that the shear strength parameters were not mobilized simultaneously (cohesion was mobilized at low strain while friction required sufficient strain to be mobilized).

De Mello (1988) showed the difference between the two classes of shear strength criteria, as indicated by Bishop (1971), by plotting the stress- strain curves on the same figure and correlating the shear strength at different strain levels (the second criterion) as compared to the maximum deviator stresses (first criterion). He showed that the available strength at working strain levels was much lower than it was according to the maximum deviator stress concept. Even

if a factor of safety was applied to the maximum resistance, the available limiting strength would not be representative of the actual mobilized strength. De Mello's (1988) study indicates that the maximum shear strength criterion should not be used and that strain should be incorporated as an independent parameter. Conlon (1966) also pointed out that the classical Mohr Coulomb criterion could not be used to predict the failure mechanism for bonded stiff clays in slope stability problems. Conlon (1966) showed that using the shear strength parameters, as a function of strain, is more beneficial for understanding and interpreting the failure mechanism of natural stiff clays. According to his view, the stability of slopes in stiff clays depends on the degree of friction mobilization relative to the degradation of the cohesive component, which cannot be captured by assigning constant parameters. Therefore, it can be concluded that the strength parameters need to be partitioned according to the strain to capture the failure mechanism in natural stiff clays that exhibit strain weakening due to bond degradation.

5.3 Partitioning of strain-dependent strength parameters in Mohr-Coulomb space

Several investigators have referred to plastic strain as the most significant parameter for capturing the changes in the microstructure from a micromechanical viewpoint (e.g., Vardoulakis and Sulem 1995; Mroz and Rodzik 1995; Sulem et al. 1999). To partition the shear strength parameters as a

function of the plastic shear strain, several assumptions must be made. The main assumptions and limitations to be considered are:

1. The Mohr-Coulomb criterion is valid at any strain level.
2. The cohesion/bonding component captures the integrity of soil bonding at various strain levels.
3. The frictional resistance represents the change in the fabric and comprises both the basic friction angle (derived from mineral texture and roughness) and the dilatancy component (the volume change component).
4. The mobilized strain-dependent parameters are considered to be fundamental parameters for a particular field stress path, and their distributions are influenced by laboratory boundary conditions and measurement techniques (local vs. external measurements).
5. This approach is applied to stiff clays and assumes that negligible particle crushing effects occurs under low stress levels and that the material deforms plastically (the elastic deformation is negligible compared to the plastic deformation).

Figure 5.1 shows a schematic representation of a typical stress- strain curve for drained triaxial compression results. The results are represented in terms of the plastic shear strain (ϵ^p) (the material was assumed to deform plastically, i.e., plastic deformation is dominant). Consequently, one can assume that the total strain increment is equivalent to the plastic strain increment as elastic

strains effects have been shown to be insignificant (Leroueil 1997). In Figure 5.1, the dashed lines represent different levels of plastic strain. At each strain level (marked as $\varepsilon^p_1, \varepsilon^p_2, \varepsilon^p_3$), the intersection of the dashed line with the stress strain curves at different confining pressures ($\sigma_{31}, \sigma_{32}, \sigma_{33}$) renders three points (as shown in the figure) with different deviator stresses (for instance, points 1,2, and 3). At each point, the principal stresses are known, and, hence, a single envelope can be drawn by obtaining the best fit at this strain level (see Figure 5.2). For each envelope, the inclination of the best fit line (α) and the intersection with the ordinate (a) can be obtained.

According to the Mohr-Coulomb criterion, the fitted data points can be expressed as a linear relationship by using the following equation:

$$[5.1] \quad \frac{\sigma_1 - \sigma_3}{2} = c \cos \phi + \frac{\sigma_1 + \sigma_3}{2} \sin \phi,$$

where σ_1 and σ_3 are the major and minor principal stresses, respectively; c is the cohesion intercept; and ϕ is the friction angle.

The cohesion and friction angles can be then obtained by using the intercept (a) as well as the inclination ($\tan \alpha$) of the fitted linear relationship by using the following equations:

$$[5.2] \quad c = \frac{a}{\cos \alpha}, \text{ and}$$

$$[5.3] \quad \phi = \sin^{-1}(\tan \alpha).$$

The values of cohesion and friction can be then plotted with the plastic shear strain, as will be shown later. Hence, multiple yield functions can be constructed at any strain and can be generally written as follows (Vermeer and De Borst 1984)

$$[5.4] \quad f(\sigma, \varepsilon^P) = f(\sigma, \varepsilon^P) + f(\sigma_n \tan \phi, \varepsilon^P),$$

where $\varepsilon^P = 2/3 (\varepsilon_1^P - \varepsilon_3^P)$ for triaxial compression conditions; ε^P is the plastic shear strain; and σ_n is the normal stress.

5.4 Partitioning of strain-dependent strength parameters for two natural stiff clays

5.4.1 Pietrafitta clay

Callisto and Rampello (2002) carried out a series of drained triaxial compression tests on natural stiff Pietrafitta clay. Figure 5.3 presents the stress-strain curves at different confining pressures. As indicated in the previous sections, the shear strength parameters are to be calculated at different strain levels. Fitting lines, with a determination coefficient of at least 0.95, which is statistically acceptable, are indicated in Figure 5.4. Figure 5.5 shows the distribution of the cohesion and friction with the plastic shear strain,

revealing that both strength components are not mobilized simultaneously. The cohesive component is fully mobilized at zero plastic strain followed by degradation to the large strain value or residual value. The friction component is mobilized with the plastic strain to a maximum value and then degrades to a slightly lower value, which cannot be taken for granted as the residual value due to strain localization. However, as Adachi and Oka (1993) and Oka et al. (1998) stated, a reduction in load-carrying capacity cannot be attributed solely to the strain localization. A reduction in the post-peak regime is also a reflection of bond degradation. At any certain strain level, the available strength is a combination of both components, which cannot be described properly by using only two constants. The cohesive component is mobilized to its maximum value (54.1 kPa) up to a strain level of 2.1%, followed by a slight reduction of the component with strain. The reduction percentage of the cohesive component is almost 23%. On the other hand, the friction component attains its maximum value (15.3°) at a strain level of 4% and degrades with a percentage reduction of 41%. Figure 5.5 also shows that the percentage of reduction in the frictional resistance is higher than for cohesion. The reduction of the load-carrying capacity can be attributed to the reduction of both components and is a function of the confining pressure. At low confining pressures, the cohesive component is prevalent, and, hence, the reduction rate of the cohesive component governs the reduction of the strength. At high confining pressures, the reduction of the frictional resistance dictates the reduction of the strength. The stress-strain curves reveal that at

low confining pressures, the reduction of the deviator stresses is not significant due to the slight reduction of the cohesive component. Conversely, at moderate confining pressures, the reduction of deviator stresses is appreciable due to the significant reduction in frictional resistance. At higher confining pressures, the reduction of the frictional resistance is not as influential as at moderate confining pressures.

5.4.2 *Nanticoke clay*

Nanticoke clay is a stiff, moderately, overconsolidated clay from Southern Ontario. Lo (1972) studied the strength of Nanticoke clay at a strain rate of 0.05%/hr under several confining pressures (Figure 5.6). Figure 5.6 reveals that strain weakening (reduction from peak to residual values) decreases with the increase in confining pressure. Based on the results of the triaxial compression tests, the data were analyzed to obtain the multiple yield envelopes (see Figure 5.7). Figure 5.8 presents the distribution of the parameters with the plastic strain. Both components of strength are shown to be neither mobilized nor degraded simultaneously, as mentioned previously. The cohesive component is fully mobilized at zero plastic strain followed by full degradation (indicating the brittleness nature of this clay). The friction component is mobilized progressively with the plastic strain to a maximum value and then degrades to a slightly lower value. The cohesive component is mobilized to its maximum value (71 kPa) up to a strain level of 0.75%, followed by an abrupt reduction in the component to zero at a strain level of

2.0 %. The reduction percentage of the cohesive component is almost 100%. On the other hand, the friction component attains its maximum value (21°) at a strain level of 3% and degrades with a percentage reduction of 19%. Figure 5.8 also shows that the reduction in the cohesive component is more significant than that in the frictional component.

This brittle clay has a strain-dependent brittleness index (IB_{ϵ}) of 1.4. This value expresses the lag in frictional strength mobilization compared to rate of cohesion degradation. Hence, at low confining stresses and small plastic strains, the loss of strength will be significant. On the other hand, only a slight reduction in strength will occur at high confining pressures.

5.5 Bonding and frictional resistance in q-p space

Traditionally, the shear strength of geomaterials is expressed in terms of either M-C space or q-p space. In q (deviator stress) -p (mean effective stress) space, the ordinates are expressed as follows:

$$[5.5] \quad q = \frac{(\sigma_1 - \sigma_3)}{2}, p = \frac{(\sigma_1 + 2\sigma_3)}{3}.$$

The strength parameters are partitioned in q-p space for Nanticoke clay in order to interpret the parameters in terms of the critical state soil mechanics (Schofield and Wroth 1968). For purely frictional materials, the slope of the yield surface is

described in terms of a frictional parameter at large strain, i.e., M_{crit} (the stress ratio at the critical state, where shear stress levels off with no variation in the volumetric strain rate), which is expressed as follows (Schofield and Wroth 1968):

$$[5.6] \quad M_{crit} = \frac{q}{p}.$$

For bonded geomaterials, the shear strength expression deviates from the previous equation. In general, the shear strength equation at any strain level can be expressed as follows:

$$[5.7] \quad q(M, p_t) = M(\varepsilon^P)[p + p_t(\varepsilon^P)],$$

where p_t is the tensile mean strength of bonds at any strain level and M is the slope of the yield surface and describes the frictional resistance. At low strain levels, the tensile strength is maintained due to the integrity of bonds' initial strength and is represented by p_{t0} . At large strain levels, the tensile strength degrades and disappears, reflecting the full consumption of the bonds during shear evolution. Consequently, the slope of the yield surface (M) progressively becomes equivalent to M_{crit} , and the shear strength equation becomes equivalent to Equation [5.7].

Multiple yield envelopes in q-p space are estimated as in M-C space at different plastic strain levels in order to obtain the distribution of the parameters (M, p_t). These two parameters (M, p_t) are normalized with respect to the stress ratio at the critical state (which is assumed to be reached at large strain) and the initial tensile strength (the initial intersection of the envelope with the horizontal axis), respectively. The mathematical relation describing the evolution of the frictional resistance in a normalized space for Nanticoke clay can be written as follows and is illustrated in Figure 5.9.

$$[5.8] \quad \frac{M}{M_{\text{crit}}} = 2.51\exp(-0.177\varepsilon^P) - 2.507\exp(-0.8597\varepsilon^P),$$

where M expresses the variation of frictional resistance with plastic strain levels. At large strain levels, this parameter reduces to the critical state parameter (M_{crit}) where bonding effects vanish.

The second expression is related to the tensile strength at various strain levels, which can be expressed as follows and is illustrated in Figure 5.10.

$$[5.9] \quad \frac{p_t}{p_{t0}} = 1.05\exp(-3.912\varepsilon^P).$$

5.5.1 Incremental form of the strength equation in q-p space

The differentiation of equation [5.7] with respect to plastic shear strain renders the following equation:

$$[5.10] \quad \frac{\delta q}{\delta \varepsilon^P} = \left[p \frac{\delta M}{\delta \varepsilon^P} + \frac{\delta p}{\delta \varepsilon^P} + M \frac{\delta p_t}{\delta \varepsilon^P} + p_t \frac{\delta M}{\delta \varepsilon^P} \right].$$

Based on [5.8] and [5.9], the distribution of the parameters with plastic shear strain can be in general expressed as follows:

$$[5.11] \quad \frac{M}{M_{\text{crit}}} = c(\exp(-d\varepsilon^P)) - e(\exp(-f\varepsilon^P)),$$

$$[5.12] \quad \frac{p_t}{p_{to}} = a \exp(-b\varepsilon^P),$$

where a,b,c,d,e, and f are fitting parameters.

The differentiation of equations [5.11] and [5.12] with respect to the plastic strain increment leads to the following two expressions:

$$[5.13] \quad \frac{\delta M}{\delta \varepsilon^P} = M_{\text{crit}} \left[-cd(\exp(-d\varepsilon^P)) + ef(\exp(-f\varepsilon^P)) \right],$$

$$[5.14] \quad \frac{\delta p_t}{\delta \varepsilon^P} = -ab(\exp(-b\varepsilon^P)).$$

Substituting equations [5.11], [5.12], [5.13] and [5.14] into equation [5.10] and simplifying the equation renders the frictional and bonding contributions in incremental form as follows:

$$[5.15] \quad \delta q = \delta q_1 + \delta q_2 ,$$

where

$$\delta q_1 = \underbrace{\left[p' M_{crit.} (-cd(\exp(-d\varepsilon^P)) + ef(\exp(-f\varepsilon^P))) + M_{crit.} (c(\exp(-d\varepsilon^P)) - e(\exp(-f\varepsilon^P))) \delta p' \right]}_{\text{frictional component}} \delta \varepsilon^P$$

, and

$$\delta q_2 = \underbrace{a M_{crit.} p_{to} (\exp(-b\varepsilon^P)) \left[(\exp(-d\varepsilon^P)) (-cd - bc) + (\exp(-f\varepsilon^P)) (eb + ef) \right]}_{\text{bonding component}} \delta \varepsilon^P .$$

The above equation can be used to render an approximate estimate of the frictional and bonding resistances at various plastic strain levels as will be shown in the following section.

5.6 Parametric study of the bearing of confining stresses on stress strain curves

5.6.1 Contribution of frictional and bonding resistance at different confining stresses

Figure 5.11 shows the stress-strain curves based on the incremental forms of Equation [5.13] to reveal the effect of confining stresses (10-150 kPa) on the

behaviour of a bonded geomaterial when an initial tensile strength (p_{to}) of 500 kPa and a critical stress ratio ($M_{crit.}$) of 1.1 are assumed. The constant mean effective stress path, (constant p), is simulated to capture the effect of shearing on the stress-strain curves, i.e., to rule out volumetric effects. Figure 5.11 illustrates the frictional resistance, bonding resistance, and total resistance at various confining stresses. The figure shows that the rate of frictional resistance mobilization with strain increases with the increase in confining stresses. At low confining stresses, the frictional resistance has minor effect on the peak resistance, and most of the available resistance results from the bonding resistance. The reduction in load-carrying capacity is due to the degradation of bonding, and the mobilized residual friction dominates the residual strength. At intermediate confining stresses the peak is due to both components; however, they are not the maximum components. A plateau is revealed, and two peaks characterize the stress -strain curves. The first is at low strain where bonding resistance starts to degrade followed by either strain hardening or strain weakening depending on the rate of frictional resistance mobilization relative to cohesive resistance degradation with strain. If full frictional resistance can be mobilized, strain hardening occurs and is accompanied with a second peak. The initial weakening is due to the degradation of the bonds while the second one is due to degradation of frictional resistance. Where strain hardening occurs, frictional resistance dominates peak strength with a negligible contribution from the bonding resistance. At high confining stresses, no observed plateau is observed and

the frictional resistance mobilization rate is greater than bonding resistance degradation rate. These results are in agreement with Conlon's (1966) conceptual framework to explain slope failures in stiff clays and their mechanical behaviour at different confining pressures (see Figure 5.12).

5.6.2 Failure, bonding, and plateau envelopes

Figure 5.13 shows the peak resistance, bonding resistance (bonding contribution at peak), and plateau strength boundaries. The failure envelope is characterized by nonlinearity, and the bonding envelope can be approximated by an elliptical shape. Malandraki and Toll (2000) captured experimentally the elliptical shape of bonding resistance for artificially cemented soils under different stress paths. At low stress levels, the bonding resistance dictates the shearing resistance. This contribution progressively reduces so that the frictional resistance becomes dominant at high confining stresses. The extension of the failure envelope at high stress levels leads to zero strength at zero confining stress. This is a typical behaviour of sheared unbonded geomaterials, i.e., frictional materials. The point at which bonding resistance vanishes marks the transition from bonded to unbonded geomaterials, in which the transition from over-consolidation state to normally consolidation state in conventional Soil Mechanics terms. Based on the two boundaries, three zones can be identified. The first describes the behaviour of geomaterials, in which the bonding is the main contributor to strength (rocks). The third zone is typical of geomaterials where friction dominates the

behaviour (soils). The middle zone is a transition zone where a quasi-frictional behaviour is manifested due to the mutual contribution of both components.

5.6.3 *Resemblance of stress-strain curves' shapes and failure envelopes of bonded geomaterials with different origin*

Conlon (1966) experimentally captured the same behaviour in terms of pre-peak wavy stress strain curves and nonlinear failure envelope for a very stiff sensitive clay deposit of fine-grained estuarine sediments in Canada, tested in a triaxial compression (see Figure 5.14). Lajtai (1974) also carried out direct shear tests on solid plaster with two voids to simulate the behaviour of jointed weak rocks and also captured the wavy stress strain curves and nonlinearity (see Figure 5.15). Figure 5.16 shows the stress strain curves at low stress range for two different materials. The first material is a weakly artificially cemented soil investigated by Lo et al. (2003) (see Figure 5.16a). The second one is based on the experimental results obtained by Lagioia and Nova (1995) in a study of a calcarenite, which is a coarse-grained weak rock formed in a marine deposition in the lower Pleistocene epoch and characterized by the existence of calcium carbonates (see Figure 5.16b). Sangrey (1972) also observed the pre-peak initial yield, due to bond destruction in Labrador clay (sensitive cemented clay) based on drained triaxial tests. Feda (1995) also reported a series of triaxial compression tests on undisturbed cemented Neogene lacustrine clay. Feda (1995) pointed out that during the pre-peak stage of testing, destruction of bonds was also

reflected in the pre-peak wavy form of stress strain curves, and, particularly at a low stress range.

Mitchell (1970) investigated the behaviour of Leda clay, which is a highly cemented sensitive soil, under triaxial compression test conditions and identified three zones (see Figure 5.17a) based on the nonlinearity of the failure envelope. In the first zone, fissures govern the behaviour and dilation results in a high friction angle. In the second zone, the bonding resistance governs the behaviour, and in the third zone, the intrinsic frictional behaviour dominates. In the present study, only the second and third zones identified by Mitchell (1970) were captured. Lefebvre and Rachelle (1974) also captured the nonlinearity due to bonding degradation effects in a sensitive Champlain clay deposit in Saint-Laurent lowlands east of Quebec City on the south shore of the Saint-Laurent River in Canada (see Figure 5.17b).

5.7 Remarks on mobilized strength of bonded geomaterials

At low strain levels and at low- to-medium confining stresses, the mutual contribution of bonding and frictional resistance governs the mobilized strength. For quasi-frictional materials, at working strain levels, in the pre-peak regime, the strength is only a fraction of the full bonding and frictional resistances. This can be approximated by the plateau strength envelope, due to the balance between frictional strength mobilization and bonding strength degradation. At this strength level, only a fraction of the bonding and full frictional strength can be relied on,

whereas at the peak strength frictional resistance dominates due to strain hardening (Figure 5.11c and d). Various investigators, based on their experimental investigations of various bonded geomaterials, indirectly stated this idea and opposed the concept of the full mobilization of the frictional resistance.

Conlon (1966) stated that the strength available at the instant of failure of a slope in bonded stiff clay is due to bonding resistance, as full frictional resistance cannot be totally mobilized prior to failure. Moreover, Mitchell (1975) carried out drained constant mean effective stress tests on Leda clay to reveal the operational strength for slope failure. Mitchell (1975) revealed that the onset of dilation is a good approximation of the operational strength for sensitive clays. Cresswell and Powrie (2004) carried out experimental work on locked sand, where bonding between particles results from the interlocking of grains rather than the cementation bonds between particles. Cresswell and Powrie (2004) showed that the onset of dilation marks a major degradation of interlocking and should be considered as the limiting strength based on a factor of safety for peak values, given the proximity of the two envelopes at different confining stresses. Cecconi and Viggiani (2001) carried out triaxial compression tests on a bonded coarse-grained weak rock. These investigators pointed out that the onset of dilation marks the onset of bond destruction and that the peak resistance corresponds to a lower bonding contribution compared to that of the onset of dilation.

It is highly recommended to reconsider either the plateau strength (whenever it can be identified from the experimental results) or the onset of dilation as an upper strength threshold for all bonded geomaterials, as shown for locked sand in the previous chapter. However, further research is needed to identify the relationship between the onset of dilation as a macroscopic threshold for destruction and the field operational strength of bonded geomaterials. Comparing the operational strength based on the back analysis of well-instrumented failure case histories can reveal the relationship between the onset of dilation and the operational strength.

5.8 Summary and Conclusions

This chapter investigated the contribution of the frictional resistance and the bonding resistance at various strain levels for two natural stiff clays using a simplified approach. The partitioning of the strength parameters was presented in two different stress spaces: M-C space and q-p space. In M-C space, partitioning was presented in terms of the cohesion and the friction angle for the two investigated clays. The results revealed that the cohesion and friction angle are not simultaneously mobilized (as the conventional M-C hypothesis implies for the peak strength). The cohesion distribution's trend indicted progressive degradation with plastic strain level. On the contrary, friction angle distribution builds up progressively with shear strain. In q-p space, partitioning was also carried out in terms of two normalized parameters corresponding to the bonding and the friction strength parameters for Nanticoke clay. An incremental form

equation based on normalized strength parameters was proposed to reveal the contribution of the frictional and the bonding resistance at various strain levels. An example of the results of this equation was also presented to show the bearing of the non-simultaneous mobilization of strength parameters on stress-strain curves and failure envelope. It was shown that strain hardening and weakening are the by-products of the balance between cohesive strength degradation and frictional strength mobilization at different confining pressures. Three yield surfaces were captured and sufficiently described the failure evolution and failure envelope's nonlinearity, the bonding contribution and its degradation, and balance between the frictional strength mobilization and bonding strength degradation (plateau strength). The significant influence of bond degradation was manifested by the initial reduction in resistance in the pre-peak regime at low confining pressures. The experimental results for various bonded geomaterials, with different origin, revealed that this initial plateau in the stress-strain curves was a characteristic behavior. In addition, the transition between soils and rocks was also captured by using such framework with supporting evidence from the literature on different bonded geomaterials.

CHAPTER 6: SIGNIFICANCE OF STRAIN-DEPENDENT STRENGTH PARAMETERS IN THE ASSESSMENT OF SLOPE STABILITY PROBLEMS

6.1 Introduction

Back analysis of failed slopes in bonded clays (stiff clays and eastern Canadian clays) revealed that the average mobilized strength at failure (the operational strength) was less than the laboratory peak strength and greater than the residual strength (e.g., Skempton 1964, 1970; Bjerrum 1967; Burland et al., 1977; Lefebvre and La Rachelle 1974; Chandler 1984; Lefebvre 1981; Cooper et al. 1998). Realization of such phenomenon introduced the concept of progressive failure as the probable cause of this, where mobilized strength along slip surface varied according to the experienced level of strain from peak to residual strength. Despite our theoretical understanding of such phenomenon, no comprehensive work has been presented numerically to explain clearly the deviation of the average operational strength from the laboratory peak strength due to progressive failure. In recognition of the importance of strain-dependent parameters as shown in the previous chapters, a parametric study is presented in this chapter to reveal the significance of strain-dependent strength parameters in the analysis of slope stability problems as compared to conventional peak strength parameters, and, in particular to capture the progressive failure of slope as a function of strain.

The distribution of strength parameters and the peak's constant strength parameters of Nanticoke clay were used to simulate the failure of a

homogeneous slope. Two computational tools have been used for the investigation in this chapter. The first computational tool was a commercial 2D finite difference program, FLAC version 4.0 (*Fast Lagrangian Analysis of continua*) developed by Itasca (2000). The essential element of this program is the explicit numerical scheme in which dynamic equations of motion in conjunction with incremental constitutive laws are solved over a very small time step. In this way, variation of field variables propagates as a real physical disturbance, and no iteration procedure is required to arrive at the solution. The program is most suitable for analyzing nonlinear behavior of materials and related instability and failure phenomena. FLAC has been used in these analyses to reveal the slip surface associated with peak strength parameters and the strain-dependent strength parameters (SDP). The second computational tool was a commercial limit equilibrium slope stability program (SLOPE/W, Geo-Slope International Ltd 2004). SLOPE/W is user friendly software that has been used to simulate complex slope geometries. This program enables the users to visualize the minimum factor of safety, the critical slip surface, and the distribution of normal stresses and shear stresses along the slip surface using different limit equilibrium methods. SLOPE/W has been used in this investigation to reveal the factor of safety and the critical slip surface obtained by using the peak strength parameters.

6.2 Limit equilibrium and deformation analysis

Limit equilibrium analysis is widely used in the field of geotechnical engineering to assess the stability of slopes. An implicit assumption in limit equilibrium analysis is that the soil exhibits constant strength regardless of experienced deformation. As LEM has no consideration for deformation, it is assumed that the selected strength is mobilized everywhere along the slip surface regardless of the deformation (Duncan, 1996). In stability problems, it is the custom to use limit equilibrium to render the factor of safety. Morgenstern and Sangrey (1978) state that one of the uses "... of the factor of safety is to provide a measure of the average shear stress mobilized in the slope." They go on to state that, "This should not be confused with the actual stresses." In addition, due to the additional assumptions for determinacy in LEM, global equilibrium is satisfied rather than equilibrium everywhere in the soil mass. Duncan (1996) and Krahn (2003) provided a comprehensive summary of the available methods and limitations of limit equilibrium according to the inherent assumptions regarding the inter-slice forces and equations of equilibrium. Fredlund and Krahn (1977) pointed out the main difference between the limit equilibrium methods and showed the similarity between the different methods and the calculated factors of safety regardless of LEM different assumptions. Krahn (2003) stated that LEM relies only on the principal of statics. The method says nothing about strains and displacements, and as a result it does not fulfill displacement compatibility. In addition, the stresses calculated in LEM do not represent the actual case, and localized shear stress concentrations are not captured. Predicted stresses in

LEM are only based on the assumption of a unique factor of safety for all slices, where the slice normal and shear stresses are derived primarily from the slice weight. Tavenas et al. (1980) and Wright et al. (1973) pointed out the importance of incorporating the actual stresses in slope stability analysis. These researchers also realized that the definition of the factor of safety assumes a certain stress path, which is not necessarily developed in the field. In addition, for a given slope, the critical slip surface associated with the minimum factor of safety may be different from the critical slip surface associated with critical acceleration (Sarma and Bhawe 1974). Yu et al. (1998) also pointed out that the collapse mechanism due to the rigid plastic assumption in LEM is usually kinematically inadmissible.

The second technique used in the assessment of the stability of slopes is the application of the deformation analysis by using either the finite element methods or finite difference methods. The numerical analysis is a very powerful tool in enhancing our understanding of civil engineering activities. Griffith and Lane (1999) applied the finite element method to calculate the factor of safety using elasto-plastic Mohr-coulomb criterion. Dawson et al. (1999) also applied finite difference method by using the strength reduction technique to estimate the factor of safety. In the deformation analysis methods, no prior assumptions are required regarding the shape, the location of the failure surface, or the inter-slice forces as in LEM. Failure occurs naturally through the zones within the soil mass in which the soil shear strength is unable to sustain the applied shear stresses.

In deformation analysis, the stresses are also closer to reality and stress concentrations are considered in the analysis. The potential failure surface for a simulated slope is approximated by using the non-convergence criterion as introduced by Zienkiewicz (1971). In the context of this approach, the shear strength parameters in a nonlinear analysis are reduced until numerical instability occurs. The factor of safety is calculated as the ratio of the available shear strength and the factorized strength that results in a converged solution prior to instability. Slope stability analysis using the strength reduction has been carried out successfully by Dawson et al. (1999) and Griffith and Lane (1999) for homogeneous slopes.

6.3 Slope geometry and material properties

A 1:1 slope with a height of 20m is used for these analyses. In FLAC version 4.0 (2000), the whole domain was divided into 100x60 square elements before the excavation stage. Displacement-type boundary conditions were assigned at the model boundaries. The domain's left and right boundaries were restrained in horizontal direction. The base of the domain was restrained in both vertical and horizontal directions (see Figure 6.1). Before the excavation stage, the material behaviour was assumed to be elastic by prescribing both the bulk and shear modulus to estimate the initial stress distribution upon reaching an equilibrium state under gravitational stresses. The excavation was carried out by the removal of the excess grid zones from the domain. After excavation, the model was run to reach an equilibrium state while prescribing an elastic model. The distributions of

the vertical stress under gravitational stresses before and after the excavation are shown in Figure 6.2 and Figure 6.3, respectively. According to FLAC conventions, negative normal and shear stresses indicate compression and anti-clockwise distortions, respectively. The excavation stage resulted in a local shear stress concentration in the vicinity of the toe as shown in Figure 6.4. Once the initial stress conditions were established, the constitutive model was altered from the elastic model to either the elasto-plastic M-C model or the strain hardening/softening M-C model. In FLAC, it is possible to assign strength parameters as a function of plastic strain using the table option. The strain-dependent strength parameters as well as the peak strength parameters for Nanticoke clay were used in the simulation. Table 6.1 lists the parameters used in the simulations. It should be noted that all the parameters are in terms of effective stresses.

6.4 Peak strength parameters simulations

6.4.1 *Finite difference simulations*

Once the initial stress conditions were established, the material was assigned M-C peak strength parameters. The equilibrium of the model was examined by recording the unbalanced forces (the maximum of the unbalanced nodal forces). The reduction of unbalanced forces with the number of steps is an indication of reaching a steady state. Non-convergence occurs when the recorded unbalanced forces are either high or when large fluctuation in the unbalanced forces occurs. In deformation analysis approach, the slip surface

evolves naturally without any assumptions for inter-slice forces as in conventional LEM. The rendered slip surface from deformation analysis give a factor of safety of 1 based on the assigned strength parameters. When the peak strength parameters were assigned to the model, no slip surface was detected. In order to get the potential slip surface, the strength reduction factor (SRF) technique was used, based on the peak strength parameters. The reduced strength parameters were calculated using the following equations:

$$[6.1] \quad \text{SRF} = \frac{c_p}{c_m} = \frac{\tan(\phi_p)}{\tan(\phi_m)},$$

where c_p is the peak cohesion, c_m is the assumed mobilized cohesion, ϕ_p is the peak friction angle, and ϕ_m is the assumed mobilized friction angle.

Using the SRF technique, the strength parameters have been incrementally decreased by applying a reduction factor to the peak strength parameters. In each case, a simulation was run to obtain the potential slip surface. The last converged model defined the potential slip surface and the factor of safety. This approach is in agreement with the definition of the factor of safety (fos) as the factor by which the strength is reduced to reach equilibrium. Table 2 summarizes the reduction factors, unbalanced forces, and the convergent solutions. Figure 6.5 and 6.6 show the unbalanced forces history for reduction

factors of 1.43 and 1.44, respectively. It can be seen from the figures that the model's convergence with a SRF of 1.44 was impossible, when compared to a SRF of 1.43. There was an increase in unbalanced forces that fluctuated between 1.5-4 kN/m for a SRF of 1.44 as compared to stabilized unbalanced forces (0.8 kN/m) for a SRF of 1.43. The potential slip surface based on a SRF of 1.43 is shown in Figure 6.7.

6.4.2 *Limit equilibrium simulation*

SLOPE/W (Geo-Slope International Ltd 2004) is commercial limit equilibrium software to assess the stability of slopes. SLOPE/W was used to obtain the minimum factor of safety and the critical slip surface associated with the peak strength parameters by using M-C plasticity model. The critical slip surface obtained from LEM is not necessarily the potential slip surface. It is merely defined as the surface which renders the minimum factor of safety. This analysis was carried out to compare the factor of safety and the critical slip surface from LEM with that obtained from the numerical simulation. Table 3 summarizes the factors of safety based on different analysis methods. Figure 6.8 shows the slope geometry, the minimum factor of safety, and the critical slip surface. The factor of safety ranged from 1.42 to 1.48. The factor of safety associated with the critical slip surface (1.45), based on the methods that satisfy both force and moment equilibrium, is relatively in agreement with the factor of safety obtained from the numerical simulation (1.43). Although the factor of safety is almost identical from the LEM and numerical simulation, the

slip surfaces are relatively different. The limit equilibrium approaches renders state of stresses that may not represent the actual stresses in order to assure a unique factor of safety for all slices. Figure 6.9 shows the distribution of the normal stresses, mobilized stresses, and available strength at the base of the slices. The first observation is that the ratio between both of the mobilized and available strength is the same for all slices. The second observation is that in order to render a unique factor of safety, tensile normal stresses are manifested at the crest of the slope, which indicates an upward movement of the slope and a negative frictional resistance. For reduced strength parameters which corresponded to the factor of safety, the same critical slip surface was obtained from LEM. In both cases, the normal and mobilized stress distributions were identical at the base of slides.

6.5 Strain-dependent strength parameters simulation

The rendered parameters from the analysis of Nanticoke clay in the previous chapter were implemented in FLAC's strain hardening/softening model. Although it is known that the softening curve is inversely related to the element size (smaller elements give a thinner shear band and results in more softening), no effort was done to investigate such phenomenon in this analysis. The aim of this analysis is neither to estimate the thickness of the band nor to quantify the shear strains within the band. The potential slip surface based on the simulation is shown in Figure 6.10. The plasticity indicator indicates a combination of tension

and shear failure along the slip surface. The tensile failure is more evidenced near the toe and the crest of the slope (represented as circles).

Figure 6.11 shows the evolution of the potential slip surface with the plastic strain. The potential slip surface evolves from the toe, where high shear stresses are recorded, progressively to the slope's crest with the increase in plastic strain level. Figure 6.12 shows the distribution of the unbalanced forces with the number of iterations. The model showed a reduction in the unbalanced forces to a threshold followed by an increase in unbalanced forces. It was assumed that initiation of global failure commenced at the point where the unbalanced forces accelerated. In order to provide a better understanding of the problem, the model was run to the assumed instability point. Marker points were assumed along the potential slip surface as shown schematically in Figure 6.13. These points served to monitor the evolution of strength parameters and stresses along the potential slip surface.

6.5.1 *Deviation of operational strength from peak strength*

Figure 6.14 and Figure 6.15 show the distribution of the mobilized cohesion and friction angle along the potential slip surface as a function of plastic strain. As shown on the figures, the plastic strain varies along the potential slip surface. The plastic strain tends to be higher at the toe and reduces progressively towards the crest of the slope. The experienced plastic strain at the toe is one order of magnitude greater than the plastic strain at the crest.

The results of the model comply with the assumptions of non-simultaneous mobilization of strength parameters. The cohesive component tends to degrade with progressive mobilization of friction angle. At the toe, the cohesive component is completely degraded, while the friction angle is fully mobilized followed by a decrease in its value. On the other hand, the cohesive component is fully mobilized at the crest of the slope with a negligible contribution of the friction angle. At any intermediate point along the slip surface, the mobilized strength is due to the mutual contribution of the friction angle and cohesive resistance that correspond to the plastic strain level. The contribution of the cohesive component increases from the toe to the crest, while the friction angle tends to decrease.

Figure 6.16 shows the distribution of the normal, shear stresses, and available strength along the slip surface from the toe to the crest. The estimated vertical, horizontal, and shear stress from the model were used to calculate the normal and shear stress at selected points along the slip surface. The normal and shear stresses on the slip surface were calculated using the following equations:

$$\text{[6.2]} \quad \sigma_n = \sigma_{xx} \sin^2(i) + \sigma_{yy} \cos^2(i) - \sigma_{xy} \sin(2i), \text{ and}$$

$$\text{[6.3]} \quad \tau_n = \sigma_{xy}(\sin 2(i) - \cos 2(i)) - \left(\frac{\sigma_{yy} - \sigma_{xx}}{2} \right) \sin 2i,$$

where σ_n , τ_n are the normal and shear stresses on the slip surface, respectively; i is the inclined angle of a segment along the slip surface with the horizontal direction; and σ_{xx} , σ_{yy} , and σ_{xy} are the normal and shear stresses acting in x- and y- coordinate directions.

The available shear strength was calculated based on the distribution of the normal and shear stresses using the following equation:

$$\text{[6.4]} \quad \tau_a = c + \sigma_n \tan(\phi),$$

where τ_a is the available strength; and c and ϕ are the cohesion and friction angle, respectively.

It can be seen from the figure that the normal and shear stresses at the toe are higher than the corresponding values at the crest. Hence, the model accounts for stress concentration due to excavation as compared to LEM. The calculated available strength is almost identical to the mobilized shear stress along the slip surface except at the crest. This indicates that at the onset of instability, the upper part of the slope is not experiencing failure. Figure 6.17 shows a hypothetical stress strain curve and the position of the monitoring points on such curve for illustration.

The average friction angle and cohesion along the slip surface are 15° and 29 kPa, respectively. The averaged normal and shear stresses are 117 kPa and 57.4 kPa, respectively. The global factor of safety based on the average values renders a factor of safety of 1.0. Using the peak strength parameters ($c=71$ kPa and $\phi=17^\circ$), the mobilized shear stresses on the slip surface are 54% of the peak strength. The residual strength parameters render a factor of safety of 0.62. According to the LEM and the numerical simulation using peak strength parameters, the mobilized shear stresses on the slip surface are 70% of the peak strength.

In summary, assuming that the SDP's slip surface is the actual slip surface, the peak strength parameters tend to overestimate the factor of safety, while the residual strength underestimates the factor of safety. Hence, the mobilized strength is greater than the peak strength and less than the residual strength. Based on the previous analysis, the mobilized strength at the assumed instance of failure is 54% of the peak strength. This average value of mobilized strength accounts for the progressive failure of slope, and in agreement with the operational strength ranges estimated based on back analysis of failed slopes in highly plastic stiff clays (Mesri and Abdel-Ghaffar 1993). Hence, the incorporation of non-simultaneous mobilization of strength parameters in slope stability analysis renders a plausible explanation for the deviation of the mobilized strength from the peak strength and efficiently

captures the evolution of failure. However, more work is needed to confirm such conclusion based on well-documented case histories.

6.6 Comparison between slip surfaces' positions

Figure 6.18 shows the potential slip surfaces obtained from the pervious analyses. The slip surface, associated with peak strength parameters, estimated from Limit equilibrium analysis is relatively shallower than the one estimated from the finite difference code (FLAC). This is an agreement with Potts et. al (1997) using the finite element method and the limit equilibrium method. The SDP's slip surface is shallower than both slip surfaces obtained from LEM and FLAC using constant parameters. If it is assumed that the cohesion degrades with the progressive mobilization of friction as a function of strain, the slip surface is anticipated to be shallower than the one obtained using constant parameters. It was shown in the previous chapter that the concept of non-simultaneous mobilization of strength parameters reflects the failure envelope non-linearity. According to Jiang et al.'s (2003) investigation on the effect of failure envelop non-linearity on the stability of slopes, the incorporation of nonlinearity of failure envelope results in shallower slip surface as compared to linear failure envelope. This is in agreement with the results presented in this investigation.

6.7 Summary and conclusions

In this chapter a parametric study was carried out to reveal the significance of non-simultaneous mobilization of strength parameters in the assessment of the

stability of slopes. The focus was to explain the deviation of the operational strength from the peak strength. For this purpose, two commercial software were used for the simulation of a 45° homogeneous slope with a height of 20 m. The finite difference software (FLAC) was used to reveal the potential slip surfaces associated with peak strength parameters and the strain dependent strength parameters by considering the hardening/softening model. The factor of safety, based on peak strength parameters, was determined by using the strength reduction technique. The slope stability analysis was also carried out by using limit equilibrium software (SLOPE/W) to reveal the factor of safety and the slip surface associated with peak strength parameters. The distribution of the strength parameters, normal and shear stresses, using the hardening/softening model, along the potential slip surface were also estimated.

The results of the finite difference model and LEM showed that the factor of safety associated with peak strength parameters was 1.43 and 1.45, respectively. The LEM's slip surface was relatively shallower than the one estimated based on the strength reduction technique. The strain-dependent strength parameters' slip surface was shallower than both of those estimated from LEM and FLAC. The numerical simulation using the hardening/softening model captured the progressive failure of the simulated slope. The mobilized shear strength parameters values varied along the slip surface according to the experienced plastic strain level. The plastic strain at the toe was at least one order of magnitude greater than the plastic strain at the crest. For an average value of

normal and shear stresses, the peak strength parameters overestimated the factor of safety. On the other hand, the residual strength parameters underestimated the factor of safety. The mobilized strength to render a factor of safety of 1 was 54% of the peak strength and accounted for the progressive failure of the slope. This was only captured through incorporation of the strain-dependent strength parameters. It was concluded that this conceptual framework is a powerful framework to explain the discrepancy of the mobilized strength in the field from the peak strength. However, more work is needed to confirm such conclusion based on well-documented case histories.

Table 6.1 Summary of M-C parameters.

Parameter	Value
Bulk Modulus (kPa)	1.19×10^6
Shear Modulus (kPa)	0.10×10^6
Peak cohesion (kPa)	71
Peak friction angle	17
Residual cohesion(kPa)	0
Residual friction angle	17

Table 6.2 SRFs and average unbalanced forces.

SRF	Average Unbalanced force (kN/m)	Convergence
1.35	0.2	Yes
1.43	0.8	Yes
1.44	1.5-4.0	No

Table 6.3 Factor of safety based on LEM.

Method	Factor of safety (fos)
Janbu method	1.42
Bishop method	1.45
Ordinary method	1.48
Morgenstern-price method	1.45
Spencer	1.45

CHAPTER 7: SUMMARY, CONCLUSIONS, AND RECOMMENDATIONS

7.1 General

This chapter presents a summary of the research objectives, and the conclusions reached during this investigation. Recommendations for future research are also provided.

7.2 Objectives of the thesis

The experience gained by back analysis of civil engineering applications in stiff clays and weak rocks has shown that the operational strength can not be expressed in terms of peak or residual strength. Despite the wealth of information on the strength of geomaterials, no generalized framework exists for identifying the operational strength, particularly in the intermediate zone between soils and rocks (quasi-frictional materials). The main challenge in determining the operational strength for such materials lies partly in capturing the relative contribution of the interlocking/bonding and frictional resistance at working stress and strain levels, or in the pre-peak regime.

The main objectives of this investigation can be summarized in the following points:

1. To examine high-quality laboratory results for various geomaterials to understand failure precursors in the pre-peak regime, and to capture the onset of failure strength thresholds for soils and rocks.
2. To conduct a comprehensive experimental study on a McMurray fabric-dominant weak rock (locked sand) to reveal the following:
 - a. The source of the exceptional uniaxial strength of such a sand formation in the absence of bonding between particles and to confirm this formation's fitting into locked sands category;
 - b. The significance of local strain, compared to our routine external strain measurements for McMurray sand formations, in terms of failure mechanism, deformation modulus, and post-peak response;
 - c. The pre-peak damage thresholds for locked sand to capture the damage evolution based on the variation of local axial and lateral strains;
 - d. The contribution of the frictional and the interlocking strength components with the plastic shear strain;
 - e. The relationship between the onset of localization and the onset of dilation as a candidate for the strength threshold;
 - f. The mechanism and kinematics of failure of locked sand;
 - g. The relationship between the onset of dilation and the long-term strength (onset of creep) of locked sand as a possible candidate for long-term strength; and
 - h. The upper and lower strength thresholds for locked sand.

3. To develop a simplified approach for partitioning the shear strength parameters (cohesion and friction angle) with plastic strain for stiff clays, and to show the significance of non-simultaneous mobilization of strength parameters in revealing:
 - a. The resemblance in bonded geomaterials' shearing responses at low confining pressure irrespective of these geomaterials' origin; and
 - b. The transition between soils (frictional materials) and rocks (bonded materials) based on the mutual contribution of frictional and bonding resistance to overall resistance.
4. To highlight the significance of the concept of non-simultaneous mobilization of strength parameters in capturing the progressive failure of slopes and to interpret the deviation of the operational strength of stiff clays from the peak strength with such conceptual framework.

7.3 Summary and conclusions

This section summarizes this thesis' research and conclusions. The first part of the thesis included a critical review of high-quality test results for various geomaterials to reveal the significance of salient pre-peak strength thresholds as compared to the peak and residual strengths. The second part provided an investigation of the behaviour of a locked sand (a quasi-frictional material with an interlocked fabric) to show the significance of local strain measurements, to identify pre-peak damage thresholds based on variations of the local strains, to

provide an understanding of failure's evolution and mechanism, to show the relative contribution of strength parameters with strain, and to give recommendations about the operational strength of such geomaterials as an example of quasi-frictional materials with interlocked fabric. The third part suggested a simplified approach to visualize the relative contribution of bonding and frictional resistance to the overall resistance for bonded geomaterials at any strain level. This concept was then employed to show the resemblance of bonded geomaterials' behaviour at low confining stresses regardless of their origin and to capture the transition between soils and rocks based on the mutual contribution of the frictional and bonding resistance to the overall resistance. The fourth part of the thesis showed the significance of the strain-dependent strength parameters in capturing the progressive failure of slopes and in revealing the discrepancy between the operational strength and the peak strength using numerical simulation.

7.3.1 Pre-peak strength thresholds for geomaterials

High-quality shear strength and volume change data for various soils and rocks were compiled and reviewed to reveal the salient pre-peak strength thresholds by using microstructural observations and localized strain measurements. The first part of the discussion revealed the relationship between the onsets of dilation (the volumetric strain reversal stress level) and localization (the loss of strain-uniformity) for various geomaterials. In the second part, three examples were provided to investigate the relationship

between the onset of dilation and the long-term strength. In the third part, another threshold was introduced for bonded geomaterials: extensile induced dilation (the initiation of bond degradation). Based on data analysis, the following conclusions were drawn.

1. Geomaterials display a marked change in their behaviour prior to reaching the laboratory peak strength.
2. The onset of shear-induced dilation (volumetric strain reversal) is an excellent indicator of the onset of localization for the investigated geomaterials regardless and can be directly estimated from global measurements.
3. The peak and residual strengths measured in our laboratory are a direct result of progression of localization and can be merely considered as merely signs of failure.
4. The ratio of the stress level required for initiating shear-induced dilation normalized to the peak strength ranges from 0.76 to 0.86 and is independent of fabric and/or bonding nature.
5. For the investigated geomaterials, the onset of shear-induced dilation is an excellent indicator of the onset of creep. Beyond this threshold, creep potential becomes significant.
6. The onset of shear-induced dilation may be considered as an upper strength threshold for the investigated geomaterials.

7. The onset of extension-induced dilation marks the initiation of bond degradation for bonded geomaterials and can be captured only by local lateral strains measurements.
8. The use of pre-peak strength thresholds (the onset of shear-induced dilation and the onset of extension-induced dilation) seem promising to determine the upper and lower strength thresholds for geomaterials.

7.3.2 High-Hill River characteristics and significance of local strain measurements

An up-to-date synopsis of the common characteristics of locked sands was presented. Based on the established framework, experimental work was presented to establish the fit of the High-Hill oil-free sand formation in the locked sands category. The experimental work was comprised of micro-structural observation, mineralogical composition analysis, and fabric analysis. Uniaxial compressive strength tests were also carried out to reveal the strength of the locked sand's unbonded coherent mass and to explore the significance of local strain measurements. The experimental set-up and the calibrations, proof testing, and stability tests were presented and discussed in detail.

It was shown that the High-Hill River sand formation is a lower Cretaceous McMurray Formation with coherent mass. The dense nature of the samples, the mineralogical composition, and the micro-structural observations were in

keeping with the characteristics of locked sands. This formation was best described as overconsolidated well-sorted unbonded friable locked sand with characteristics similar to those of oil-sands' middle members. The formation was subjected to mild post-depositional diagenesis that transformed its detrital sand-sized particles into a weak rock with interlocked fabric through deposition of authigenic silica. SEM images and petrographic analysis of thin sections disclosed that the grain contacts were dominated by tangential, long-to straight, occasional interpenetrative and sutured contacts created via overgrowth and dissolution. The small percentage of kaolinite in the form of coating or bridges was responsible for this deposit's friability. The fine particles presumably originated from either the diagenesis of the overlying shale formation or the feldspar inherited from parent rocks. The deposit appeared to have been subjected to overburden loads that were adequate to cause this fracturing, and, hence, influenced the structure of the deposit. The clean cracks within quartz grains implied that either the clay minerals were deposited following the compaction stage, or the clay minerals were so weak nature to prevent loss of porosity due to compaction by early cementation. The existence of a fresh skeletal grain by dissolution suggested that the process of dissolution occurred after the compaction stage and is still in process; otherwise, the compaction process would have destroyed this skeleton.

A local measurement system for both axial and lateral strains was used and modified for this friable material in conjunction with a routine external axial measurement system for characterization. The formation exhibited a uniaxial compressive strength of 2 MPa and, hence, was classified as a “weak rock”. The interlocking between particles was the main source of this high uniaxial strength and axial stiffness in the absence of bonding between sand particles. The axial stiffness based on local strain measurement was approximately 0.87 GPa and almost 2 times the externally measured axial stiffness. In the post-peak regime, both measuring systems indicated strain weakening; however, the local one exhibited a slightly less abrupt reduction in strength. In terms of the failure mechanism and strain-rate effects, the variation in the local axial strain rate provided more insight into failure evolution stages than externally measured axial strain rate. Hence, for proper characterization of such geomaterials and their oil-sand counterparts, the interpretation of experimental founded on commonplace external strain measurements are less reliable, particularly when the coupling strength and deformation are targeted. Local strain measurements are necessary to obtain proper behavioral characterization and to interpret the failure mechanism interpretation of locked sands.

7.3.3 High-Hill river geomechanical characteristics: damage thresholds, mobilized strength parameters, failure kinematics, and long-term strength

The geomechanical characteristics of the High-Hill River sand formation were explored in detail under uniaxial compression test conditions. The first part of the discussion was to identify damage thresholds that marked a significant variation in the stress-strain response identified by the variation in the local axial and lateral strains. Four thresholds were identified and discussed in terms of the failure mechanism during shearing. The relationship between the onset of dilation (the damage coalescence threshold) and the damage localization threshold was established by using local strain laboratory measurements results. The mechanism and kinematics of failure in locked sand was also described. For practical purposes, the contribution of frictional and interlocking resistance at different strain levels was obtained, and their mutual contribution was discussed. In the second part, the discussion explained how the columnar structures and kinematics of deformation for locked sand were captured by the creation of a relatively homogeneous strain field throughout the shearing process. The experimental observations were compared to investigate the dominant mode of deformation at the onset of localization. The formation of dilation bands as the dominant mode of deformation in the pre-peak regime was discussed and its significance during the progression of failure in locked sands was substantiated by using the theoretical framework previously established for porous rocks. The third part

presented a multistage uniaxial creep test to confirm the significance of the onset of shear-induced dilation as an excellent indicator of long-term strength. Finally, the direct shear test results were presented to reveal the maximum mobilized strength under pure shear conditions. The following conclusions were made in the chapter.

1. The exceptional high uniaxial strength and axial stiffness compared to those in dense sands were the by-products of the particles' angularity and the interlocking between particle contacts and was manifested as enhanced ability to resist moments at contacts.
2. The stress-strain curves were partitioned in the pre-peak regime based on the local axial and lateral strain responses to describe the evolution of failure, i.e., the closure of cracks and pores, initiation of unlocking, onset of localization, and coalescence and unstable propagation of damage.
3. No coupling occurred between the axial and lateral stiffness. The lateral strain exhibited extensile strains throughout the shearing process.
4. The maximum dilatancy factor, 3.6, for the investigated locked sand exceeded the maximum dilatancy factor for dense sands.
5. The onset of unlocking (the damage initiation threshold) occurred at 28 % of peak strength and was coincident with our observations of the crack closure strength threshold.
6. The onset of localization and dilation took place at 55% and 67% of the peak, respectively.

7. The interlocking strength component and frictional components were not simultaneously mobilized. The interlocking component degraded with the plastic strain, resulting in the progressive mobilization of frictional resistance. The interlocking component tended to be consumed in the pre-peak regime and leveled off before attaining peak strength.
8. The basic frictional resistance mobilized and stabilized at low strain levels in the pre-peak regime after approximately 40% of the interlocking had been overcome.
9. At peak strength, the resistance resulted from the frictional contribution (basic friction and dilation) with less contribution from the interlocked component (accounting for 17% of peak strength) due to its consumption during the unlocking stage.
10. At the onset of dilation threshold, 60% of the mobilized resistance was attributable to the interlocked fabric. The remaining resistance reflected the mobilization of the basic frictional resistance.
11. A brittleness index value of 1.5 was calculated based on our experimental results. This value was indicative of brittle failure, for the loss of interlocking resistance exceeded the mobilization of frictional resistance. Hence, the mobilized strength in boundary value problems constructed in or on this geomaterial is much lower than the peak strength unless full frictional resistance is mobilized. This issue is considered of major concern in stress-induced excavation problems where the confining

pressure is reduced so that little frictional resistance can be mobilized, and , hence, brittle failure is inevitable.

12. Columnar structures were captured by the creation of a homogeneous strain field to hinder the onset of localization and to allow for the complete formation of such columns/slabs. The pattern of failure was dominated by the formation of vertical slabs/walls in the direction of major principal stress as a result of uniform unlocking through lateral expansion and the formation of dilation bands.
13. The comparison of this study's experimental results to those of the theoretical studies of failure modes of porous brittle rocks revealed that dilation bands were the dominant mode of deformation (a predominantly open-mode of deformation propagating in the direction of the major principal stress) and whereby such columnar failure patterns were created
14. Under constant loading conditions, the material exhibited a creep potential that became more significant beyond the onset of dilation.
15. Creep lateral strains and their rates were more significant than axial strains. Creep lateral strain rates were one order of magnitude greater than axial strain rates beyond the onset of dilation.
16. Creep volumetric strains were dilative in nature at all stages of creep. This finding signified the progressive damage and damage propagation in axial direction during creep stages.
17. The results of DSB tests indicated that the mobilized strength under low normal strength was independent of the normal stress levels. The

mobilized strength was dominated by the interlocking strength component and was equivalent to the damage initiation strength threshold estimated from the uniaxial compression test results.

18. In boundary value problems constructed in or on locked sands, damage coalescence and initiation thresholds are recommended to be the upper and lower strength boundaries. However, further work is required to investigate such argument at higher confining pressures.

7.3.4 Simultaneous mobilization of strength parameters for bonded geomaterials

For locked sand, it was shown that the concept of the non-simultaneous mobilization of strength is very important to interpret the failure mechanism and to capture failure evolution. This concept was extended to explain some of the peculiar pre-peak characteristics of bonded geomaterials, to reveal the contribution of strength parameters at different confining pressures, and to capture the transition between soils and rocks.

The contribution of frictional resistance and bonding resistance was investigated at various strain levels for two natural stiff clays by using a simplified partitioning approach. The partitioning of the strength parameters was presented in two different stress spaces: M-C space and q-p space. In M-C space, the partitioning was presented in terms of the cohesion and friction angle for the two investigated clays. The results revealed that the cohesion/bonding and friction angle were not simultaneously mobilized (as

the conventional M-C hypothesis implies based on the peak strength criterion). The cohesion/bonding distribution's trend indicated progressive degradation with the plastic strain level at low strain levels. In contrast, the friction angle built up progressively with the plastic shear strain and necessitated a higher strain to be mobilized. In terms of q-p space, partitioning was carried out in terms of two normalized parameters corresponding to the cohesion/bonding and friction strength parameters for Nanticoke clay. An incremental equation based on the normalized strength parameters was proposed to reveal the contribution of frictional and bonding resistance at various strain levels as follows:

$$[7.1] \delta q = \delta q_1 + \delta q_2,$$

$$\delta q_1 = \underbrace{\left[p' M_{crit.} (-cd(\exp(-d\varepsilon^P)) + ef(\exp(-f\varepsilon^P))) + M_{crit.} (c(\exp(-d\varepsilon^P)) - e(\exp(-f\varepsilon^P))) \delta p \right]}_{\text{frictional component}} \delta \varepsilon^P$$

, and

$$\delta q_2 = \underbrace{a M_{crit.} p_{to} (\exp(-b\varepsilon^P)) \left[(\exp(-d\varepsilon^P)) (-cd - bc) + (\exp(-f\varepsilon^P)) (eb + ef) \right]}_{\text{bonding component}} \delta \varepsilon^P$$

A parametric study was carried out to show the bearing of the non-simultaneous mobilization of strength parameters on the stress-strain curves and failure envelope. It was shown that strain hardening and weakening are the by-products of the balance between cohesive strength degradation and

frictional strength mobilization at different confining pressures. Three yield surfaces were captured that sufficiently described the failure surface and its nonlinearity, the bonding contribution and its degradation effects, and the balance between bonding strength degradation and frictional strength mobilization as reflected in an initial “plateau” in pre-peak regime. The influence of bond degradation was manifested through the initial reduction in resistance in the pre-peak regime, followed by either strain hardening or weakening. Strain hardening was shown to be controlled by the ability to mobilize full frictional resistance after initiation of bonding degradation. The compiled experimental results for various bonded geomaterials of different origins revealed that this initial plateau in stress-strain curves is a characteristic behavior where bonding is a major source of strength. In addition, the transition between hard rocks and soils was also captured by using such framework, and was substantiated by experimental results of different bonded geomaterials. The transition was described in terms of the contribution of bonding and frictional resistance to the peak strength.

7.3.5 The significance of strain dependent strength parameters in slope stability problems

A parametric study was carried out to reveal the significance of non-simultaneous mobilization of strength parameters in the assessment of the stability of slopes. The focus was to explain the deviation of the operational strength from the peak strength. For this purpose, two commercial software

were used for the simulation of a 45° homogeneous slope with a height of 20 m. The finite difference software (FLAC) was used to reveal the potential slip surfaces associated with peak strength parameters and the strain dependent strength parameters by using the hardening/softening model. The factor of safety, based on peak strength parameters, was determined by using the strength reduction technique. The slope stability analysis was also carried out by using limit equilibrium software (SLOPE/W) to reveal the factor of safety and the slip surface associated with peak strength parameters. The distribution of the strength parameters, normal and shear stresses, using the hardening/softening model, along the potential slip surface were also estimated.

The results of the finite difference model and LEM showed that the factor of safety associated with peak strength parameters was 1.43 and 1.45, respectively. The LEM's slip surface was relatively shallower than the one estimated based on the strength reduction technique. The strain-dependent strength parameters' slip surface was shallower than both of those estimated from LEM and FLAC. The numerical simulation using the hardening/softening model captured the progressive failure of the simulated slope. The mobilized shear strength parameters values varied along the slip surface according to the experienced plastic strain level. The plastic strain at the toe was at least one order of magnitude greater than the plastic strain at the crest. For an average value of normal and shear stresses, the peak strength parameters

overestimated the factor of safety. On the other hand, the residual strength parameters underestimated the factor of safety. The mobilized strength to render a factor of safety of 1 was 54% of the peak strength and accounted for the progressive failure of the slope. This was only captured through incorporation of the strain-dependent strength parameters. It was concluded that this conceptual framework is a powerful framework to explain the discrepancy of the mobilized strength in the field from the peak strength. However, more work is needed to confirm such conclusion based on well-documented case histories.

7.4 General framework for simulation of boundary value problems in strain weakening materials

Based on the presented work in this thesis, it is recommended to consider either of the following approaches to carry out a numerical simulation:

1. Incorporating the onset of dilation as an upper strength threshold within an elasto-plastic model along with appropriate deformation parameters that are based on local strain measurements.
2. Incorporating the strain-dependent strength parameters in a strain hardening/softening model to capture the overall failure mechanism. However, the results should be treated carefully due to the dependence of the shear strains on the size of the grid. Initially, the model should be

calibrated with high quality experimental data so that the model can be as close as possible to the real conditions.

7.5 Recommendations for future investigation

The following topics are suggested as a potential research subjects:

1. The effect of incorporating the concept of non-simultaneous mobilization of strength parameters in evaluating the stability of real boundary value problems: reanalyze well-documented case histories with high quality experimental data using such framework and compare the results with traditional design approaches.
2. The effect of strain rate, sample configuration (the slenderness ratio), and end effects (lubricated vs. non-lubricated ends) on the normalized dilation ratio: characterize the temporary strain hardening beyond the onset of shear-induced dilation for bonded weak rocks.
3. The significance of pre-peak thresholds as operational strength thresholds: reanalyze well-documented case histories augmented with high-quality experimental data obtained from local strain measurements.
4. The relationship between the ratios of onset of shear-induced dilation normalized to extensile-induced dilation and the ratio between the peak and residual strength for bonded weak rock under different confining pressure: conduct a comprehensive experimental investigation using local strain measurement and determine these thresholds using the framework in this thesis.

5. Exploiting discrete element method with bonded model, e.g. PFC to better understand the concept of the non-simultaneous mobilization of strength parameters and its relation to the overall mobilized strength: use the built-in bond model in PFC .
6. It was recommended in Canadian sensitive clays, that the mobilized strength in slope stability problems can be roughly estimated at 8% strain. However, this is only an approximation, and an interesting research subject is to reveal the relationship between the 8% strain strength threshold and damage thresholds: procure block specimens and conduct an experimental program at low stress levels to reveal the damage thresholds, creep limit, and its relation to the 8% strain strength level.

REFERENCES

- Abdelaziz, T., Martin, C.D., Chalaturnyk, R. 2005. The onset of dilation in soils and rocks. *In the 58th Canadian Geotechnical Conference & 6th Joint CGS & IAHCNC Groundwater Specialty Conference, 11-14 September 2005, Saskatoon, Canada, Paper No. 583.*
- Abdelaziz, T., Martin, C.D., Chalaturnyk, R. 2006. Geomechanical behaviour of a McMurray sand formation using local strain measurements. *In the 59th Canadian Geotechnical Conference & 7th Joint CGS & IAHCNC Groundwater Specialty Conference, 1-4 October 2006, Vancouver, Canada, No. 158.*
- Abdelhamid, H., Kondo, D., Henry, J.P. 2000. Strain localization in Fontainebleau sandstone. *Mechanics of Cohesive-Frictional Materials*, **5**:239-253.
- Adachi, T., Oka, F., 1993. An elastic-viscoplastic constitutive model for soft rock with strain softening. *In Proceedings of the International Conference on Geotechnical Engineering of Hard Soils and Soft Rocks, Athens, Greece, 20-23 September 1993, A. Anagnostopoulos et al.(eds.), Balkema, Rotterdam, Netherlands, pp. 327-334.*
- Agar, J. R., 1984. Geotechnical behavior of oil sands at elevated temperatures and pressures. Ph.D. dissertation, Department of Civil Engineering, University of Alberta, Canada.

- Agar, J.G., Morgenstern, N.R. and Scott, J.D. 1987. Shear strength and stress-strain behaviour of Athabasca oil sands at elevated temperatures and pressures. *Canadian Geotechnical Journal*, **24**(1):1-10.
- Alberta Energy Utilities Board (EUB) and Alberta Geological Survey (AGS) 2005. Alberta GIS and Interactive Maps: Geology of Alberta. Available at http://www.ags.gov.ab.ca/GIS/gis_and_mapping.shtml [cited 24th February 2006].
- Alshibli, K.A., Alramahi, B.A. 2006. Microscopic evaluation of strain distribution in granular materials during shear. *Journal of Geotechnical and Geoenvironmental Engineering*, **132**(1): 80-91.
- Alva-Hurtado, J. E. and Selig, E. T., 1981. Survey of Laboratory Devices for Measuring Soil Volume Change. *Geotechnical Testing Journal*, **4**(1): 11–18.
- Amorosi, A., Rampello, S. 1998. The influence of natural soil structure on the mechanical behavior of a stiff clay. *In Proceedings of the International Conference on Geotechnical Engineering of Hard Soils and Soft Rocks, Athens, Greece, 20-23 September 1993*, A. Anagnostopoulos et al. (eds.), Balkema, Rotterdam, Netherlands, pp. 395-402.
- Baghini, A.T. 1998. Absolute permeability of McMurray formation oil sands at low confining stresses. Ph.D. Dissertation, Department of Civil Engineering, University of Alberta, Edmonton, Alberta.
- Barnes, D.J., Dausseault, M.B. 1982. The influence of diagenetic fabric on oil sands behaviour. *Canadian Journal of Earth Sciences*, **19**: 804-818.
- Barton, M. E. 1993. Cohesive sands: the natural transition from sands to sandstones. *In Proceedings of the 1st international symposium on*

- geotechnical engineering of hard soils-soft rocks, Athens, Greece, 20-23 September 1993, A. Anagnostopoulos et al. (eds.), Balkema, Rotterdam, Netherlands , Vol.1, pp. 367-374.
- Barton, M.E., Palmer, S.N., Wong, Y.L. 1986. A geotechnical investigation of 3 Hampshire tertiary sea beds- Are they locked sands. Quarterly Journal of Engineering Geology, **19**(4): 399-412.
- Barton, N. 1973. Review of a new shear strength criterion for rock joints. Engineering geology, **7**: 287-332.
- Bésuelle, P. 2001. Compacting and dilating shear bands in porous rock: Theoretical and experimental conditions. Journal of Geophysical Research, **106**(B7): 13435-13442.
- Bésuelle, P., Desrues, J., Raynaud, S. 2000. Experimental characterization of the localization phenomenon inside a Vosges sandstone in a triaxial cell. International Journal of Rock Mechanics & Mining Sciences, **37**: 1223-1237.
- Bhandari, A.R., Inoue, J. 2005. Experimental study on strain rates effects on strain localization characteristics of soft rocks. Soils and Foundations, **45**(1):125-140.
- Bieniawski, Z.T. 1967a. Mechanism of brittle rock fracture: Part III- fracture in tension and under long-term loading. International Journal of Rock Mechanics and Mining Sciences & Geomechanical Abstracts, **4**(4): 425-430.
- Bieniawski, Z.T. 1967b. Mechanism of brittle rock fracture: Part II- experimental studies. International Journal of Rock Mechanics and Mining Sciences & Geomechanical Abstracts, **4**(4): 407-423.

- Bishop, A. W. 1967. Progressive failure with special reference to the mechanism causing it. *In Proceedings of the Geotechnical Conference, Oslo, Norway, Norwegian Geotechnical Institute publication, Oslo, Vol. 2, pp. 142-150.*
- Bishop, A.W. 1971. Stress-Strain behaviour of soils. *In the Proceedings of the Roscoe Memorial Symposium, Cambridge University, UK, 29-31 March 1971, R.H.G. Parry (ed.), Henley-on-Thames, pp. 3-58.*
- Bishop, A.W., Green, G.E. 1965. The influence of end restraint on the compressive strength of a cohesionless soil. *Geotechnique*, **15**(3): 243-266.
- Bjerrum, L. 1967. The Third Terzaghi lecture: progressive failure in slopes of overconsolidated plastic clay and clay shales. *Journal of Soil Mechanics and Foundations Division*, **93**(5): 1-50.
- Bolton, M. D. (1986). The strength and dilatancy of sands. *Geotechnique*, **36**(1): 65–78.
- Borja, R.I., Aydin, A. 2004. Computational modeling of deformation bands in granular media. I. Geological and mathematical framework. *Computer Methods in Applied mechanics and Engineering*, **193**:2667-2698.
- Bowman, E.T., Soga, K. Creep, ageing and microstructural change in dense granular materials. *Soils and Foundations*, **43**(4): 107-117.
- Brace, W.F. 1964. Brittle fracture of rocks. *In Proceedings of the International Conference on State of Stress in the Earth's Crust, Santa Monica, 13-14 June 1963, California, W.R. Judd (ed.). American Elsevier Publishing Company, New York, pp. 110.178.*

- Brace, W.F., Paulding, B.W., Jr., and Scholz, C. 1966. Dilatancy in the fracture of crystalline rocks. *Journal of Geophysical Research*, **71**(16): 3939-3953.
- Brady, B., Brown, E. T. 1985: *Rock mechanics for underground mining*. 3rd Edition, Kulwer Academic Publishers, Boston.
- Burland, J. B., Rampello, S., S., Georgiannou, V. N., Calabresi, G. 1996. A laboratory study of the shear strength of four stiff clays. *Geotechnique*, **46**(3): 491-514.
- Burland, J.B., Longworth, T.I. Moore, J.F.A. 1977. A study of ground movement and progressive failure caused by a deep excavation in Oxford clay. *Geotechnique*, **27**:557-591.
- Callisto, L., Rampello S. 2002. Shear strength and small-strain stiffness of a natural clay under general stress conditions. *Geotechnique*, **52**(8): 547-560.
- Carrigy, M.A. 1967. The physical and chemical nature of typical tar sand: bulk properties and behavior. *In the Proceedings of the 7th World Petroleum Congress, Mexico, 2-8 April 1967, Vol. 3, pp. 573-581.*
- Carrigy, M.A., Mellon, G.B. 1964. Authigenic clay mineral cements in Cretaceous and Tertiary sandstones of Alberta. *Journal of Sedimentary Petrology*, **34**(3): 461-472.
- Carrigy, M.A.. 1959. Geology of the McMurray Formation. *In General geology of the McMurray area, Part III, Alberta Research Council, Memoir 1, 130 pp.*
- Carrigy, M.A.. 1973a. Mesozoic geology of the Fort McMurray area. *In Guide to the Athabasca Oil Sands Area. M.A. Carrigy and J.W. Kramers (eds.), Alberta Research Council Information series, Vol. 65, pp. 77-101.*

- Cecconi, M., Viggiani, G.M.B. 2001. Structural features and mechanical behaviour of a pyroclastic weak rock. *International Journal of Numerical and Analytical Methods in Geomechanics*. **25**:1525-1557.
- Chandler, R.J. 1984. Recent European experience on landslides in overconsolidated clays and soft rocks. In *Proc 4th Int. Symposium on Landslides*, Toronto, No. 1, pp. 61-81.
- Chang, S.-H., Lee, C.-I. 2004. Estimation of cracking and damage mechanisms in rock under triaxial compression by moment tensor analysis of acoustic emission, *International Journal of Rock Mechanics & Mining Sciences*, **41**:1069–1086
- Chau, K.T., 1993. Antisymmetric bifurcations in a compressible pressure-sensitive circular cylinder under axisymmetric tension and compression. *Journal of Applied Mechanics*, **60**: 282-289.
- Conlon, R.J. 1966. Landslide on the Toulousouc River, Quebec. *Canadian Geotechnical Journal*, **3**(3): 113-144.
- Coop, M. R., and Atkinson, J. H. 1993. The mechanics of cemented carbonate sands. *Geotechnique*, **43**(1): 53–67.
- Cooper, M.R., Bromhead, E.N., Petley, D.J, and Grants, D.I. 1998. The Selborne cutting stability experiment. *Geotechnique*, **48**(1): 83-101.
- Cotecchia, F., Chandler, R.J. 1997. The influence of structure on the pre-failure behavior of a natural clay. *Geotechnique*, **47**(3): 523-544.
- Cotecchia, F., Chandler, R.J. 2004. A general framework for the mechanical behavior of clays. *Geotechnique*, **50**(4): 431-447.

- Crawford, C.B.. 1963. Cohesion in undisturbed sensitive clay, *Geotechnique*, **13**: 132-146.
- Cresswell, A., Powrie, W. 2004. Triaxial tests on an unbonded locked sand, *Geotechnique*, **54**(2): 107-115.
- Cresswell, A.W. 2001. Block sampling and test sample preparation of locked sands. *Geotechnique*, **51**(6): 567-570.
- Cresswell, A.W., Barton ,M.E. 2003. Direct shear tests on an uncemented, and a very slightly cemented, locked sand. *Quarterly Journal of Engineering Geology*, **36**: 119-132.
- Cristescu, N., Hunsche, U. 1998. Time effects in rock mechanics_Series: Materials, Modelling and Computation, Wiley, Chichester, UK, 342 pp.
- Cuccovillo, T., and Coop, M. R. 1999. On the mechanics of structured sands. *Geotechnique*, **49**(6): 741–760.
- Curry, J. R. 1956. The analysis of two-dimensional orientation data. *Journal of Geology*, **64**:117-131.
- Dawson, E.M., Roth, W.H., Drescher, A. 1999. Slope stability analysis by strength reduction. *Géotechnique*, **49**(6): 835–840.
- De Mello, V.F.B. 1988. Risk in Geotechnical Engineering: Conceptual and Practical Suggestions. *Geotechnical Engineering*, **19**:171-207.
- Desrues, J., Chambon, R. 2002. Shear band analysis and shear moduli calibration. *International Journal of Solids and Structures*, **39**:3735-3776.

- Desrues, J., Chambon, R., Mokni, M., Mazerolle, F. 1996. Void ratio evolution inside shear bands in triaxial sand specimens studied by computed tomography. *Geotechnique*, **46**(3): 529-546.
- Desrues, J., Lanier, J., Stutz, P. 1985. Localization of the deformation in tests on sand sample. *Engineering Fracture Mechanics*, **21**(4): 909-921.
- Diederichs M.S., Kaiser, P.K., Eberhardt, E. 2004. Damage initiation and propagation in hard rock during tunneling and the influence of near-face stress rotation. *International Journal of Rock Mechanics & Mining Sciences*, **41**:785-812
- Dittes, M., Labuz ,J.F. 2002. Field and laboratory testing of St. Peter sandstone. *Journal of Geotechnical and Geoenvironmental Engineering*, **128**(5): 372-380.
- Du Bernard, X., Eichhubl, P., Aydin, A. 2002. Dilation bands: A new form of localized failure in granular media. *Geophysical Research Letters*, **29**(24):2176-2179.
- Duncan, J.M. 1996. Limit Equilibrium and Finite Element analysis of slopes: state of the art. *Journal of Geotechnical and Geoenvironmental Engineering*, **122**(7):577-596.
- Dusseault, L., Morgenstern, N.R. 1978. Shear strength of Athabasca soil sands, *Canadian Geotechnical Journal*, **15**:.216-238.
- Dusseault, M.B. 1977. The geotechnical characteristics of the Athabasca oil sands, Ph.D. dissertation, Department of Civil Engineering, University of Alberta, Edmonton, Canada.

- Dusseault, M.B., Morgenstern, N.R. 1979. Locked sands. *The Quarterly Journal of Engineering Geology*, **12**(2): 117-131.
- Eberhardt, E., Stead, D., Stimpson, B., Read, R.S. 1998. Identifying crack initiation and propagation thresholds in brittle rock. *Canadian Geotechnical Journal*, **35**: 222-233.
- ERCB 1990. Crude bitumen reserves atlas, Energy Resources conservation Board, Calgary, 76pp.
- Feda, J. 1995. Behavior of a cemented clay. *Canadian Geotechnical Journal*, **32**(5): 899-904.
- Feda, J. 2004. Physical models of soil behaviour. *Engineering Geology*, **72**: 121-129.
- Finno, R.J., Rechenmacher, A.L. 2003. Effects of consolidation history on critical state of sand. *Journal of Geotechnical and Environmental Engineering*, **129**(4): 350–360.
- FLAC-Fast Lagrangian Analysis of Continua, version 4.0. 2000. ITASCA Consulting Group, Inc., Minneapolis, USA.
- Flach, P.D., Mossop, G.D. 1985. Depositional environments of Lowe Cretaceous McMurray Formation, Athabasca oil sands, Alberta. *American Association of Petroleum Geologists Bulletin* 69, No. 8, pp. 1195-1207.
- Fredlund, D.G., and Krahn, J. 1977. Comparison of slope stability methods of analysis. *Canadian Geotechnical Journal*, **14**:429-439.
- Friedman, G.M., Sanders, J.E. 1978. *Principles of Sedimentology*. John Wiley & Sons, New York.

- Frost, J.D., Lang, D.J. 2000. Evolution of sand microstructure during shearing. *Journal of Geotechnical and Geoenvironmental Engineering*, 126(2): pp.116-130.
- Frost, J.D., Yang, C.H. 2003. Effect of end platens on microstructure evolution in dilatant specimens. *Soils and Foundations*, **43**(4): 1-11.
- Fujii, Y., Kiyama, T., Ishijima, Y., Kodama, J. 1998. Examination of a rock failure criterion based on circumferential tensile strain. *Pure Applied Physics*, **152**: 551-577.
- Gibson, R.E. 1953. Experimental determination of the true friction-cohesion in clays. *In the Proceedings of the 3rd International conference on soil Mechanics and Foundation Engineering, Montreal, Vol. 1, pp. 126-130.*
- Gingras, M., Rokosh, D. 2004. A brief overview of the geology of heavy oil bitumen and oil sand deposits. *In 2004 CSEG National Convention, 10-14 May 2004, Calgary, Alberta, Canada. Available online at www.cseg.ca/conventions/2004/sessions/ws-exploration-heavy-oil.html* [Accessed on July 3, 2006].
- Goddard, J.D., Bashir, Y.M. 1990. On Reynolds dilatancy. *In Recent Development in Structured Continua, Longman, New York, Vol. 2, pp. 23-35.*
- Griffith, D.V. and Lane, P.A. 1999. Slope stability analysis by finite elements. *Geotechnique*, **49**(3): 387-403.
- Hajiabdolmajid, V. 2001. Mobilization of Strength in Brittle Failure of Rock, Ph.D. Thesis, Department of Mining Engineering, Queen's University, Kingston, Canada.

- Hawkes, I., Mellor, M. (1970): Uniaxial testing in rock mechanics laboratories. *Engineering Geology*, **4**:177–285.
- Hayano, K., Matsumoto, M., Tatsouka, F., Koseki, J. 2001. Evaluation of time-dependent deformation properties of sedimentary soft rock and their constitutive modeling, *Soils and Foundations*, **41**(2): 21-38.
- Hayano, K., Matsumoto, M., Tatsouka, F., Koseki, J. 2001. Evaluation of time-dependent deformation properties of sedimentary soft rock and their constitutive modeling. *Soils and Foundations*, **41**(2): 21-38.
- Heald, M.T., Larese, R.E. 1974. Influence of coatings on quartz cementation. *Journal of Sedimentary Petrology*, **46**(4): 881-896.
- Hein, F.J., Cotterill, D.K., Berhane, H. 2000. An atlas of lithofacies of the McMurray Formation, Athabasca oil sands deposit, Northeast Alberta: Surface and Subsurface. Alberta Geological Survey Earth Sciences Report 2000-07, 225 pp.
- Hunsche, U., Albrecht, H. 1990. Results of true strength tests on rock salt. *Engineering Fracture Mechanics*, **35**(4-5): 867-977.
- Hunsche, U., Hampel, A., 1999. Rock salt – The mechanical properties of the host rock material for a radioactive waste repository. *Engineering Geology*, **52**:271-291.
- Hvorslev, M.J. 1960. Physical components of the shear strength of saturated clays. *In* Research conference on Shear Strength of Cohesive soils, University of Colorado, Boulder, June 1960. American Society of Civil Engineers, New York, pp. 169-273.

- Ibrahim, E., Di Benedetto, H. 2005. New local system of measurement of axial strains for triaxial apparatus using LVDT. *Geotechnical Testing Journal*, **28**(5): 1-9.
- ISRM. 1978b. Suggested methods for the quantitative descriptions of discontinuities in rock masses. *International Journal of Rock Mechanics & Mining Sciences*, **15**:319-368.
- Issen, K.A., Rudnicki, J.W. 2000. Conditions for compaction bands in porous rock. *Journal of Geophysical Research*, **105**(B9): 21529-21536.
- Jiang, J.C., Baker, R., Yamagami, T. 2003. The effect of strength envelope nonlinearity on slope stability computation. *Canadian Geotechnical Journal*, **40**: 308-325.
- Korinets, A., Alehossein, H. 2002. On the initial non-linearity of compressive stress-strain curves for intact rock. *Rock Mechanics and Rock Engineering*, **35**(4): 319-328.
- Krahn, J. 2003. The 2001 R.M. Hardy Lecture: The limits of limit equilibrium analyses. *Canadian Geotechnical Journal*, **40**: 643-660.
- Kuwano, R., Jardine, R.J. 2002. On measuring creep behaviour in granular materials through triaxial testing. *Canadian Geotechnical Journal*, **39**:1061-1074.
- Labuz, J.F., Dai, S.T. 2000. Residual strength and fracture energy from plain-strain testing. *Journal of Geotechnical and Geoenvironmental Engineering*, **126**(10): 882-889.

- Ladanyi, B. & Archambault, G. 1970. Simulation of shear behavior of a jointed rock mass. *In* Rock Mechanics, theory and practice, Proceedings of 11th international Symposium on Rock Mechanics, Berkeley, 1969, California, USA, Society of Mining Engineers and American Society of Mining, Metallurgy and Petroleum Engineers, New York, USA, Chapter 7, pp. 105-125.
- Lade, P.V. 1982. Localization effects in triaxial tests on sand. *In* the Proceedings of Symposium on Deformation and Failure of Granular Materials, Delft, Netherland, 31 August - 3 September 1982, P.A. Vermeer and H.J. Luger (eds.), Balkema, Rotterdam, pp. 461-471.
- Lade, P.V., Liu, Chi-Tseng. 1998. Experimental study of drained creep behavior of sand. *Journal of Engineering Mechanics*, **124**(8):912-920.
- Lagioia, R., Nova, R., 1995. An experimental and theoretical study of the behavior of a calcarenite in triaxial compression. *Geotechnique*, **45**(4): 633-648.
- Lajtai, E.Z. 1969. Strength of discontinuous rocks in direct shear. *Geotechnique*, **19**: 218-233.
- Lajtai, E.Z. 1974. Shear strength of weakness planes in rocks, *International Journal of Rock Mechanics and Mining Sciences*, **6**: 499-515.
- Lajtai, E.Z., and Lajtai, V.N. 1974. The evolution of brittle fracture in rocks. *Journal of the Geological Society*, **130**(1): 1.18.
- Lajtai, E.Z., Carter, B.J., Ayari, M.L.1990. Criteria for brittle fracture in compression. *Engineering Fracture Mechanics*, **37**(1): pp.25–49.

- Lajtai, E.Z. 1998. Microscopic processes in a granite. *Rock Mechanics and Rock Engineering*, **31**(4): 237–250.
- Lambe, W. 1960. A mechanistic picture of shear strength in clay. *In* Research conference on Shear Strength of Cohesive soils, University of Colorado, Boulder, June 1960. American Society of Civil Engineers, New York, pp. 555-580.
- Lau, J.S.O, Chandler, N.A. 2004. Innovative laboratory testing. *International Journal of Rock mechanics & Mining Sciences*. **41**: 1427-1445.
- Lee, K.L. 1978. End restraint effects on undrained static triaxial strength of sand. *Journal of Geotechnical Engineering*, **104**(GT6): 687-704.
- Lefebvre, G., LA Rochelle, P. 1974. The analysis of toe slope failures in cemented Champlain clays. *Canadian Geotechnical Journal*, **11**: 69-77.
- Lefebvre , G. 1981. Fourth Canadian Geotechnical Colloquium: strength and slope stability in Canadian soft clay deposits. *Canadian Geotechnical Journal*, **18**(3):420-442.
- Leong, E.C., Agus, S.S., Rahardjo, H. 2004. Volume change measurement of soil specimen in triaxial test. *Geotechnical Testing Journal*, **27**(1), paper ID GTJ10704_271.
- Leroueil, S. 1997. Critical state soil mechanics and the behaviour of real soils. In *Symposium on Recent developments in Soil and Pavement Mechanics*. Rio de Janeiro, Brazil. pp. 41-80.
- Leroueil, S., and Vaughan, P. R. 1990. The general and congruent effects of structure in natural soils and weak rocks. *Geotechnique*, **40**(3): 467–488.

- Lin, Q.X., Tham , L.G., Yeung, M.R., Lee, P.K.K. 2004. Failure of granite under constant loading. *In* Proceeding of ISRM SINOROCK 2004 Symposium, May 2004, China, International Journal of Rock Mechanics & Mining Sciences, **41**(1): 49-54.
- Lo, S.R., Lade, P.V., Wardani, S.P.R. 2003. An Experimental study of the mechanics of two weakly cemented soils. *Geotechnical Testing Journal*, **26**(3) 1-14.
- Lo, S.R., Wardani, S.P.R. 2002. Strength and dilatancy of a silt stabilized by cement and fly ash mixture *Canadian Geotechnical Journal*, **39**:77-89.
- Lo, Y.K. 1972. An approach to the problem of progressive failure. *Canadian Geotechnical Journal*, **9**:407-429.
- Lockner, D.A., Byerlee, J.D., Kuksenko, V., Ponomarev, A., Sidorin, A. 1992. Observation of quasi-static fault growth from acoustic emissions. *In*: Fault Mechanics and Transport Properties of Rocks, Academic Press Ltd, San Diego, USA, Chapter 1, pp. 3-31.
- Lockner, D.A., Moore, D.E., Reches, Z. 1990. Microcrack interaction leading to shear fracture. *In* Proceeding of the 33rd USA Symposium on Rock Mechanics, Tillerson and Wawersik (eds.), Balkema, Rotterdam, pp. 807-816.
- Malandraki, V., Toll, D. 2000. Drained probing triaxial tests on a weakly bonded artificial soil. *Geotechnique*, **50**(2): 141-151.
- Maranini, E., Brignoli, M. 1999. Creep behaviour of a weak rock: experimental characterization. *International Journal of Rock Mechanics and Mining Sciences*, **36**: 127-138.

- Martin, C.D. 1997. Seventeenth Canadian Geotechnical Colloquium: the effect of cohesion loss and stress path on brittle rock strength. *Canadian Geotechnical Journal*, **34**(5): 698–725.
- Martin, C.D., Chandler, N.A. 1994. The Progressive fracture of Lac Du Bonnet granite. *International Journal of Rock Mechanics and Mining Sciences & Geomechanical Abstracts*, **31**(6): 643-659.
- McKay, J.G. 1989. Undisturbed oil sand sampling and sample quality evaluation. M.Sc. dissertation, Department of Civil Engineering, University of Alberta, Edmonton, Alberta, Canada.
- Menci, W. 1965. Proportions of cohesion and of internal friction in strength of rocks. In *Contribution of Shear Strength Parameters to the Geomaterials's Shear Strength*, Oslo , Norwegian Geotechnical Institute, Vol. 16, pp. 17-19.
- Menendez ,B., Zhu, W., Wong, T.F. 1996. Micromechanics of brittle faulting and cataclastic flow in Berea sandstone. *Journal of structural Geology*, **18**(1): 1-16.
- Mesri, G., Abdel-Ghafar, M.E.M. 1993. Cohesion intercept in effective stress stability analysis. *Journal of Geotechnical Engineering*, **119**(8): 1229-1249.
- Mesri, G., Feng, T.W., Benak, J.M. 1990. Postdensification penetration resistance of clean sands. *Journal of Geotechnical Engineering*, **116**(7): 1097-1115.
- Mitchell , J.K. 1993. *Fundamentals of soil behaviour*. John Wiley & Sons, New York.

- Mitchell, R.J. 1970. On the yielding of Leda clay. *Canadian Geotechnical Journal*, **34**: 297-312.
- Mitchell, R.J. 1975. Strength parameters for permanent slopes in Champlain sea clays. *Canadian geotechnical Journal*, **12**(4): 447-455.
- Mitchell, J.K. 1986. Practical problems from surprising soil behaviour. *Journal of Geotechnical Engineering*, **110**(11): 1559-1576.
- Morgenstern, N.R., Sangrey, D.A. 1978. Methods of stability analysis. Chapter 7, In *Landslides — Analysis and control*, National Academy of Sciences, Washington D.C., Special Report 176.
- Mroz, Z., Rodzik, P. 1995. On the control of deformation process by plastic strain, *International Journal of Plasticity*, **11**(7):827-842.
- Muhunthan, B., Pillai, V.S.,Olcott, D. 2004. Measurement of Energy and Strength of Sand at critical state. *Geotechnical testing Journal*, **27**(2): 1-7.
- Murayama, S., Michihro, K., Sakagami, T. 1984. Creep characteristics of sands. *Soils and Foundations*, **24**(2): 1-15.
- Muir Wood, D. 2002. Some observations of volumetric instabilities in soils. *International Journal of Solids and Structures*, **39**:3429-3449.
- Novello, E.A., Johnston, I.W. 1995. Geotechnical materials and the critical state. *Geotechnique*, **45**(2): 223-235.
- Oda, A., Vardoulakis, I., Kajewski, R. 1991. Shear band formation in Gasford sandstone. *International Journal of Rock mechanics and Mining Sciences& Geomechanics Abstracts*, **28**(5): 397-411.

- Oda, M. 1972a. Initial fabrics and their relations to mechanical properties of granular material. *Soils and Foundations*, **12**(1):17-36.
- Oda, M. 1972b. The mechanism of fabric change during compressional deformation of sand. *Soils and Foundations*, **(12)** 2:1-18.
- Oda, M., Konishi, J. 1974. Microscopic deformation mechanism of granular material in simple shear. *Soils and Foundations*, **(14)** 4:25-38.
- Oda, M., Takemura, T., Takahashi, M. 2004. Technical Note: Microstructure in shear band observed by microfocus X-ray computed tomography. *Geotechnique*, **54**(8):539–542.
- Oda, M., Kazama, H. 1998. Microstructure of shear band and its relation to the mechanism of dilatancy and failure of dense granular soils. *Geotechnique*, **48**(4): 465-481.
- Oka, F., Adachi, T., Yahima, A. 1998. A constitutive model for soft rock with both strain softening and negative dilatancy. In the proceedings of the Second International Symposium on Hard Soils and Soft Rocks, Naples, Italy, 12-14 October 1998, A. Evangelista and L. Picarelli (eds.), Brookfield, Balkema, Rotterdam, Vol.2, pp. 737-744.
- Olalla, C., Cuellar, V. 2001. Failure mechanism of Aznacollar tailing dam, Seville, Spain. *Geotechnique*, **51**(5): 399-406.
- Pelli, F., Kaiser, P.K, Morgenstern NR. 1991. An interpretation of ground movements recorded during construction of the Donkin–Morien tunnel, *Canadian Geotechnical Journal*, **28**(2): 239–54.

- Pemberton, S.G, Falch, P.D., Mossopta, G.D. 1982. The Athabasca oil sands, Alberta, Canada. *Science*, **217**: 825-827.
- Perrin, G., Leblond, J.B. 1993. Rudnicki and Rice's analysis of strain localization revisited. *Journal of Applied Mechanics*, **60**(4): 842-846.
- Pettijohn, F.J., Potter, P.E., Siever, R. 1972. *Sand and Sandstone*. Springer, New York.
- Pittman, E. D. 1972. Diagenesis of quartz in sandstones as revealed by scanning electron microscopy *Journal of Sedimentary Petrology*, **42**(3): 507–519.
- Potts, D.M., Kovacevic, N., Vaughan, P.R. 1997. Delayed collapse of cut slopes in stiff clay. *Geotechnique*, **47**(5):953-982.
- Protulipac, D.G. 1991. Comparing strength characteristics of St. Petersburg sandstone and oil saturated McMurray sand. M.Sc. Thesis, University of Waterloo, Canada.
- Raju, V.S., Sadasivan, S.K. and Venkataraman, M. 1972. Use of lubricated and conventional end platens in triaxial tests on sands. *Soils and Foundations*, **12**(4): 35-43.
- Rampello, S. Viggiani, G., Calabresi, G. 1994. Some remarks on the strength and dilatancy of a stiff and overconsolidated clay. In *Proc. XIII ICSMFE*, New Delhi, India, pp.93-96.
- Ranger, M.J., Pemberton, S.G. 1992. The sedimentology and ichnology of estuarine point bars in the McMurray Formation of the Athabasca oil sands deposit, northeastern Alberta, Canada. In *17th Workshop on Application of Ichnology to Petroleum Exploration*, Calgary, Alberta, Canada, 12 June 1992,

- S.G. Pemberton (ed.), Society of Economic Paleontologists and Mineralogists, pp. 401-421.
- Rechenmacher, A.L..2006. Grain-scale processes governing shear band initiation and evolution in sands. *Journal of the Mechanics and Physics of Solids*, **54**: 22-45.
- Renshaw, C.E., Schulson, E.M. 2001. Universal behavior in compressive failure of brittle materials. *Nature*, **412**: 897-900.
- Reynolds, O. 1885. On the dilatancy of rigid particles in contact: with experimental illustration. *Philosophy Magazine*, **20**:469-482.
- Richards, N.P., Barton, M.E. 1999. The Folkstone bed sands: microfabric and strength. *Quarterly Journal of Engineering Geology*, **32**:21-44.
- Roscoe, K.H., 1970. The influence of strains in soil mechanics. *Geotechnique*, **20**: 129-170.
- Rowe, P.W. 1962. Stress–dilatancy relation for static equilibrium of an assembly of particles in contacts. In the *Proceedings of Royal Society of London Series - A Mathematical and Physical Sciences*, vol. 269, pp. 500–527.
- Rowe, P.W. 1969. The relation between shear strength of sands in triaxial compression, plane strain and direct shear. *Geotechnique*, **19**(1): 75–86.
- Rowe, P.W. and Barden, L. 1964. Importance of free ends in triaxial testing. *Journal of Soil Mechanics and Foundations Division*, **90**(SM1) 1-27.
- Rowe,P.W., Oates,D.B., Skermer, N.A. 1963. The stress dilatancy performance of two clays. *In Symposium On Laboratory Shear testing of Soils*, ASTM

- Special Technical Publication, Ottawa, Ontario, ASTM, Philadelphia, Vol. 361. pp.134-143.
- Rudnicki, J.W., Rice, J.R. 1975. Conditions for the localization and deformation in pressure-sensitive dilatant materials. *Journal of Mechanics and Physics of solids*, **23** (6):371-394.
- Rusch, H. 1959. Physical problems in the testing of concrete. *Zement-Kalk-Gips* (Cement and Concrete Association Library Translation), 1960, No. 86, pp.1-9.
- Rusch, H. 1960. Research towards a general flexural theory for structural concrete. *In Proc. Am. Concrete Inst.*, No. 57, pp.1-28.
- Saada, A.S., Liang, L., Figueroa, J.L., Cope, C.T. 1999. Bifurcation and shear band propagation in sands. *Geotechnique*, **49**(3): 367-385.
- Samieh, A.M., Wong, R.C.K. 1997. Deformation of Athabasca oil sand at low effective stresses under varying boundary conditions. *Canadian Geotechnical Journal*, **34**: 985-990.
- Sammis, C.G., Ashby, M.F. 1986. The failure of brittle porous solids under compressive stress state. *Acta Metall.*, **34**: 511-526.
- Sangha, C.M., Talbot, C.J., Dhir, R.K. 1974. Microfracturing of a sandstone in uniaxial compression. *International Journal of Rock Mechanics and Mining Sciences & Geomechanical Abstracts*, **11**: 107-113.
- Sangrey, D.A. 1972. Naturally cemented sensitive soils. *Geotechnique*, **22**(1):139-152.

- Santarelli, E.J., Brown, E.T. 1989. Failure of three sedimentary rocks in triaxial and hollow cylinder compression tests. *International Journal of Rock Mechanics and Mining Sciences & Geomechanical Abstracts*, **26**(5): 401-413.
- Sarma, S. K. & Bhave, M. V. 1974. Critical acceleration versus static factor of safety in stability analysis of earth dams and embankments. *Geotechnique*, **24**(4): 661–665.
- Schmertmann, J.H., Osterberg, J.O. 1960. An experimental study of the development of cohesion and friction with axial strain in saturated cohesive soils. *In* Research conference on Shear Strength of Cohesive soils, University of Colorado, Boulder, June 1960. American Society of Civil Engineers, New York, pp. 643-694.
- Schmertmann, J.H. 1963. Generalization and measuring the Hvorslev effective components of shear resistance. *In* Symposium On Laboratory Shear testing of Soils, ASTM Special Technical Publication, Ottawa, Ontario, ASTM, Philadelphia, pp.147-157.
- Schmertmann, J.H., 1991. The mechanical ageing of soils. *Journal of Geotechnical Engineering*, **117**(9): 1288-1330.
- Schmidtke, R.H., Lajtai, E. 1985. The long term strength of Lac du Bonnet granite, *Engineering Geology*, **22**: 461-465.
- Schofield, A. 1998. Don't use the C word. *Ground Engineering*, August 1998, pp. 29-32.
- Schofield, A.N. 2006. Interlocking, and peak and design strengths. *Geotechnique*, **56**(5): 357-358.

- Schofield, A.N., Wroth, C. P.1968. Critical state soil mechanics. McGraw-Hill, London, New York.
- Scholey, G.K., Frost, D.F., Lo Presti, C.F., Jamiolkowski, M. 1995. A review of instrumentation for measuring small strains during triaxial testing of soil specimens. *Geotechnical Testing Journal*, **18**(2): 137-156.
- Schubnel, A., Nishizawa, O., Masuda, K., Lei, X.J., Gurguen, Y. 2003. Velocity measurements and crack density determination during wet triaxial experiments on Oshima and Toki granites, *Pure and Applied Geophysics*, **160**: 869-887.
- Schulson, E.M., Iliescu, D. 1999. On the initiation of shear faults during brittle compressive failure: A new mechanism. *Journal of Geophysical Research*, **104**(B1): 697-705.
- Schultz, R.A., Siddharthan, R. 2005. A general framework for the occurrence and faulting of deformation bands in porous granular rocks. *Tectonophysics*, **411**: 1-18.
- Schulze, O., Popp, T., Kern,H. 2001. Development of damage and permeability in deforming rock salt, *Engineering Geology*, **61**: 163-180.
- Sheng, D., Westerberg, D., Mattsson, H., Axelsson, K. . 1997. Effects of end restraint and strain rate in triaxial tests. *Computers and Geotechnics*, **21**(3): 163-182.
- Shibuya, A.S., Park,C.- S., Tatsouka, F., ABE, F., Teachavorasinskun, S., Kohata, Y. 1994. The significance of local lateral-strian measurement of soil specimens for a wide range of strain. *Soils and Foundations*, **34**(2): 95-105.

- Sibley, D.F., Blatt, H. 1976. Intergranular pressure solution and cementation of the Tuscarora orthoquartzite. *Journal of Sedimentary Petrology*, **46**(4): 881-896.
- Siever, R. 1959. Petrology and geochemistry of silica cementation in some Pennsylvania sandstones. *Silica in Sediments*. Society of Econ. Paleontologists and Mineralogists Special Publications, Tulsa, No. 7, pp.56-79.
- Sippel, R.F 1968. Sandstone petrology, evidence from luminescence petrology. *Journal of Sedimentary Petrology*, **38**(2): 530-554.
- Skempton, A.W. 1964. Long term stability of clay slopes. *Geotechnique*, **14**(2):77-101.
- Skempton, A.W. 1970. First time slides in overconsolidated clays. *Geotechnique*, **20**:320-324.
- SLOPE/W version 6.1 .2004. Geo-Slope International Ltd., Calgary, Alberta, Canada.
- Su, H., Chen, J.F., GE, X.R. 2004. Deformation characteristics of silty clay subjected to triaxial loading, by computerized tomography, *Geotechnique*, **54**(5): 307–314.
- Sulem, J., Ouffroukh, H. 2006. Shear banding in drained and undrained triaxial tests on a saturated sandstone: porosity and permeability evolution. *International Journal of Rock Mechanics & Mining Sciences*, **43**:292-310.

- Sulem, J., Vardoulakis, I., Papamichos, E., Oulaha, A., Tronvoll, J. 1999. Elasto-Plastic modeling of Red Wildmoor sandstone. *Mechanics of Cohesive-Frictional Materials*, **4**: 215-245.
- Takemura, T., Oda, M. 2005. Changes in crack density and wave velocity in association with crack growth in triaxial tests of Indiana granite. *Journal of Geophysical Research*, **10**(B05401): 1-14.
- Taylor, D. W. 1948. *Fundamentals of soil mechanics*. John Wiley, New York.
- Taylor, G.M. 1950. Pore-space reduction in sandstones. *AAPG Bulletin*, No. **34**, pp. 701-716.
- Tavenas, F., Trak, B., Leroueil, S. 1980. Remarks on the validity of stability analyses. *Canadian Geotechnical Journal*, **17**:61-73.
- Thurairajah, A. 1961. Some properties of kaolin and of sand. PhD thesis, Cambridge University, Cambridge, London.
- Trollope, D.H. 1967. Discussion on shear strength of stiff clay. In *Proc. of the Geotechnical Conference on Shear Strength Properties of Natural Soils and Rocks*, Oslo , Norwegian Geotechnical institute, Oslo, Vol. 2, pp. 178-180.
- Ueng,T-S., Cheng, T-J. 2000. Energy aspects of particle breakage in drained shear of sands. *Geotechnique*, **50**(1): 65-72.
- Vallejo, L.E. 1987. The influence of fissures in a stiff clay subjected to direct shear. *Geotechnique*, **37**(1): 69-82.
- Vallejo, L.E. 1989. Fissure parameters on stiff clays under compression. *Journal of Geotechnical and Geoenvironmental Engineering*, **115**(9): 1303-1317.

- Vardoulakis, I., Sulem, J. 1995. Bifurcation analysis in geomechanics. Blackie Academic and Professional, Glasgow.
- Vermeer, P. A. & de Borst, R. 1984. Non-associated plasticity for soils, concrete and rock. *Heron*, **29** (3):3-64.
- Wan, R.G., Guo, P.J. 2004. Stress dilatancy and fabric dependencies on sand behavior. *Journal of Engineering Mechanics*, **130**(6):635-645.
- Watterson, J. 1999. The future of failure: stress or strain?. *Journal of Structural Geology*, **21**: 939-948.
- Wawersik, W.R., and Fairhurst, C. 1970. A study of brittle rock fracture in laboratory compression experiments. *International Journal of Rock Mechanics and Mining Sciences & Geomechanical Abstracts*, **7**(5): 561-575.
- Wightman, D., Rottenfusser, B., Kramers, J. and Harrison, R. 1989. Geology of the Alberta oil sands deposits, AOSTRA technical handbook on oil sands, bitumens and heavy oils. L.G. Hepler and Ch. Hsi (eds.), AOSTRA Technical Publication Series , No.6, pp. 1-9.
- Wightman, D.M., Pemberton, S.G. 1997. The Lower Cretaceous (Aptian) McMurray Formation; an overview of the Fort McMurray area, northeastern Alberta. In *Petroleum Geology of the Cretaceous Mannville Group, Western Canada*. Pemberton and D.P. James (eds.), Canadian Society of Petroleum Geologists, Memoir 18, pp. 312-344.
- Wilson, M.D., Pittman, E.D. 1977. Authigenic clays in sandstones: recognition and influence on reservoir properties and paleoenvironmental analysis. *Journal of Sedimentary Petrology*, **47**(1): 3-31.

- Wong, R.C.K. 1999. Mobilized strength components of Athabasca oil sand in triaxial compression. *Canadian Geotechnical Journal*, **36**: 718-735.
- Wright, S.G, Kulhawy, F.H., Duncan, J.M. 1973. Accuracy of equilibrium slope stability analysis. *Journal of Geotechnical Engineering*, **SM10**:783-791.
- Yimsiri, S., Soga, K. 2002. Technical note: A review of local strain measurement systems for triaxial testing of soils. *Journal of the Southeast Asian Geotechnical Society*, **33**(1): 41-52.
- Yimsiri, S., Soga, K., Chandler, S.G. 2005. Cantilever-type local deformation transducer for local axial strain measurement in triaxial test. *Geotechnical Testing Journal*, **28**(5): 1-7.
- Yu, H.S., Salgado, R., Sloan, S.W., Kim, J.M. 1998. Limit Analysis versus Limit Equilibrium for Slope Stability. *Journal of Geotechnical and Geoenvironmental Engineering*, **124**:1-11.
- Zienkiewicz, O.C. 1971. *The finite element method in engineering science*. McGraw-Hill, London.

Appendix A

Published conference papers

This appendix contains the published conference papers during the preparation of this thesis in the same format as published in the conferences proceedings. The full citation for the papers, in the same order as published and attached, is as follow:

1. Abdelaziz, T., Martin, C.D., Chalaturnyk, R. 2005. Mechanistic view of strength mobilization in stiff clays and weak rocks. In the Proceedings of the Fifth international Geotechnical Engineering conference, January 2005, Cairo, Egypt, pp. 171-182.
2. Abdelaziz, T., Martin, C.D., Chalaturnyk, R. 2005. The onset of dilation in soils and rocks. *In* the 58th Canadian Geotechnical Conference & 6th Joint CGS & IAHCNC Groundwater Specialty Conference, 11-14 September 2005, Saskatoon, Canada, Paper No. 583.
3. Abdelaziz, T., Martin, C.D., Chalaturnyk, R. 2006. Geomechanical behaviour of a McMurray sand formation using local strain measurements. *In* the 59th Canadian Geotechnical Conference & 7th Joint CGS & IAHCNC Groundwater Specialty Conference, 1-4 October 2006, Vancouver, Canada, No. 158.

LIST OF FIGURES

	Page
Figure 1.1 Peak and residual strength envelopes for geomaterials.....	29
Figure 1.2 Classification of geological materials based on frictional and bonding/interlocking contribution to strength	30
Figure 1.3 Peak strength envelopes for cohesive and bonded clays.....	31
Figure 1.4 Failure modes of cylindrical specimens based on confining pressures and bonding/interlocking between particles.	31
Figure 1.5 Typical stress strain curves at different confining pressure and plastic strain along failure surfaces.....	32
Figure 1.6 Mobilized strength ratio (τ_m/τ_p) and brittleness indices (IB) for stiff clays and weak rocks.	32
Figure 1.7 Variation of mobilized strength at different strain levels and mobilized strength based on conventional factor of safety (modified from De Mello 1988).	33
Figure 1.8 Stress strain perspective for strength mobilization in bonded/interlocked geomaterials.....	33
Figure 1.9 A schematic diagram of a frictional and bonded/interlocked geomaterial with equivalent constraint level.	34
Figure 1.10 Loss of internal confining for bonded/interlocked geomaterial due to internal constraint destruction and its effect of stress strain curve compared to a frictional geomaterial.....	34
Figure 1.11 A schematic diagram to illustrate the interference between testing conditions and measured global strains.	35
Figure 2.1 Stress-strain and volumetric strain curves for dense sand (modified from Finno and Rechenmacher 2003): (a) Deviator stress-strain curve; (b) Volumetric strain curve; (c) lateral strain curves; and (d) dilatancy angle.....	63

Figure 2.2 Stress ratio-strain and volumetric strain curves for interlocked sand (modified from Cresswell and Powrie 2004): (a) Stress ratio-strain curve, and (b) Volumetric and local strain curves.	64
Figure 2.3 The ratio of onset of dilation normalized to the peak strength for locked sand at various confining pressures.	65
Figure 2.4 Stress strain and volumetric strains curves for Vosges sandstone (modified from Besuelle et al. 2000): (a) Deviator stress- axial strain curve; (b) Volumetric strain curve; and (c) axial strain difference curves.	66
Figure 2.5 The ratio of onset of dilation normalized to the peak strength for Vosges sandstone at various confining pressures.	67
Figure 2.6 Stress strain and volumetric strains curves for Fontainebleau sandstone (modified from Sulem and Ouffroukh 2005): (a) Deviator stress-axial strain curve; (b) Volumetric strain curve; and (c) axial and lateral strain differences curves.	68
Figure 2.7 The ratio of onsets of dilation and localization normalized to the peak strength for Fontainebleau sandstone at various confining pressures.	69
Figure 2.8 Stress-strain and variation of CT number with strain (modified from Su et al. 2004): (a) Deviator-strain curve; and (b) variation of CT number with strain.	70
Figure 2.9 The ratio of onset of dilation normalized to the peak strength for an OC clay at various confining pressures.	71
Figure 2.10 Stress-strain and volumetric strain for granite (modified from Lockner et al. 1992): (a) Deviator stress -strain curve; and (b) Volumetric strain curve.	72
Figure 2.11 The ratio of onset of dilation normalized to the peak strength for La Du Bonnet granite at various confining pressures (modified from Martin and Chandler 1994).	73
Figure 2.12 Independence of dilation ratio of geomaterials' nature.	74

Figure 2.13 Undrained axial creep strain with time under different stress levels for Ham River Sand (modified from Kuwano and Jardine 2002).	75
Figure 2.14 Normalized creep stress ratio versus time to failure at different confining pressures (modified from Lau and Chandler 2004).	75
Figure 2.15 Normalized ultrasonic velocities and deviator stress vs. axial strain for rock salt (modified from Schulze et al. 2001).....	76
Figure 2.16 Normalized dilation ratio of rock salt (modified from Hunsche and Hampel 1999).	76
Figure 2.17 Results of a true triaxial creep test for rock salt at constant mean stress at four shear stress increments prior to and past to onset of dilation (modified from Hunsche and Hampel 1999).	77
Figure 2.18 Stages of crack development for Lac Bu Bonnet granite using damage tests (modified from Martin and Chandler 1994).	78
Figure 2.19 Results of a cyclic uniaxial test indicating the variation of permanent axial and lateral strains with evolution of deformation below onset of dilation threshold (modified from Lajtai et al. 1990). ...	79
Figure 2.20 Analogue for deformation mechanism in bonded geomaterials.	80
Figure 3.1 World 's Crude oil reserves.....	119
Figure 3.2 Distribution of Alberta Oil sands.	120
Figure 3.3 Geomaterials categories according to Diagenetic processes (Modified from Barton 1993 and according to ISRM 1978).	121
Figure 3.4 Classification of contacts in sandstones (After Siever 1959).	122
Figure 3.5 Physiography of the Athabasca oil sands and location of sampling area (modified from Dusseault 1977).	123
Figure 3.6 Bedrock geology in the investigated vicinity (AEUB and AGS 2005)	124
.Figure 3.7 (a) An illustration of tripartite classification of McMurray formation members; and (b) Grain size distribution of Athabasca oil sands (after Carrigy 1967).	125
Figure 3.8 Selected SEM micrographs of High-Hill sand formation.	126

Figure 3.9 Map for collected particles under optical microscope.	127
Figure 3.10 Energy dispersion X-ray results for mapped particles.	128
Figure 3.10 Energy dispersion X-ray results for mapped particles.	129
Figure 3.11 Micrograph of well -sorted band under PPL: width of view 3.5 mm, illustrating quartz grains as white, very fine grained rock fragments, and clay as grey and pores in blue.	130
Figure 3.12 Micrograph under PPL showing kaolinite bridge between three quartz particles: width of view 0.35 mm.	130
Figure 3.13 Micrograph under CPL showing particle fracture: width of view 0.7 mm.	131
Figure 3.14 Micrograph of less-sorted band under CPL: width of view 1.4 mm, illustrating quartz grains as white and light to dark grey; very fine grained rock fragments as black with white spots, siliceous siltstone (S), chert (C); and pores as black.	131
Figure 3.15 Micrograph under CPL: width of view 0.7 mm, illustrating quartz overgrowth, quartz grains as white and light to dark grey, and pores as black.	132
Figure 3.16 Micrograph under PPL: width of view 0.7 mm, illustrating existence of a skeletal grain due to dissolution during diagenesis...	132
Figure 3.17 Distribution of particles orientation in horizontal and vertical direction: (a) Horizontal section; and (b) Vertical section.	133
Figure 3.18 Signals cycle and laboratory components.	134
Figure 3.19 Micrometer for LVDTs calibration.	135
Figure 3.20 A sample of LVDTs calibration charts.	136
Figure 3.21 Accuracy versus Output voltage.	136
Figure 3.22 Transducers setup for stability test.	137
Figure 3.23 A picture of the thermistor embedded in ice water container for calibration purpose.	137
Figure 3.24 Stability of an LVDT for almost 24 hrs.	138
Figure 3.25 Variation of temperature with time.	138

Figure 3.26 An illustration for variation of deformation with temperature for 24 hrs.	139
Figure 3.27 Proof testing results of a PVC sample.	139
Figure 3.28 Original mechanical configuration and accessories.	140
Figure 3.29 Mechanical configuration, accessories and mounting steps (modified set).	141
Figure 3.30 Local and external axial stress vs. axial strain curves.	142
Figure 3.31 Comparison of external and local axial strain's rate.	142
Figure 4.1 Experimental results illustrating variation of deviator stress, axial, lateral and volumetric strains during shear evolution.	190
Figure 4.2 Variation in tangential axial stiffness, volumetric stiffness, and lateral stiffness during shear evolution.	191
Figure 4.3 Relationship between the deviator stress, plastic axial, lateral, and volumetric strains.	192
Figure 4.4 Mechanism of failure in cylindrical locked sand specimen.	193
Figure 4.5 Variation of frictional as well as interlocking strength components with plastic shear strain.	194
Figure 4.6 Mobilized strength components with plastic shear strain in terms of interlocking component, friction angle, and dilation angle.	194
Figure 4.7 Formation of axially extended columnar structures under homogeneous strain field (observe curvature at columns interface): (a) longitudinal view of failure pattern; and (b) cross sectional view.	195
Figure 4.8 Deformation bands boundaries and orientation for axisymmetrical compression stress path derived from bifurcation criterion for porous rocks (Poisson's ratio $\nu=0.2$).	196
Figure 4.9 Stress-strain and volumetric strain curves during creep test.	197
Figure 4.10 Variation of axial strain with time during creep stages.	198
Figure 4.11 Variation of axial strain rates during creep stages.	198
Figure 4.12 Variation of lateral strain with time during creep stages.	199
Figure 4.13 Variation of lateral strain rates during creep stages.	199
Figure 4.14 Variation of volumetric strains during creep stages.	200

Figure 4.15 Direct shear test apparatus and its components.....	200
Figure 4.16 Shear stress vs. horizontal deformation in DSB.	201
Figure 4.17 Vertical deformation vs. horizontal deformation in DSB.....	201
Figure 4.18 Failure envelope for locked sand from direct shear tests.	202
Figure 4.19 Corrected shear stresses for a specimen tested under a normal stress of 10 kPa.....	202
Figure 5.1 A schematic diagram of three stress-strain curves.....	224
Figure 5.2 Multiple envelopes at different strain contours.....	226
Figure 5.3 Pietrafitta clay stress-strain curves (modified from Callisto and Rampello 2002).	226
Figure 5.4 Multiple-Yield envelopes in terms of plastic shear strain contours (Pietrafitta clay).....	227
Figure 5.5 Distribution of strength parameters with plastic shear strain level (Pietrafitta clay).....	228
Figure 5.6 Nanticoke clay stress-strain curves (modified from Lo 1972).	229
Figure 5.7 Multiple-Yield envelopes in terms of plastic shear strain contours (Nanticoke clay).....	230
Figure 5.8 Distribution of strength parameters with plastic shear strain level (Nanticoke clay).....	231
Figure 5.9 Distribution of normalized frictional strength parameter with plastic shear strain.....	232
Figure 5.10 Distribution of normalized tensile strength with plastic shear strain.....	233
Figure 5.11 Stress-strain curves at various confining stress based on the incremental form of equation [5.15].	234
Figure 5.12 Conceptual framework to visualize contribution of frictional and bonding resistance to stiff clay shearing response (modified from Conlon 1966).	235
Figure 5.13 Failure, Bonding strength and plateau strength envelopes.....	236
Figure 5.14 Stress-strain curves and failure envelope for Toulmoustou Stiff clay (modified from Conlon 1966).....	237

Figure 5.15 Stress-strain curves and failure envelope for Jointed weak rock (modified from Lajtai 1974).....	238
Figure 5.16 Stress-strain curves of Artificially cemented soil and Calcarenite (modified from (a) Lo et al. 2003; and (b) Lagioia and Nova 1995).....	239
Figure 5.17 Failure envelopes for cemented sensitive clay (modified from (a) Mitchell 1970; and (b) Lefebvre and Rochelle 1974).	240
Figure 6.1 Schematic diagram of excavated slope.	258
Figure 6.2 Vertical stress contours before excavation.	258
Figure 6.3 Vertical stress contours after excavation.	259
Figure 6.4 Shear stress contours after excavation.....	260
Figure 6.5 Unbalanced forces versus no of steps based on a SRF of 1.43.....	261
Figure 6.6 Unbalanced forces versus no of steps based on a SRF of 1.44.....	262
Figure 6.7 The potential slip surface obtained from the SRF technique implemented in FLAC.....	263
Figure 6.8 The minimum factor of safety and the critical slip surface obtained from LEM.	264
Figure 6.9 The distribution of normal and shear stresses from LEM: (a) the normal stress distribution; and (b) the available and mobilized strength.....	265
Figure 6.10 The potential slip surface obtained from hardening/softening model implemented in FLAC.	266
Figure 6.11 The evolution of potential slip surface at different plastic strain levels: (a) (0-0.017); (b) (0-0.12); (c) (0-0.24); and (d) (0-0.4).	267
Figure 6.12 The unbalanced forces from hardening/softening model implemented in FLAC.	268
Figure 6.13 Monitoring point along the potential slip surface.....	268
Figure 6.14 Distribution of cohesion along the potential slip surface.	269
Figure 6.15 Distribution of friction angle along the potential slip surface.	270
Figure 6.16 Distribution of normal, shear stresses, and available strength along the slip surface associated with SDP.....	271

Figure 6.17 A schematic illustration of monitoring point's position on stress-strain curve.	271
Figure 6.18 A comparison between the positions of slip surfaces based on peak strength and strain-dependent strength parameters.....	272

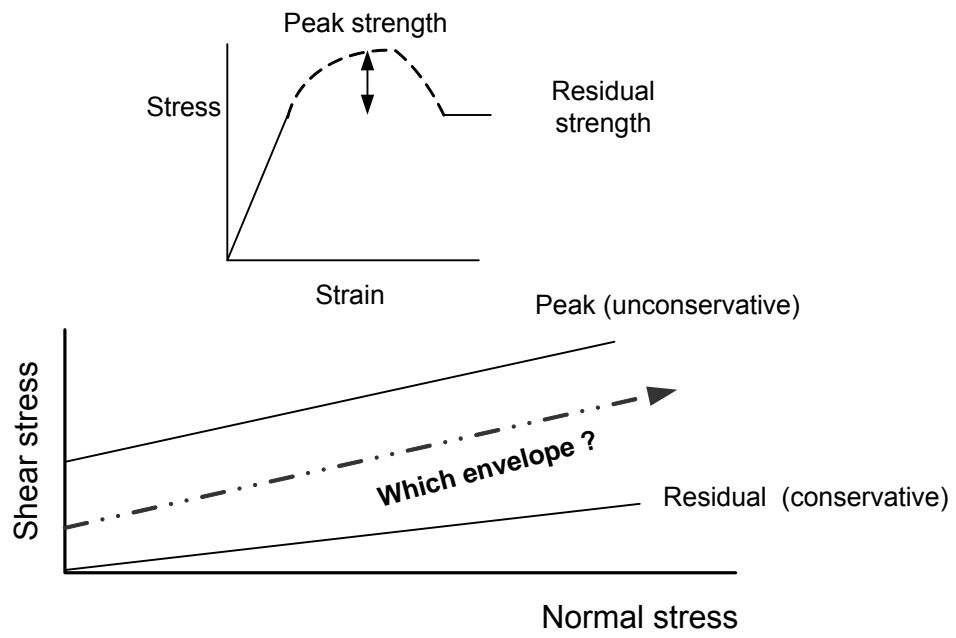


Figure 1.1 Peak and residual strength envelopes for geomaterials.

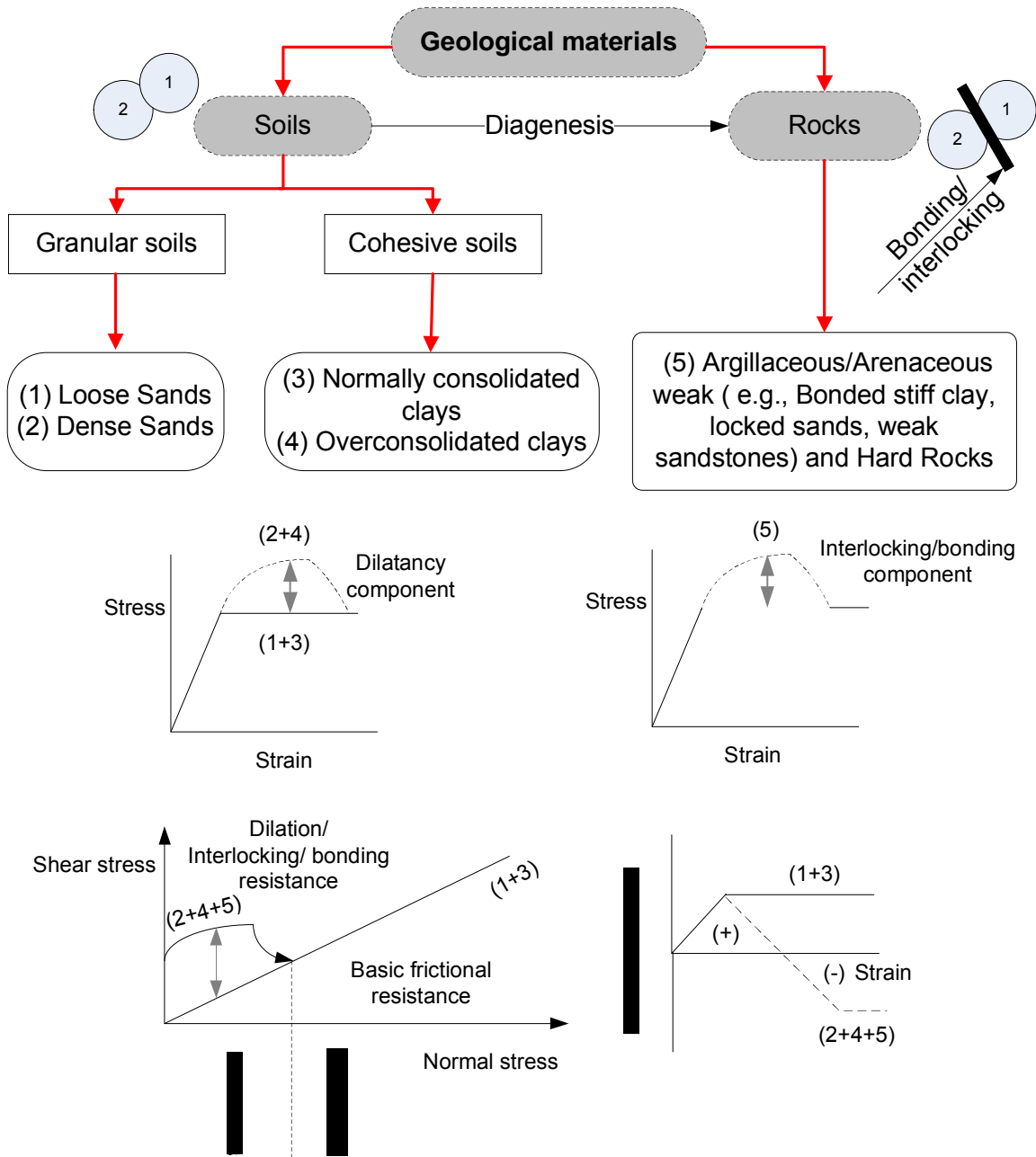


Figure 1.2 Classification of geological materials based on frictional and bonding/interlocking contribution to strength.

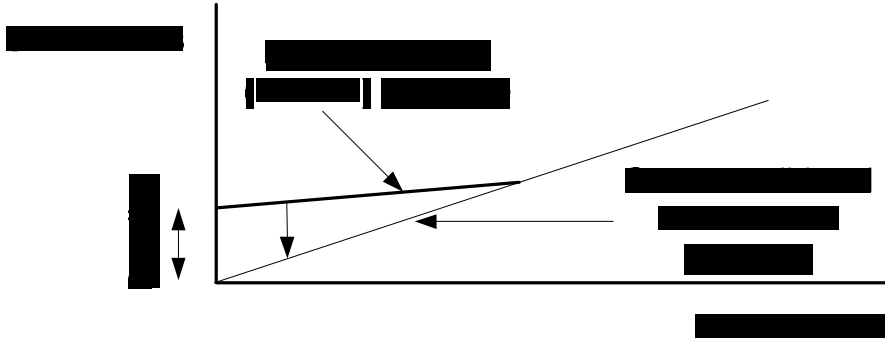


Figure 1.3 Peak strength envelopes for cohesive and bonded clays.

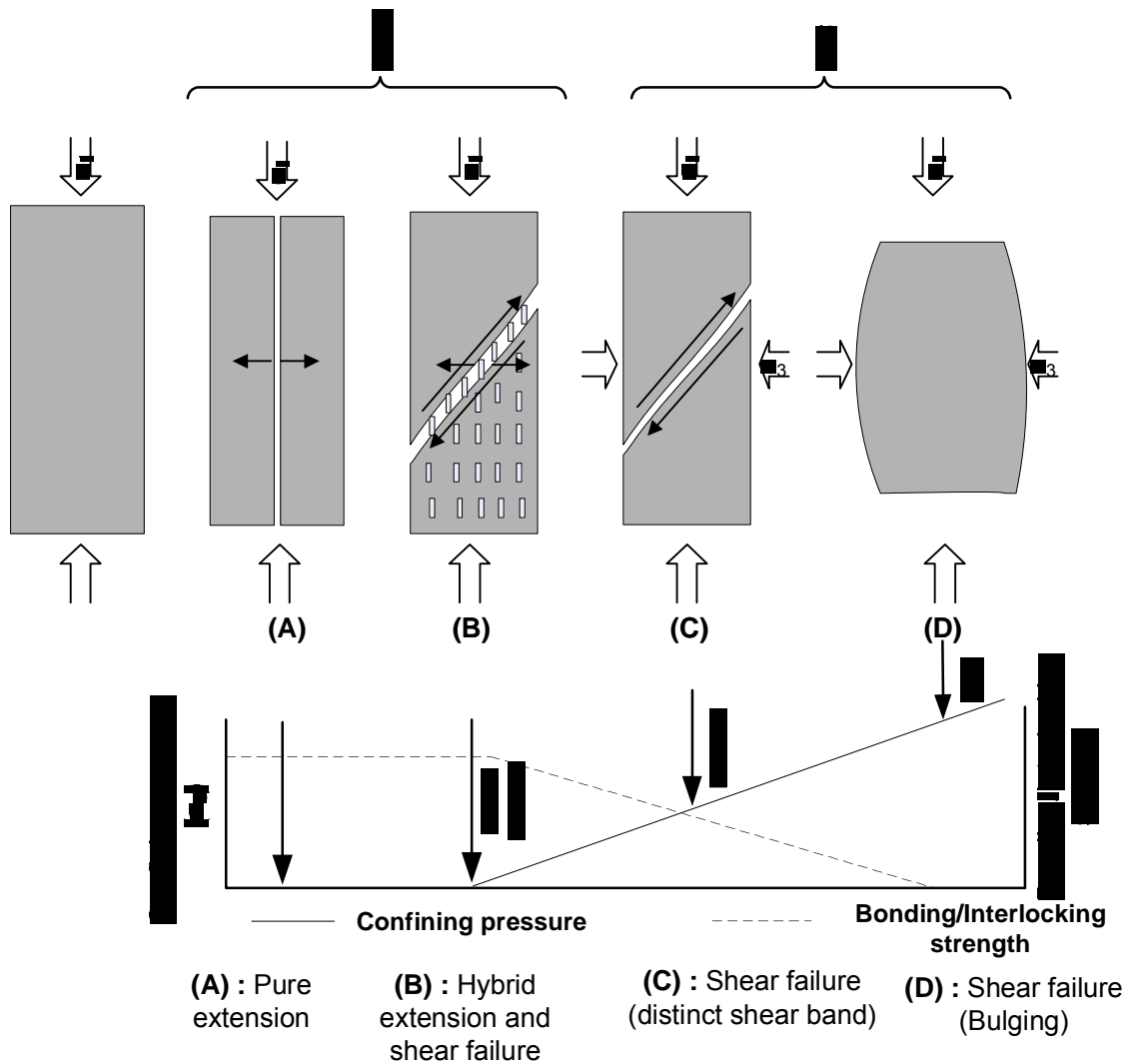


Figure 1.4 Failure modes of cylindrical specimens based on confining pressures and bonding/interlocking between particles.

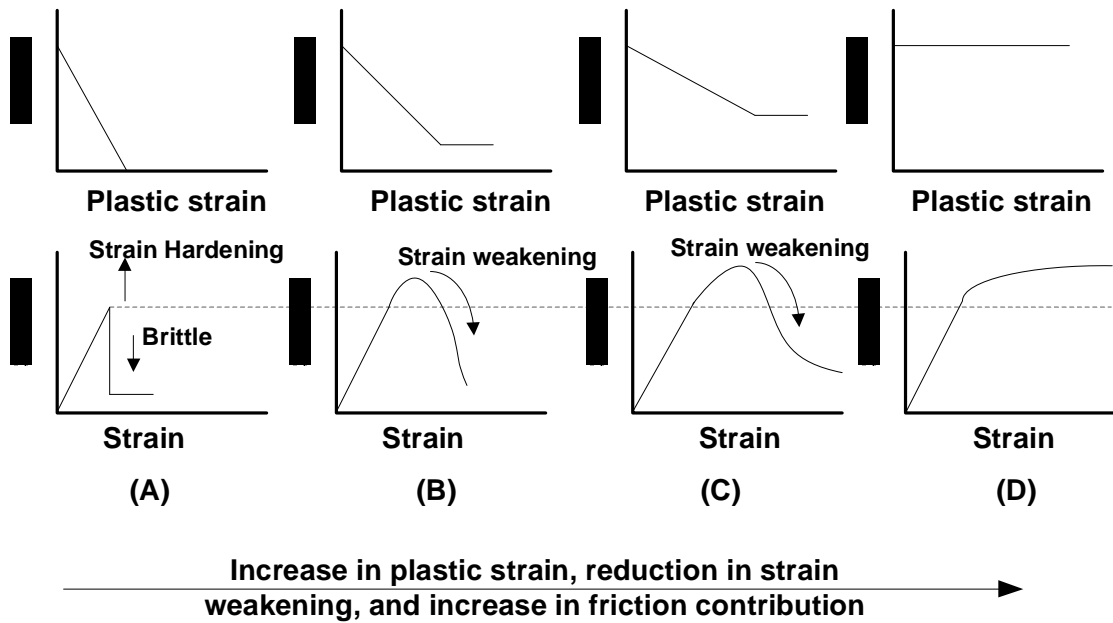


Figure 1.5 Typical stress strain curves at different confining pressure and plastic strain along failure surfaces.

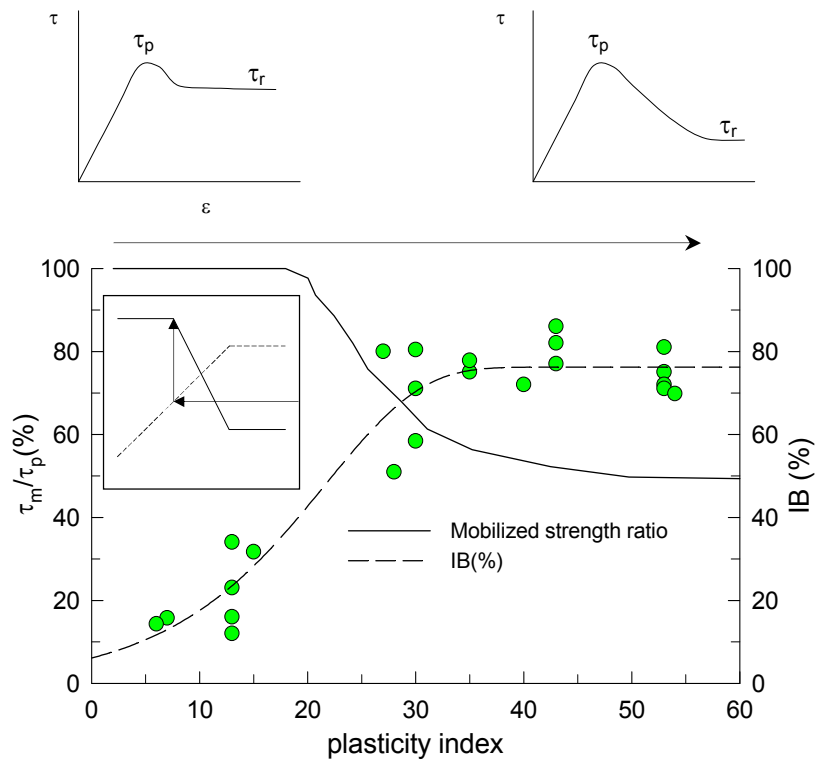


Figure 1.6 Mobilized strength ratio (τ_m/τ_p) and brittleness indices (IB) for stiff clays and weak rocks.

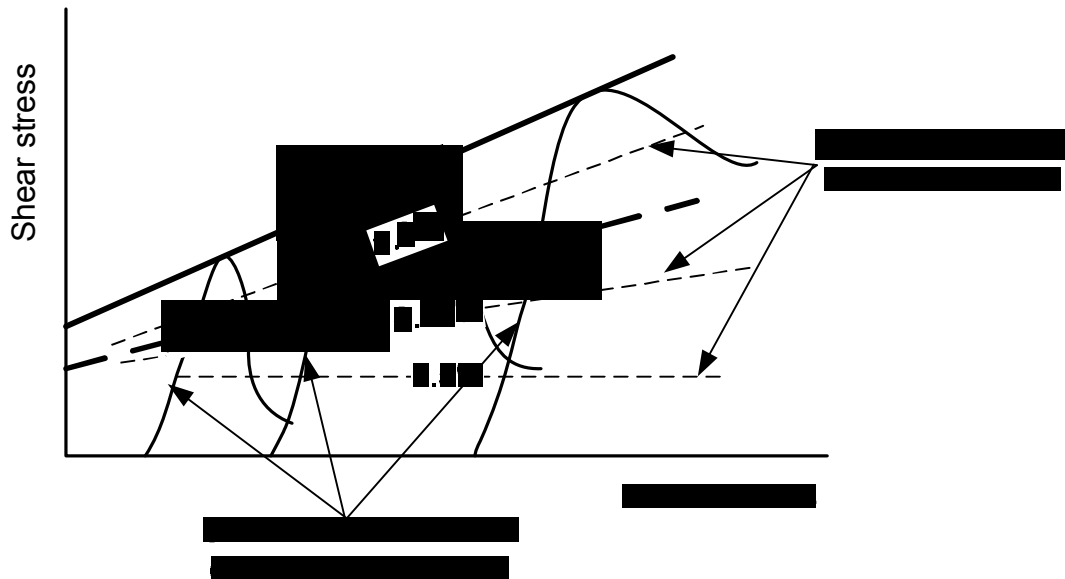


Figure 1.7 Variation of mobilized strength at different strain levels and mobilized strength based on conventional factor of safety (modified after De Mello 1988).

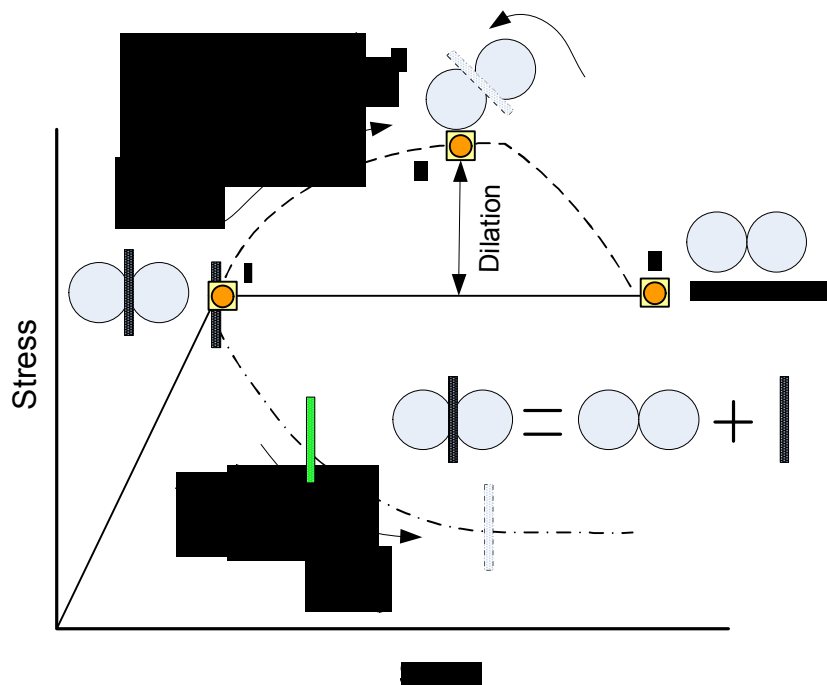


Figure 1.8 Stress strain perspective for strength mobilization in bonded/interlocked geomaterials.

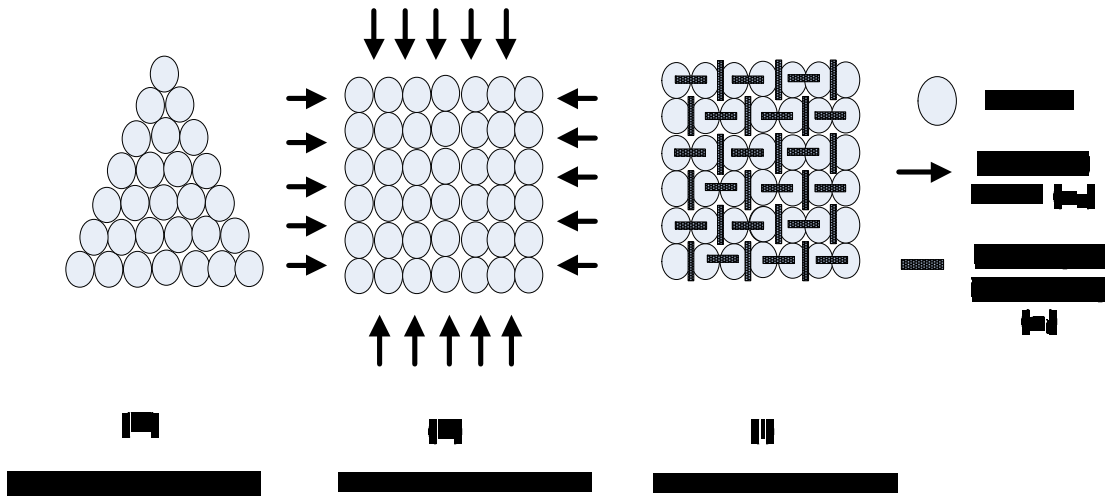


Figure 1.9 A schematic diagram of a frictional and bonded/interlocked geomaterial with equivalent constraint level.

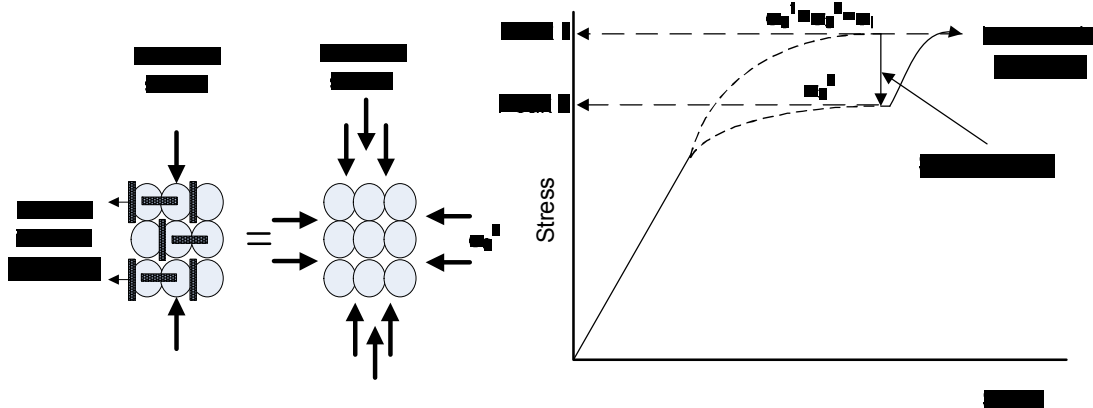


Figure 1.10 Loss of internal confining for bonded/interlocked geomaterial due to internal constraint destruction and its effect of stress strain curve compared to a frictional geomaterial.

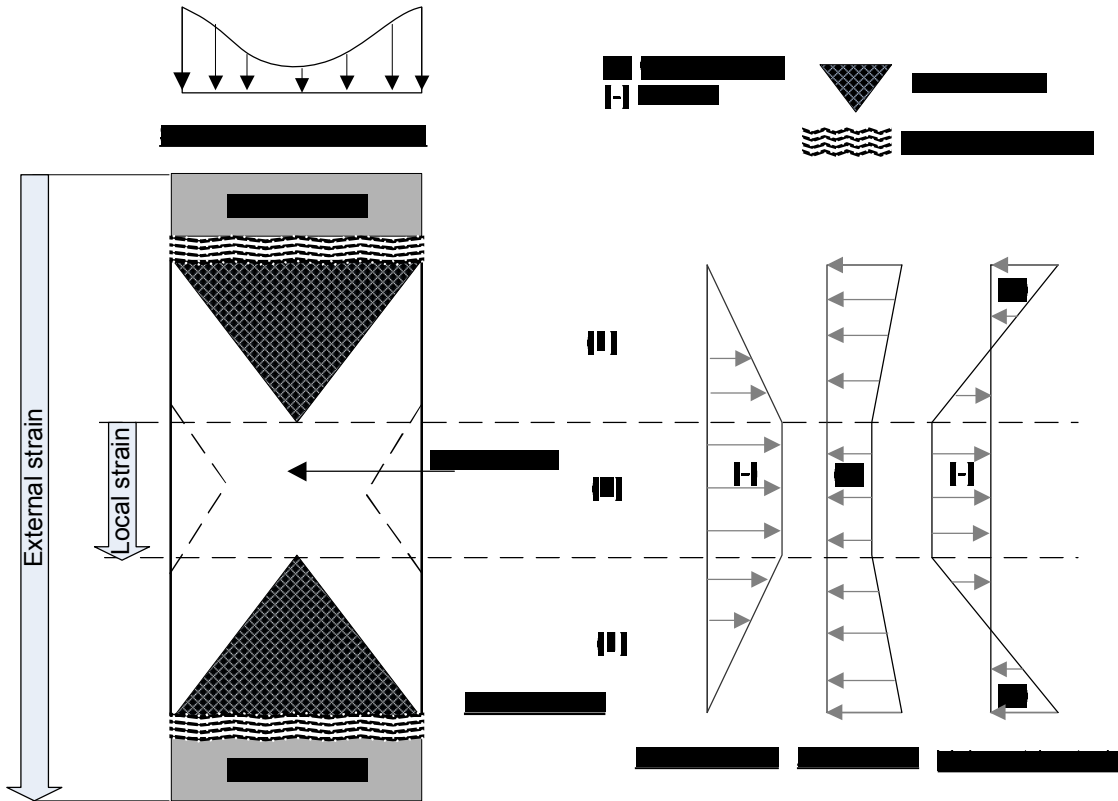


Figure 1.11 A schematic diagram to illustrate the interference between testing conditions and measured global strains.

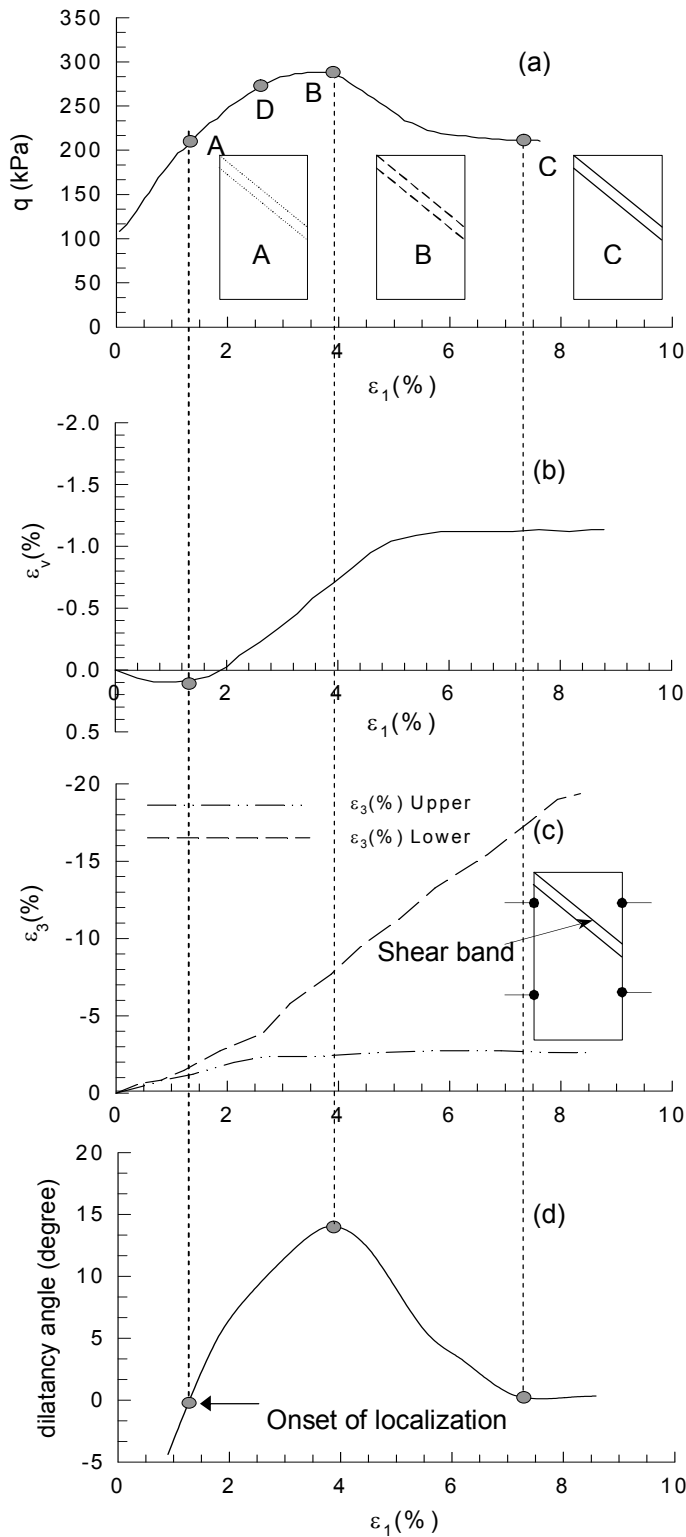


Figure 2.1 Stress-strain and volumetric strain curves for dense sand (modified from Finno and Rechenmacher 2003): (a) Deviator stress-strain curve; (b) Volumetric strain curve; (c) lateral strain curves; and (d) dilatancy angle.

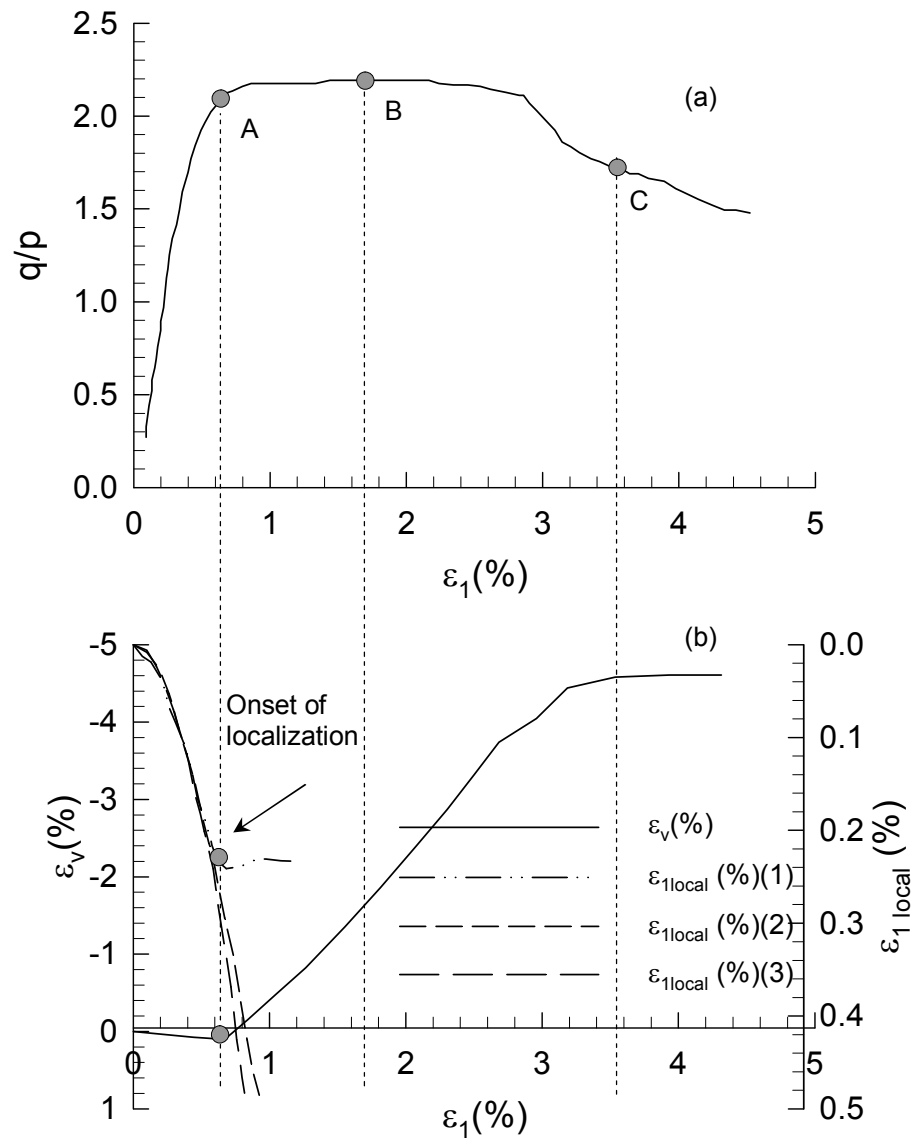


Figure 2.2 Stress ratio-strain and volumetric strain curves for interlocked sand (modified from Cresswell and Powrie 2004): (a) Stress ratio-strain curve, and (b) Volumetric and local strain curves.

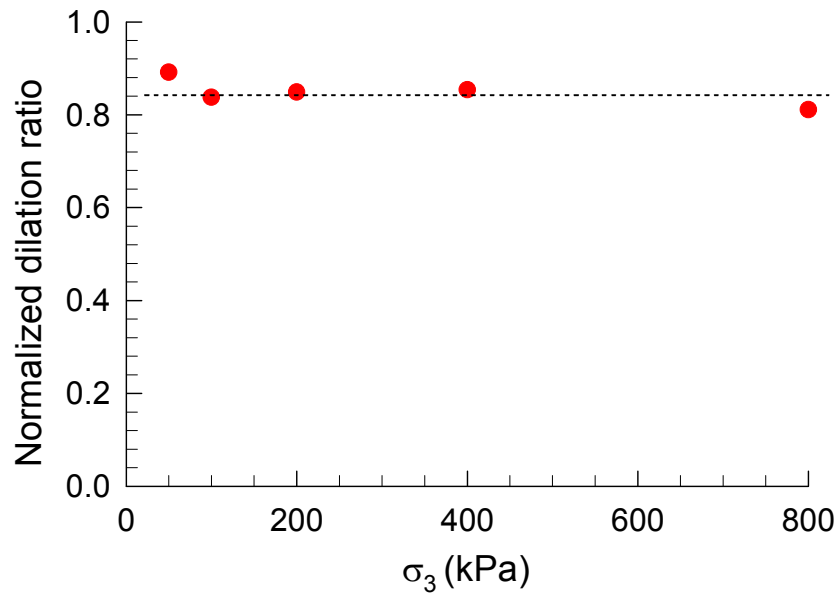


Figure 2.3 The ratio of onset of dilation normalized to the peak strength for locked sand at various confining pressures.

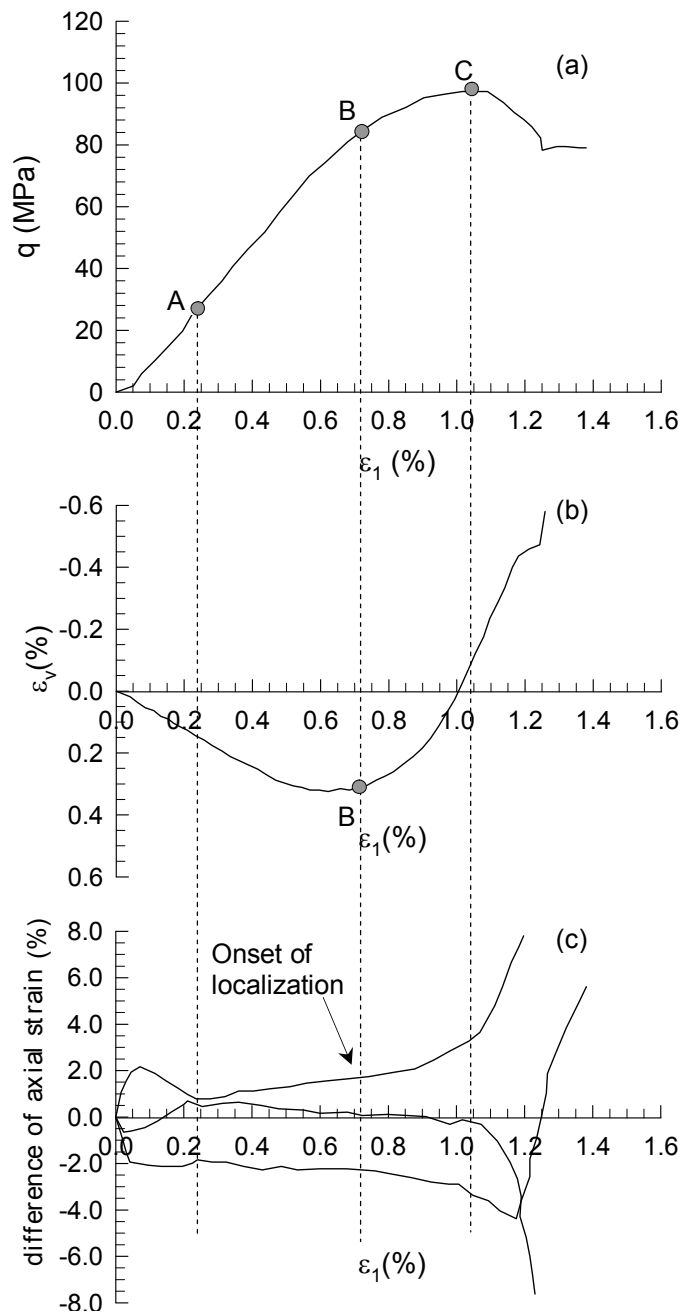


Figure 2.4 Stress strain and volumetric strains curves for Vosges sandstone (modified from Besuelle et al. 2000): (a) Deviator stress- axial strain curve; (b) Volumetric strain curve; and (c) axial strain difference curves.

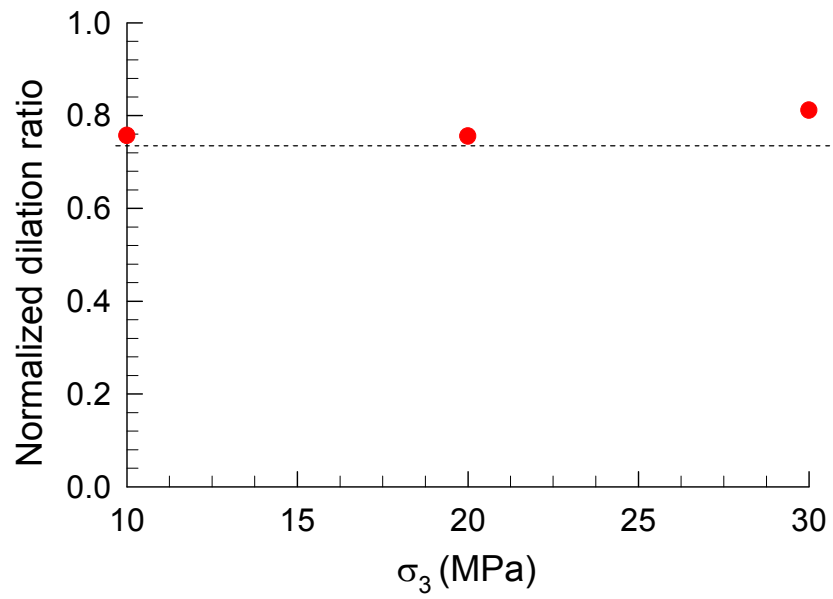


Figure 2.5 The ratio of onset of dilation normalized to the peak strength for Vosges sandstone at various confining pressures.

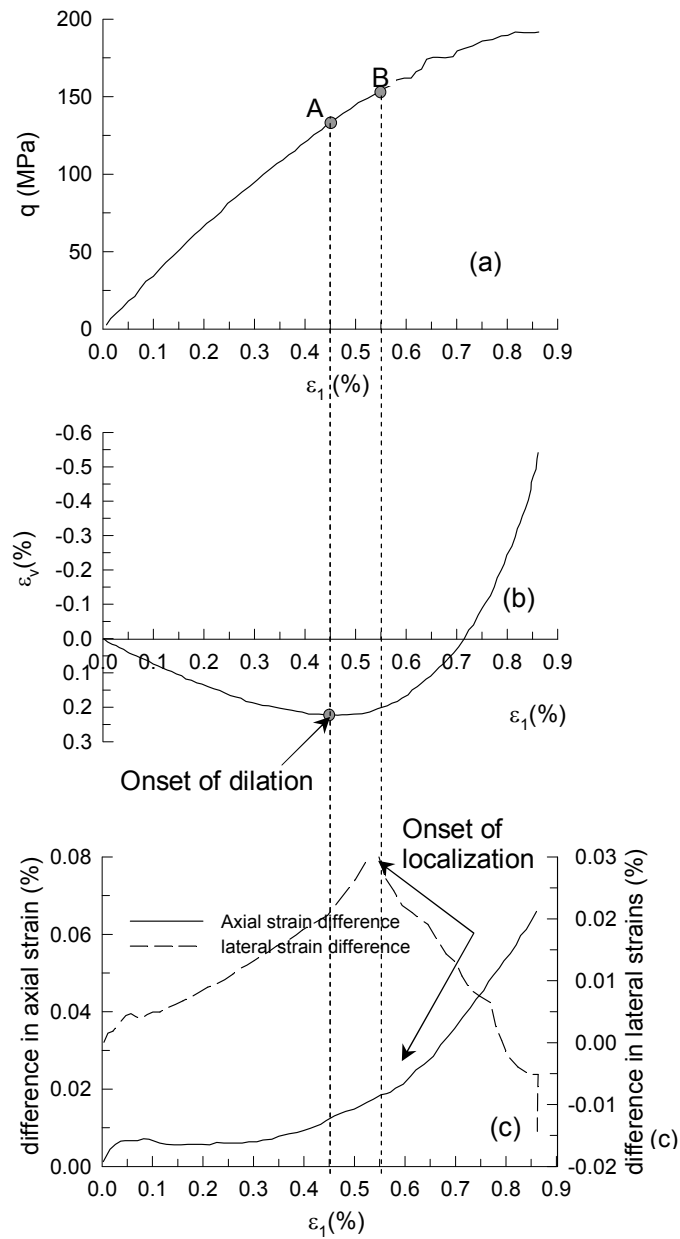


Figure 2.6 Stress strain and volumetric strains curves for Fontainebleau sandstone (modified from Sulem and Ouffroukh 2005): (a) Deviator stress-axial strain curve; (b) Volumetric strain curve; and (c) axial and lateral strain differences curves.

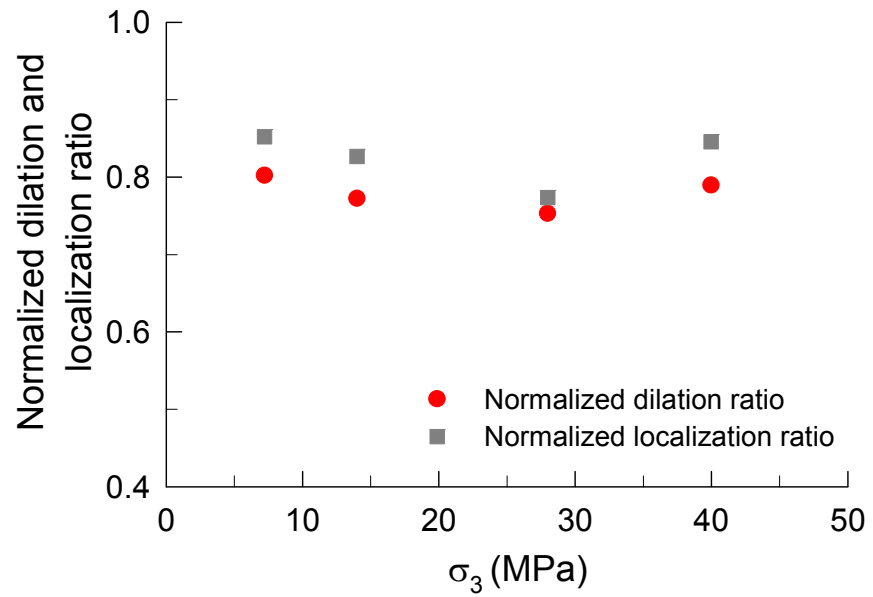


Figure 2.7 The ratio of onsets of dilation and localization normalized to the peak strength for Fontainebleau sandstone at various confining pressures.

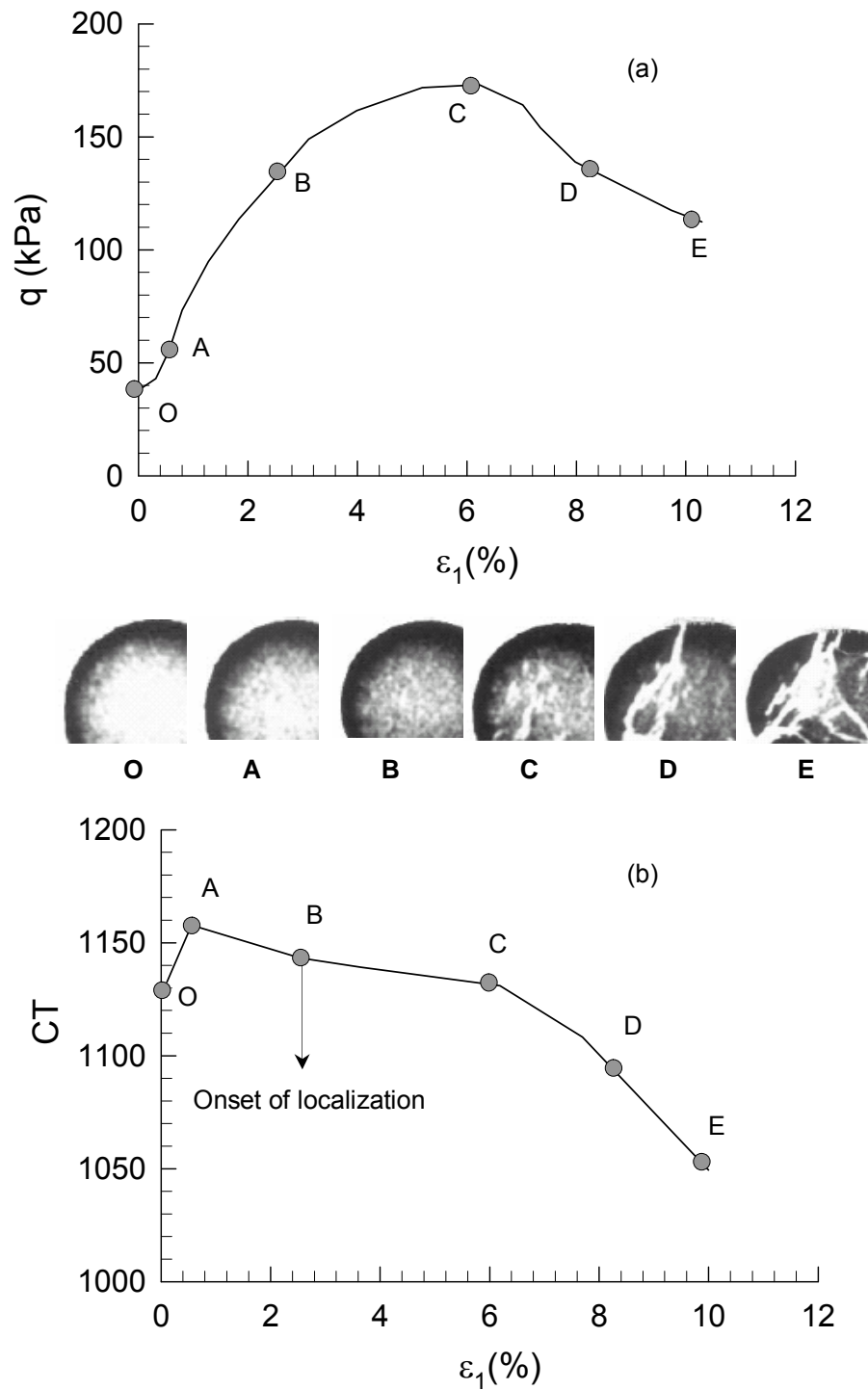


Figure 2.8 Stress-strain and variation of CT number with strain (modified from Su et al. 2004): (a) Deviator-strain curve; and (b) variation of CT number with strain.

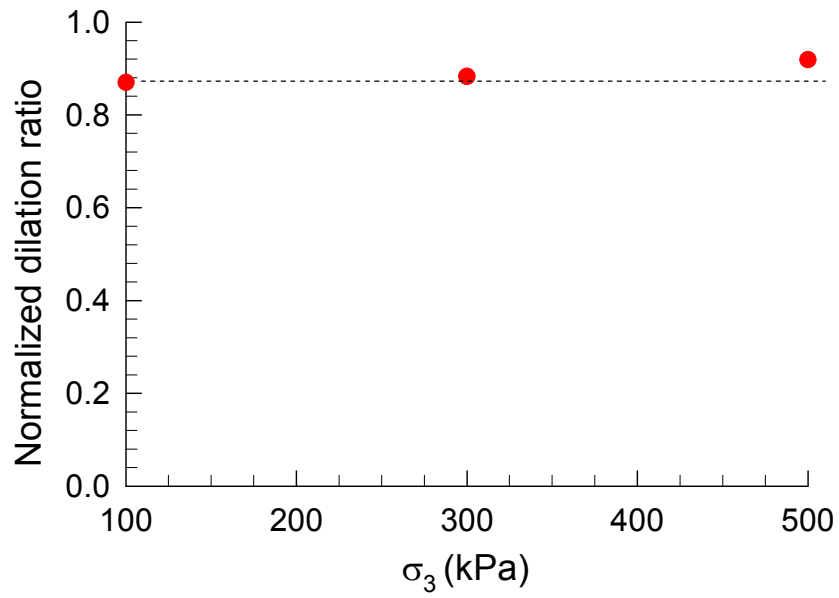


Figure 2.9 The ratio of onset of dilation normalized to the peak strength for an OC clay at various confining pressures.

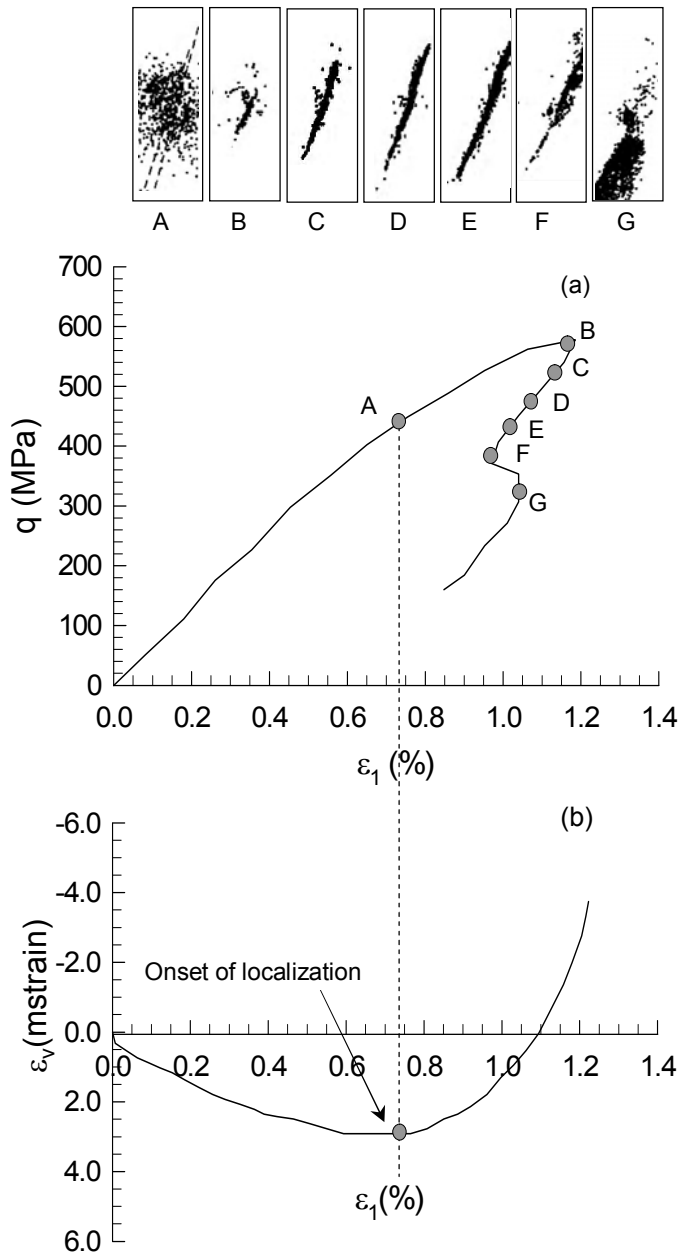


Figure 2.10 Stress-strain and volumetric strain for granite (modified from Lockner et al. 1992): (a) Deviator stress -strain curve; and (b) Volumetric strain curve.

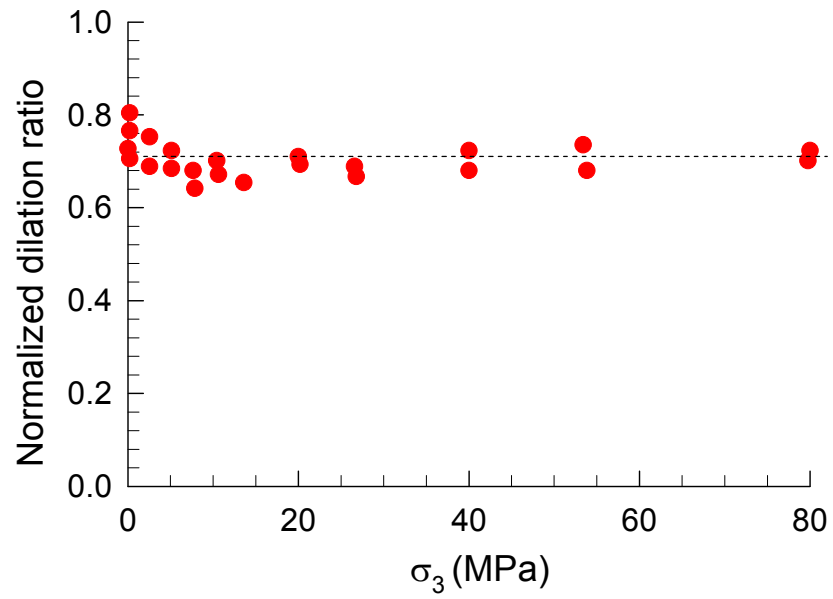


Figure 2.11 The ratio of onset of dilation normalized to the peak strength for La Du Bonnet granite at various confining pressures (modified from Martin and Chandler 1994).

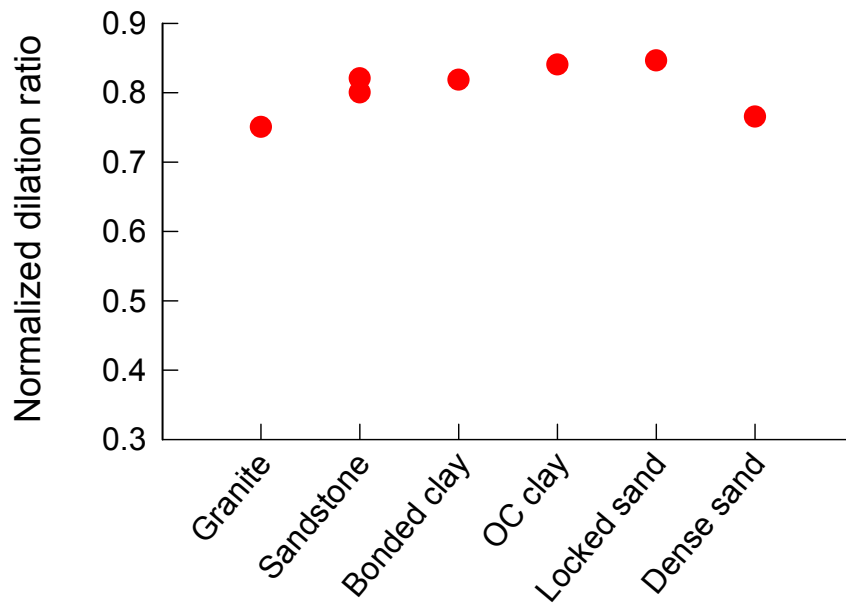


Figure 2.12 Independence of dilation ratio of geomaterials' nature.

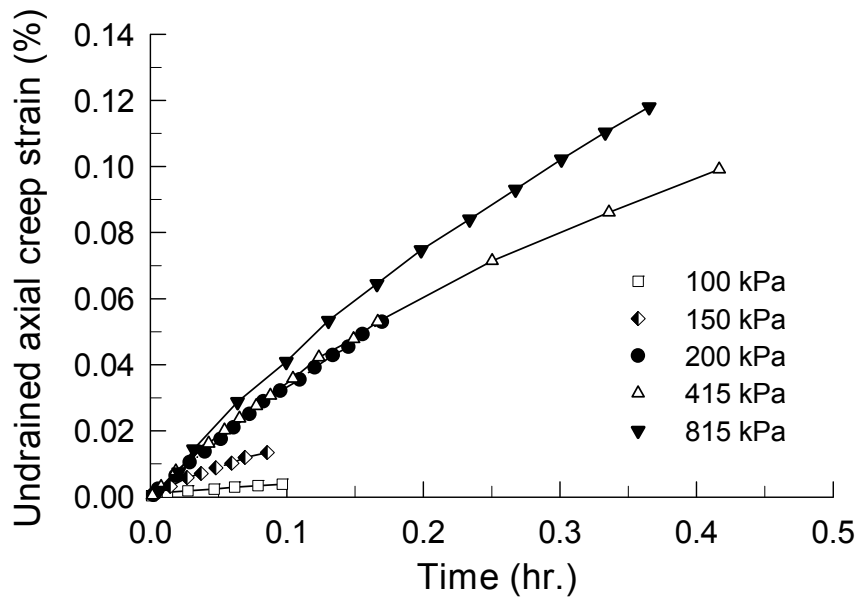


Figure 2.13 Undrained axial creep strain with time under different stress levels for Ham River Sand (modified from Kuwano and Jardine 2002).

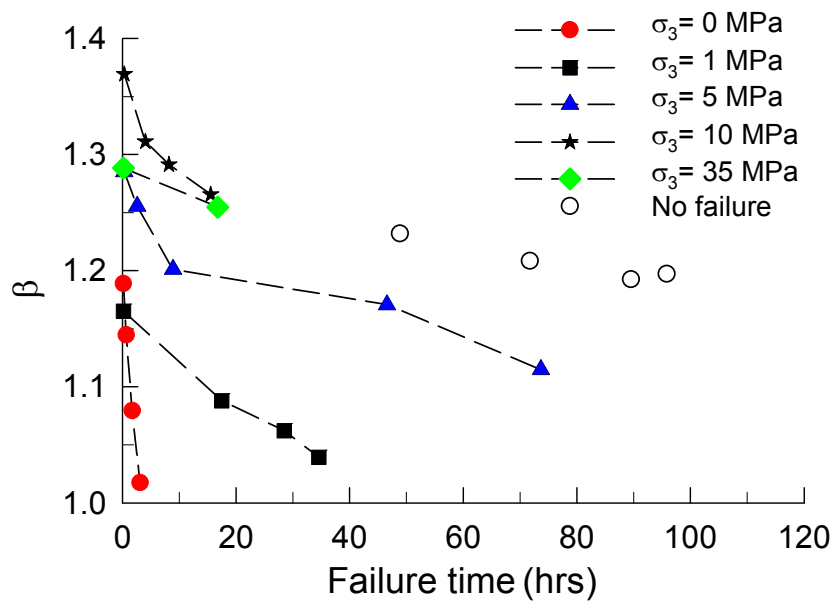


Figure 2.14 Normalized creep stress ratio versus time to failure at different confining pressures (modified from Lau and Chandler 2004).

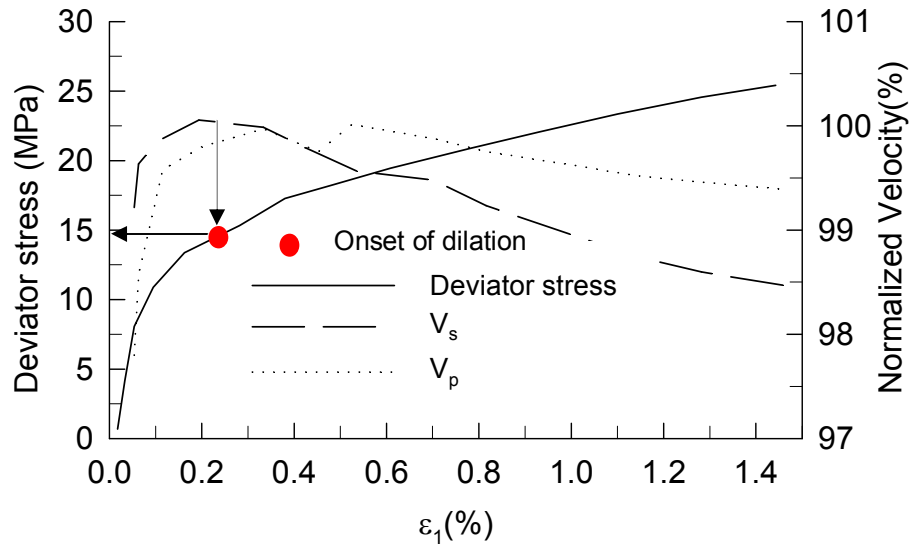


Figure 2.15 Normalized ultrasonic velocities and deviator stress vs. axial strain for rock salt (modified from Schulze et al. 2001).

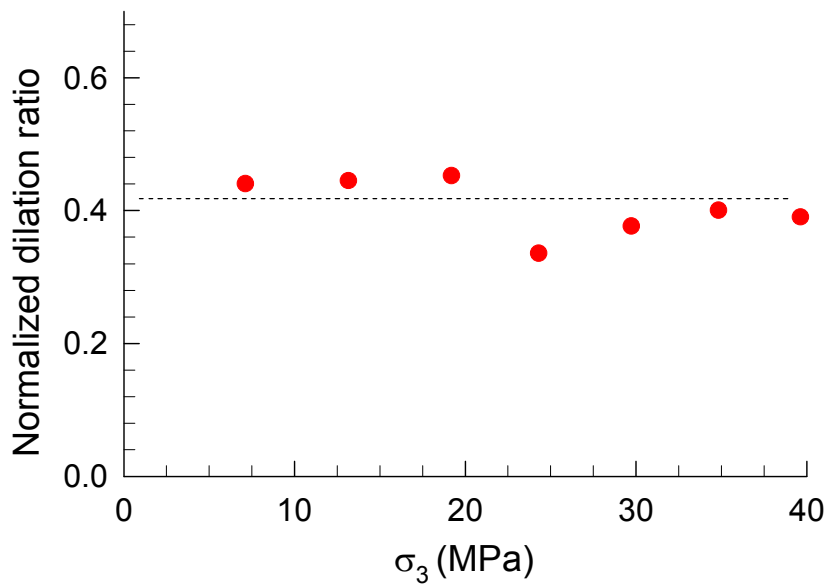


Figure 2.16 Normalized dilation ratio of rock salt (modified from Hunsche and Hampel 1999).

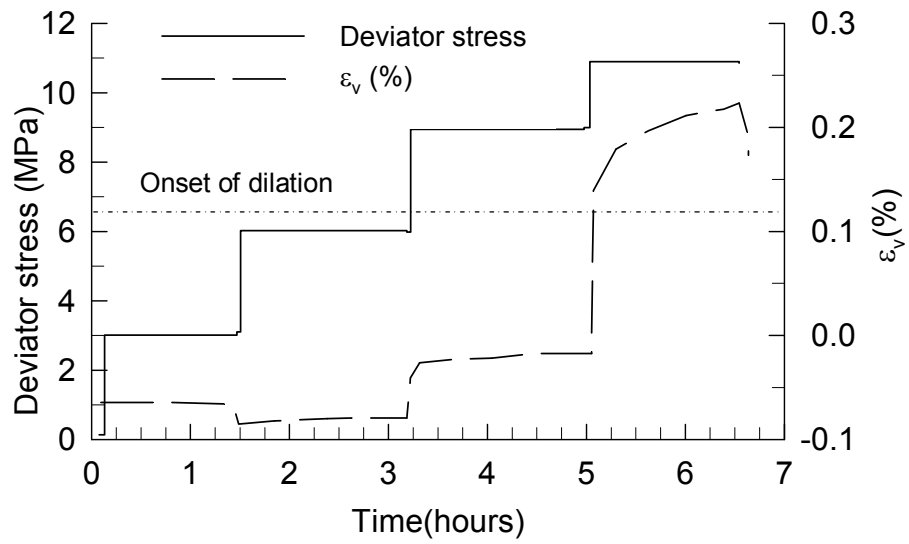


Figure 2.17 Results of a true triaxial creep test for rock salt at constant mean stress at four shear stress increments prior to and past to onset of dilation (modified from Hunsche and Hampel 1999).

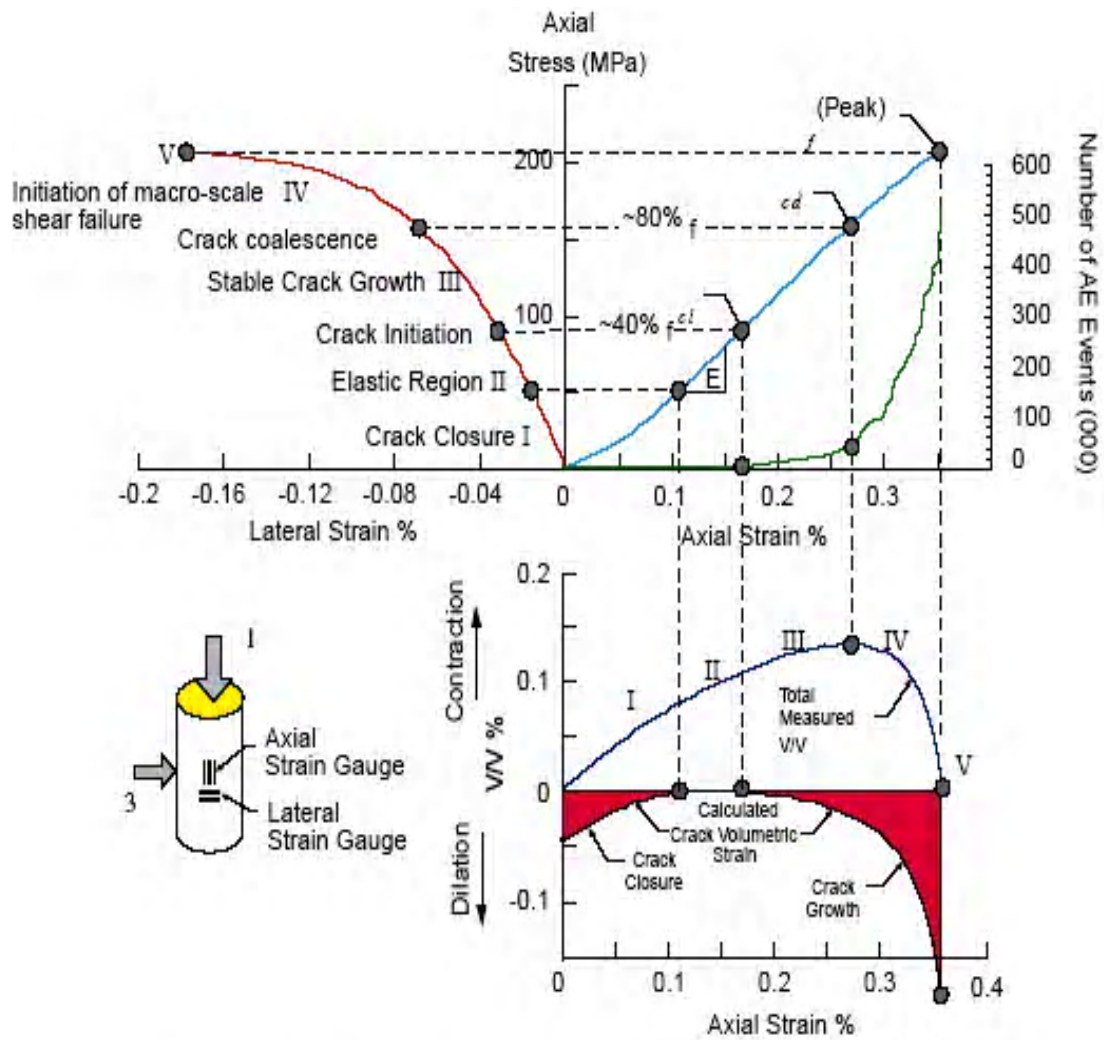


Figure 2.18 Stages of crack development for Lac Bu Bonnet granite using damage tests (modified from Martin and Chandler 1994).

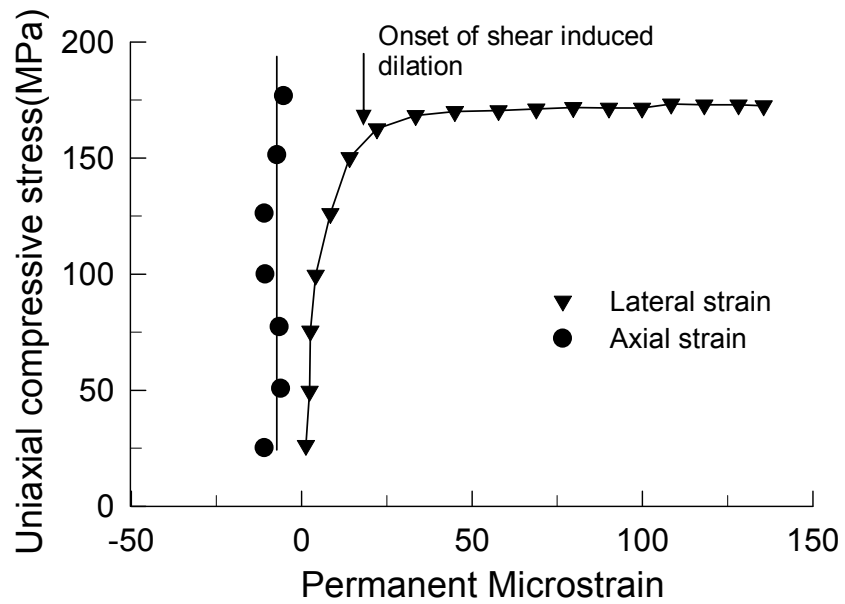


Figure 2.19 Results of a cyclic uniaxial test indicating the variation of permanent axial and lateral strains with evolution of deformation below onset of dilation threshold (modified from Lajtai et al. 1990).

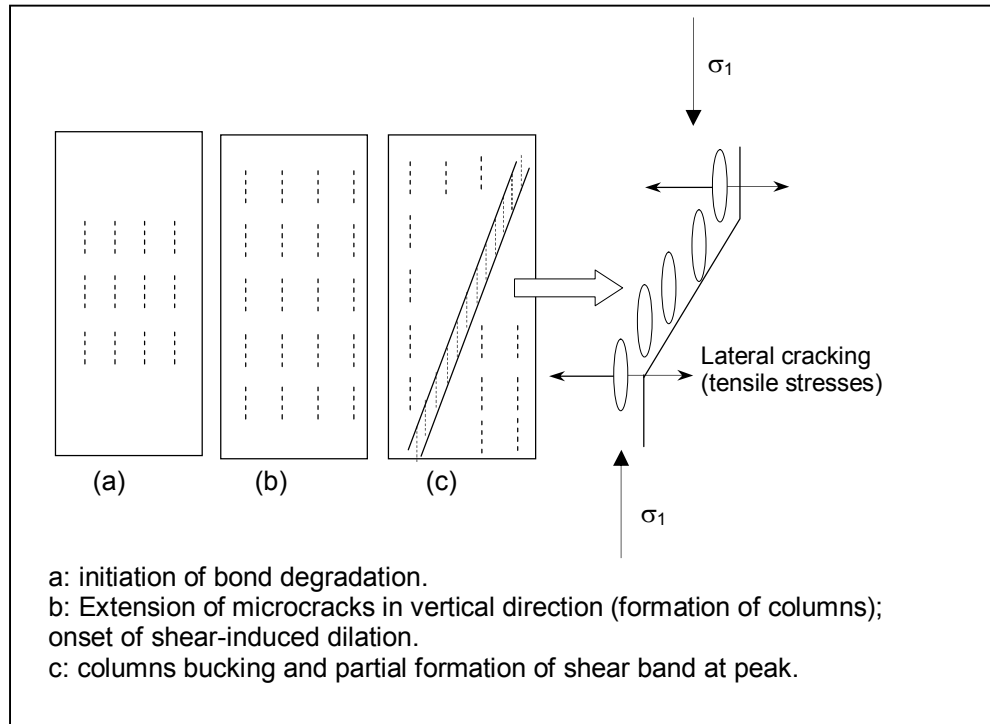


Figure 2.20 Analogue for deformation mechanism in bonded geomaterials.

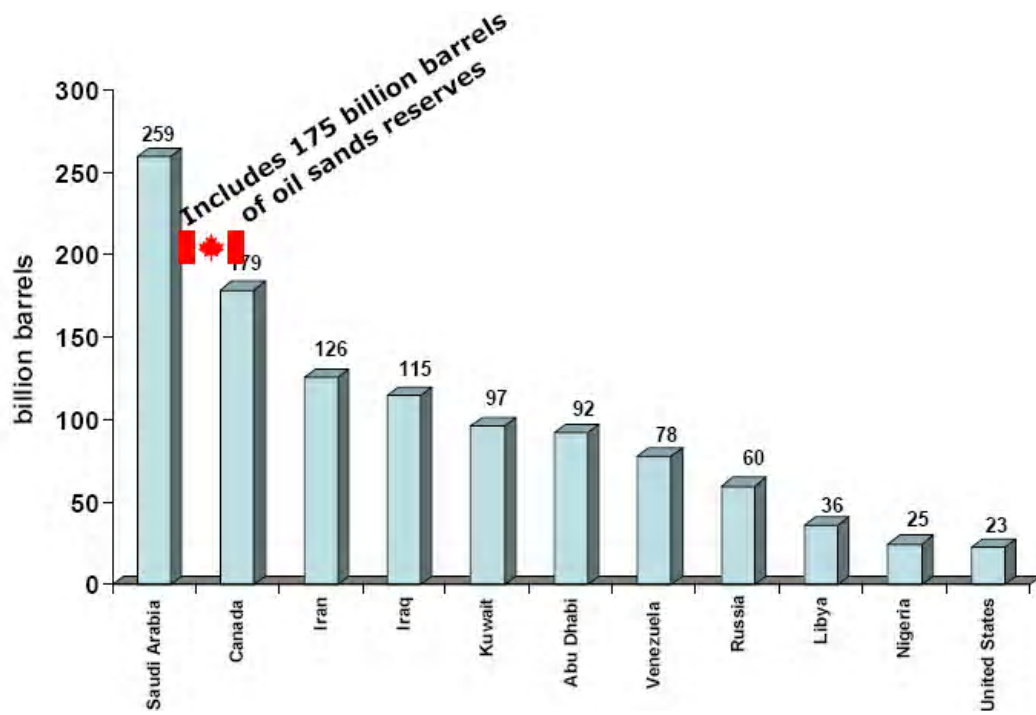


Figure 3.1 World 's Crude oil reserves
 (<http://www.syncrude.ca/users/folder.asp?FolderID=5987>)



Figure 3.2 Distribution of Alberta Oil sands
 (http://upload.wikimedia.org/wikipedia/commons/7/7a/Athabasca_Oil_Sands_map.png).

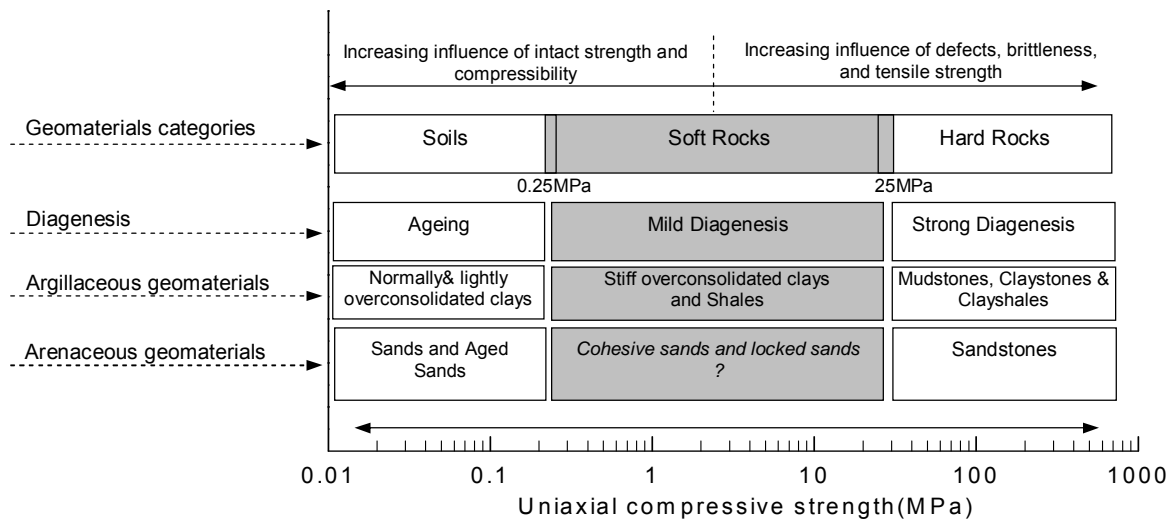


Figure 3.3 Geomaterials categories according to Digenetic processes (modified from Barton 1993 and according to ISRM 1978).

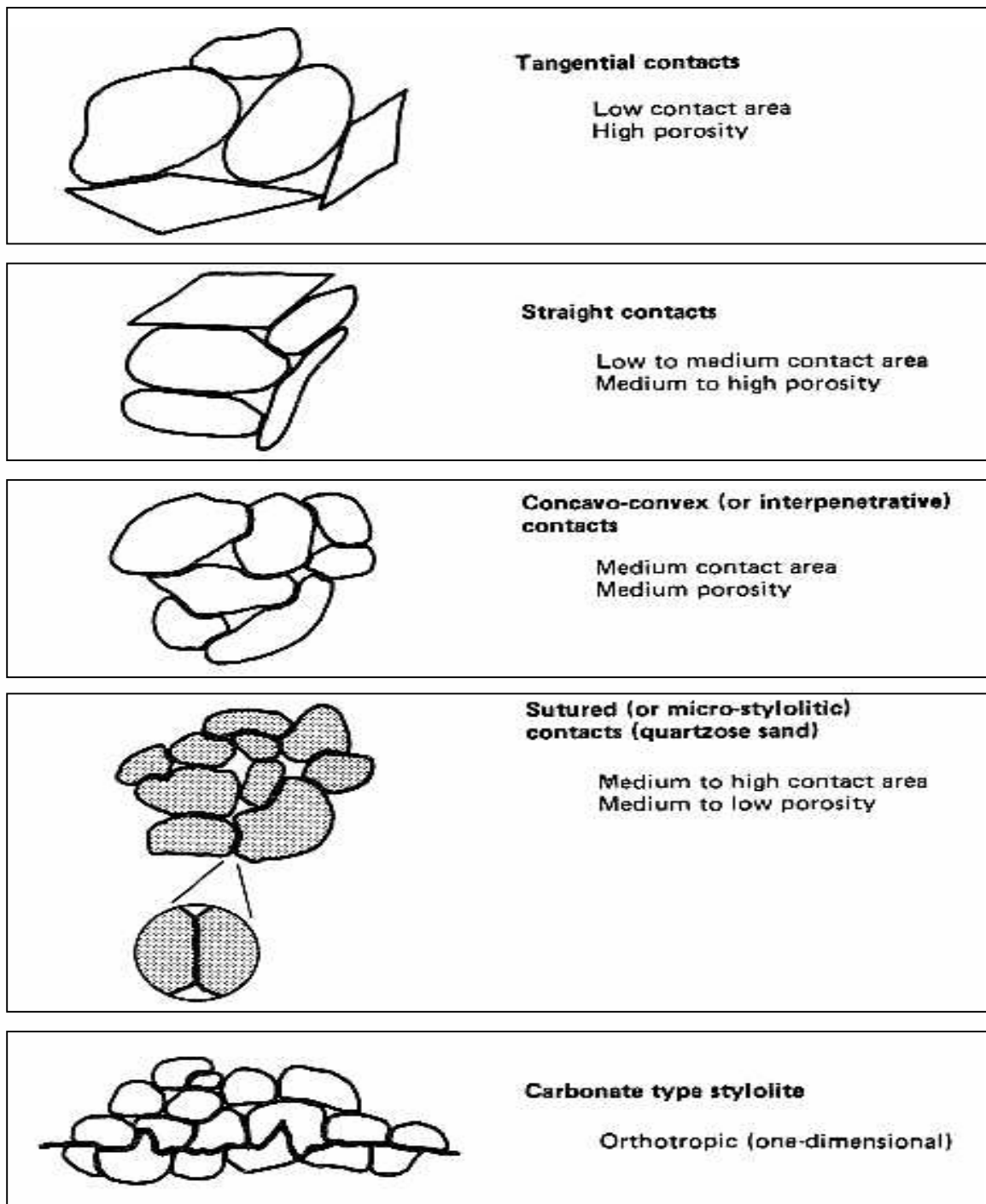


Figure 3.4 Classification of contacts in sandstones (modified from Siever 1959).

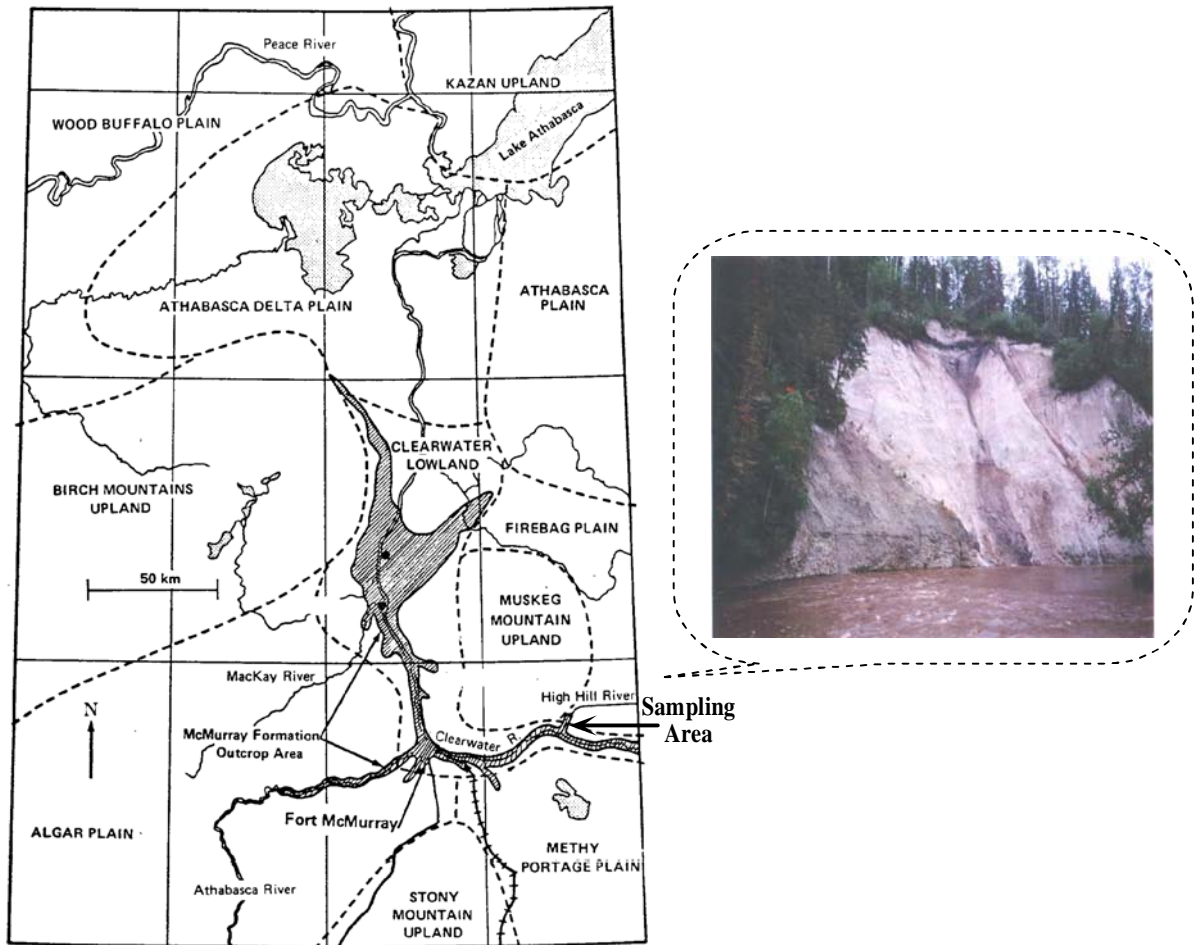
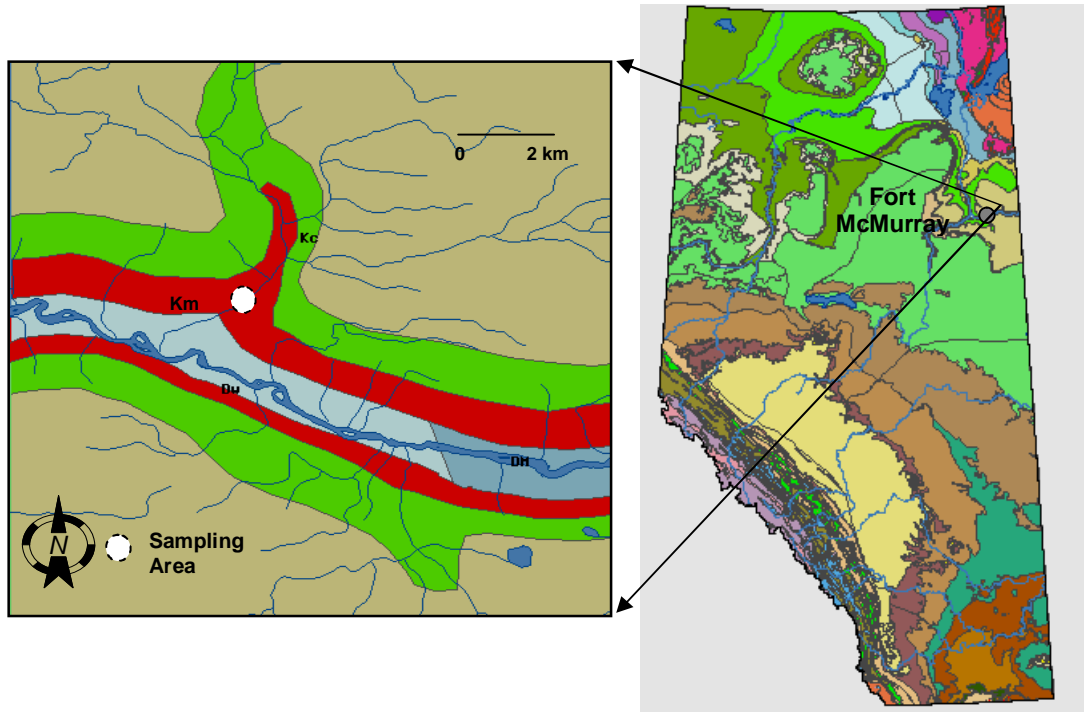
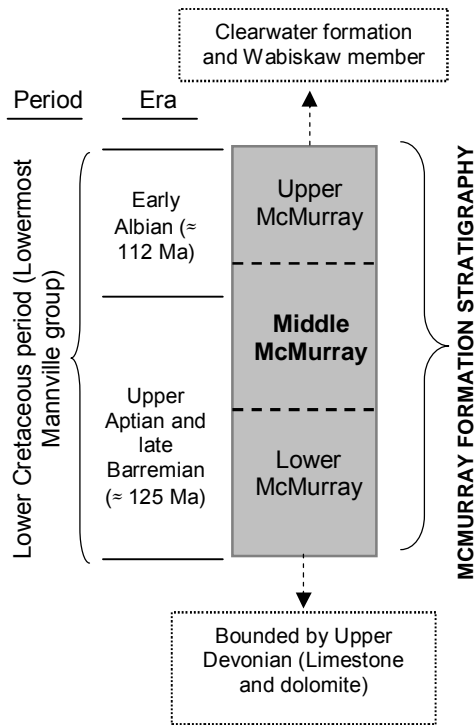


Figure 3.5 Physiography of the Athabasca oil sands and location of sampling area (modified from Dusseault 1977).

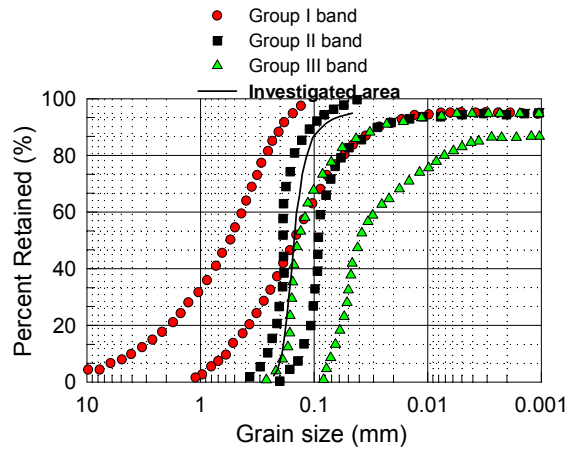


Color Code for investigated vicinity	Bedrock Geology
	LOWER CRETACEOUS PELICAN FORMATION: fine-grained quartzose sandstone, silty and glauconitic in lower part; marine
	LOWER CRETACEOUS MCMURRAY FORMATION (≈130 Ma; Million years ago): Thick-bedded quartzose sandstone and siltstone; oil- impregnated, grey silty shale interbeds in upper part; non-marine to detalic
	LOWER CRETACEOUS CLEARWATER FORMATION: dark grey, fossiliferous, silty shale, laminated siltstone and fine-grained cherty sandstone; glauconitic sandstone (Wabiskaw member) near base; marine.
	UPPER DEVONIAN WATERWAYS FORMATION (pre-cretaceous erosion surface): grey and greenish grey shale and argillaceous limestone interbedded with grey and grayish brown, fine-grained to coarse clastic limestone; marine.
	MIDDLE DEVONION (undivided): arkosic sandstone (La Loche Formation); grey-green silty and sandy shale, reddish shale; dolomite; minor anhydrite (Mc Lean River Formation); brown and buff, massive, porous dolomite; brown to grey thin-bedded dolomite; dolomite limestone (Methy formation); gypsum; anhydrite; grey-green silty and dolomitic shale; minor dolomite (leached Prairie Evaporite Formation); marine and evaporitic

Figure 3.6 Bedrock geology in the investigated vicinity (AEUB and AGS 2005).



(a)



(b)

Figure 3.7 (a) An illustration of tripartite classification of McMurray formation members; and (b) Grain size distribution of Athabasca oil sands (after Carrigy 1967).

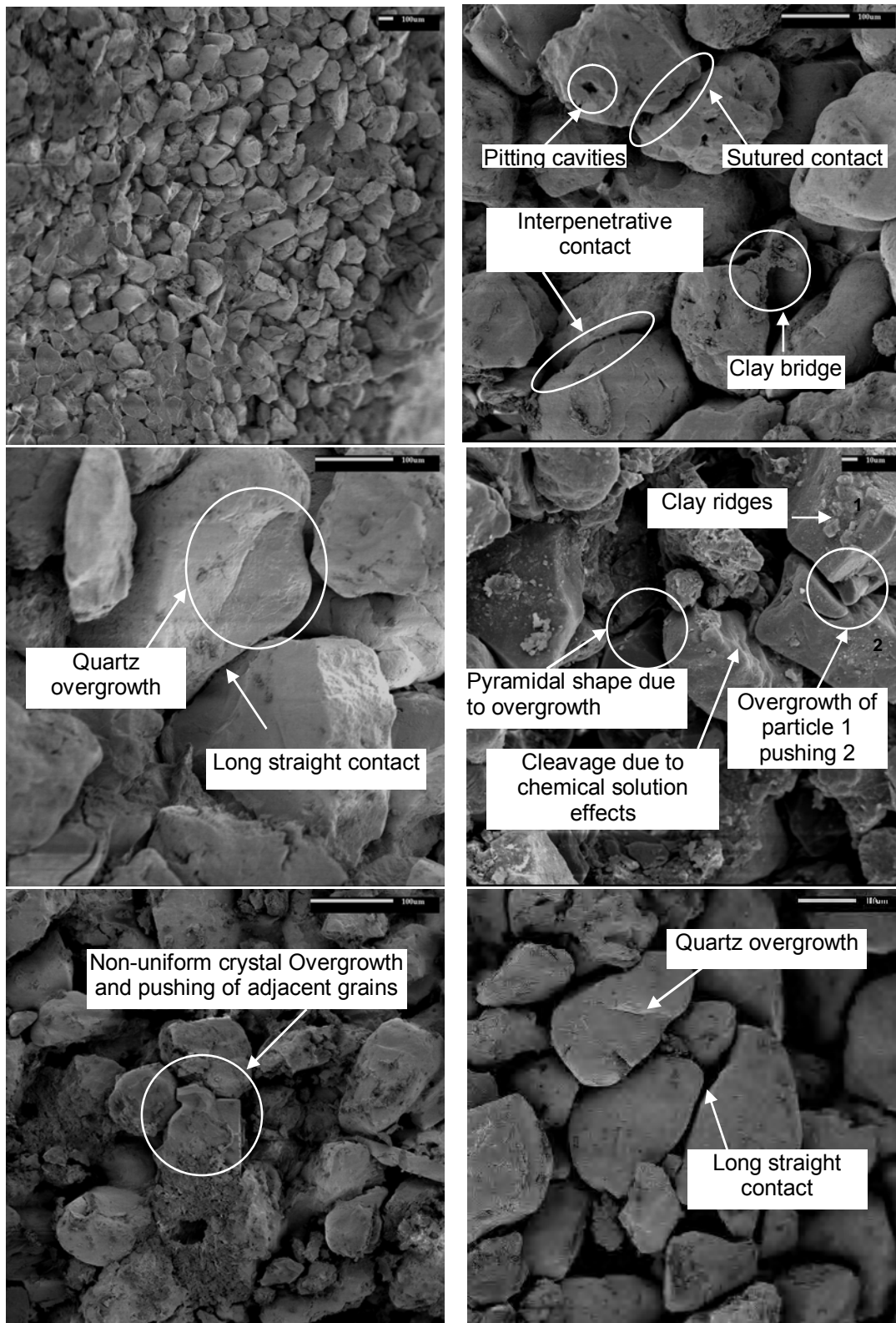


Figure 3.8 Selected SEM micrographs of High-Hill sand formation.

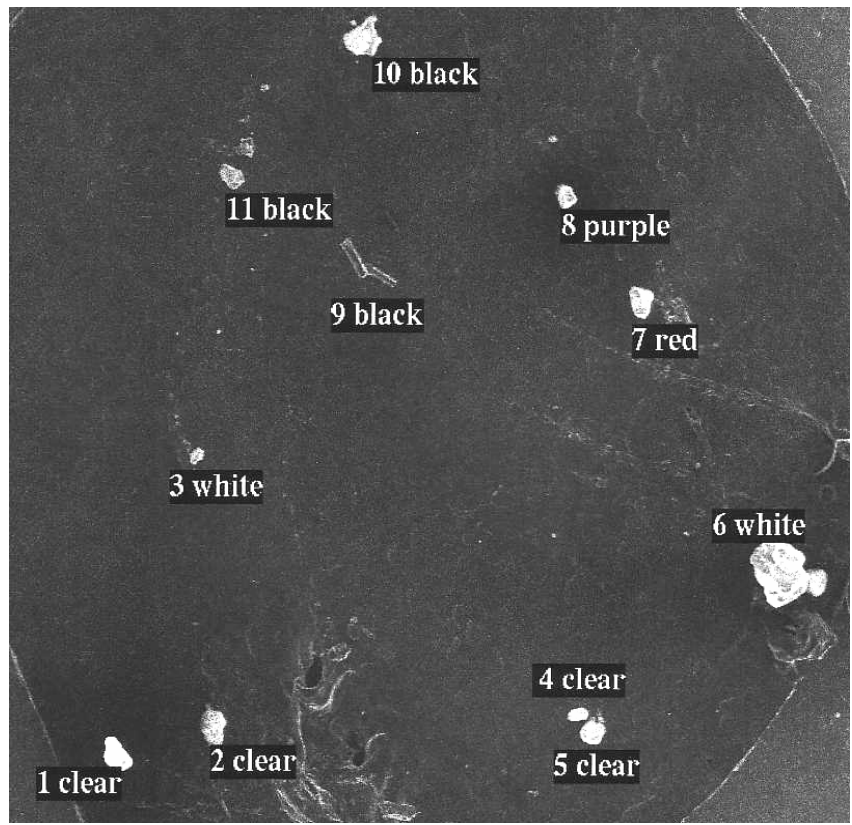
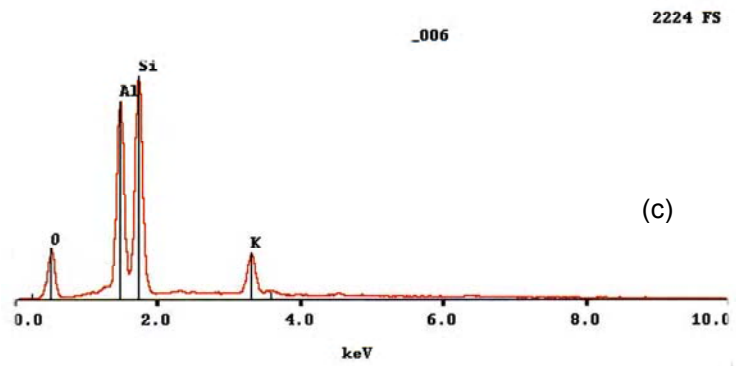
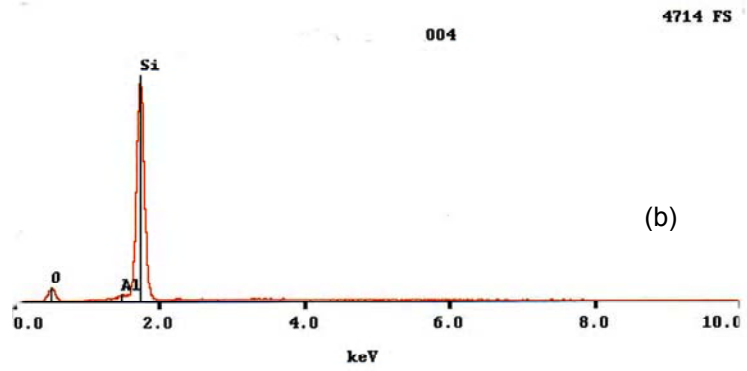
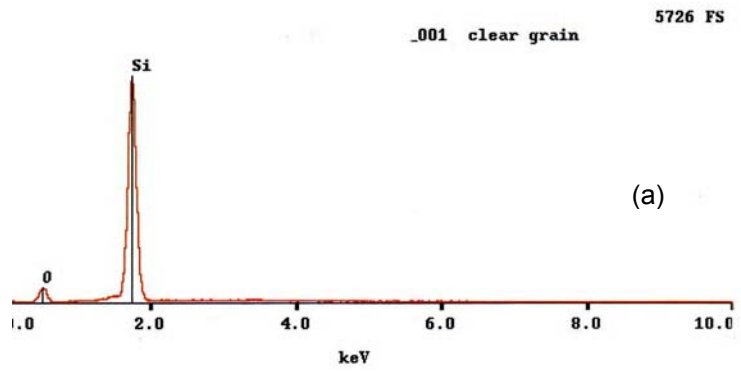


Figure 3.9 Map for collected particles under optical microscope.



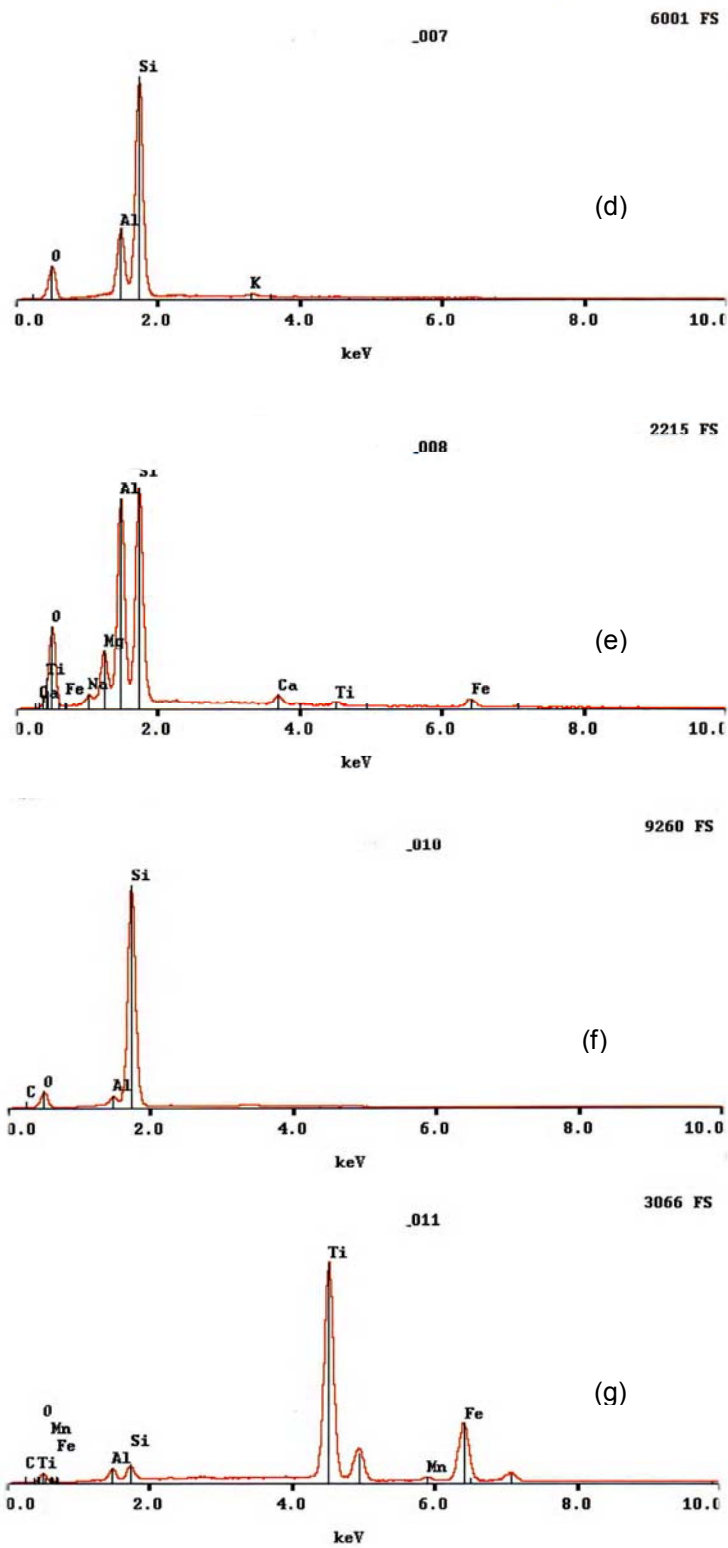


Figure 3.10 Energy dispersion X-ray results for mapped particles: (a-b) quartz; (c): kaolinite; (d) feldspar; (e) amphibole; (f) chert; and (g): titanium

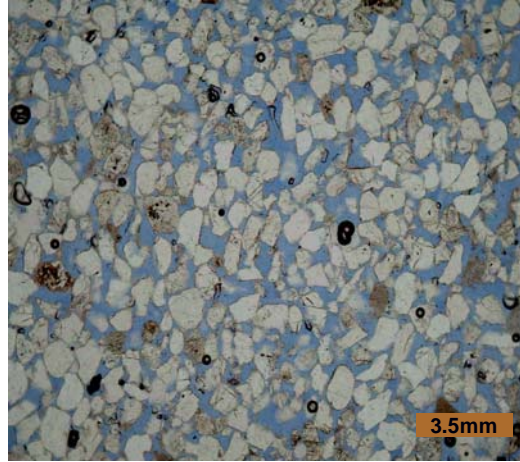


Figure 3.11 Micrograph of well -sorted band under PPL: width of view 3.5 mm, illustrating quartz grains as white, very fine grained rock fragments, and clay as grey and pores in blue.

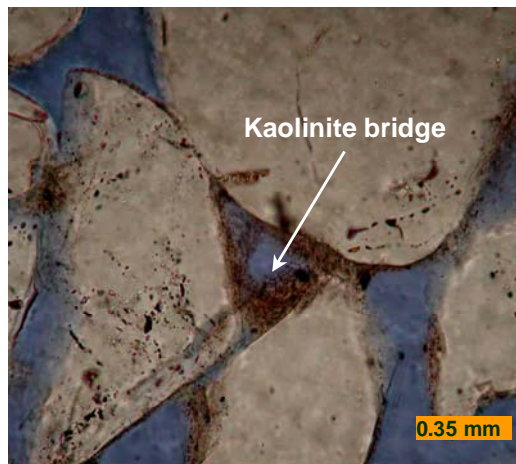


Figure 3.12 Micrograph under PPL showing kaolinite bridge between three quartz particles: width of view 0.35 mm.

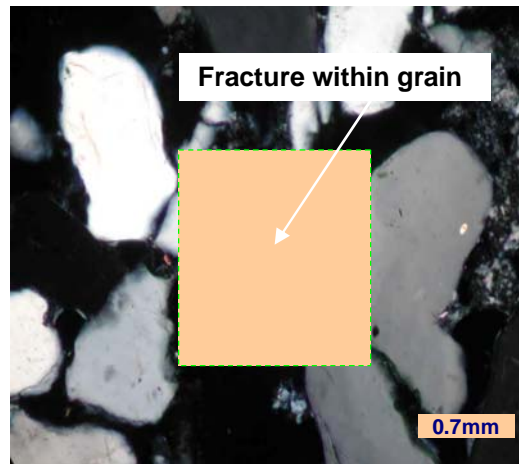


Figure 3.13 Micrograph under CPL showing particle fracture: width of view 0.7 mm.

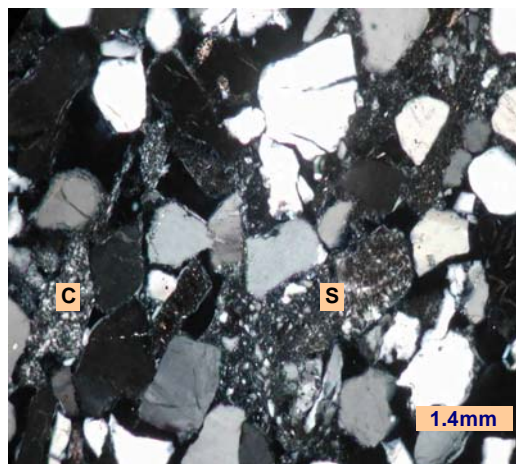


Figure 3.14 Micrograph of less-sorted band under CPL: width of view 1.4 mm, illustrating quartz grains as white and light to dark grey; very fine grained rock fragments as black with white spots, siliceous siltstone (S), chert (C); and pores as black.

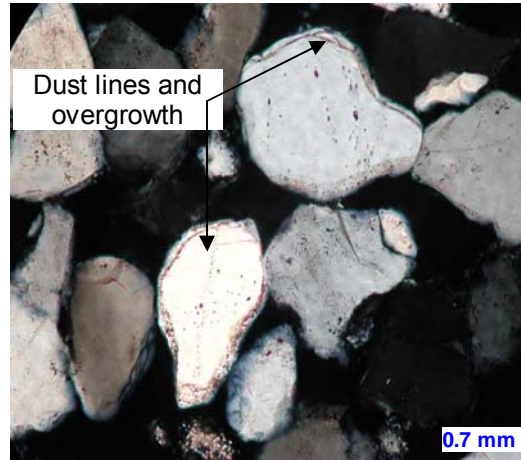


Figure 3.15 Micrograph under CPL: width of view 0.7 mm, illustrating quartz overgrowth, quartz grains as white and light to dark grey, and pores as black.

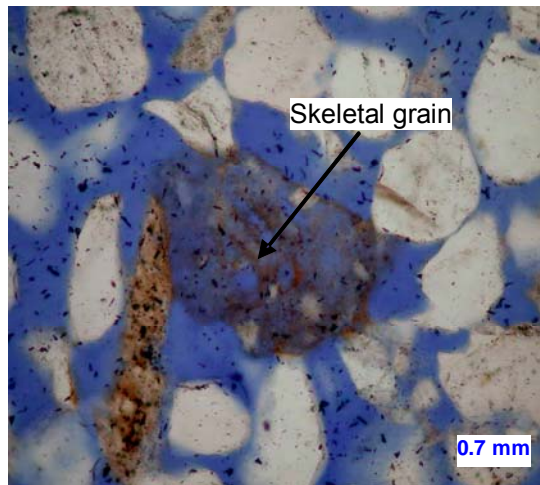
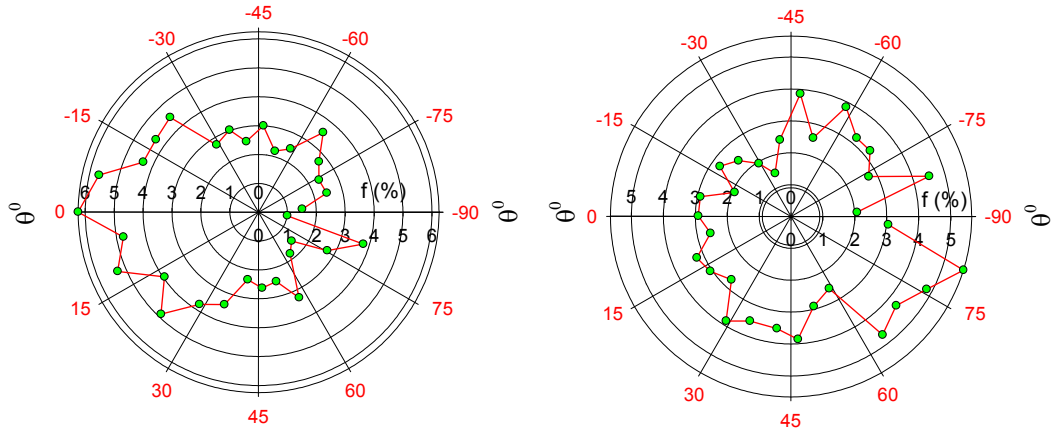


Figure 3.16 Micrograph under PPL: width of view 0.7 mm, illustrating existence of a skeletal grain due to dissolution during diagenesis.



(a) Vertical section

(b) Horizontal section

Figure 3.17 Distribution of particles orientation in horizontal and vertical direction: (a) Horizontal section; and (b) Vertical section.

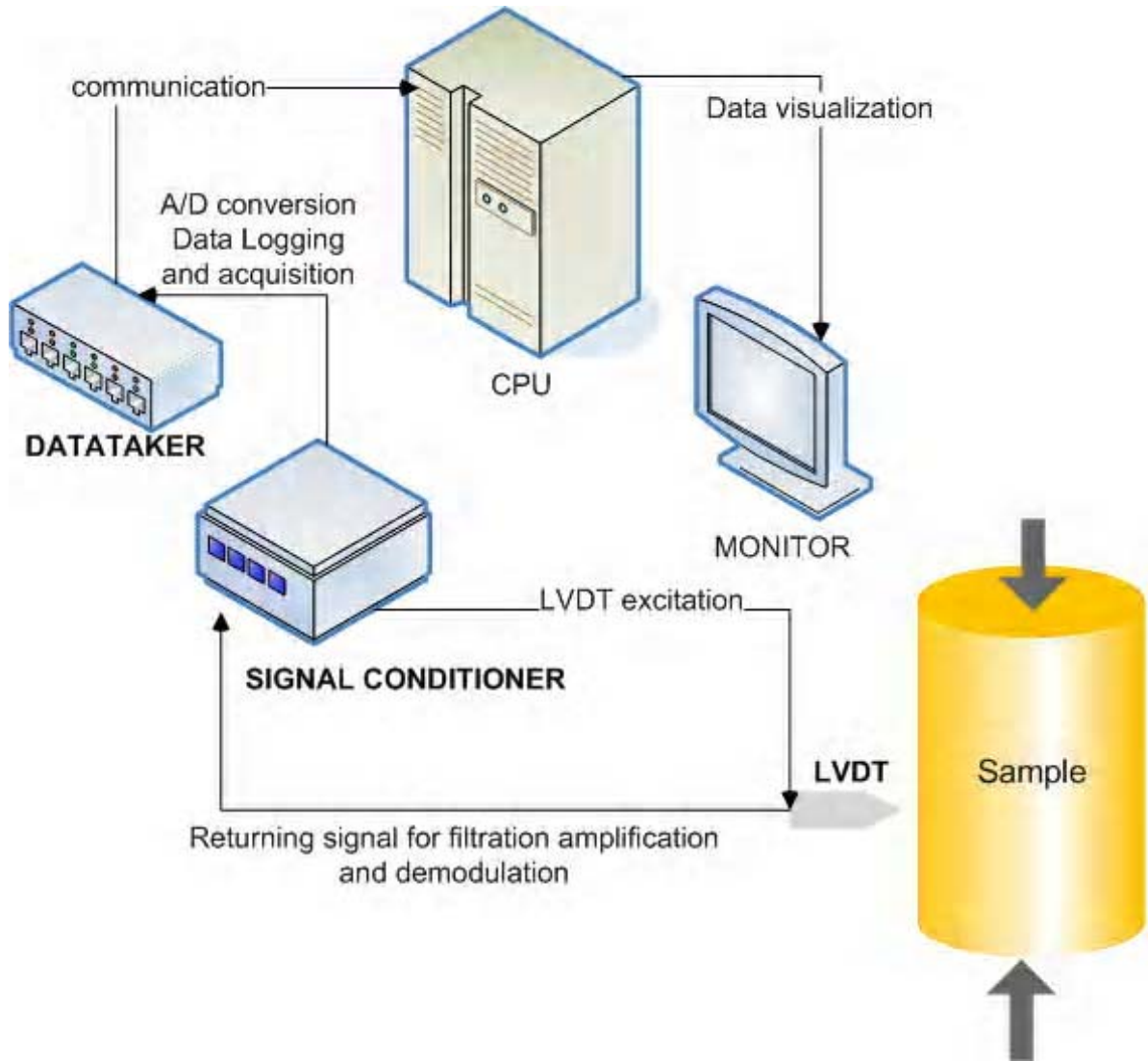


Figure 3.18 Signals cycle and laboratory components.

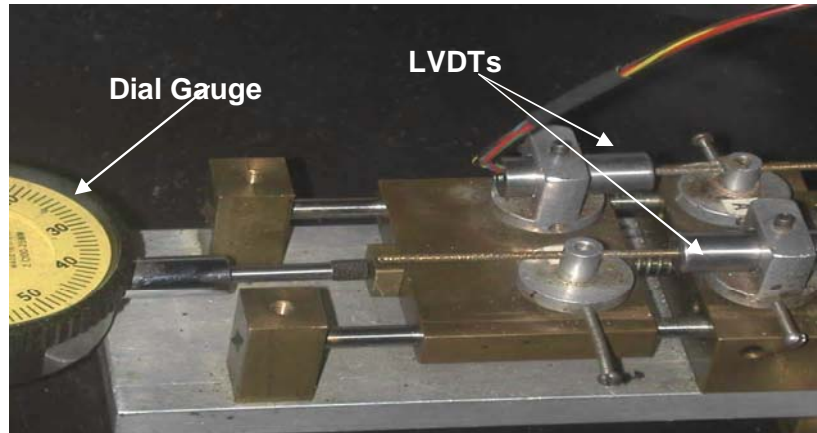


Figure 3.19 Micrometer for LVDTs calibration.

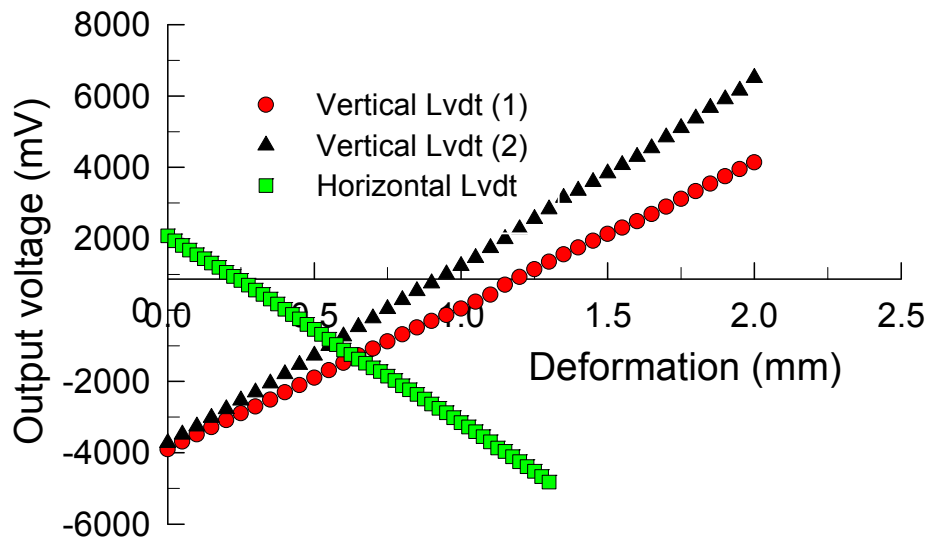


Figure 3.20 A sample of LVDTs calibration charts.

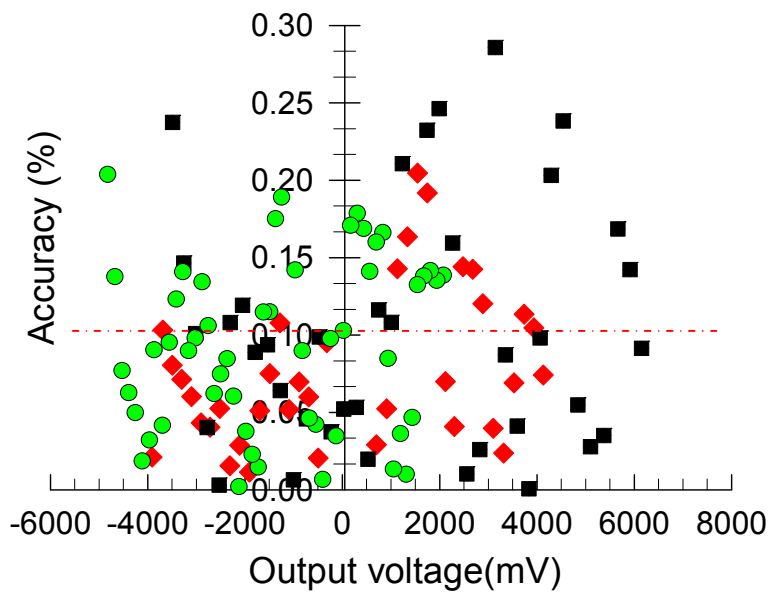


Figure 3.21 Accuracy versus Output voltage.

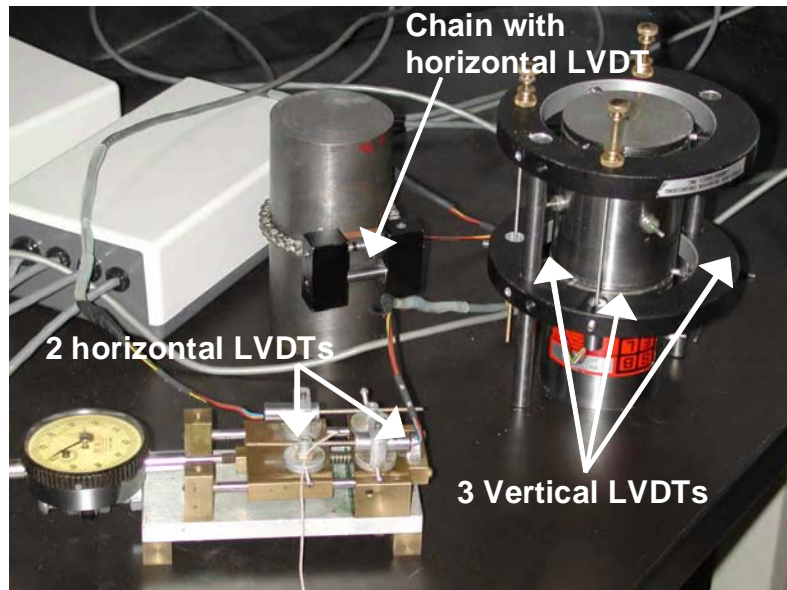


Figure 3.22 Transducers setup for stability test.

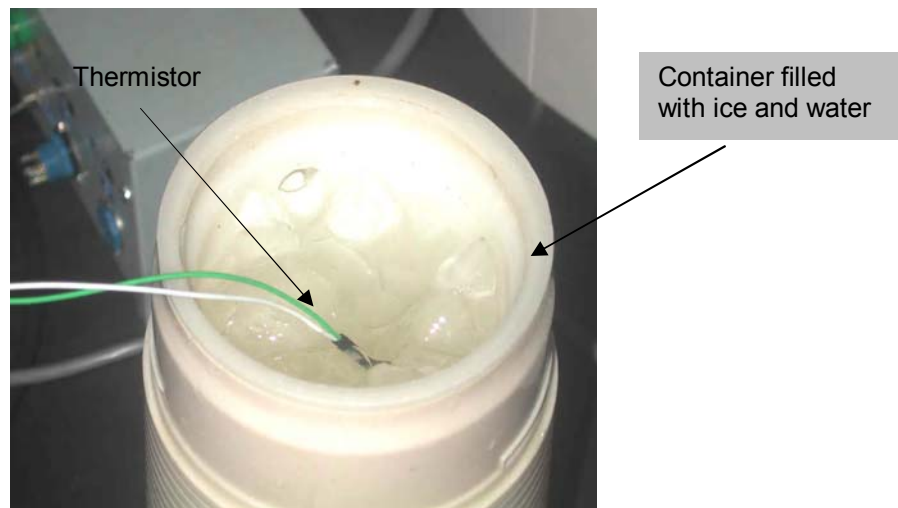


Figure 3.23 A picture of the thermistor embedded in ice water container for calibration purpose.

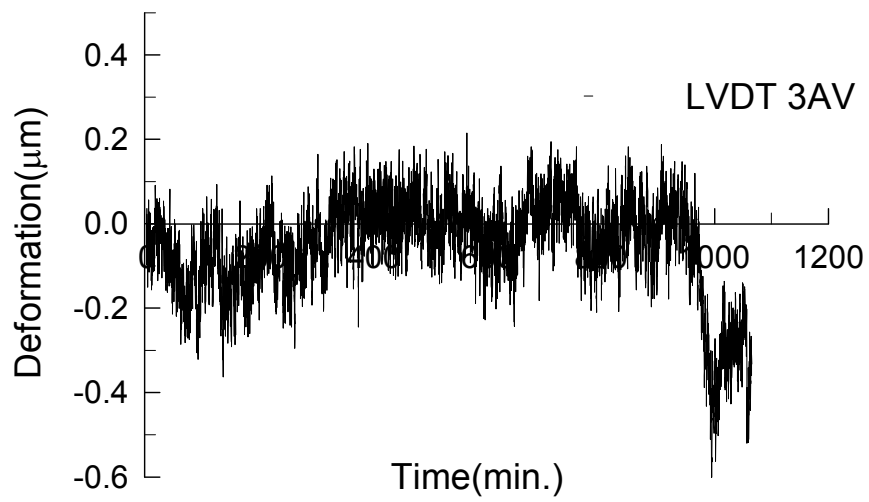


Figure 3.24 Stability of an LVDT for almost 24 hrs.

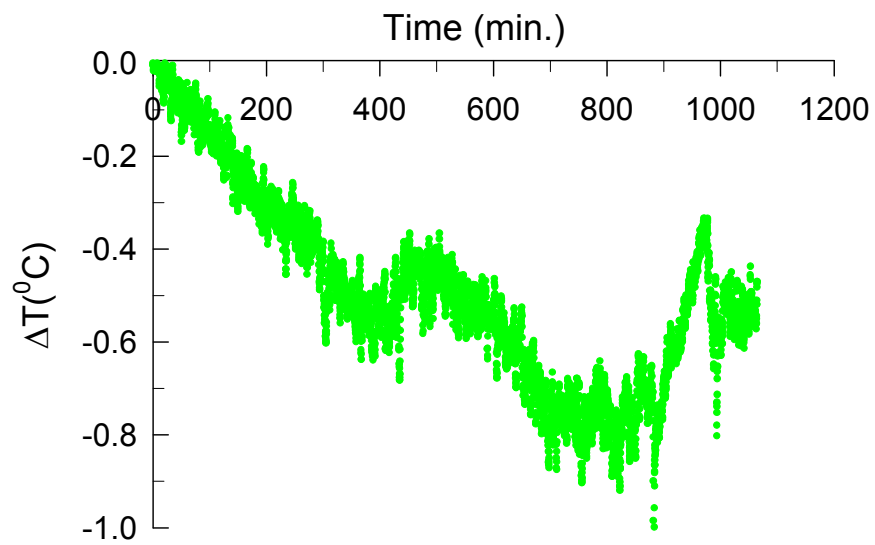


Figure 3.25 Variation of temperature with time.

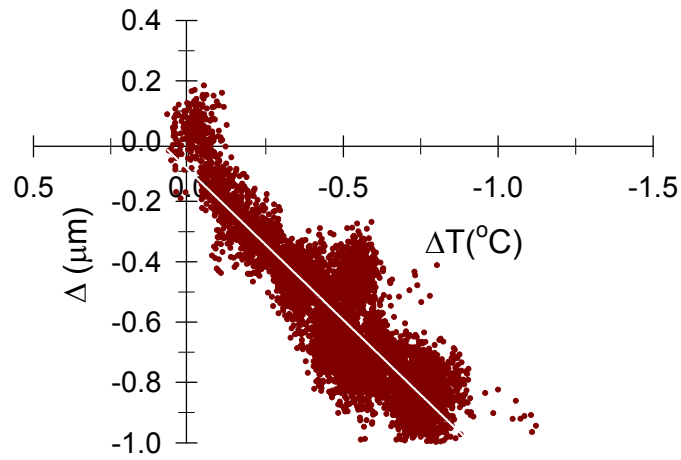


Figure 3.26 An illustration for variation of deformation with temperature for 24 hrs.

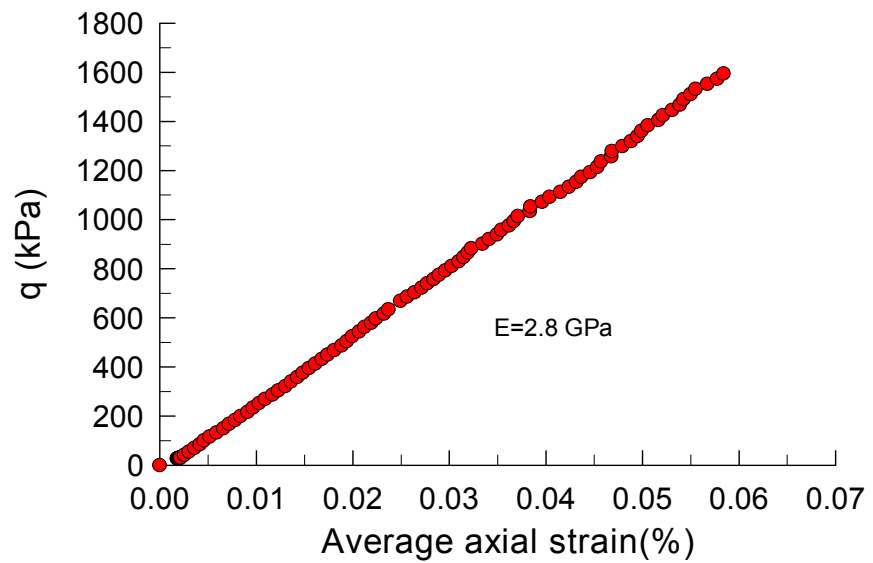


Figure 3.27 Proof testing results of a PVC sample.

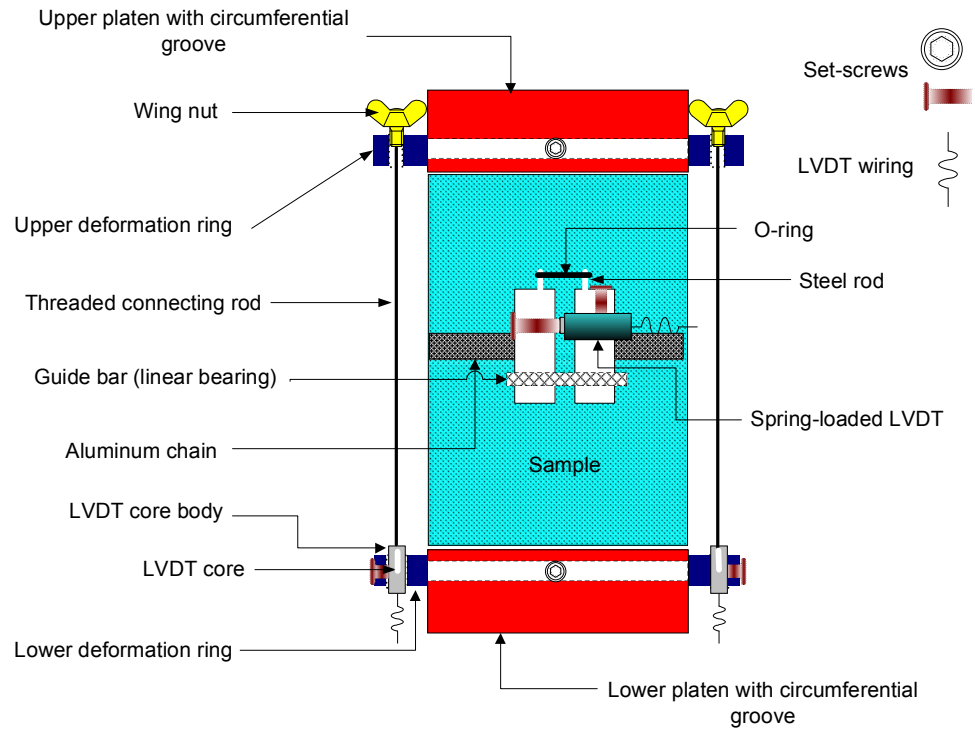


Figure 3.28 Original mechanical configuration and accessories.

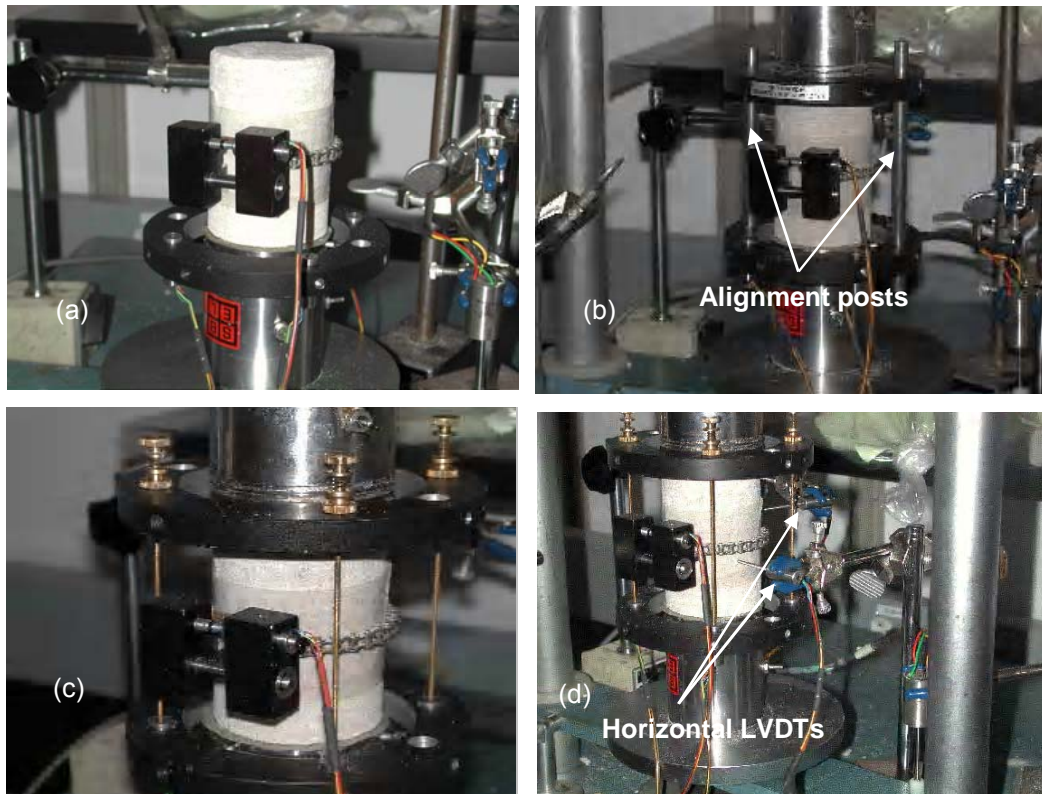


Figure 3.29 Mechanical configuration, accessories and mounting steps (modified set).

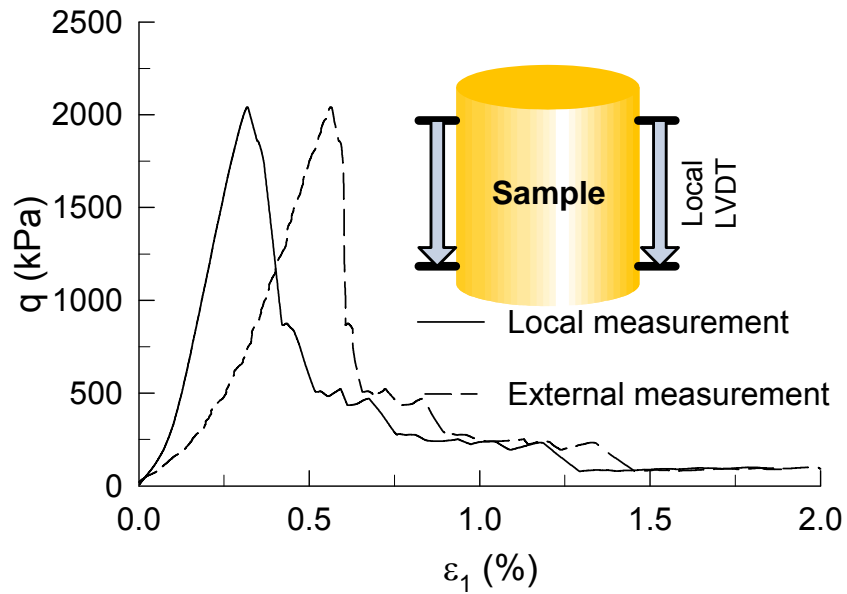


Figure 3.30 Local and external axial stress vs. axial strain curves.

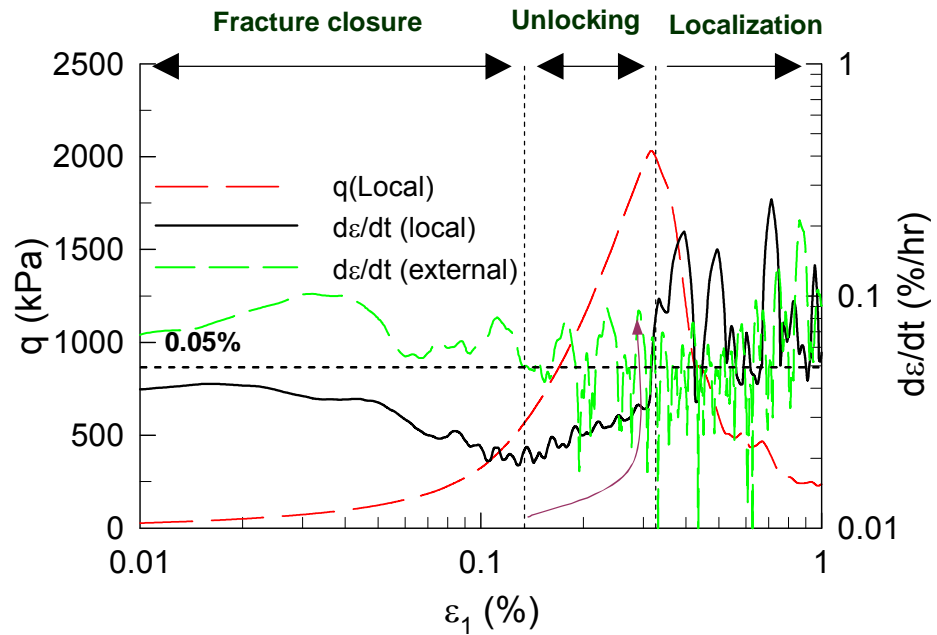


Figure 3.31 Comparison of external and local axial strain's rate.

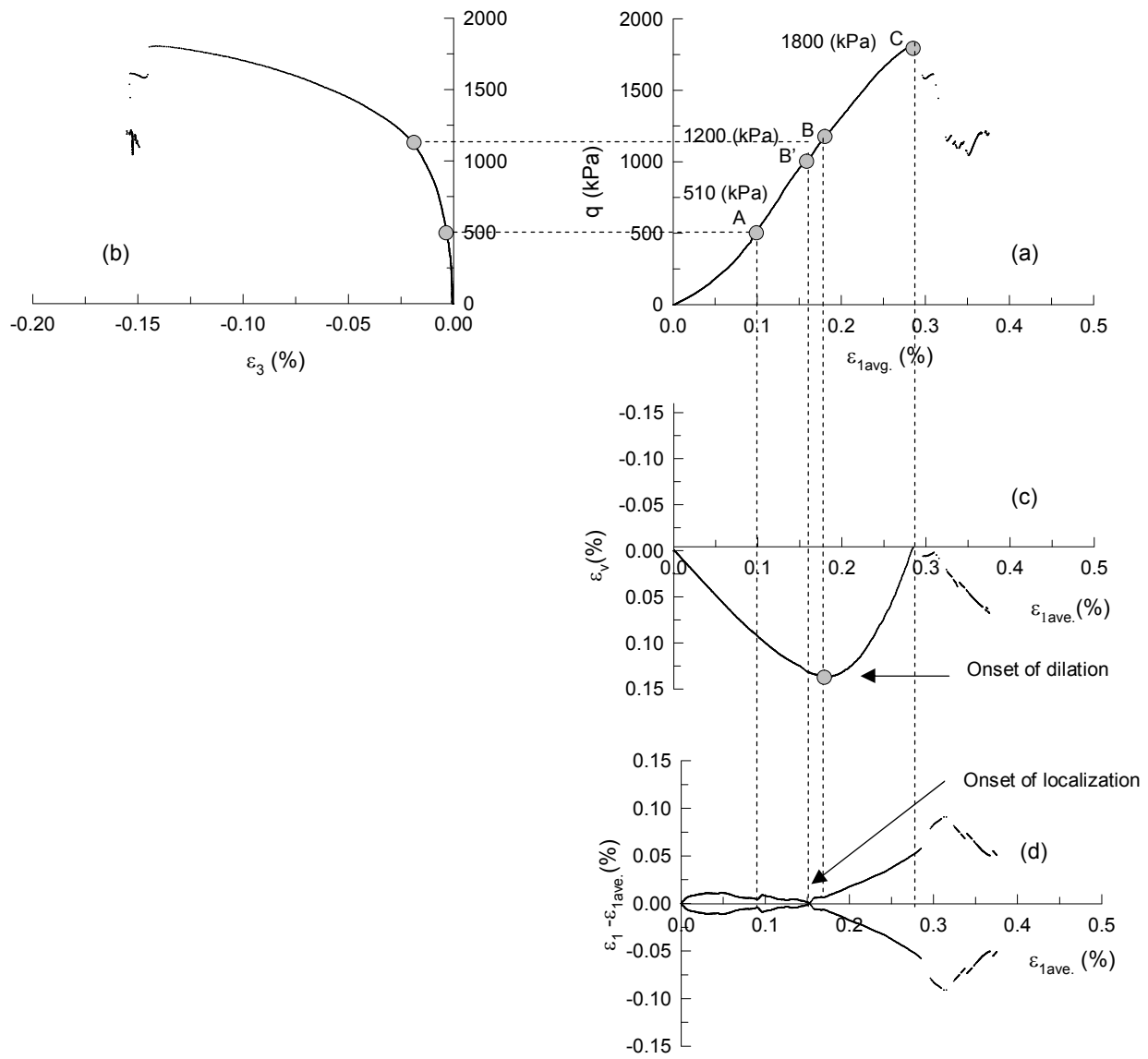


Figure 4.1 Experimental results illustrating variation of deviator stress, axial, lateral and volumetric strains during shear evolution.

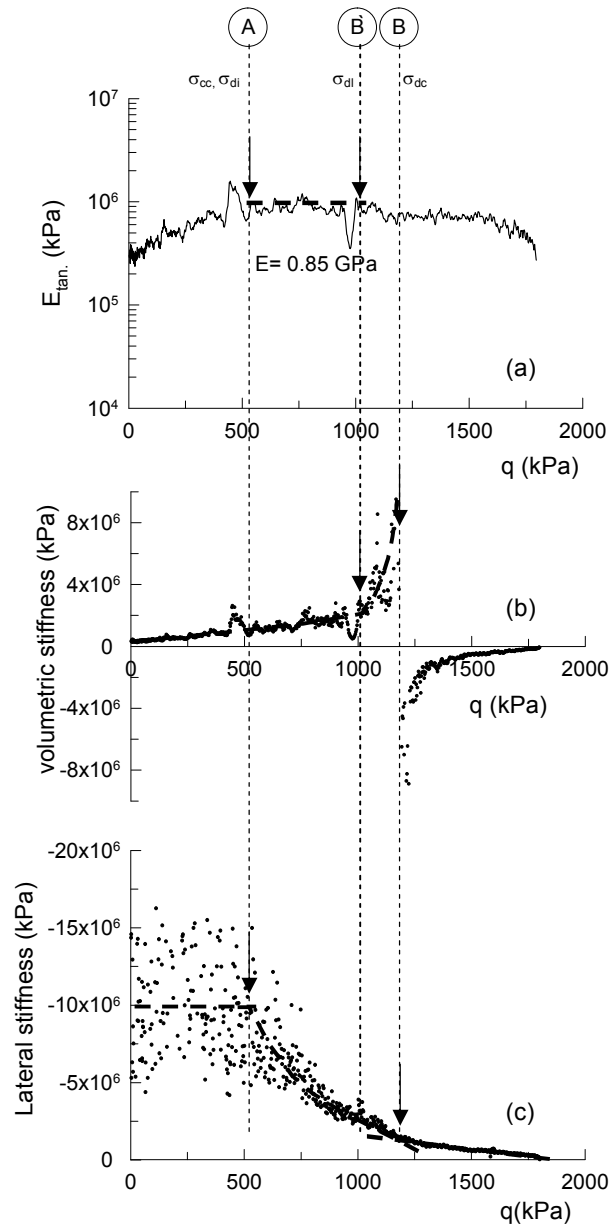


Figure 4.2 Variation in tangential axial stiffness, volumetric stiffness, and lateral stiffness during shear evolution.

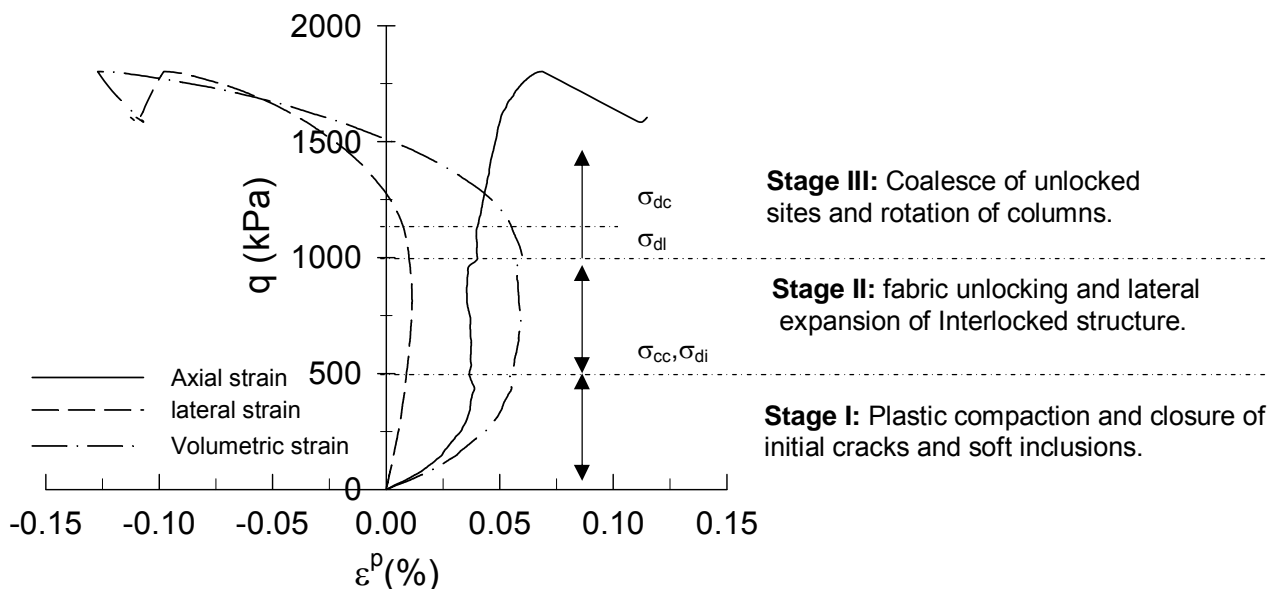


Figure 4.3 Relationship between the deviator stress, plastic axial, lateral, and volumetric strains.

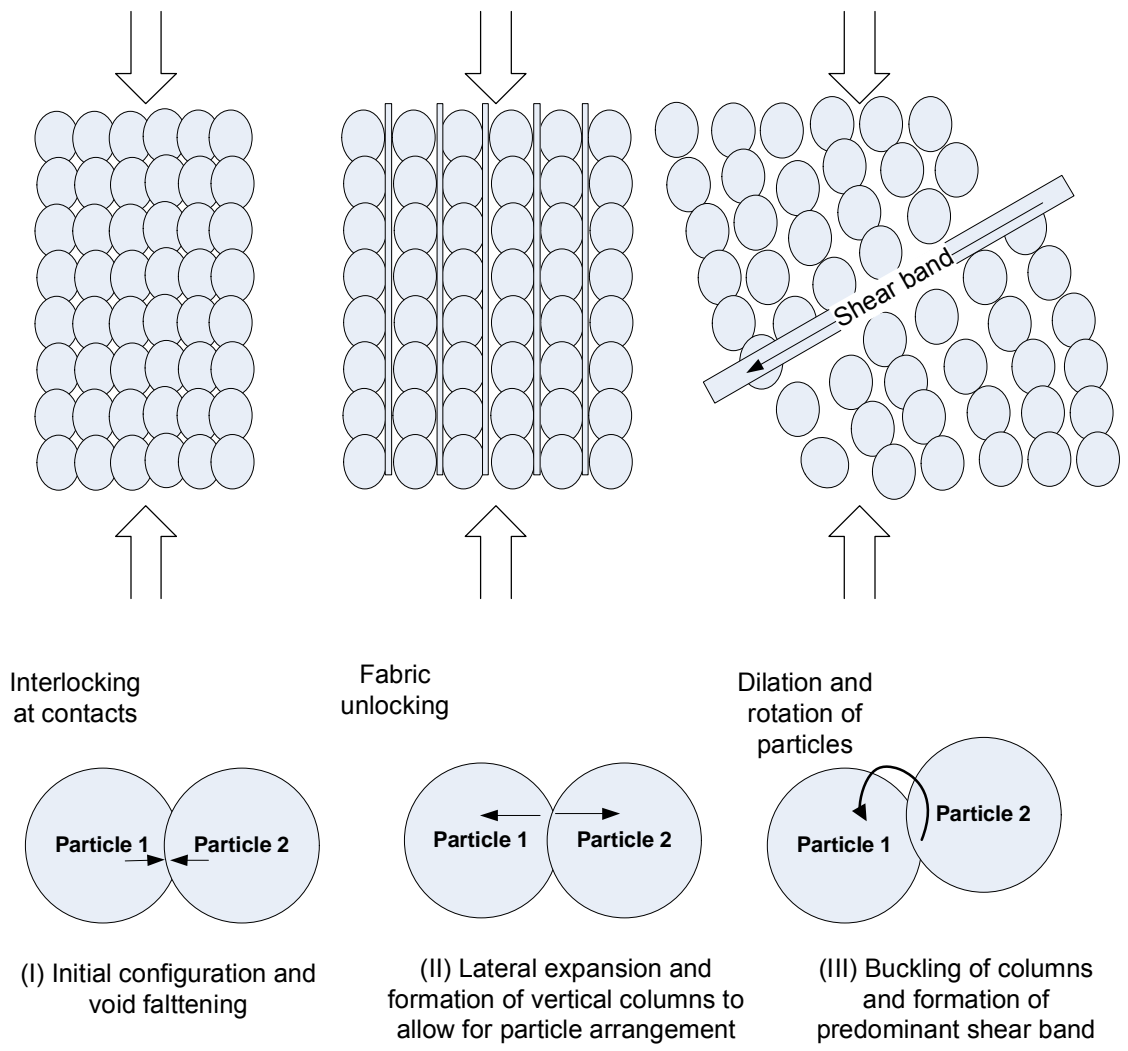


Figure 4.4 Mechanism of failure in cylindrical locked sand specimen.

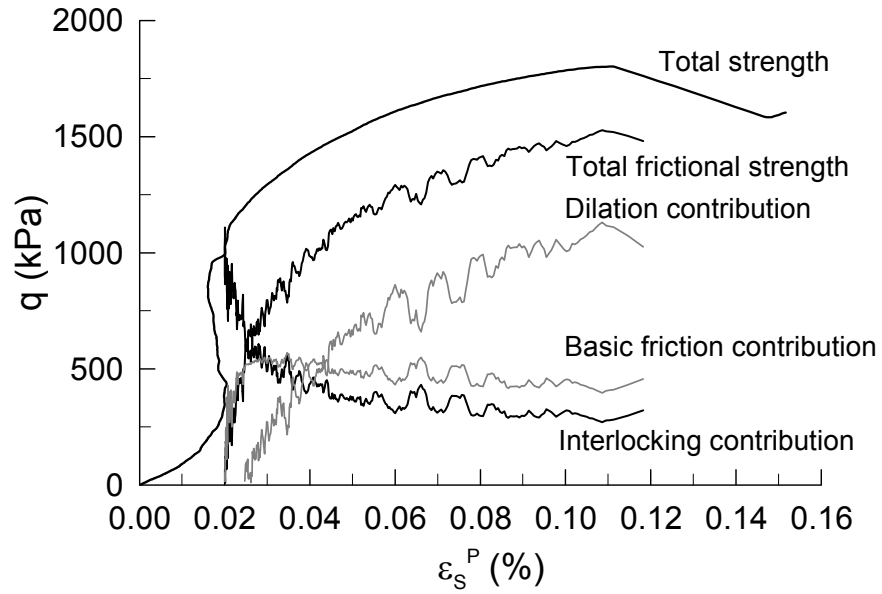


Figure 4.5 Variation of frictional as well as interlocking strength components with plastic shear strain.

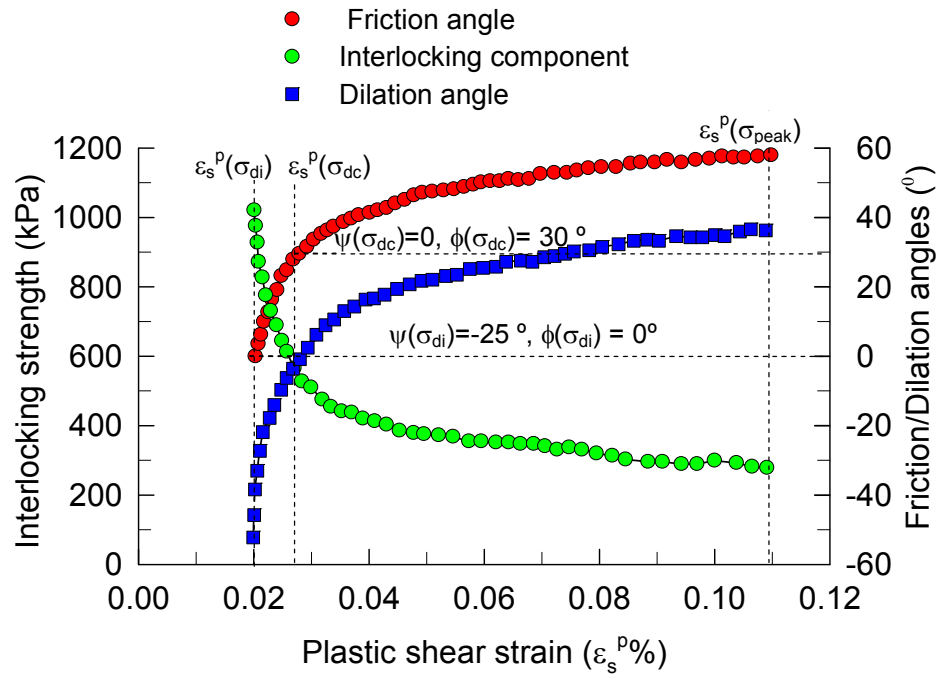
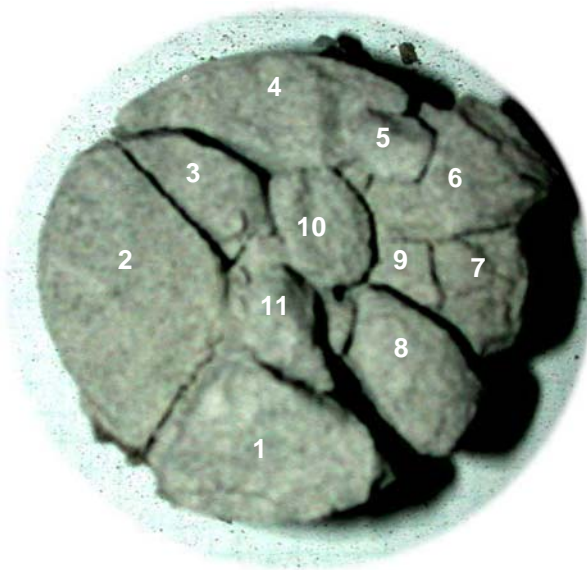


Figure 4.6 Mobilized strength components with plastic shear strain in terms of interlocking component, friction angle, and dilation angle.



(a)



(b)

Figure 4.7 Formation of axially extended columnar structures under homogeneous strain field (observe curvature at columns interface): (a) longitudinal view of failure pattern; and (b) cross sectional view.

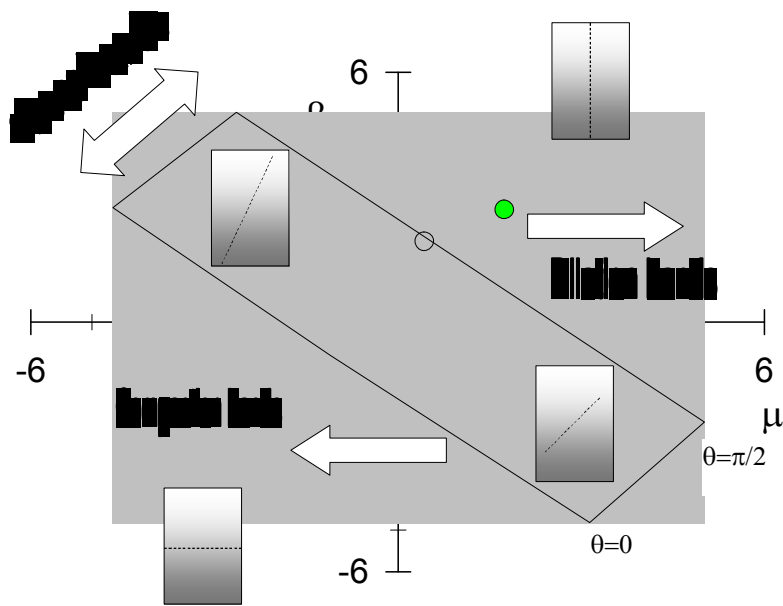
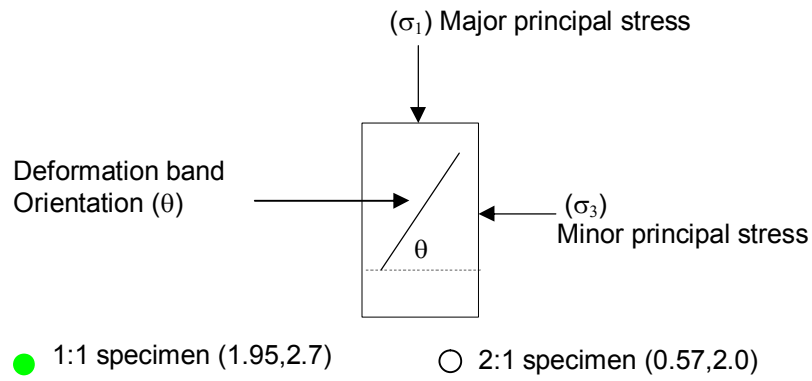


Figure 4.8 Deformation bands boundaries and orientation for axisymmetrical compression stress path derived from bifurcation criterion for porous rocks (Poisson's ratio $\nu=0.2$).

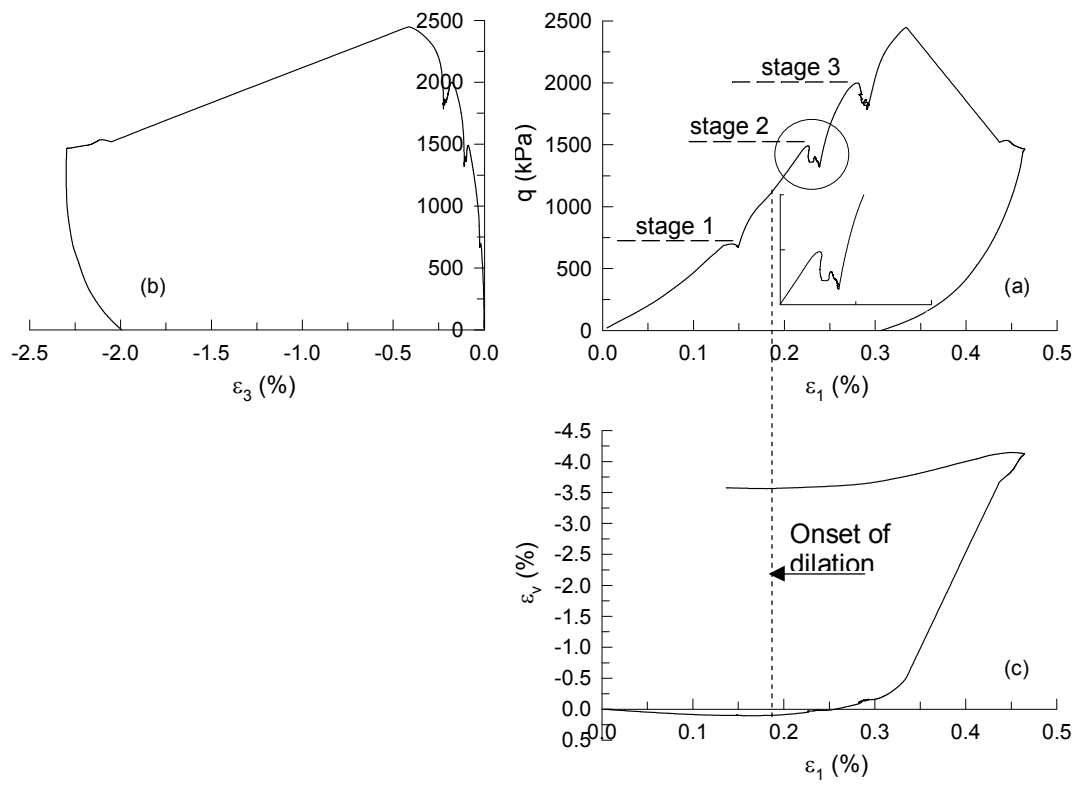


Figure 4.9 Stress-strain and volumetric strain curves during creep test.

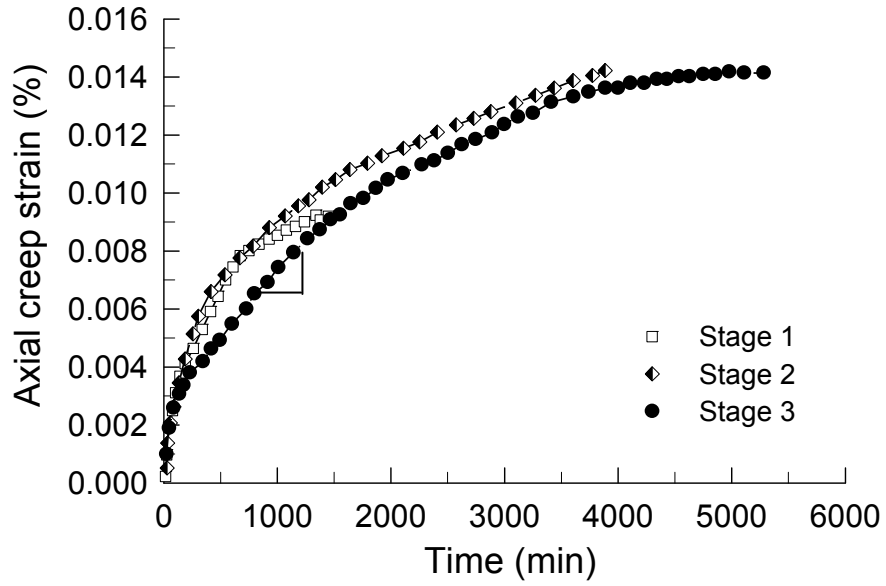


Figure 4.10 Variation of axial strain with time during creep stages.

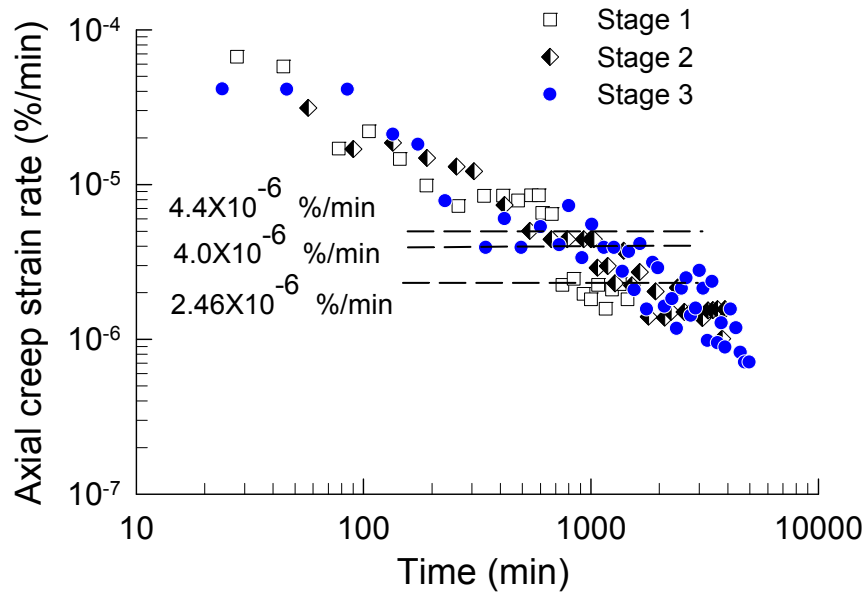


Figure 4.11 Variation of axial strain rates during creep stages.

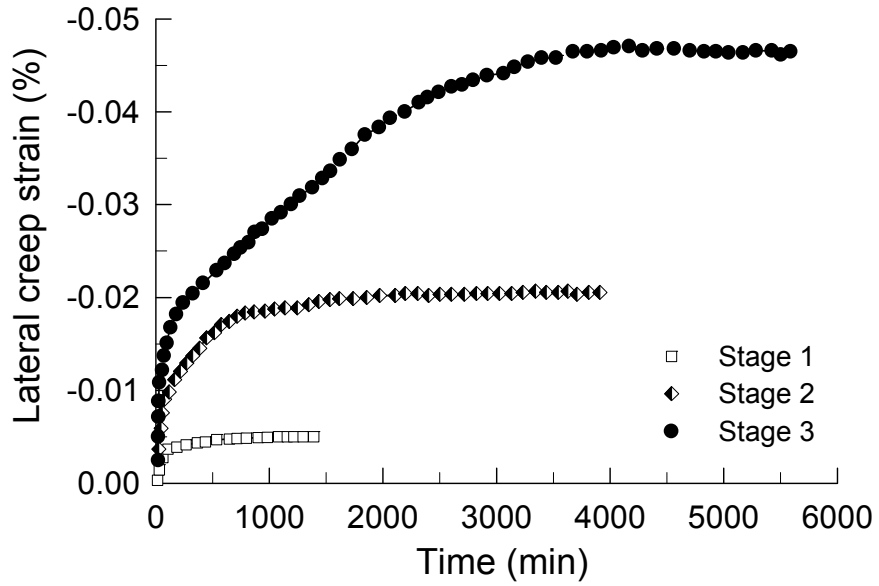


Figure 4.12 Variation of lateral strain with time during creep stages.

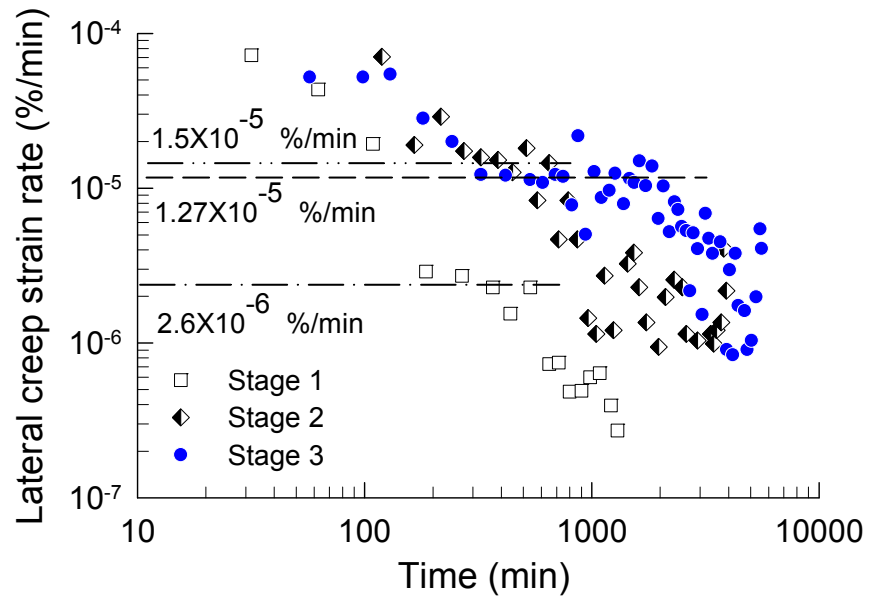


Figure 4.13 Variation of lateral strain rates during creep stages.

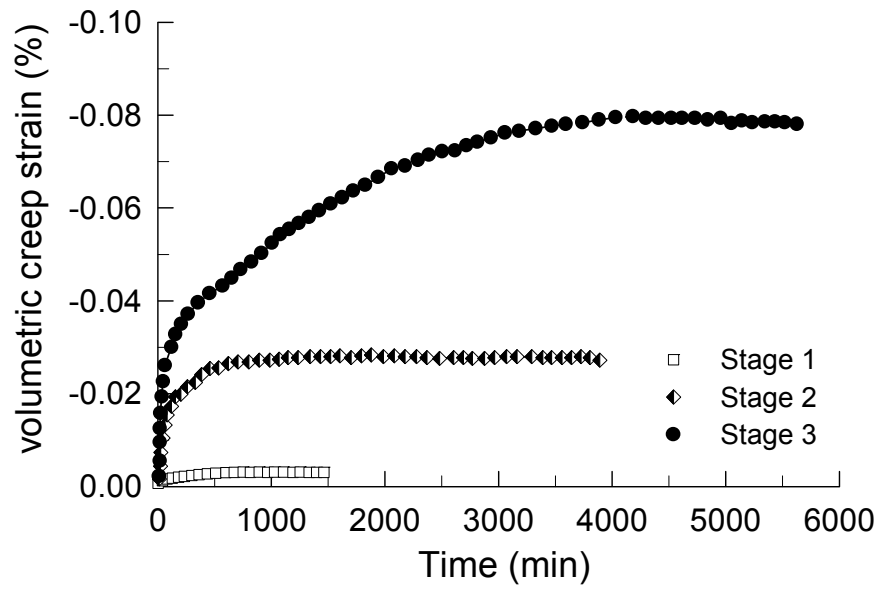


Figure 4.14 Variation of volumetric strains during creep stages.

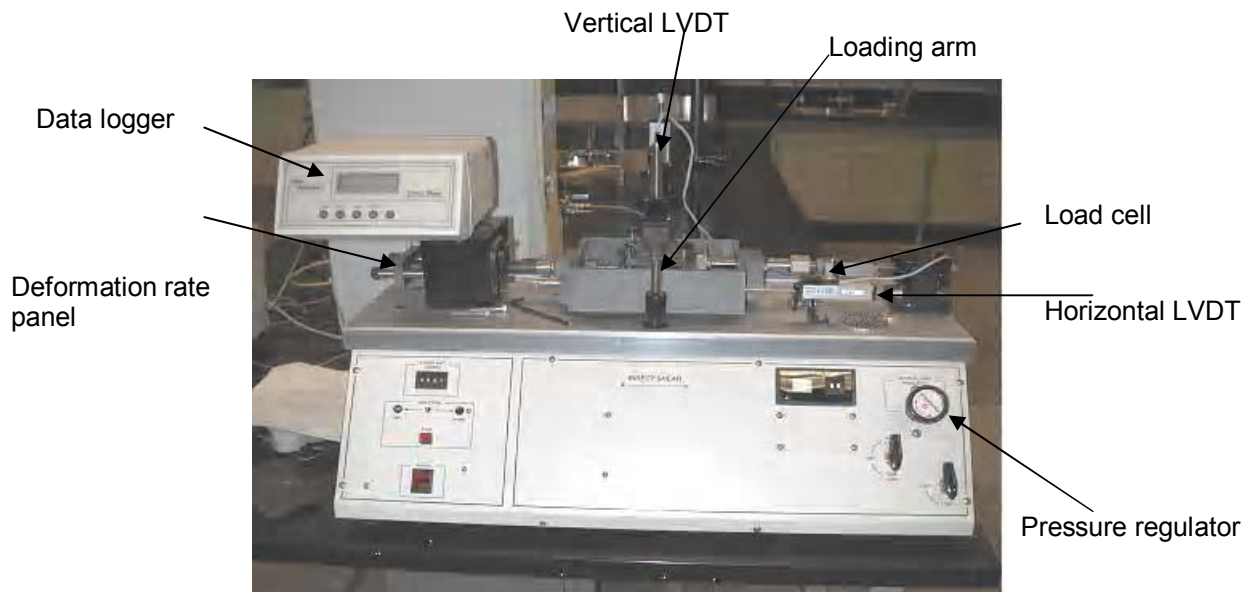


Figure 4.15 Direct shear test apparatus and its components.

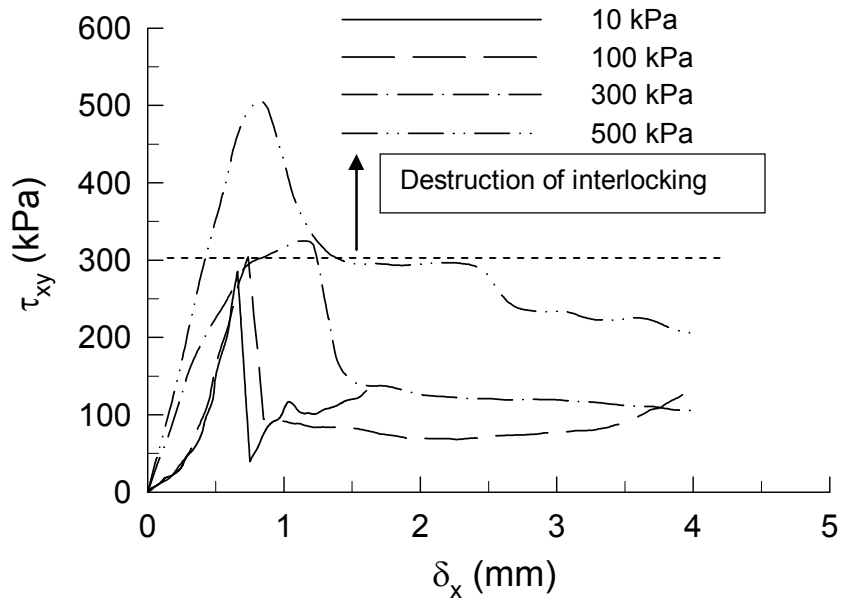


Figure 4.16 Shear stress vs. horizontal deformation in DSB.

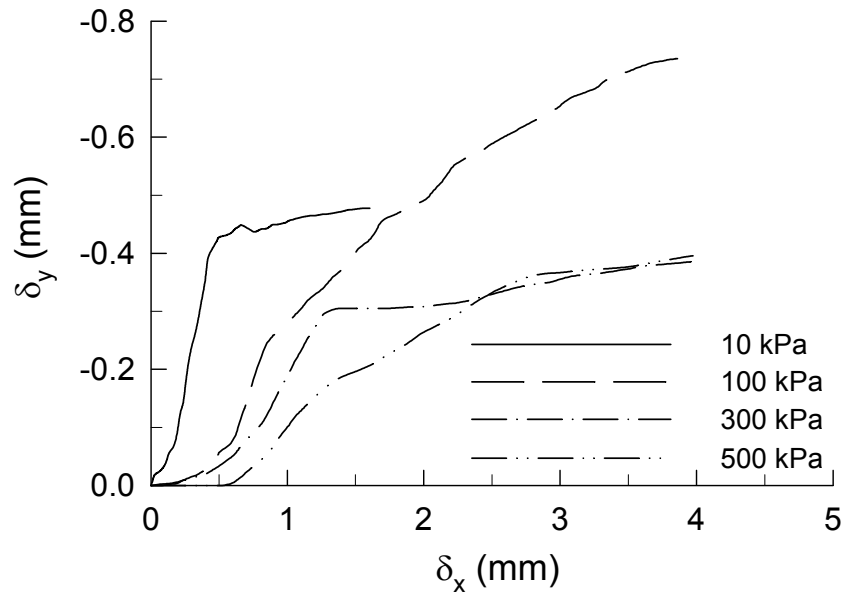


Figure 4.17 Vertical deformation vs. horizontal deformation in DSB.

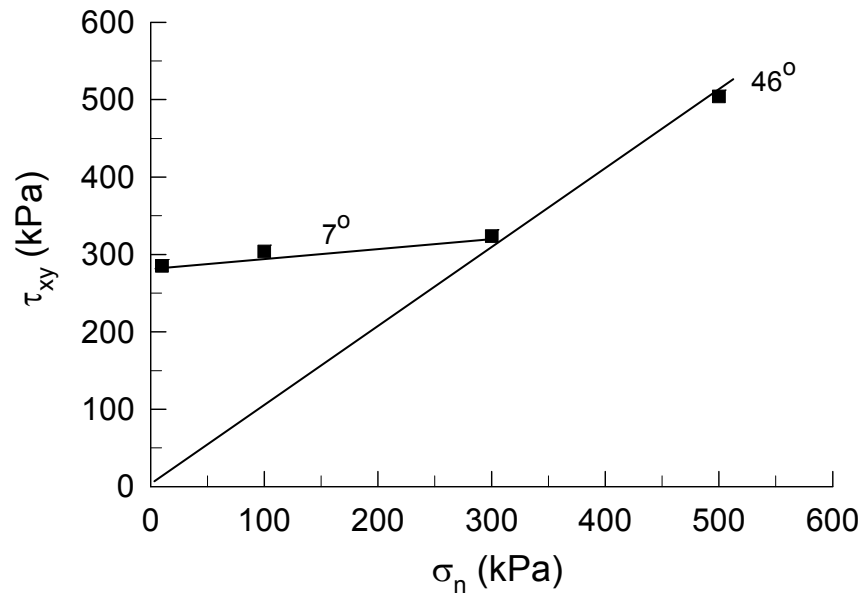


Figure 4.18 Failure envelope for locked sand from direct shear tests.

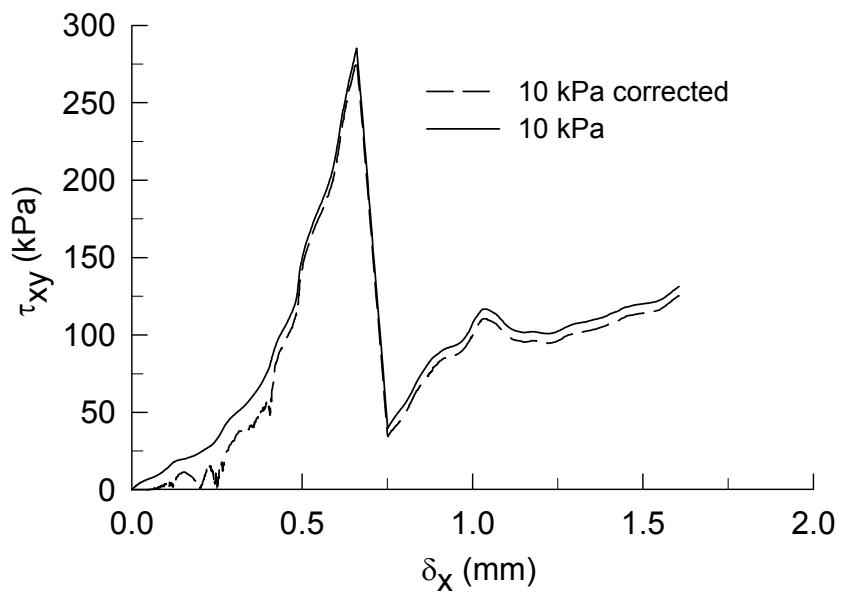


Figure 4.19 Corrected shear stresses for a specimen tested under a normal stress of 10 kPa.

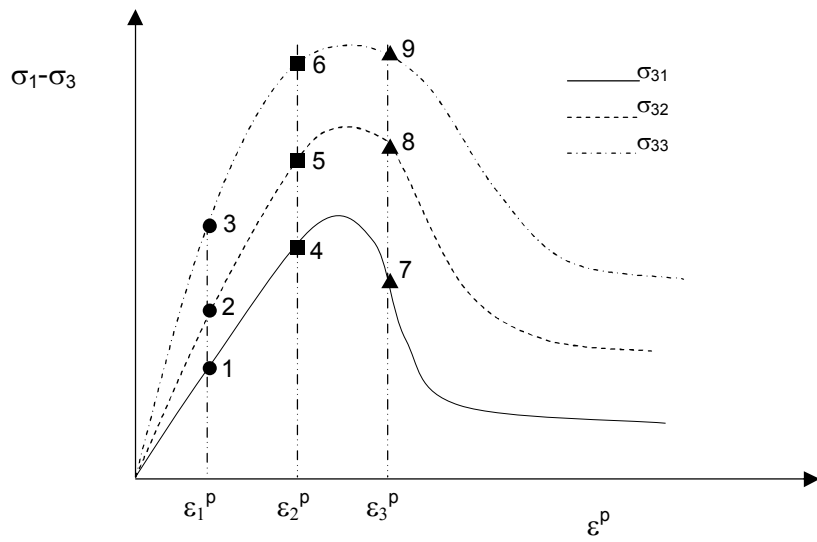


Figure 5.1 A schematic diagram of three stress-strain curves.

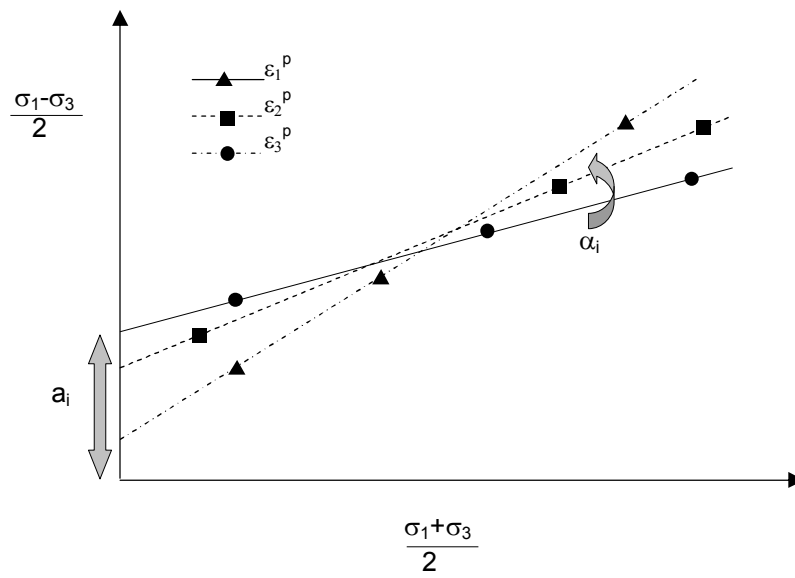


Figure 5.2 Multiple envelopes at different strain contours.

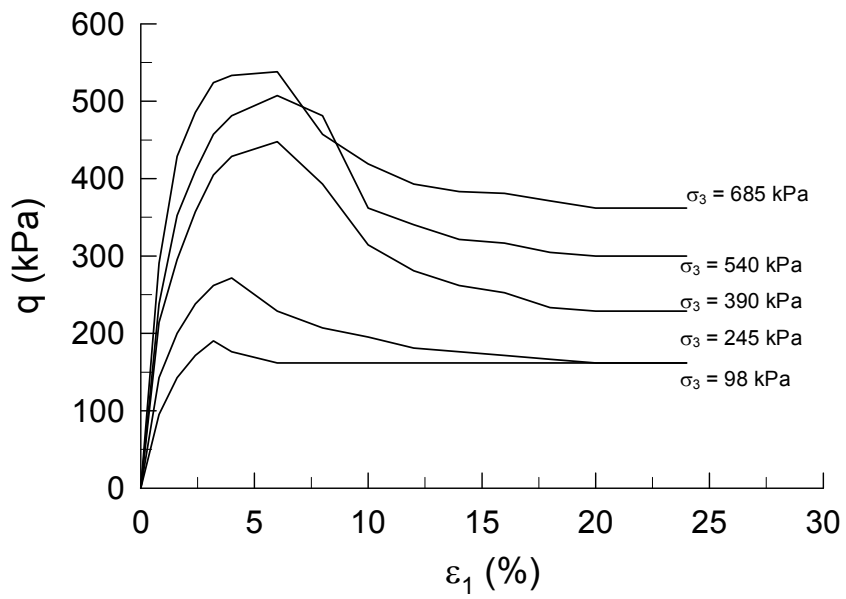


Figure 5.3 Pietrafitta clay stress-strain curves (modified from Callisto and Rampello 2002).

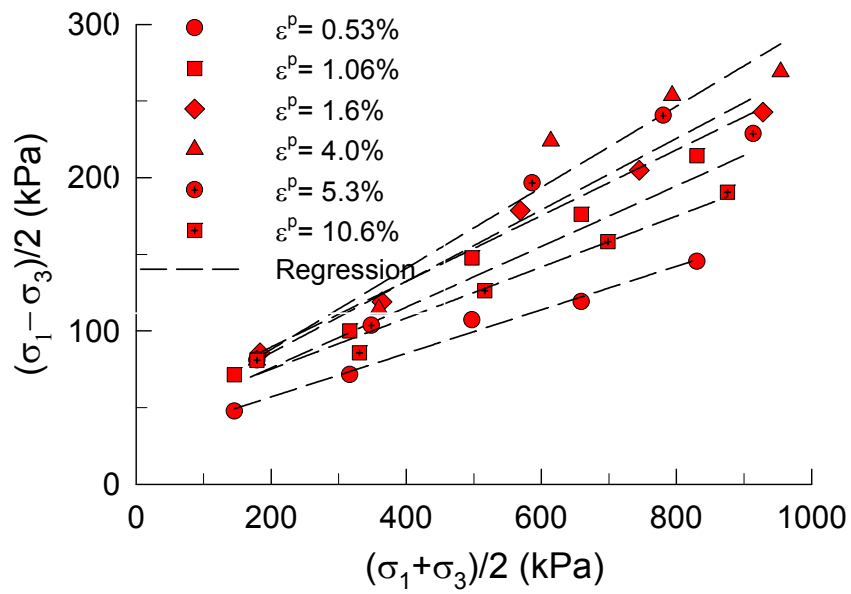


Figure 5.4 Multiple-Yield envelopes in terms of plastic shear strain contours (Pietrafitta clay).

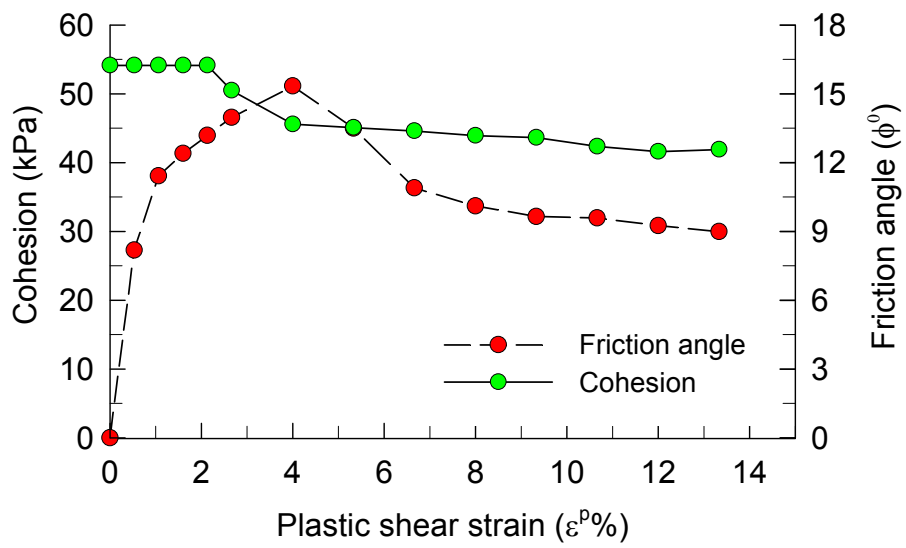


Figure 5.5 Distribution of strength parameters with plastic shear strain level (Pietrafitta clay).

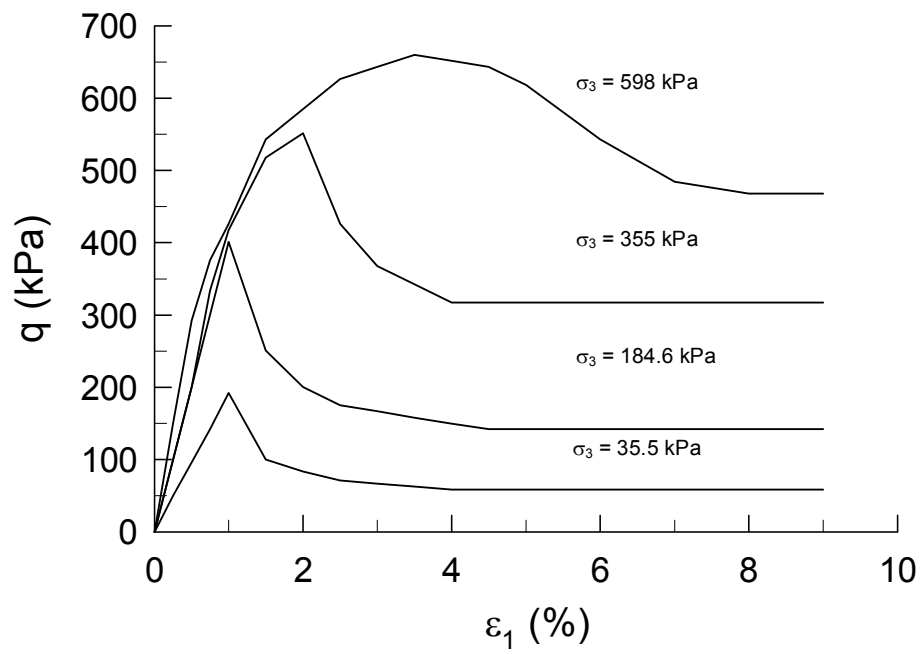


Figure 5.6 Nanticoke clay stress-strain curves (modified from Lo 1972).

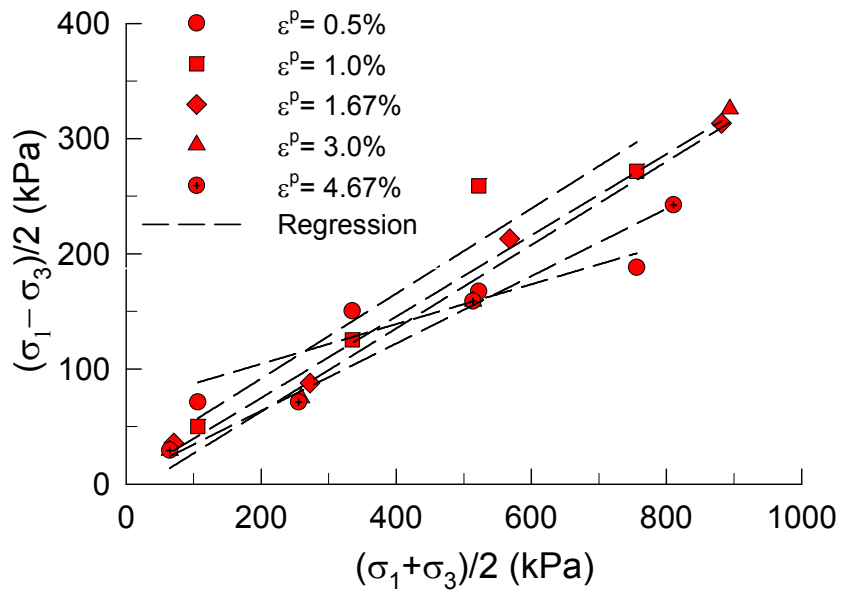


Figure 5.7 Multiple-Yield envelopes in terms of plastic shear strain contours (Nanticoke clay).

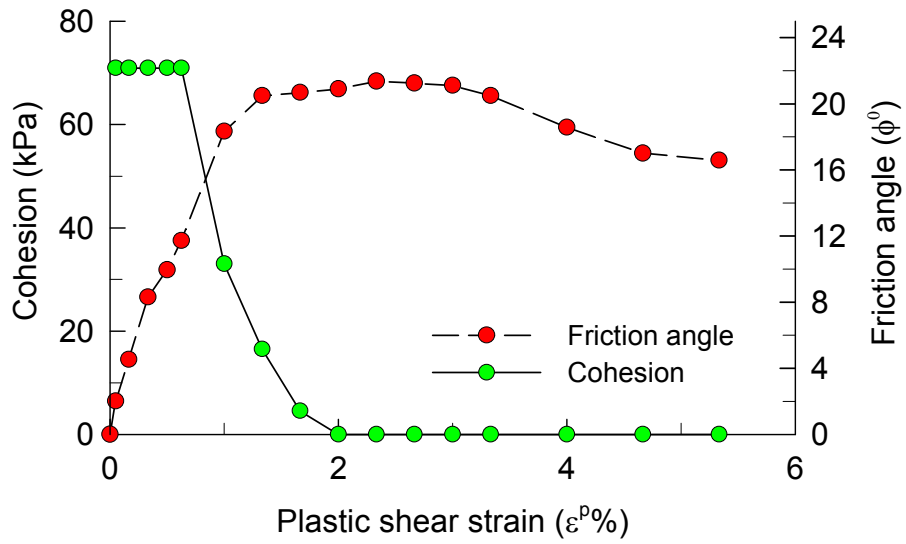


Figure 5.8 Distribution of strength parameters with plastic shear strain level (Nanticoke clay).

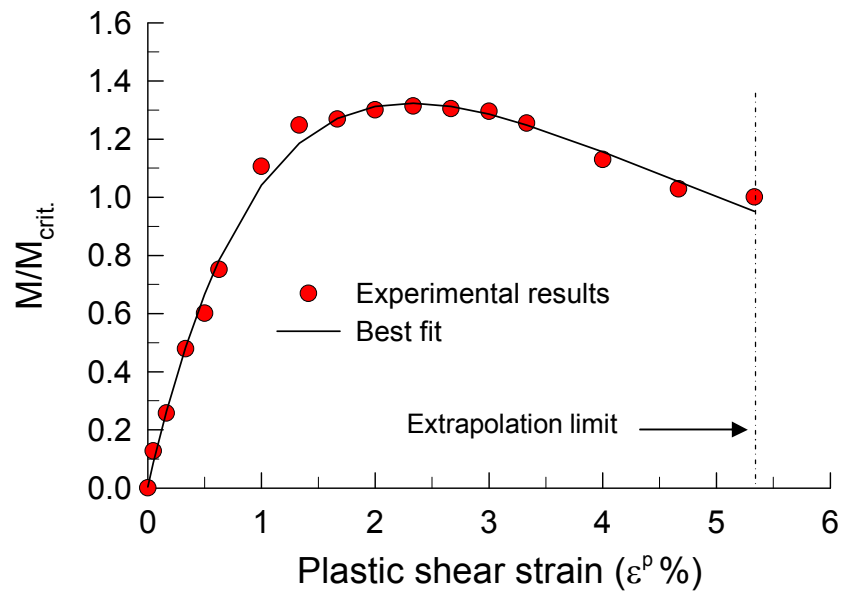


Figure 5.9 Distribution of normalized frictional strength parameter with plastic shear strain.

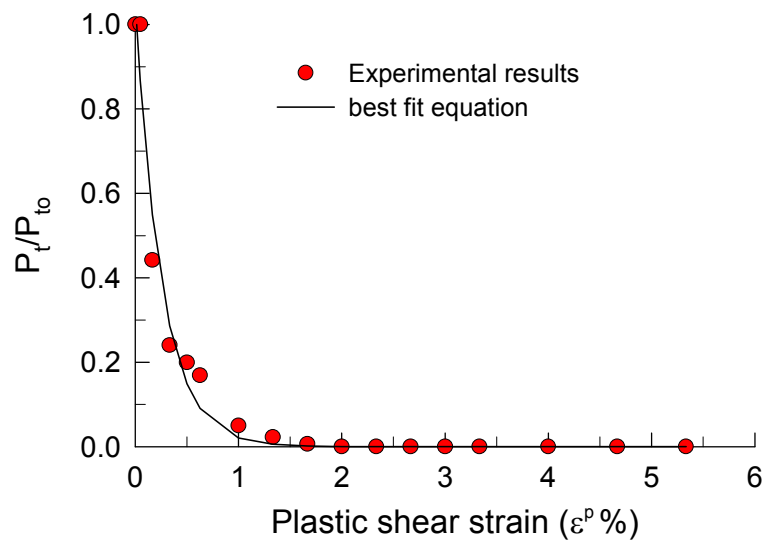


Figure 5.10 Distribution of normalized tensile strength with plastic shear strain.

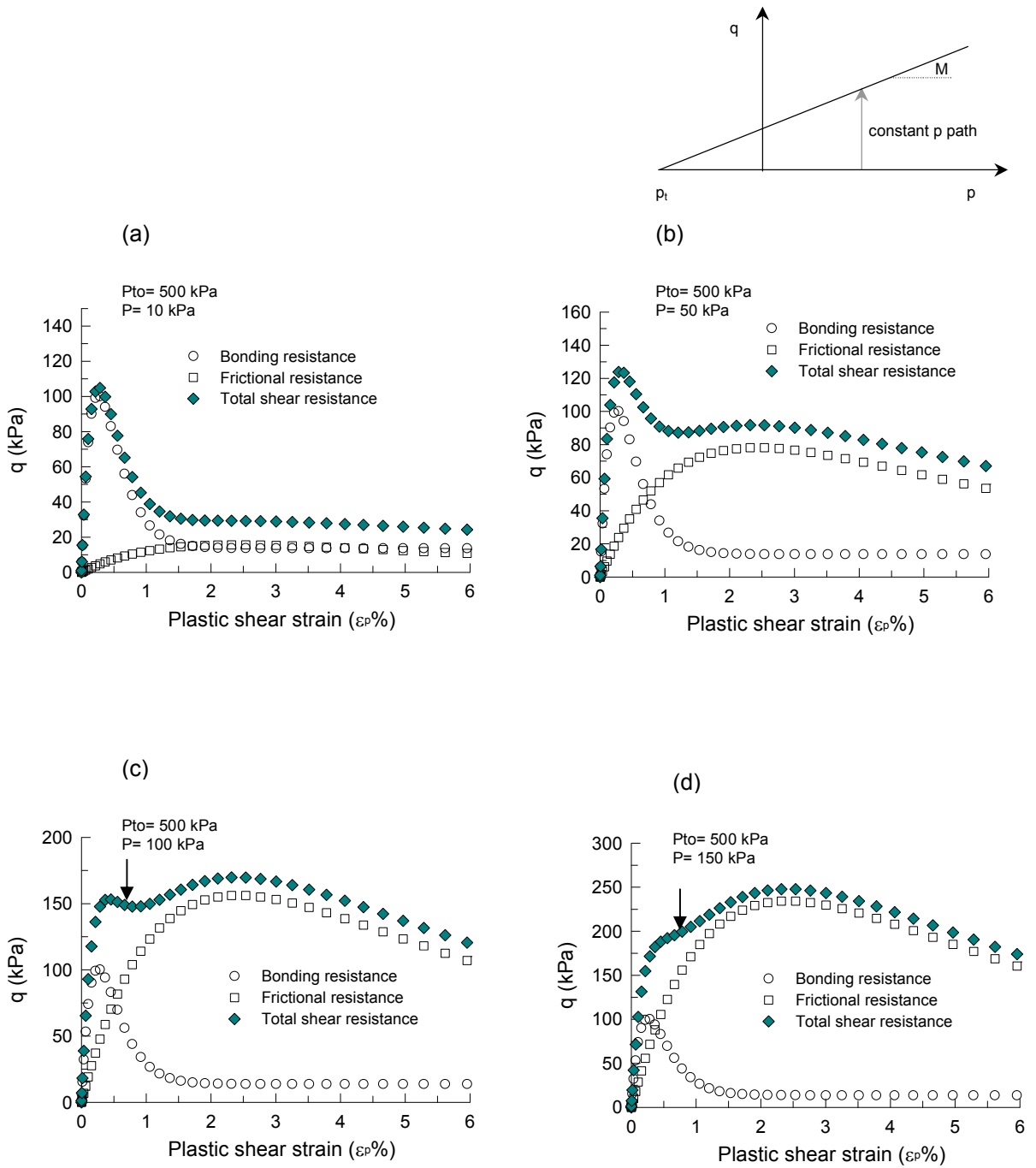


Figure 5.11 Stress-strain curves at various confining stress based on the incremental of equation [5.15].

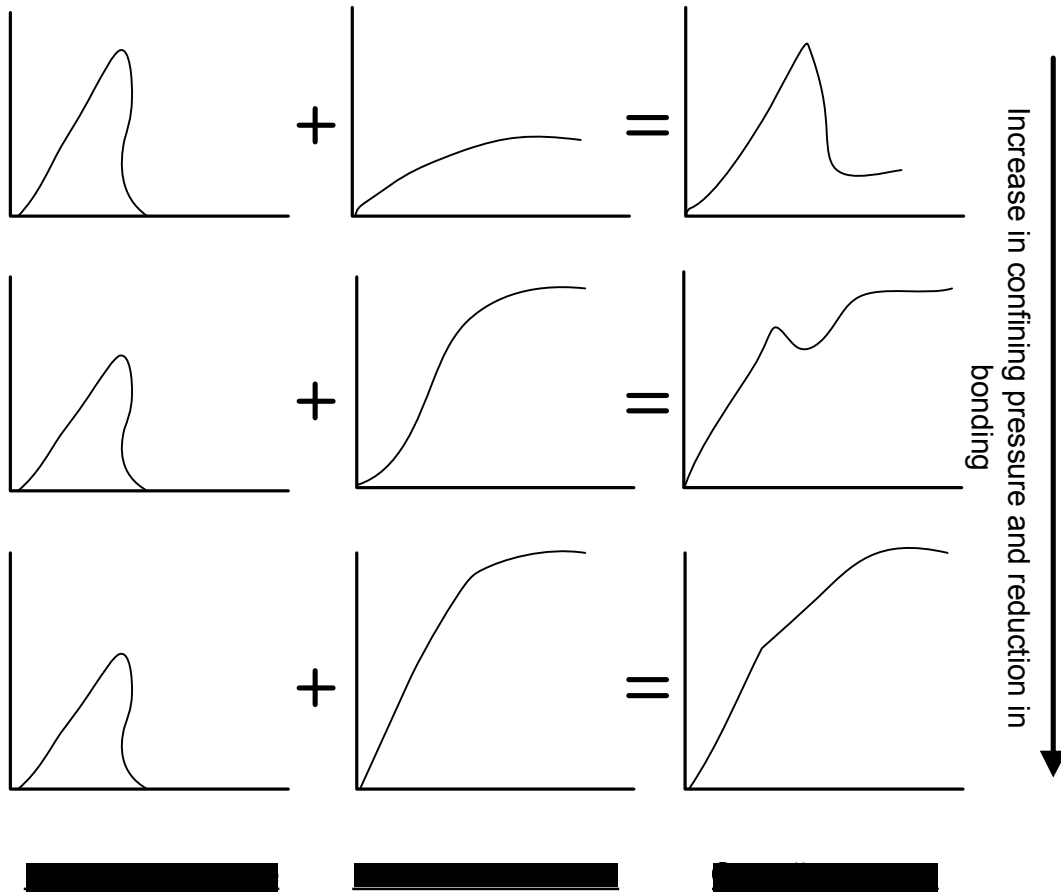


Figure 5.12 Conceptual framework to visualize contribution of frictional and bonding resistance to stiff clay shearing response (modified from Conlon 1966).

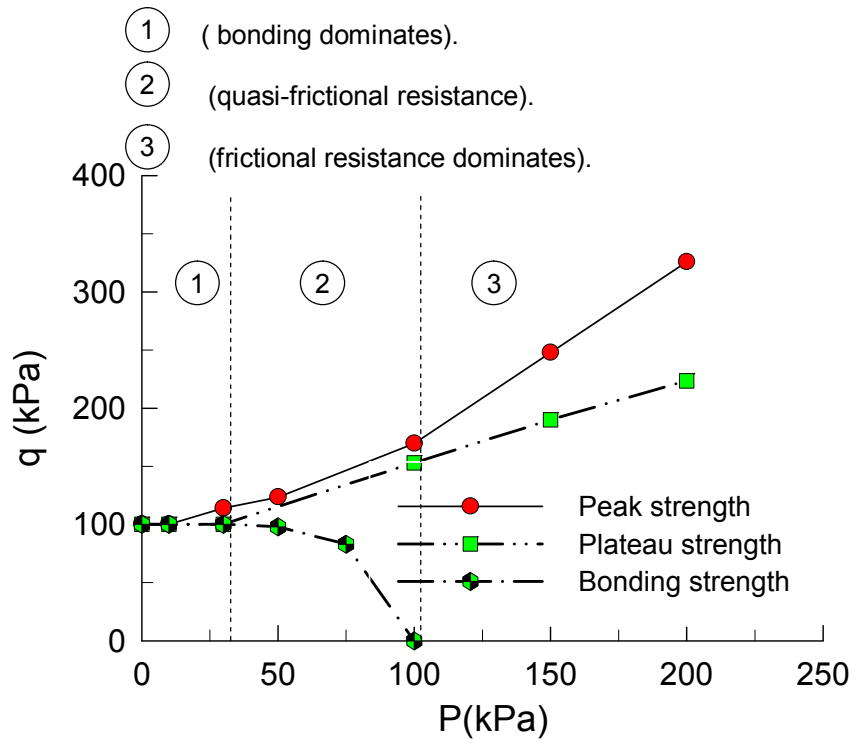
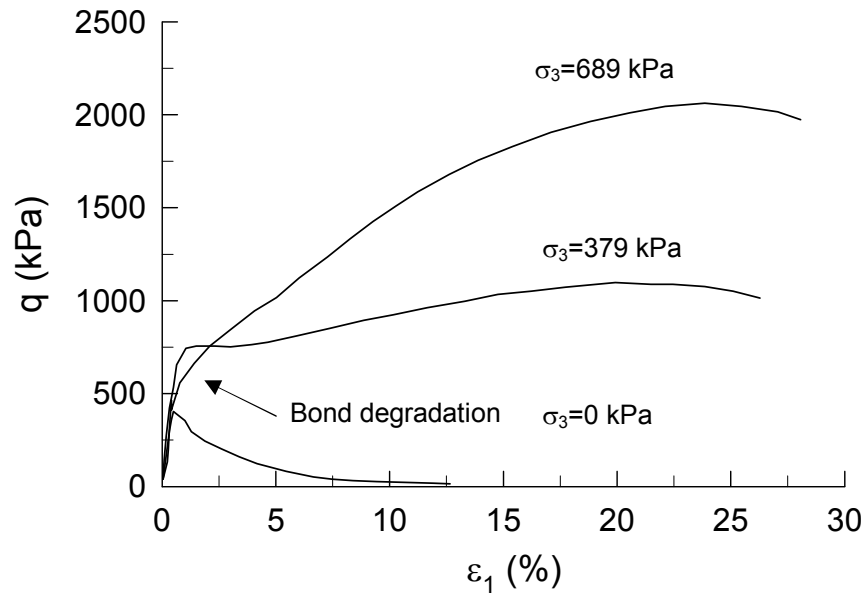


Figure 5.13 Failure, Bonding strength and plateau strength envelopes.

(a) Stress strain curves



(b) Failure envelope

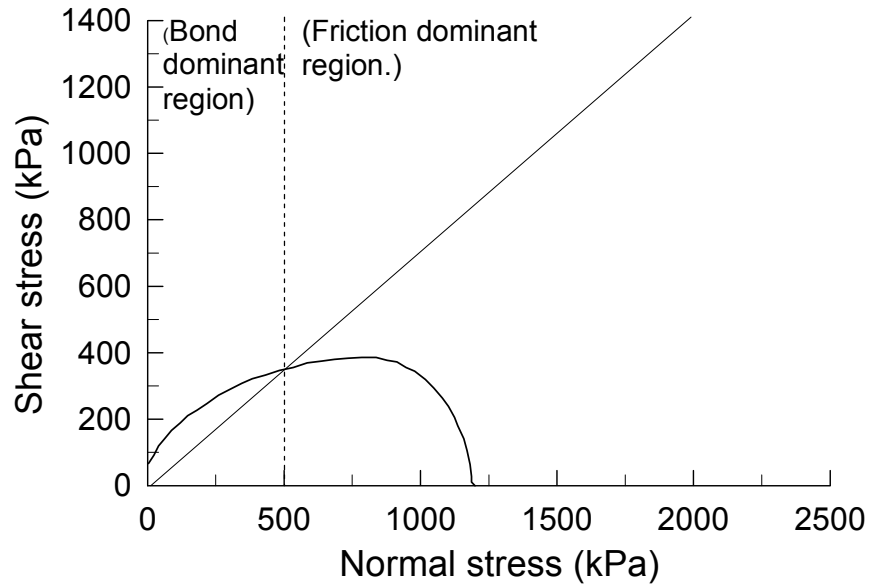


Figure 5.14 Stress-strain curves and failure envelope for Toulnostouc Stiff clay (modified from Conlon 1966).

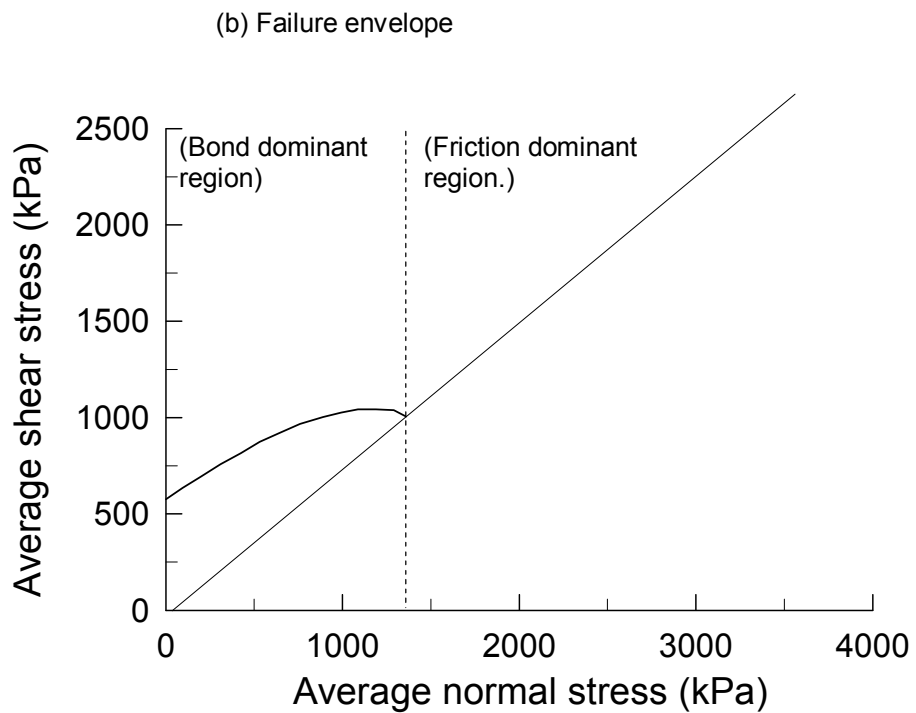
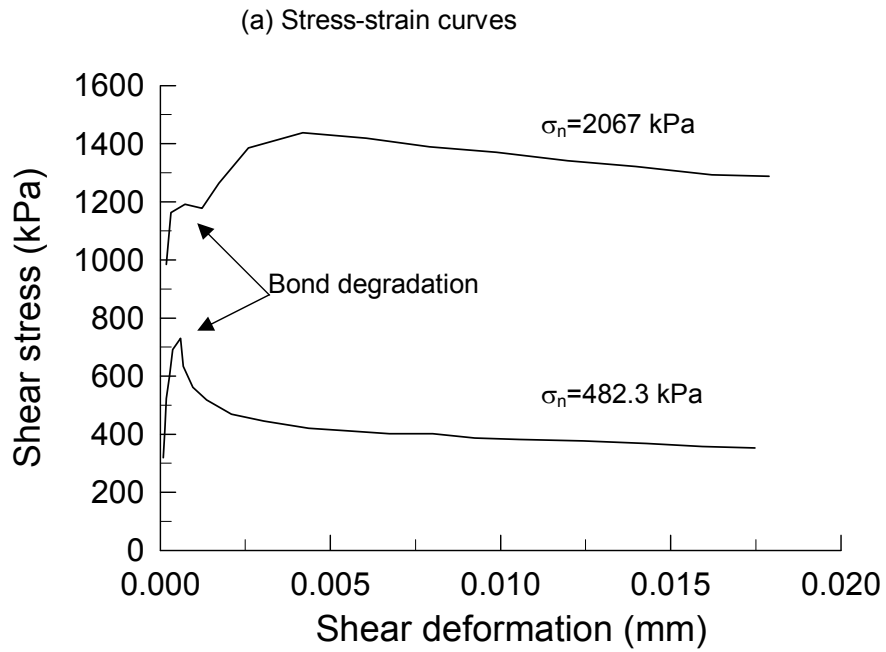


Figure 5.15 Stress-strain curves and failure envelope for Jointed weak rock (modified from Lajtai 1974).

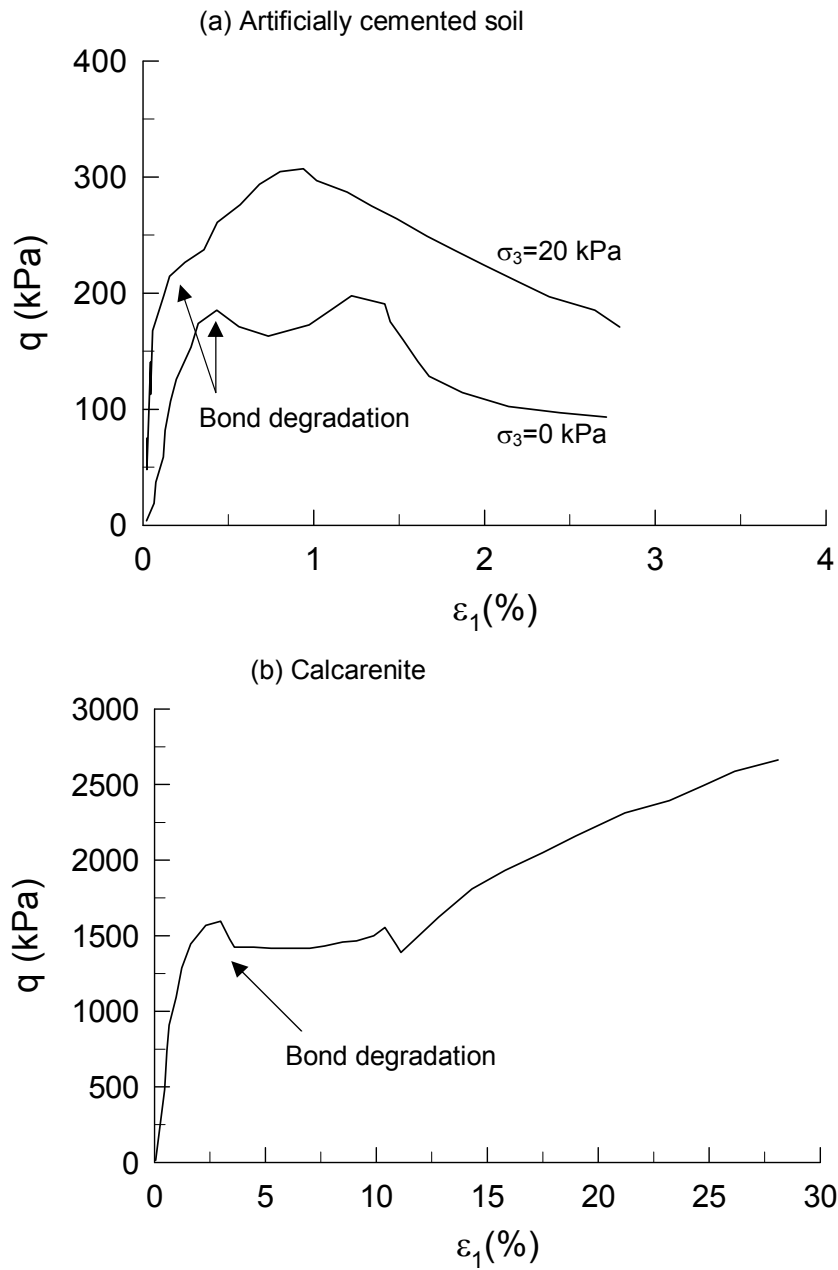


Figure 5.16 Stress-strain curves of Artificially cemented soil and Calcarenite (modified from (a) Lo et al. 2003; and (b) Lagioia and Nova 1995).

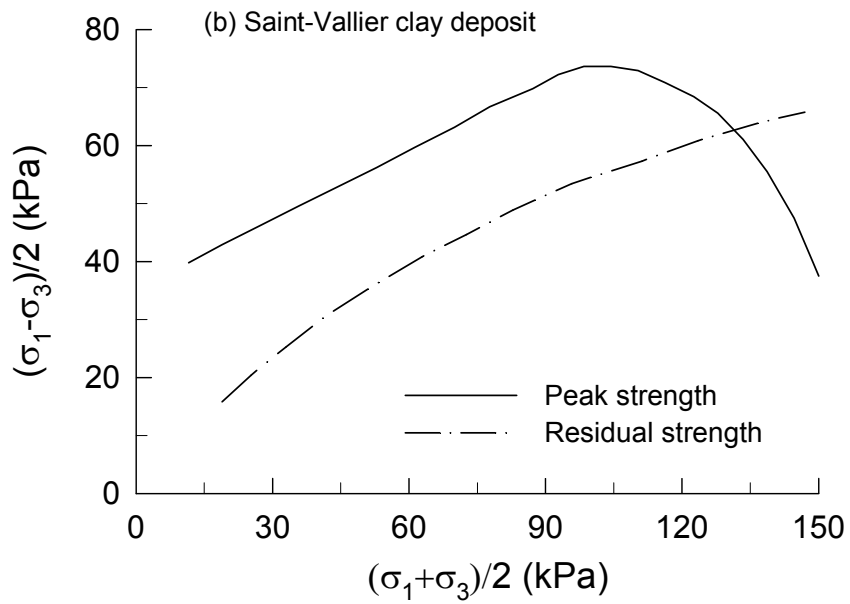
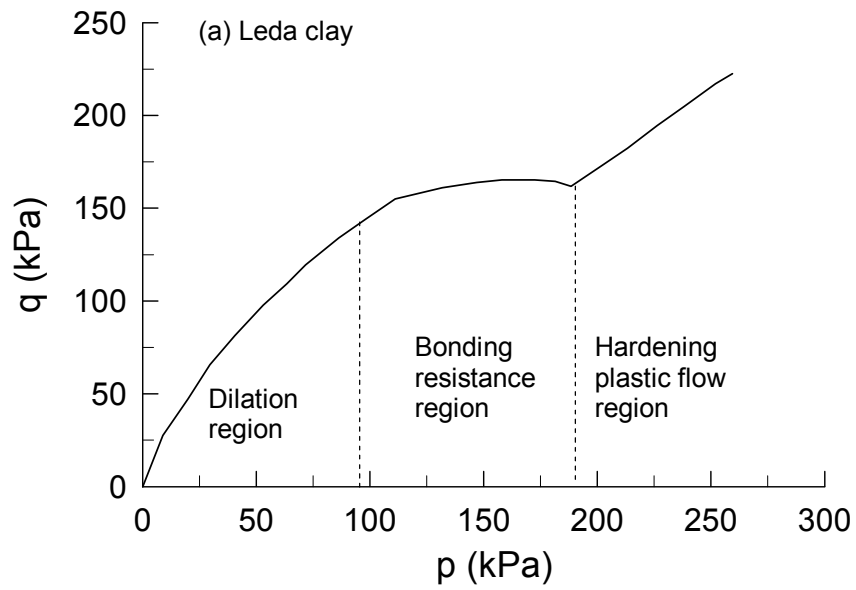


Figure 5.17 Failure envelopes for cemented sensitive clay (modified from (a) Mitchell 1970; and (b) Lefebvre and Rochelle 1974).

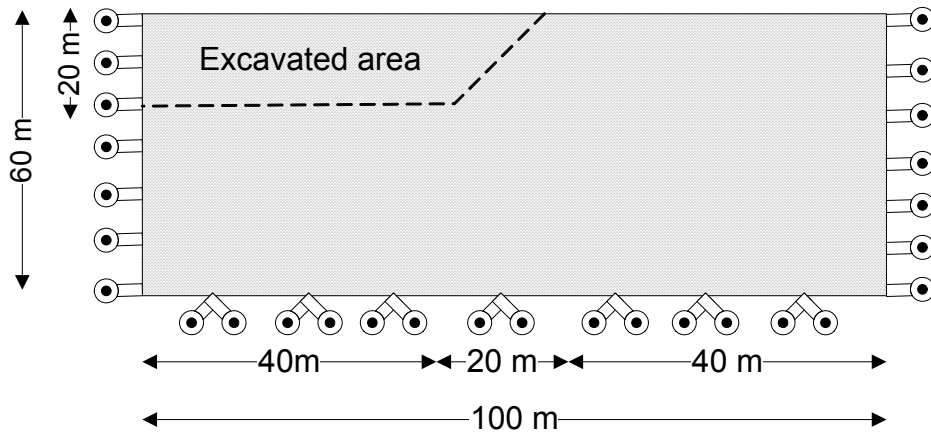


Figure 6.1 Schematic diagram of excavated slope.

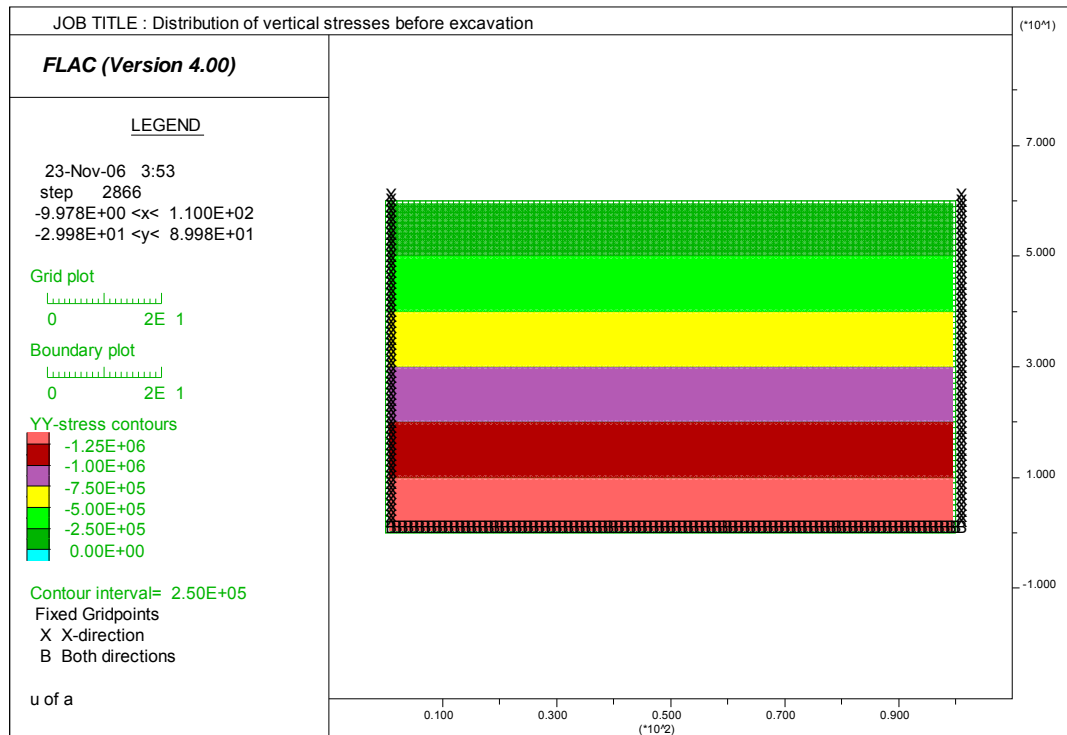


Figure 6.2 Vertical stress contours before excavation.

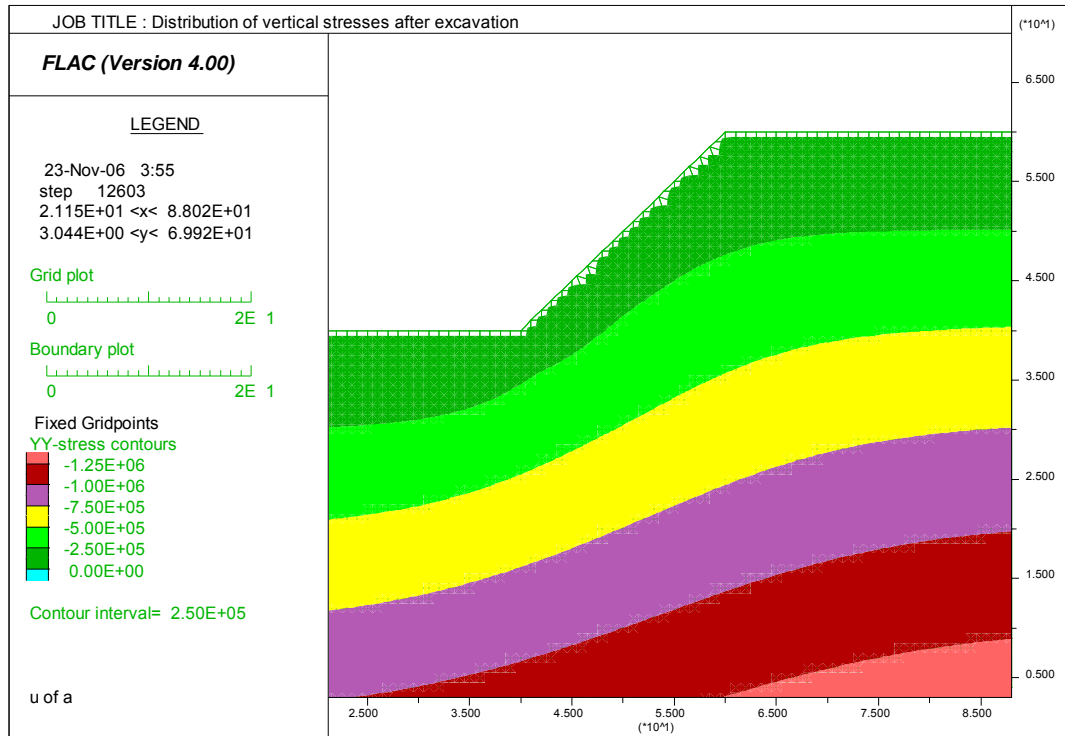


Figure 6.3 Vertical stress contours after excavation.

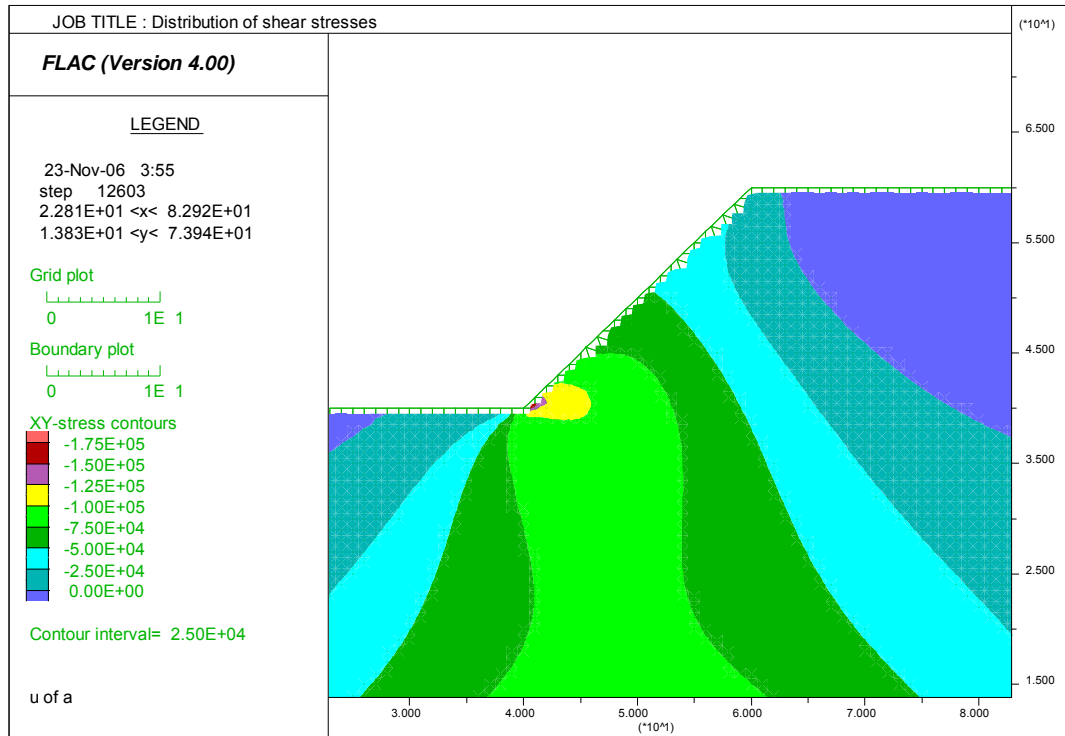


Figure 6.4 Shear stress contours after excavation.

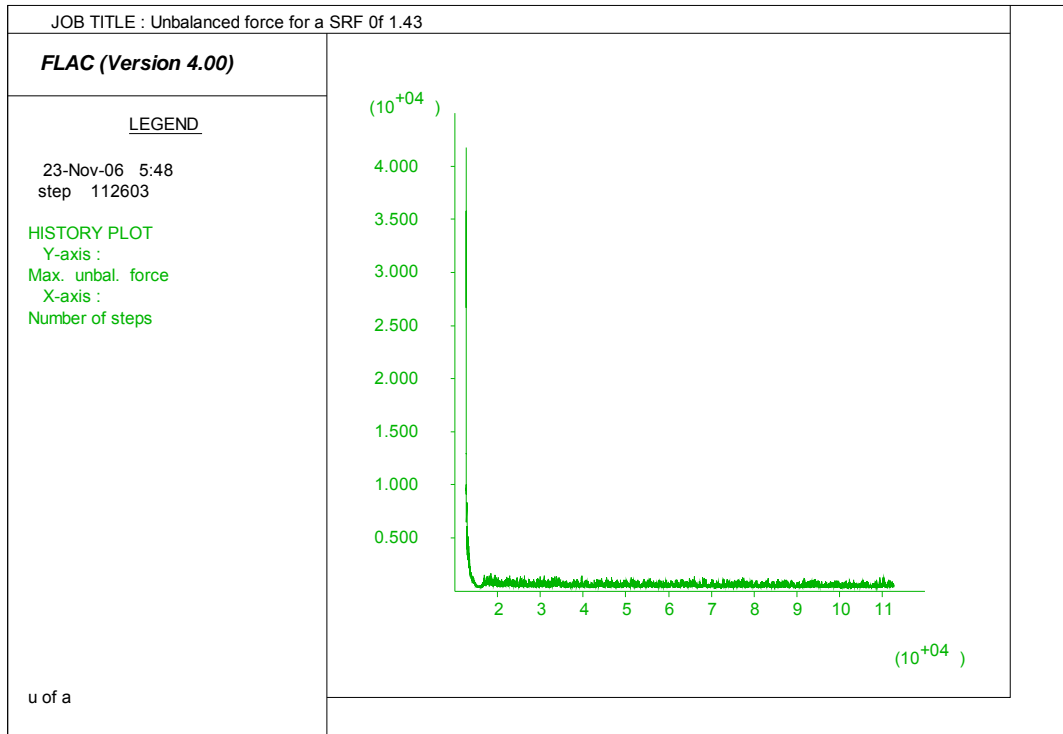


Figure 6.5 Unbalanced forces versus no of steps based on a SRF of 1.43.

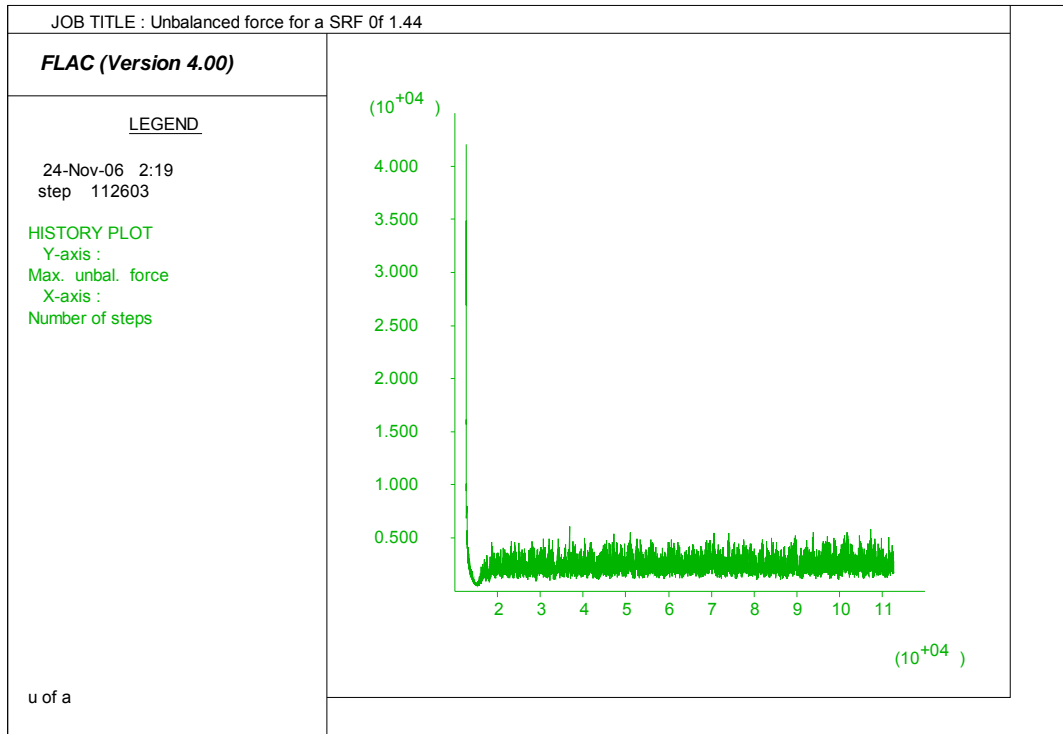


Figure 6.6 Unbalanced forces versus no of steps based on a SRF of 1.44.

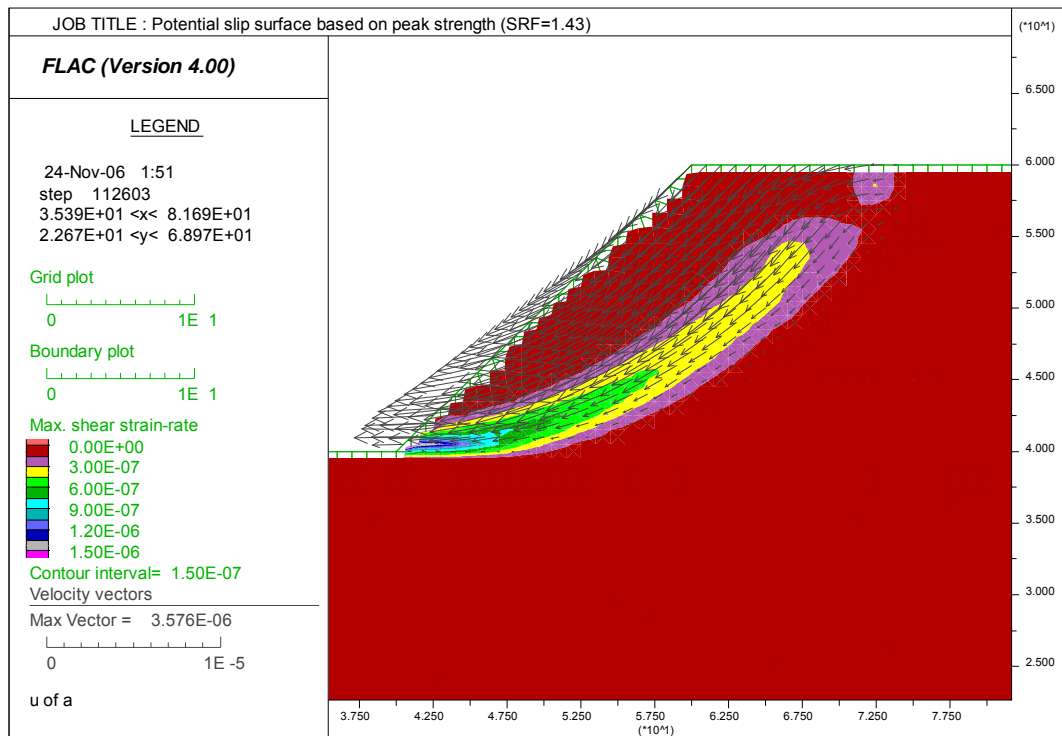


Figure 6.7 The potential slip surface obtained from the SRF technique implemented in FLAC.

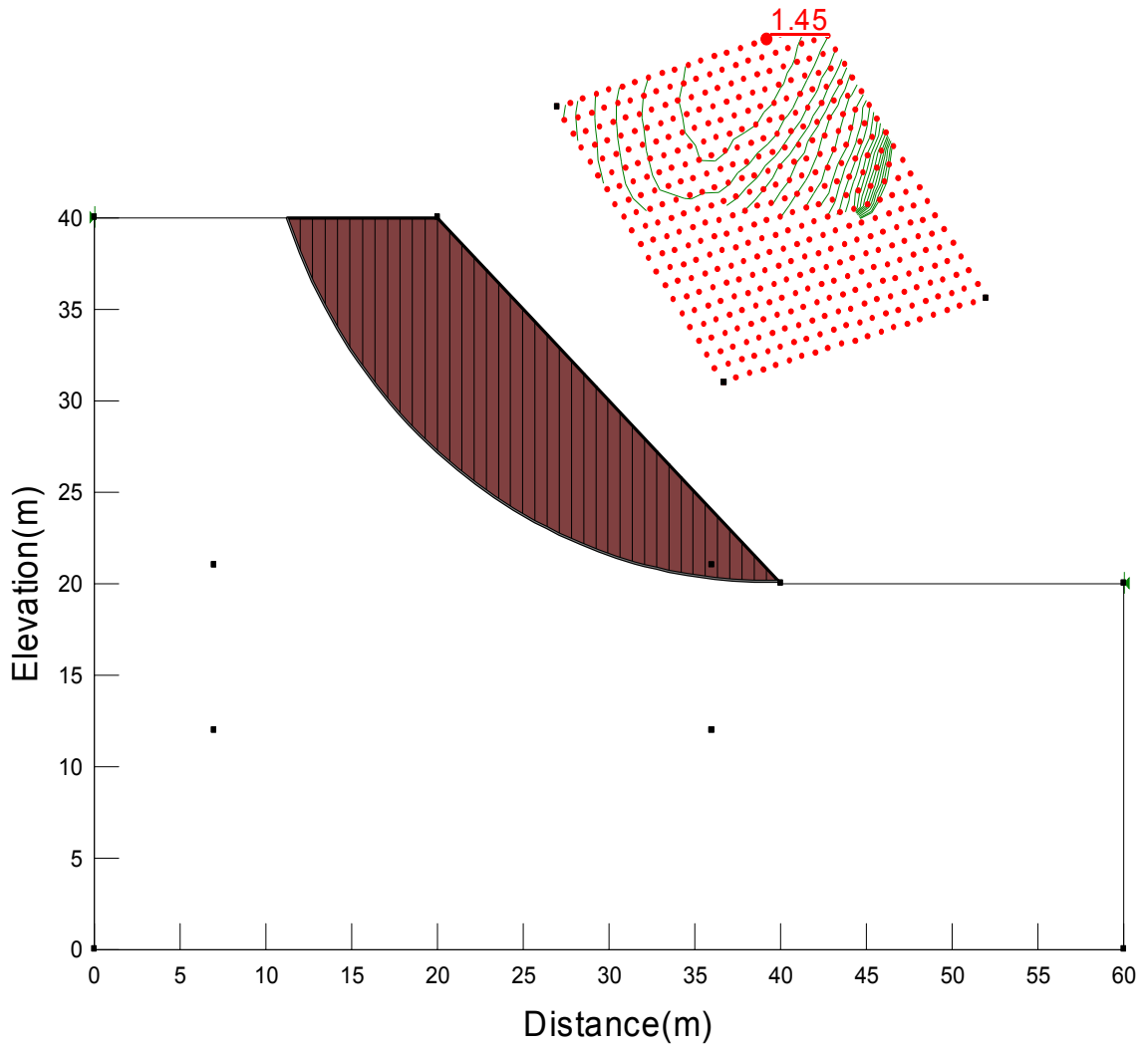
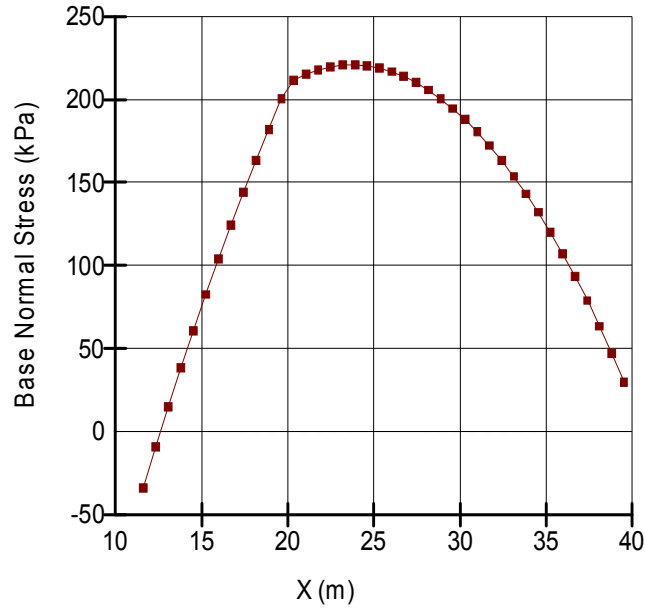
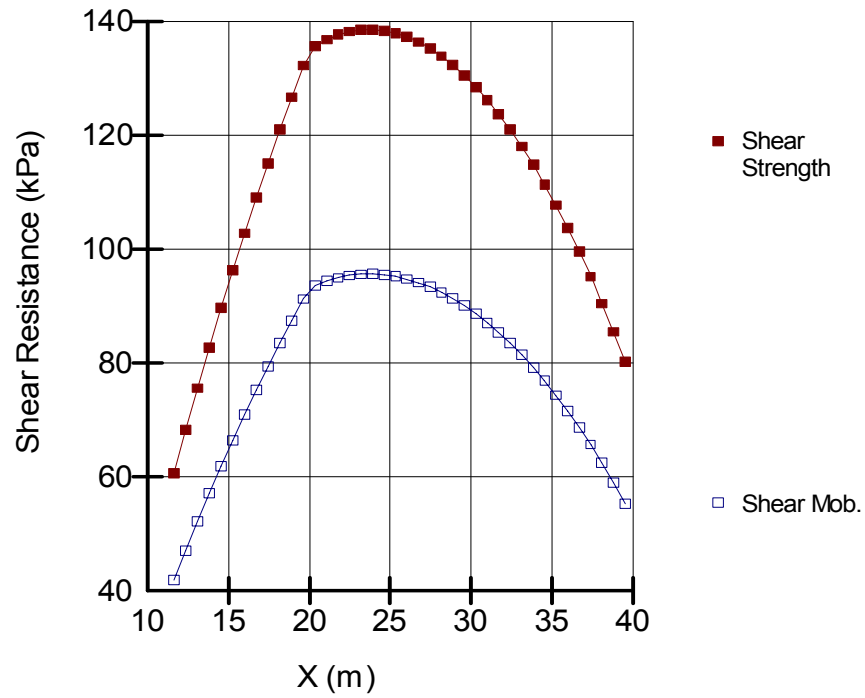


Figure 6.8 The minimum factor of safety and the critical slip surface obtained from LEM.



(a)



(b)

Figure 6.9 The distribution of normal and shear stresses from LEM: (a) the normal stress distribution; and (b) the available and mobilized strength.

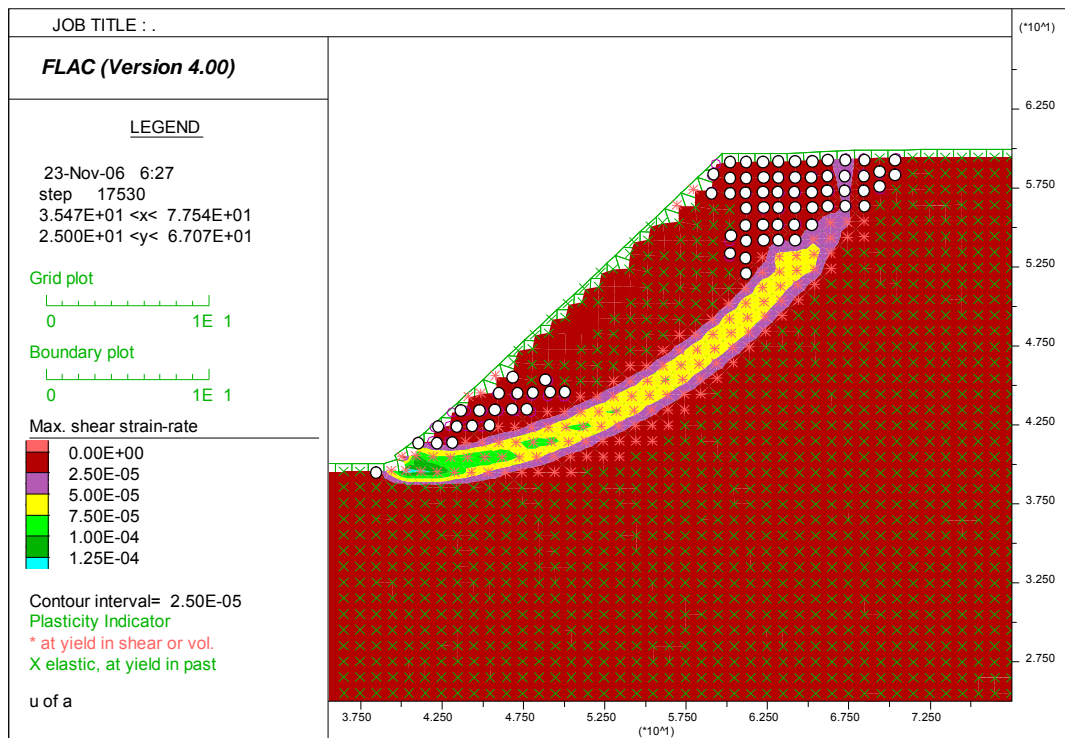
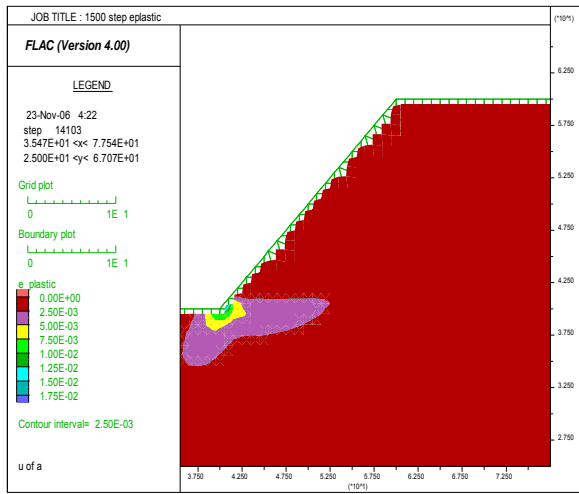
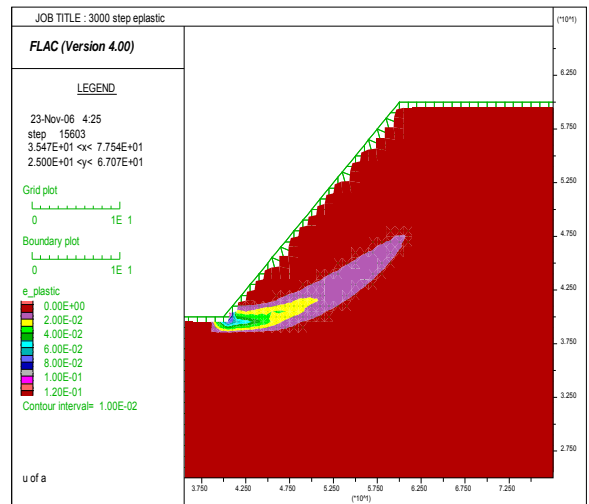


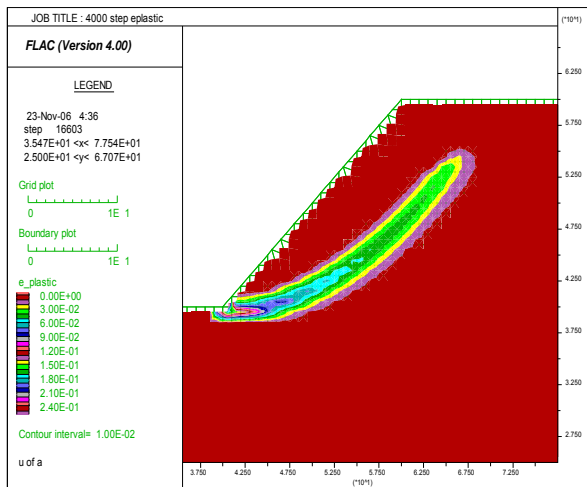
Figure 6.10 The potential slip surface obtained from hardening/softening model implemented in FLAC.



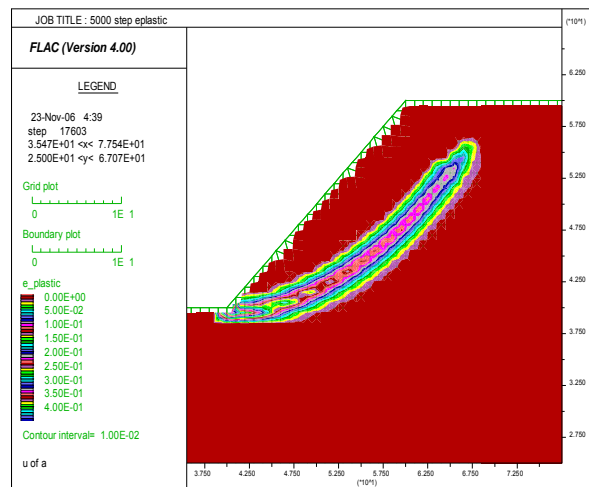
(a)



(b)



(c)



(d)

Figure 6.11 The evolution of potential slip surface at different plastic strain levels: (a) (0-0.017); (b) (0-0.12); (c) (0-0.24); and (d) (0-0.4).

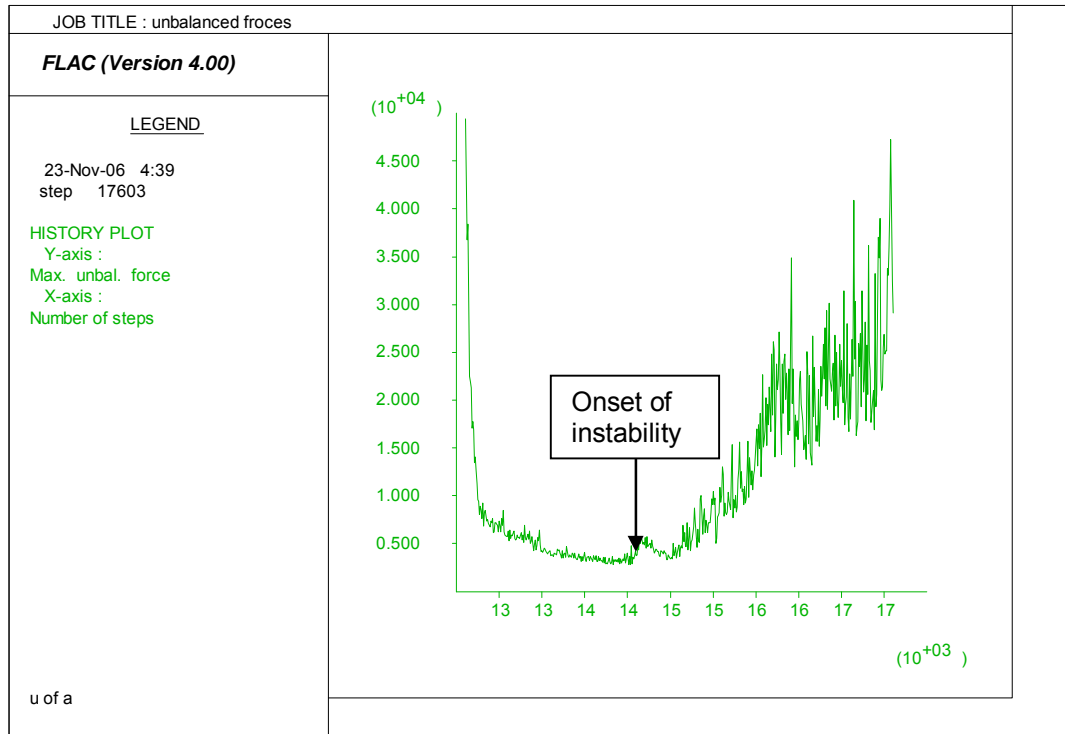


Figure 6.12 The unbalanced forces from hardening/softening model implemented in FLAC.

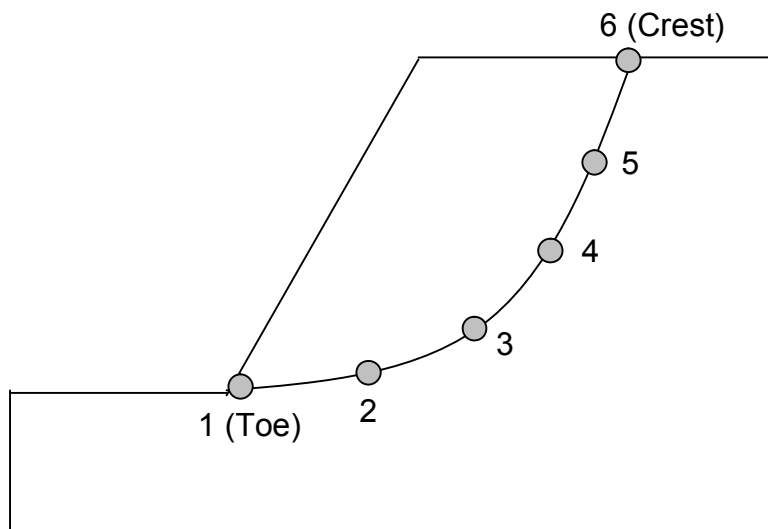


Figure 6.13 Monitoring point along the potential slip surface.

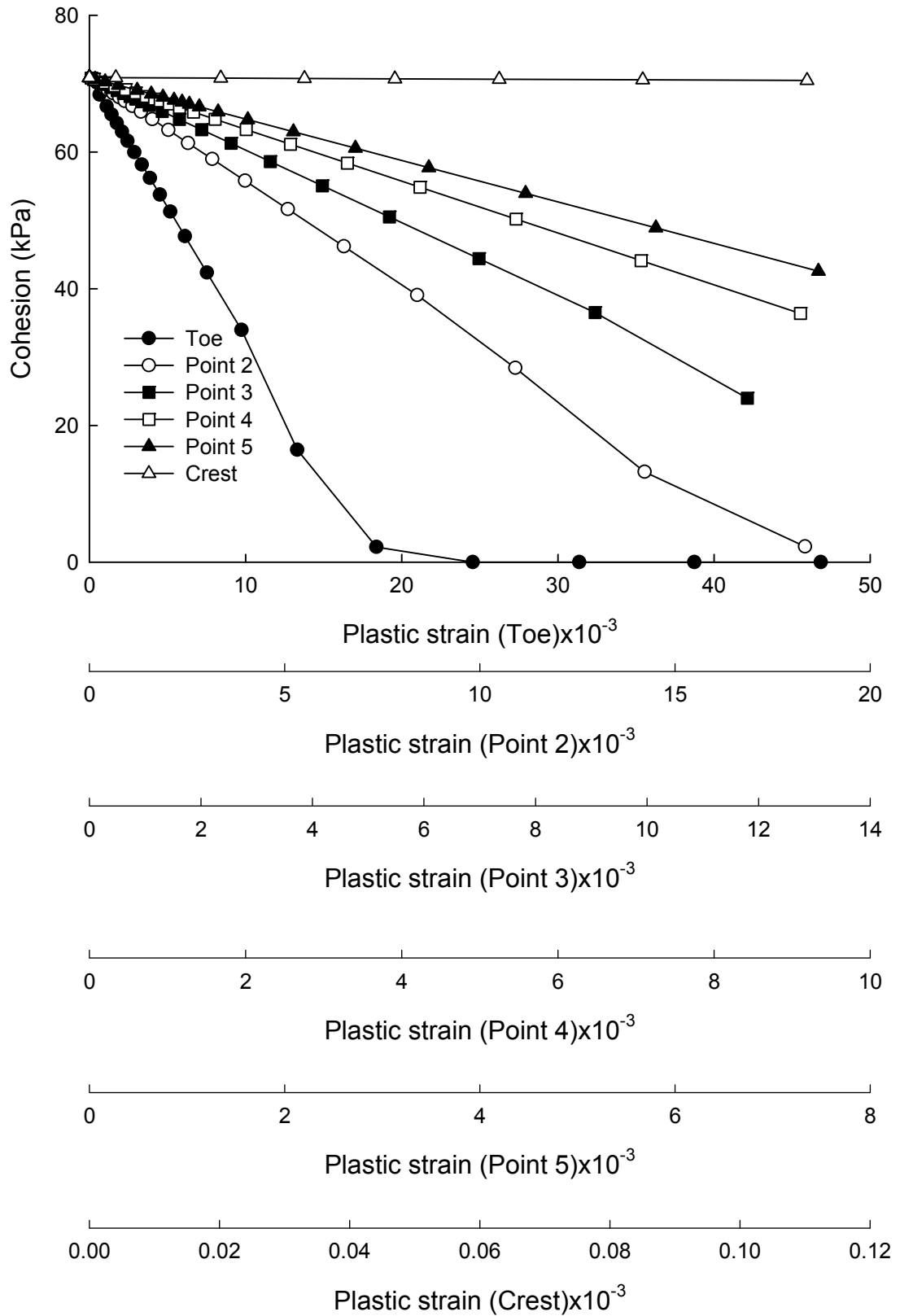


Figure 6.14 Distribution of cohesion along the potential slip surface.

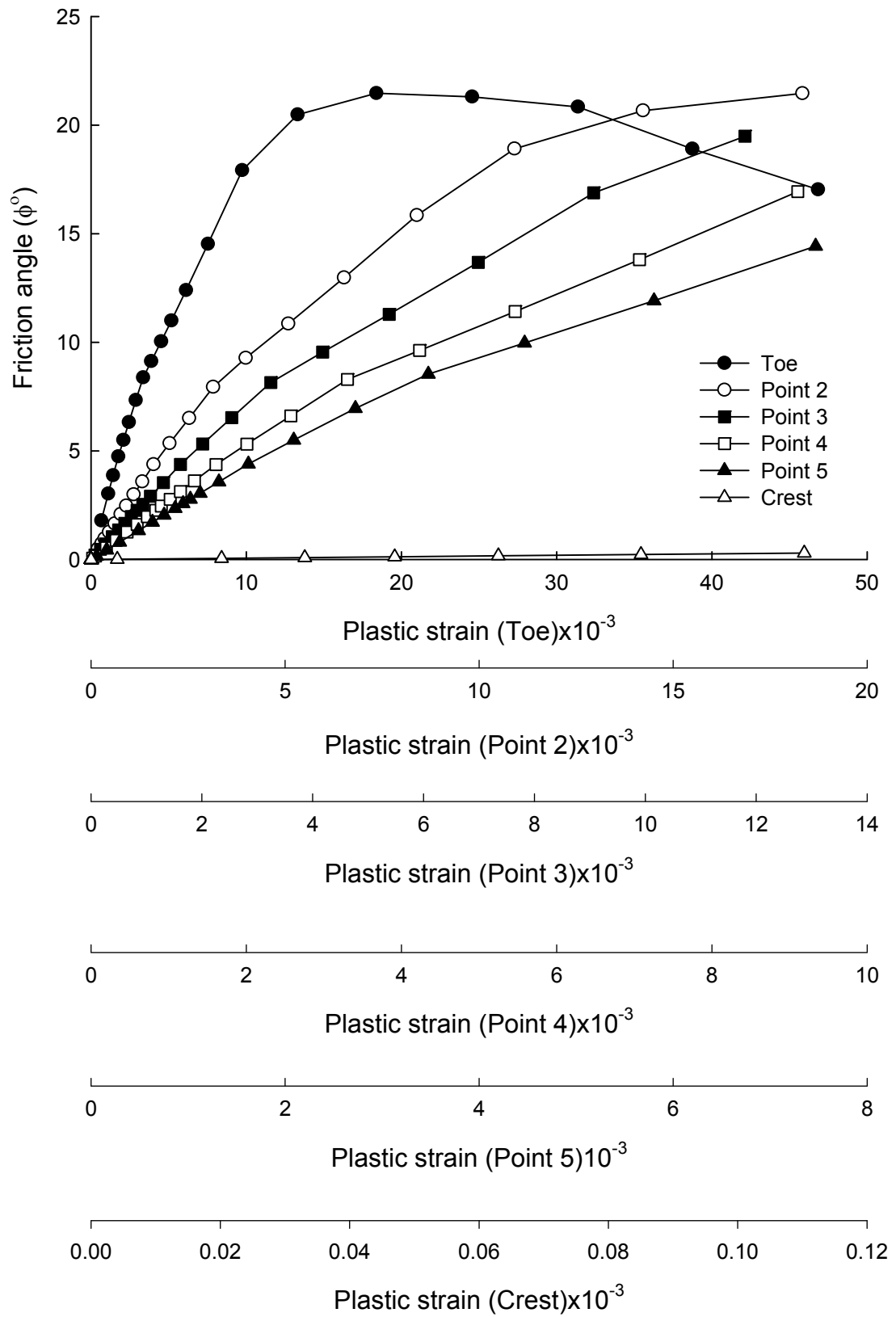


Figure 6.15 Distribution of friction angle along the potential slip surface.

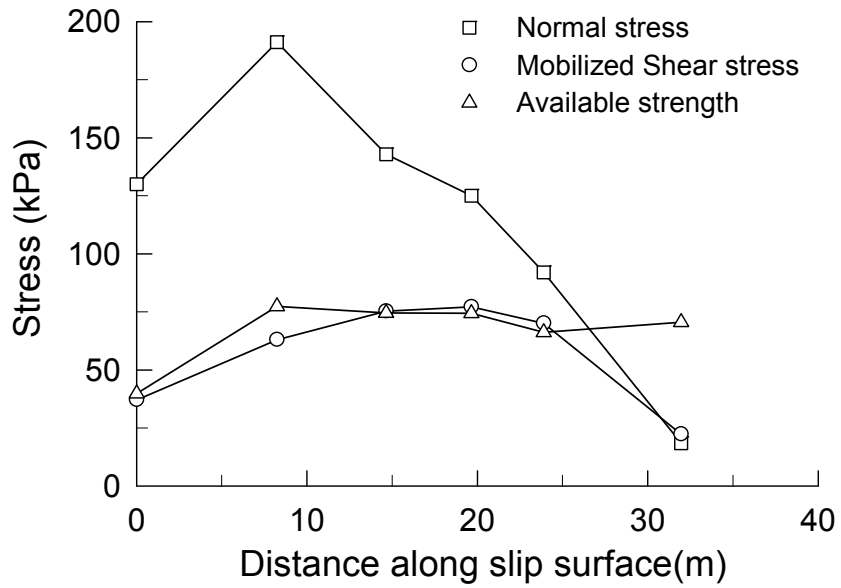


Figure 6.16 Distribution of normal, shear stresses, and available strength along the slip surface associated with SDP.

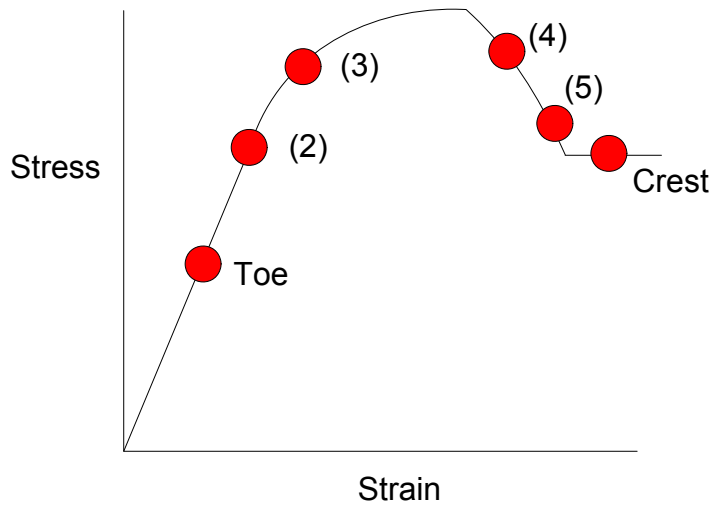


Figure 6.17 A schematic illustration of monitoring point's position on stress-strain curve.

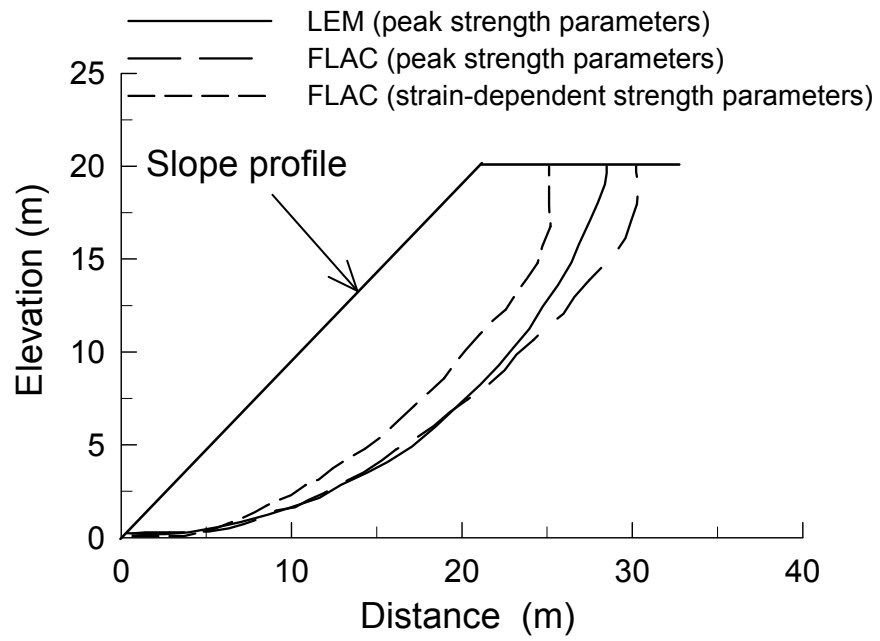


Figure 6.18 A comparison between the positions of slip surfaces based on peak strength and strain-dependent strength parameters.

